



# A. Yücel Odabaşı Colloquium Series

## ***2<sup>nd</sup> International Meeting***

### ***Recent Advances in Prediction Techniques for Safe Manoeuvring of Ships and Submarines***

17 - 18 NOVEMBER 2016

FACULTY OF NAVAL ARCHITECTURE AND OCEAN ENGINEERING

ISTANBUL TECHNICAL UNIVERSITY

[www/ayocol.itu.edu.tr](http://www/ayocol.itu.edu.tr)

Edited by

Kadir Sarıöz  
Hayriye Pehlivan Solak



Faculty of Naval Architecture and Ocean Engineering





# A Yücel Odabaşı Colloquium Series

## ***2<sup>nd</sup> International Meeting***

### ***Recent Advances in Prediction Techniques for Safe Manoeuvring of Ships and Submarines***

17 - 18 November 2016

FACULTY OF NAVAL ARCHITECTURE AND OCEAN ENGINEERING  
ISTANBUL TECHNICAL UNIVERSITY

[www.ayocol.itu.edu.tr](http://www.ayocol.itu.edu.tr)

Edited by

Kadir Sarıöz  
Hayriye Pehlivan Solak



Faculty of Naval Architecture and Ocean Engineering



## TABLE OF CONTENTS

|                             |      |
|-----------------------------|------|
| SPONSORS .....              | i    |
| PREFACE .....               | iii  |
| COLLOQUIUM COMMITTEES ..... | v    |
| PROF. A. YÜCEL ODABAŞI..... | viii |

### Keynote Lectures

|  |    |
|--|----|
| Modelling of Manoeuvring in Calm Water and Waves .....                     | 1  |
| <i>Odd Faltinsen</i>   |    |
| Ship Manoeuvrability, Controllability and Safety ( <i>Abstract</i> ) ..... | 11 |
| <i>Kazuhiko Hasegawa</i>   |    |

### Papers

|  |     |
|--|-----|
| Current Status of Manoeuvring Prediction Methods, Their Mutual Pros and Cons and Ways to Quantify The Capabilities ..... | 13  |
| <i>Frans Quadvlieg</i>   |     |
| The Hydrodynamics of a Spheroidal Submarine Close to the Free Surface.....   | 21  |
| <i>Ioannis K. Chatjigeorgiou, Touvia Miloh</i>   |     |
| Developments of Hydrodynamic Modeling Techniques for Underwater Vehicles.....  | 31  |
| <i>Sertaç Arslan</i>   |     |
| A Mathematical Model for Studying Maneuvering Motions and Course Instabilities of Sailing Yachts.....                    | 39  |
| <i>Manolis Angelou, Kostas J. Spyrou</i>   |     |
| The Gate Rudder Application to Ships Suffering from Poor Coursekeeping Ability .....                                     | 49  |
| <i>Serkan Türkmen, Noriyuki Sasaki, Mehmet Atlar, Adrian Miles, Toshifumi Takeda</i>                                     |     |
| A Prediction Program of Manoeuvrability for a Ship with a Gate Rudder System.....  | 57  |
| <i>Alessandro Carchen, Weichao Shi, Noriyuki Sasaki, Mehmet Atlar</i>  |     |
| Towards Establishing Minimum Installed Power for safe Manoeuvring of Ships in Adverse Environmental Condition.....       | 67  |
| <i>Emmanuel Irimagha, Richard Birmingham, Michael Woodward, Zhiqiang Hu</i>  |     |
| On the State-of-Art for Hydrodynamic Assessment of Offshore Heavy Lift & Installation Vessels DP Systems .....           | 75  |
| <i>Zafer Ayaz</i>  |     |
| Design and Development of a New Free-Running Manoeuvring test Facility at ITU .....                                      | 85  |
| <i>Cansin Özden, Sertaç Kurdoğlu, Ersin Demir</i>  |     |
| Numerical Investigation of Viscous Effects on the Static PMM Tests of Ships .....  | 89  |
| <i>Süleyman Duman, Şakir Bal</i>   |     |
| Design and Implementation of a Planar Motion Mechanism at ITU Ship Model Basin .....                                     | 99  |
| <i>Cansin Özden, Sertaç Kurdoğlu, Ersin Demir</i>  |     |
| Performance Prediction for Tractor type Escort Tugs .....  | 105 |
| <i>Gürbüz Bilici, Çağrı Aydin, Uğur Oral Ünal, Kadir Sarıöz</i>  |     |

|   |                 |
|---|-----------------|
| Maneuvrability Analysis of Twin Screw Ships by CFD .....        | (not available) |
| <i>Mustafa İnsel, Ahmet Ziya Saydam, Serhan Gökçay</i>          |                 |
| A Deforming Grid Approach for Ship Maneuvering Simulations..... | 117             |
| <i>Ömer Faruk Sukas, Ömer Kemal Kinaci</i>                      |                 |
| Author Index .....  | 123             |

## SPONSORS



Istanbul Technical University



Turkish Chamber of Shipping



Türk Loydu



Turkish Shipbuilders'  
Association



Nippon Kaiji Kyokai



Anadolu Shipyard



Det Norske Veritas and Germanischer Lloyd



## PREFACE

The first of this Colloquium Series was organized in 2014 to commemorate the life-long scientific endeavors of Prof. A. Yücel Odabaşı and it was decided to carry on the colloquium series biennially. The second colloquium is now scheduled to take place on November 17-18, 2016. The theme of the second colloquium is selected as ‘Recent Advances in Prediction Techniques for Safe Manoeuvring of Ships and Submarines’. The goal of this colloquium would be to create a platform where the recent developments in experimental and computational methods for predicting manoeuvring performance of surface vessels and submarines are discussed and new opportunities for collaborative research are sought. On the one hand, safe manoeuvring of ships is gradually becoming an important focus of interest among naval architects. On the other hand, ITU is currently working on the design, development and then eventually installation of a new PMM in its towing tank and a free-running manoeuvring system in the small lake at ITU campus. We hope to discuss our approaches and designs in front of the experts of the international ship manoeuvring community.

The Colloquium gathers under stressful environment and conditions which affect the world and particularly Turkey. Under these circumstances we owe a lot to the international contributors and participants who do not let us alone in this event. Our special thanks go to our sponsors which made this colloquium possible. We hope that the world turns out to be a peaceful place in the near future which – we believe – can make the things including this colloquium sustainable.

Ömer Gören  
*on behalf of the Local Organizing Committee*  
İstanbul, Nov. 15, 2016



## **COLLOQUIUM COMMITTEES**

### **Standing Committee**

Dr. Mehmet Atlar, *University of Strathclyde, Scotland*  
Dr. Sander Çalışal, *University of British Columbia, Canada / Piri Reis University, Turkey*  
Dr. Atilla İncecik, *University of Strathclyde, Scotland*  
Dr. Barbaros Okan, *Istanbul Technical University, Turkey*  
Dr. Öner Şaylan, *Istanbul Technical University (Retired), Turkey*

### **Technical Committee**

Dr. David Clarke, *University of Newcastle, UK*  
Dr. Odd M. Faltinsen, *Norwegian University of Science and Technology, Norway*  
Dr. Kazuhiko Hasegawa, *Osaka University, Japan*  
Dr. Kadir Sarıöz, *Istanbul Technical University, Turkey*

### **Local Organizing Committee**

Dr. Devrim B. Danışman, *Istanbul Technical University, Turkey*  
Dr. Ömer Gören (Chair), *Istanbul Technical University, Turkey*  
Mr. M. Cansın Özden, *Istanbul Technical University, Turkey*  
Mrs. Hayriye Pehlivan Solak, *Istanbul Technical University, Turkey*  
Mr. Şafak C. Karakaş, *Istanbul Technical University, Turkey*  
Dr. Burcu Ünal (Secretary), *Istanbul Technical University, Turkey*



## **PROF. A. YÜCEL ODABAŞI**



(1945 – 2009)

Professor Odabaşı, a graduate of ITU (1967), earned his Ph.D. degree from the same university in 1971. Following his Ph.D., he joined Strathclyde University where his work on the application of Lyapunov's theory to ship stability gained him a well deserved international reputation which was acknowledged by STAB Award in 2012 post mortem. In 1974 he joined BSRA where he worked on every field of ship hydrodynamics and made significant contributions, in particular in the field of wake scaling. In 1988 he moved to USA to set up BMT International as its first director and CEO. He returned to ITU-Turkey in 1991 where he inspired a generation of young academics while at the same time succeeding to lead Turkish Lloyd to worldwide recognition. He was awarded the gold medal of NECIES-UK and numerous awards from NAVSEA, SNAME, BSRA.



## Modelling of Manoeuvring in Calm Water and Waves

**Odd M. Faltinsen\***

*Centre for Autonomous Marine Operations and Systems (AMOS),  
Department of Marine Technology, NTNU, NO-7491 Trondheim, Norway*

**Abstract:** CFD, PMM testing and simplified modular manoeuvring models are discussed. Important flow parameters and Reynolds number scaling in PMM testing are described. A modular maneuvering model for calm-water ship manoeuvring at small and moderate Froude numbers using a combination of theory and empirical formula is presented. A limited error analysis for the numerical simulation of the "MARINER" hull during 20.9 degrees starboard turn manoeuvre shows satisfactory results. How to simulate ship maneuvering in waves by a two time-scale method using results for mean wave loads in regular waves is briefly described. Satisfactory agreement between numerical simulations and experiments of the trajectory of the SR-108 container vessel in a turning manoeuvre in regular waves is demonstrated. Finally, we discuss by theory and experiments when the frequency of encounter between the ship and the incident waves is small and one has to solve the seakeeping and maneuvering problems simultaneously. The case is a 21-meter long modern fishing vessel with a large ship beam-to-length ratio operating at Froude numbers up to 0.46 in following and stern quartering seas where surf riding and broaching can occur. Further improvements in the modular manoeuvring model are needed in this case.

**Keywords:** CFD, PMM, Scaling, modular simulation method, maneuvering in waves.

### 1 INTRODUCTION

Analysis of ship manoeuvring requires integrated knowledge about resistance, propulsion, ship machinery, seakeeping, steering and automatic control. Manoeuvring is analyzed traditionally in calm-water conditions. However, broaching in waves represents a potentially dangerous situation for smaller vessels and must be accompanied with proper steering strategies. Furthermore, replenishment and lightering operations are influenced by environmental conditions. Replenishment operations in open sea are "the most dangerous naval operations in peacetime". When one vessel approaches or leaves the other, large interacting, strongly time-dependent and alternating transverse forces, yaw moments and associated rudder angles happen. Xiang & Faltinsen (2010) present a potential-flow method without lift to predict the calm- water interacting loads in open or restricted water for small and moderate Froude numbers. The method can consider several objects with different speeds and motion directions. Additional interacting mean wave loads can be analyzed by state-of-the-art numerical methods by means of a two-time scale method as explained in section 5. Accurate manoeuvring simulations by rational methods of a damaged ship in waves and wind to find the time of capsizing are beyond state-of-the-art.

It is most often sufficient for displacement vessels to consider only the effect of lateral and longitudinal velocities and "yaw rate". Higher speeds need to incorporate the effect of heel. Experimental results for trimarans have shown that linear manoeuvring analysis is more limited than for monohulls and catamarans. Hydrofoil vessels require an analysis of six degrees of

freedom during manoeuvring. There is an increased importance of dynamic instabilities with increasing speed of high-speed vessels (Faltinsen 2005). For instance, calm-water broaching of semi-displacement round-bilge monohulls may suddenly happen beyond a certain Froude number. Spinout is a serious consequence of bad fast-boat driving, can occur when the boat is altering course, and slows down. The bow will therefore drop. Directional stability is lost because of the reduced draft at transom. A scenario can be rounding a mark in a race. Pike (2004) describes other spinout scenarios involving waves.

Faltinsen (2005) discusses how the Froude number and depth affect hydrodynamic manoeuvring terms. Confined areas and ship-to-ship interactions are also of concern. Muddy areas with generations of undulations on the water-mud interface can greatly affect the ship behavior and control. The mud problem has similarities with the "dead water" (internal wave) problem occurring when a layer of fresh water is on top of salt water. This occurs, for instance, associated with melting of ice. The internal waves have a critical speed. There are only divergent waves at supercritical speed. Sellmeijer & van Oortmerssen (1984) studied the behavior of a ship in muddy areas by model tests. The full-scale conditions corresponded to ship draft 18.90 m, mud height 2.5 m and mud density 1140 kg/m<sup>3</sup>. The critical speed was 3 knots. The mud was modelled as a combination of chlorinated paraffin and kerosene with a kinematic viscosity coefficient  $2.5 \times 10^{-5} \text{ m}^2/\text{s}$ . The errors caused by that the non-Newtonian properties of mud was not correctly modelled are not known. The maximum wave was about 3 m occurring at a keel clearance of 10% of the draft at 5

\* Corresponding author e-mail: odd.faltinsen@ntnu.no

to 7 knots. The experiments show that an appreciable increase of propeller rate of revolution is necessary to keep speed. The ship squat and trim are less above the mud than above a hard bottom. Rate of turn is appreciably less. Overshoot in zig-zag tests are much smaller. The manoeuvres depend greatly on mud thickness, keel clearance and mud density.

CFD, simplified modular methods and experiments are used in manoeuvring analysis and represent all valuable tools. Simplified modular methods have the advantage in doing real-time analysis and can either be based on a combination of empirical results and potential-flow theory or by obtaining hydrodynamic coefficients from experiments such as PMM tests. Recommended error analysis by ITTC ought to be mandatory for numerical and experimental tools.

We will limit ourselves to unrestricted water of infinite depth. We start with giving a brief summary of CFD. Even though the development of CFD is promising, we are still not yet to the point that CFD can be the only tool. It is difficult to imagine that experiments will be replaced by CFD in the future. PMM testing is discussed with emphasis on flow parameters and Reynolds number scaling. We will use a simplified modular manoeuvring model for calm-water conditions of a single ship as a basis for a limited error analysis to illustrate factors influencing manoeuvring at moderate Froude numbers. A model for incorporating wave effects in ship manoeuvring by a two-time scale method is shortly presented. The important wave effects are speed and heading dependent mean wave loads. The method is a generalization of state-of-the art slow-drift analysis of moored or dynamically positioned floating structures in waves. Finally, we discuss when the frequency of encounter between the ship and the incident waves is small and one has to solve the seakeeping and maneuvering problems simultaneously.

## 2 COMPUTATIONAL FLUID DYNAMICS (CFD)

CFD is commonly used in marine hydrodynamics and is often associated with methods solving the Navier-Stokes equations. There is a broad variety of numerical methods based on CFD. An advantage of CFD methods is flow visualization providing details such as vorticity distribution similarly as it could be done through model tests. Navier-Stokes CFD methods are usually robust and their flow simulations may look convincing by themselves, but reliability is still an issue and must be assessed with verification and validation. The required computational time by CFD is a limiting factor. The computational time prohibits presently solutions of the fully nonlinear seakeeping problem during the duration of a sea state.

In order to reduce computational time, a domain decomposition strategy could be pursued. The water domain is then divided into a domain near the ship where vorticity matters and an outside domain, which can be described by potential flow theory of incompressible

water. Fredriksen et al (2015) followed a procedure as that for a 2D body in waves. The Navier-Stokes equations were solved by a finite volume method while a cell method describing the flow by harmonic polynomials were used in the outer domain. Another benefit of such a method is that high accuracy is achieved in describing the propagating waves. Since the described method is not a complete manoeuvring model and one has to account separately for rudders, propellers and thrust deduction factors, one should have in mind the fact that "the weakest link breaks the chain" and that one must not have imbalance in how accurately that sub problems are described. However, it is the accuracy of the relevant response that matters such as described by procedures for lightering and replenishment operations and by IMO manoeuvring criteria for ships longer than 100 m at service speed in terms of turning circle and zig-zag manoeuvres and stopping ability. An important consideration is that some applications such as manoeuvring simulators require real time simulations. The latter constraint is hard to achieve with the described method.

CFD is well established in predictions of calm-water ship resistance. Durante et al. (2010) solved the unsteady RANS equations for the turning manoeuvre of a fully appended ship in calm water. A finite volume pseudo-compressible formulation was applied and the free surface was captured by a single-phase level set approach. Local time stepping, multi-grid technique and parallelization were used to reduce the computational time. Dynamic overlapping grid was applied to handle a movable rudder. An approximation is that propeller loads are based on an actuator disc model. Their method was validated by comparing with model tests of turning circle manoeuvre carried out at the lake of Nemi close to Rome. Three test series were performed with large discrepancy between test series I and test series II and III. The two latter test series were therefore the basis for the comparisons with the CFD calculations. Fine (with 6.2 M cells) and medium (every other cell in each direction is removed) grids were selected for comparisons. Only the fine grid gave satisfactory agreement with the experimental turning circle trajectory and was selected for further detailed studies. Both the drift angle and the yaw rate agreed well with the experiments while the speed drop was slightly overestimated. Examples of error sources are the modelling of turbulence and the propeller model.

## 3 PMM TESTS

PMM (Planar Motion Mechanism) testing determines unknown coefficients in assumed differential equations of ship manoeuvring in a body-fixed coordinate system. When flow separation occurs, the functional form of the nonlinear part of forces and moments assumed in PMM testing and their dependence on flow parameters such as Reynolds number can be questioned. Furthermore, Reynolds-number scaling to full scale is an issue.

Ishiguro et al. (1993) used PMM tests to obtain linear hydrodynamic coefficients in sway and yaw of the high-speed vessel “Super Slender Twin Hull” (SSTH). Hydrodynamic derivative terms  $Y_v$ ,  $Y_r$ ,  $N_v$ ,  $N_r$  are presented as a function of Froude number for Froude numbers larger than 0.184. Here  $Y$  is the transverse hydrodynamic force component.  $N$  is the hydrodynamic turning moment,  $v$  is the lateral component of ship velocity and  $r$  is yaw angular velocity. The results show a very clear Froude number dependence indicating that ship wave generation matters. The vessel without skegs becomes directional unstable for  $Fn > 0.25$  in the tested Froude number range up to  $Fn = 0.735$ . The considered skegs cause the vessel to be directional stable up to  $Fn = 0.37$ .

If the ship has zero forward speed and flow separation occurs, U-tube experiments (Sarpkaya 2010) with ambient unidirectional harmonically oscillating flow past a circular cylinder gives an indication of what flow parameters influence forces. The mass and drag coefficients  $C_M$  and  $C_D$  in a Morison equation-type formulation are in U-tube experiments for circular cylinders functions of Keulegan-Carpenter number  $KC = U_m T/D$ , Reynolds number  $Rn = U_m D/v$  and average roughness height-to-diameter ratio. Here  $U_m$  is the ambient velocity amplitude,  $T$  is the period of flow oscillation,  $D$  is the cylinder diameter and  $v$  is the kinematic viscosity coefficient of the water. The U-tube experiments for circular cylinders show that  $C_M$  does not vary strongly up to  $KC \approx 6$  and that a first approximation is the potential-flow  $C_M$ . The drag coefficient  $C_D$  varies strongly with the  $KC$ -number for small  $KC$ . In addition, the Reynolds number is an important flow parameter and scaling from model to full scale represents a challenge due to laminar boundary layer flow. Introducing roughness will help in the scaling problem. A similar scaling problem occurs for ship cross-sections without sharp corners. The reasons are that the flow separation along curved surfaces depends on laminar or turbulent boundary layer flow ahead of flow separation and that the viscous forces are strongly dependent on where flow separation occurs. Since the flow always separates from sharp corners, one should not exclude bilge keels on a ship in model testing. Since Morison equation does not follow from first principles, the equation is not always a perfect fit to experimental time histories even if forces directly associated with the vortex shedding frequency are excluded. An issue is how to define a proper Keulegan-Carpenter for non-harmonic body motions.

Flow separation depends on the forward speed. When the forward speed is high relative to the transverse velocity component along the vessel, it is relevant to consider a  $2D + t$  approach where  $t$  indicates the time variable (Faltinsen 2005). The method uses Earth-fixed transverse cross-planes that the ship passes through. If we focus on one of the cross-planes, the flow in the cross-plane starts when the bow goes through the cross plane. The subsequent shed vorticity as the ship goes through the

cross-plane will only be advected in the cross-plane. The consequence is that different cross-sections of the ship experience different vorticity fields in the cross-sectional plane and therefore different forces. The problem in Earth-fixed cross planes of the slender body is the same as a 2D time dependent cross-flow past a body. If the 2D body has no sharp corners, it takes time for flow separation to occur. The discussion is consistent with that flow separation is more dominant in the aft part than in the fore part of a ship during manoeuvring at forward speed. The cross-flow principle does not account for this fact. The drift angle becomes an important parameter for the transverse loads due to flow separation at forward speed. If the transverse ship velocity is oscillating, the Keulegan-Carpenter ( $KC$ ) number becomes a flow parameter. However, the ship may at forward speed partly run away from the returning cross-flow-generated vortices and hence cause a reduced  $KC$ -number influence. We have illustrated in Figure 1 how thin shed free shear layers roll up according to a  $2D + t$  theory by considering a slender body in infinite fluid in a vertical cross-flow with constant angle of attack.

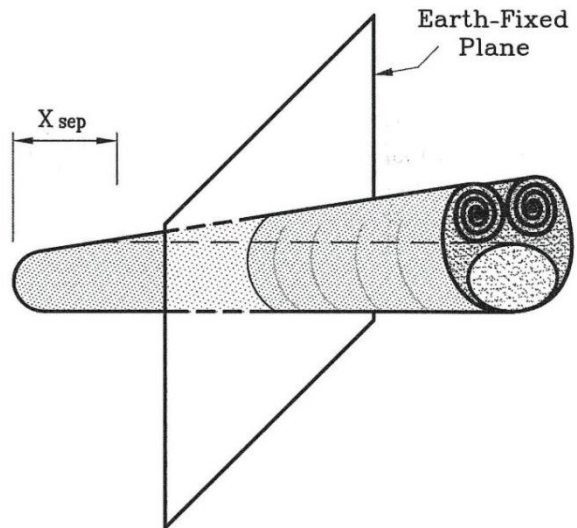


**Figure 1:  $2D + t$  analysis of a forward moving cylinder with constant angle of attack relative to the cylinder axis. The vertical cross-flow starts to separate at longitudinal distance  $x_{sep}$  from the front end (Faltinsen 2005).**

Ersdal & Faltinsen (2006) reported model tests of the transverse forces on submerged cylinders in nearly axial flow. The results give suggestions about the Reynolds and Keulegan-Carpenter number dependence of transverse viscous forces. The complete set-up (see Figure 2) was mounted on the towing carriage in the Marine Cybernetics Laboratory at the Marine Technology Center, NTNU. This basin is 30 m long, 6 m wide and 1.5 m deep. The carriage allows forced motions of a model in five degrees of freedom. The tow depth of the cylinder axis was 540mm, or about 11 diameters in order to minimize free-surface effects. Two rigid cylinders with length-to-diameter ratios of 10 and 30 were towed with angles  $\alpha$  from  $0^\circ$  to  $20^\circ$  between their centerline and the incoming

flow, and with a combination of forced harmonic oscillations in the normal direction and constant speeds along the cylinder axis. Originally, a pair of struts was placed in front of the test-section. The presence of the struts was found to give significant bias errors by changing the flow separation pattern along the cylinder. The boundary layer along the cylinders was tripped by a band of silica grains around the nose by adopting standard procedures for ship resistance tests that ensures turbulent layer along nearly the complete cylinder when  $\alpha = 0^\circ$ .

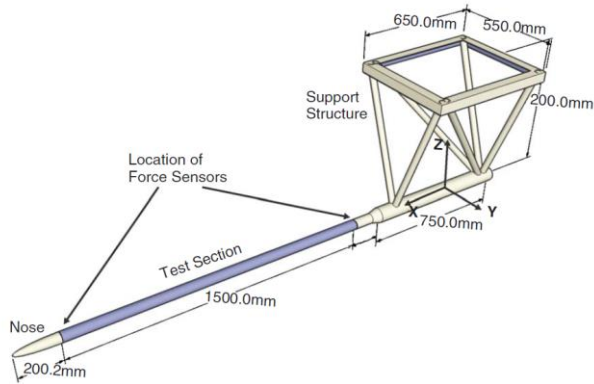


**Figure 2: Experimental set-up for transverse forces on a submerged, rigid cylinder, here with the long test-section. Oscillations were performed along the  $y$ -axis.**

If the angle of attack is less than about  $4^\circ - 5^\circ$ , the normal force depends linearly on the normal velocity component of the ambient flow. The results with constant angle of attack larger than  $5^\circ$  were expressed in terms of the normal coefficient  $C_n = F_n/(0.5\rho V^2 LD)$  where the measured normal force on the test section is  $F_n$ ,  $\rho$  is the mass density of water,  $V$  is the inflow velocity and  $D$  and  $L$  the diameter and length of the test section. An interesting result was found by presenting the transverse drag coefficient  $C_D = C_n(\sin\alpha)^{-2}$  as a function of the Reynolds number  $VD/(vsin\alpha)$ , which was denoted the “real” Reynolds number. Introducing  $C_D$  is similar, as one would do by using the cross-flow principle. However, the Reynolds number would then be  $VD\sin\alpha/v$ . A similarity with classical experimental results for cross-flow past a circular cylinder was demonstrated. A transition between laminar and turbulent boundary layer flow seems to occur in the region between  $VD/(vsin\alpha) \approx 2 \times 10^5$ , and  $3.5 \times 10^5$ , which corresponds closely to the transition region for the 2D case ( $\alpha = 90^\circ$ ); see, e.g., Faltinsen (1990, Chapter 6). For “real” Reynolds number below this, which corresponds to high angles of attack, the flow is sub-critical according to the 2D nomenclature, with an expected  $C_D \approx 1.2$ . As the angle decreases, and/or the velocity increases, the “real” Reynolds number increases (as does the scatter) and the flow becomes critical and eventually transcritical where  $C_D \approx 0.8$  is expected. This suggests some similarity of the current case and the drag reduction found in 2D when a proper Reynolds number is applied. To investigate further the effect of the boundary layer transition, a screen was placed upstream to trigger turbulent boundary layer flow along the cylinder in the

inflow for constant drift angle. The force results with the screen follow the expected results for a turbulent boundary layer. The length-to-diameter ratio was found to be of less importance than a  $2D + t$  theory might suggest.

The most important parameters for the cases with oscillating angle of attack were also found to be the angle of attack (ratio of transverse velocity amplitude to the axial velocity) and a “real” Reynolds number defined similarly as for constant drift angle. The length-to-diameter ratio and the Keulegan–Carpenter number are found to be less influential. It was not possible as in the constant angle of attack case to use a screen to trigger turbulence in the boundary layer for all angle of attack cases. The latter fact is important to study in connection with PMM testing. For instance, Hama strips are commonly used in model testing of foils. Since they are thin, they have a minor influence on the foil profile. The latter fact is also a consideration in PMM testing of ships. The placement of the Hama strips on ships is not as straightforward as it is for foils. They have to be placed upstream of possible flow separations. A consideration is also that the transverse flow velocity component just outside the boundary layer and tangential to the body surface at the Hama strips must not be too small.

Ersdal & Faltinsen (2006) presented an error analysis. The 95% confidence interval as outlined in ITTC (1990) and Coleman & Steele (1989) expressed the accuracy of the results with both precision and bias errors included. For the oscillating case, the errors in the estimated force might be quite high; the expected standard error of estimation is about 15% of the force amplitude.

#### 4 CALM-WATER MODULAR MANOEUVRING MODEL

Real time simulations of ship manoeuvring require a modular manoeuvring simulation model. Skejic (2008) and Xiang (2012) have developed a calm-water modular manoeuvring model during their doctoral studies. The model solves for surge, sway, roll, yaw, and can consider two interacting ships. The hydrodynamic manoeuvring coefficients for the hull assume a rigid free-surface condition, which implies that the Froude number roughly speaking should be less than 0.2. Søding’s (1982) slender-body theory for one hull is used to calculate the hydrodynamic derivative terms in sway and yaw. Søding’s model involves an empirical longitudinal position where flow separation in the aft direction of the ship starts. The latter position is essential for determining the hull lift. The viscous cross-flow model is based on the cross-flow principle with constant drag coefficient along the ship. A cross-flow principle can be questioned at forward speed as discussed in section 3. A main cause of speed loss in a turning motion is the inertia term  $-Mvr$  on the left side and  $X_{vr}vr$  on the right side of the longitudinal component of Newton’s second law in the body-fixed coordinate system. Here  $M$  is the ship mass and  $X_{vr}$  is added mass in sway if flow separation can be neglected. Norrbin (1971) reported that  $X_{vr}$  can be as low

as 20% to 50% of the potential-flow value. The viscous effect on the resistance term  $X_{vr}vr$  is given empirically. An alternative would be to use PMM tests to obtain hydrodynamic hull coefficients.

The resistance is calculated either by Holtrop's (1984) formula or by using the ITTC formulation for the viscous resistance combined with direct calculations of the wave resistance. Air resistance can be added by using empirical drag coefficients Open water diagram for the propulsion are input. The wake is found by Holtrop's formula (1984) while Holtrop & Mennen (1982) give the thrust deduction coefficients. The rudder forces are predicted according to Søding (1982). The fact that the propeller race increases the longitudinal inflow flow velocity over part of a rudder is not considered. Ankudinov et al.'s (1993) flow rectification factors of the inflow to the rudder caused by the hull and the propeller is implemented. The inflow velocity to the rudder is expressed as  $V_{RS} = (u_{RS}^2 + v_{RS}^2)^{1/2}$  where  $v_{RS} = \gamma_v v + \gamma_r x_d r$ ,  $\gamma_v$  and  $\gamma_r$  are the flow rectification factors,  $v$  is the transverse velocity of the COG of the ship,  $x_d$  is the longitudinal  $x$ -coordinate of the rudder center relative to COG and  $r$  is the yaw rate. The modelling of the propulsion machinery is avoided by assuming a constant number of propeller revolutions per second. In addition, automatic control procedures can be used such as in lightering and replenishment operations. An autopilot is then implemented by using rudder and propulsion control to achieve the desired (safe) transverse/longitudinal clearances and heading angles for operation by compensating for the deviations caused by the hydrodynamic interacting forces and moments between ships.

The non-lifting dynamic hull loads accounting for ship interactions can be calculated by either a 3D potential flow method using BEM (Xiang & Faltinsen 2010) or by Tuck & Newman's (1974) far-field slender-body theory. The 3D method allows for arbitrary relative configurations of the ships up to the point of collision. Further, more than two ships and other interacting structures can be considered. The expressions involve added mass coefficients accounting for body interactions. One term is expressed as the time derivative of a sum of terms that are products of added mass coefficients and velocities. There are also terms with added mass coefficients that are not time differentiated. Finally, there is a term involving integration of velocity square terms over the mean wetted hull surface. Tuck & Newman's theory assumes the two ships to be on parallel course. The ships must not be too close to each other. Since the ship ends have important contribution to the interaction loads, a slender-body theory is only adequate for slender ship ends. So far, we have only applied the 3D method to unrestricted water of infinite depth. However, no problems are expected in using the method for finite depth with a solid bottom and in channels as long as ship-wave generation does not matter and cross-flow separation is secondary. The interaction model by Xiang & Faltinsen (2010) has been validated by comparing with

model tests of the transverse interaction force between two oil tankers at parallel course with the same speed and different stagers.

#### 4.1 Error Analysis of Manoeuvring of a Single Ship

Skejic (2008) validated the described modular manoeuvring model by comparing with full scale trials of "MARINER" and "Esso Osaka". The speed loss of "Esso Osaka" during 35 degrees port turn manoeuvre with approach forward speed 7.7 knots is well predicted. The trajectories differ more. Similar trends appear for the trajectories and speed loss of "Esso Osaka" for 20/20 degrees zig-zag manoeuvre with approach forward speed 7.8 knots. The trajectory of the "MARINER" hull during 20.9 degrees starboard turn manoeuvre with approach forward speed 15.4 knots was well predicted. The latter case is the basis for a limited error analysis presented by Faltinsen (2011) with the help of Skejic (2011, personal communication). The error sources with base value are:

- Drag coefficient  $C_D$  associated with hull crossflow is 1.35
- Thrust deduction factor  $t = 0.1732$
- Wake factor  $w = 0.267$
- Flow rectification factors  $\gamma_v$  and  $\gamma_r$  are 1.0.

The base values of the error sources were varied with  $\pm 10$  percentage. The justification for this variation can be questioned. Other error sources such as choice of "trailing" cross-section in the hull-lift formulation by Søding (1982) and the propeller race effect on the rudder ought to have been considered. Furthermore, varying only the constant drag coefficient in the cross-flow drag formulation does not reflect the fact that flow separation is more pronounced in the aft part than in the fore part of the vessel. The turning trajectories following from varying drag coefficient, thrust deduction factor, wake factor and flow rectification factors were presented showing good agreement with full-scale values. The variation in the drag coefficient has the largest influence while the influences of the wake factor and thrust deduction factor are not large. The flow rectification factors matter.

The advance and the tactical diameter are measures of ship manoeuvrability according to IMO manoeuvring criteria from 2002 for ships longer than 100 m at service speed. The full-scale trial predicts the advance and tactical diameter as  $4.11L_{pp}$  and  $6.15L_{pp}$ , respectively. Here  $L_{pp} = 160.934m$  is the length between perpendiculars. Using the base values in the described modular model give an advance of  $4.37L_{pp}$  and a tactical diameter of  $6.06L_{pp}$ . The error analysis for the advance and the tactical diameter predicted by the numerical method assumed that the error associated with each error source is independent of the error associated with other error sources. The resulting error of the advance and the tactical diameter by this limited error analysis is small and equal to  $0.13L_{pp}$  and  $0.37L_{pp}$ , respectively. Obviously, one should not generalize the quality of the simulation model by only one ship case, but consider also a vessel that is less directional stable.

## 5 MANOEUVRING IN A SEAWAY

Skejic & Faltinsen's (2008) manoeuvring model of a ship in waves assumes different time scales for the manoeuvring and the linear wave-induced loads. Potential-flow theory can largely be used in seakeeping analysis except for roll viscous damping. The fact that manoeuvring models operate with a body-fixed accelerated coordinate system while linear and weakly nonlinear seakeeping problems are traditionally solved in an inertial system must be recognized in the analysis. The effect of regular waves on ship manoeuvring in the horizontal plane is expressed in terms of mean wave forces and moments acting on the ships that are functions of the slowly varying ship heading relative to the incident waves, ship speed and the frequency of encounter between the ship and the waves. The procedure may be generalized to a short-term irregular sea by creating a time history of the wave elevation and approximating the wave elevation between two successive zero-crossings as a regular wave. The calculations of mean wave loads are done interactively with the ship manoeuvring. Faltinsen et al. (1980) give the needed mean wave load expressions for any wave directions and ship speeds in terms of an asymptotic small wavelength formulation and a direct pressure integration method in the wave-frequency range of non-negligible ship motions. A direct pressure integration method can be numerically sensitive to wrongly predicted flow details at the ship hull. Examples are at non-vertical hull sides at the waterline and sharp corners. Using far-field methods based on conservation of fluid momentum/energy seem to be not as sensitive to details as that. Mean wave load results depend on how the linear wave-induced ship motions are evaluated. Skejic & Faltinsen (2008) used the Salvesen-Tuck-Faltinsen strip theory (Salvesen et al. 1970). Some manoeuvring models in waves are incomplete in the way that mean wave loads are accounted for, e.g. the only considered effect is due to integration of the linear pressure over the instantaneous wetted surface. It is well known from direct pressure integration methods of mean wave loads that accounting only partly for terms can lead to erroneous answers. The latter fact is illustrated in Faltinsen (1990) by applying the direct pressure integration method in the estimation of the mean wave loads on a 2D body. The method can be generalized to include mean wave loads in six DOF and applied to manoeuvring of a submarine in the wave zone.

Xiang & Faltinsen (2011) followed a different way than Faltinsen et al. (1980) to calculate the mean wave loads. The linear wave induced motions are found by a 3D Rankine source method that solves the Neumann-Kelvin problem in the time domain. Xiang and Faltinsen (2011) validated the method for the two interacting independent ships studied experimentally by Ronæss (2002). The two ships were towed side-by-side in regular head waves at the MARINTEK towing tank in Trondheim, which is 270 m long and 10.5 m wide. The distance between the centerlines of the two models was maintained as 2.47 times the average beam of the two ships (1.25 m) during the tests. The comparisons were made when the two ships

advanced with amid-ship sections approximately side-by-side (i. e. non-staggered), and the forward speed corresponds to Froude number 0.1 when using the length of the largest ship. The heave and pitch motions of the two ships and the roll motion of the largest ship are adequately predicted by the present method, while the roll motion prediction of the smallest ship is clearly larger than the model test results. This is consistent with Ronæss (2002), which commented that the reason was from the experimental setup. Further, the predictions and model tests show that the hydrodynamic interaction effects have much greater influence on the motions of the smallest ship than the largest ship. The described method neglects the local interaction between the steady and unsteady flow, which matters, in particular, for non-slender ships. When local interaction between steady and unsteady flow is accounted for in methods formulated in an inertial coordinate system, a difficulty occurs at body surface areas with high curvature. The reason is the so-called  $m_j$ -terms in the unsteady body boundary conditions containing terms involving second-derivatives of the steady velocity potential. Actually, the  $m_j$ -terms are singular at sharp comers. If a body-fixed coordinate system is used instead of an inertial coordinate system in formulating the boundary value problem, the  $m_j$ -terms do not appear (Shao & Faltinsen 2012).

Xiang & Faltinsen's (2011) method for calculating mean wave loads are based on time averaging expressions for the time rate of change of momentum and angular momentum of the flow. Part of the mean wave-load expressions involves integrations over control surfaces that can be chosen at an arbitrary distance from a ship. However, it is advantageous from a computational point of view to choose the control surface not too far away from the considered ship. The arbitrary choice of control-surface position is important when studying two interacting ships. The expressions have been validated by Xiang (2012) for single advancing ships by comparing with the added resistance experiments for the S-175 ship by Fujii & Takahashi (1975) and Nakamura & Naito (1977) at Froude numbers  $Fn = 0.15$  and  $Fn = 0.25$  in head sea ( $180^\circ$ ) and bow seas with  $150^\circ$  and  $120^\circ$  headings. Satisfactory agreement with the experimental results for the container ship SR-108 reported by Yasukawa (2006) was also documented. Yasukawa (2006) presented results for added resistance in head and beam sea and mean transverse wave force and yaw moment in beam sea at forward speed. There is a need for more experimental results of mean sway force and yaw moment on single ships at forward speed as a function of wave heading and frequency. Further, we are not aware of reliable experimental results for mean wave loads on interacting ships at forward speed.

The two-time scale method for manoeuvring in regular waves has been validated by comparing with model test results of a turning circle manoeuvre reported by Yasukawa (2006). Yasukawa (2008) did also zig-zag and stopping manoeuvres. Free-running model tests were carried out in regular and irregular waves using the SR-

108 container ship model. The model tests were conducted at the Seakeeping and Maneuvering Basin, Nagasaki R & O Center, MHI. The regular wave tests were carried out in various wavelengths in initially head and beam sea waves. The comparison with the model test in regular waves with wavelength-to-ship length ratio  $\lambda/L = 0.7$ , wave height-to-ship length ratio 0.02, initially head sea waves and Froude number  $Fn = 0.15$  are presented in Figure 3 together with numerical simulation results by Yasukawa (2006). The ship track and speed loss are clearly influenced by the waves. Our simulation results agree better with the experiments than Yasukawa's simulations. Since the two simulation methods agreed well for calm water, the reason must be how the mean wave loads are estimated. Yasukawa (2006) uses a database-based method. Two sets of added resistance are prepared, i.e.,  $Fn = 0$  and  $Fn = 0.15$ , for different wave headings. Then the added resistance is obtained via linear interpolation during the simulation. The calculation of added resistance at  $Fn = 0.15$  is strip-theory based, by use of formulations by Maruo (1960) and Fujii & Takahashi (1988) while the calculations at zero speed are based on a 3D panel method. No speed effects were considered in evaluating the mean sway force and yaw moment. The latter fact is an error source to be further investigated.

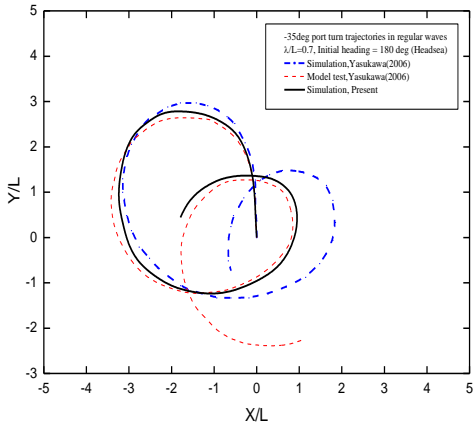


**Figure 3: Comparison between numerical simulations and experiment of the trajectory of the SR-108 container vessels in a turning manoeuvre with 35 degrees port turn in regular waves with  $\lambda/L = 0.7$  and wave height-to-ship length ratio 0.02. Initial wave heading is head sea. Initial speed corresponds to Froude number 0.15. L represents the ship length (Xiang 2012).**

When the frequency of encounter between the ship and the waves is small, one has to solve simultaneously the seakeeping and manoeuvring problems. An example is in analyzing steering due to broaching in following waves. The mean wave loads, which play a crucial role in the two-time scale method of maneuvering in waves, are negligible at small frequency of encounters. Thys (2013) and Thys & Faltinsen (2014) studied theoretically and experimentally hydrodynamic aspects of a 21m modern fishing vessel with a large ship beam-to-length ratio for

Froude numbers up to 0.46 during manoeuvring in a seaway at small frequencies of encounter, corresponding to following and stern quartering seas, where fishing vessels are susceptible to capsize. The modular numerical model was based on de Kat and Paulling (1989). The model combined a six degrees of freedom (DOF) blended seakeeping model with a four DOF non-linear manoeuvring model. The 3D non-linear Froude-Krylov and hydrostatic restoring loads were computed by pressure integration up to the incident free surface. The added mass, damping and wave diffraction loads were obtained by generalizing the STF (Salvesen et al. 1970) strip theory. Since a strip theory is a high-frequency theory, 3D flow effects were partly included by calculating the zero-speed velocity potentials by means of WAMIT. Corresponding time-domain formulations were expressed by standard convolution integrals. The six DOF seakeeping model was combined with a nonlinear manoeuvring model that included Søding's (1980) model and a cross-flow drag model. However, Søding's model does not account for the Froude number dependence of hydrodynamic derivative terms at the high considered Froude numbers. When combining the seakeeping model and the manoeuvring model, special care is needed to avoid duplicating forces in the formulation and to account for the differences in the manoeuvring and seakeeping coordinate systems.

The special ship form and the high Froude numbers considered made it impossible to use existing empirical formula for calm water resistance and wake factor. Instead, model tests were performed. In addition, rudder forces and cross-flow drag in calm water were experimentally studied. The experimentally determined wake factor is shown in Figure 4 for different forward speeds in model scale. The wake factor varies with the forward speed, where the decrease is believed to be mainly due to the frictional wake for lower Froude numbers and the increase due to the wave wake for the higher speeds. The figure also shows predictions based on the forward-speed independent empirical formula by Taylor (1942), which agrees poorly with the experiments.

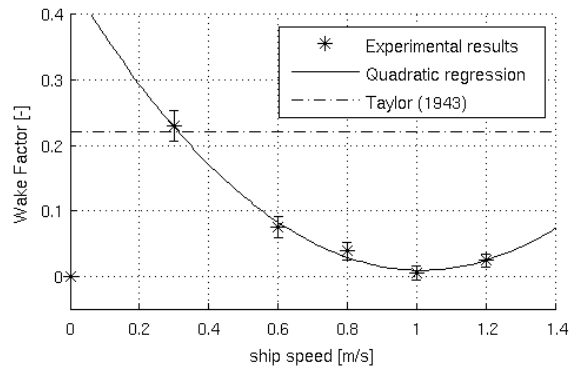


**Figure 4: The experimentally determined wake factor and the regression formula used in the simulation model as a function of ship speed in model scale. The model length between perpendiculars is 0.800m. (Thys & Faltinsen 2014).**

It was also found that:

- The cross-flow principle combined with the hull-lift forces simulates adequately the side forces on a ship, even though the cross-flow principle is questionable for small drift angles ( $|\alpha| < 20^\circ$ )

- The slope of the rudder lift coefficient decreases with the rudder angle  $\delta$ . A linear rudder lift model fitted to the experimental data for small  $\delta$  over-predicts the rudder force by more than 25 % for  $\delta > 15^\circ$  with an over-prediction of 92% at  $\delta=35^\circ$ .

Free running manoeuvres in calm water were performed to validate the simulation model. Based on a sensitivity analysis during calm-water turning circle manoeuvres, it was found that the manoeuvring model is most sensitive to the rudder lift coefficient and the position of the aft flow separation section in Søding's model. The wave-induced surge forces in following seas were measured by use of captive experiments in following seas. The simulated wave-induced surge forces over-predicted the experimental results, probably because the interaction between the local steady and unsteady flow was not accounted for. Free-running experiments at small frequency of encounter were performed and compared to simulations. Over-predicted wave-induced surge forces in following seas by up to 50% lead to simulations with surf riding and broaching, which were not observed in the experiments. The latter facts follow from Figure 5 and Figure 6, which show the maximum forward speed and the maximum absolute heading angle, during the manoeuvres in following seas ( $\beta = 0^\circ$ ), for different wave steepness  $H/\lambda$  as a function of the wavelength-to-ship length ratio  $\lambda/L_{wl}$ . The simulations over predicted the maximum forward speed. The ship was surf-riding in the simulations with:

- $\frac{H}{\lambda} = 1/25$  and  $0.8 \leq \frac{\lambda}{L_{wl}} \leq 1.2$ ,
- $\frac{H}{\lambda} = 1/10$  and  $\frac{\lambda}{L_{wl}} \geq 0.8$ ,
- $\frac{H}{\lambda} = 1/8$  and  $\frac{\lambda}{L_{wl}} \geq 0.8$ ,

where surf-riding is defined here as the behaviour where the ship is forced by the waves to move with a constant speed equal to the wave celerity. One should note that surf-riding cannot be experimentally determined based on the maximum forward speed, but was determined by looking at the ship behaviour in time.

The maximum absolute yaw angles were smaller than  $\pm 15^\circ$  in the experiments, while very large maximum yaw angles are seen in the simulations. Surf-riding behaviour and large yaw angles are clear indications of broaching in the simulations. Broaching was not observed in the experiments but occurred in the simulations for  $H/\lambda = 1/10$  and  $1/8$ , and for  $\lambda/L_{wl} > 0.8$ .

Satisfactory agreement was obtained between the experimental and the simulated ship behavior during manoeuvres at small frequency of encounter by reducing the wave excitation forces in surge, based on the results of the captive experiments in following seas.

An error source in the simulations was the fact that the influence of the waves on the rudder and propulsion

forces was neglected. The reduction of the rudder effectiveness due to the small relative velocity between the ship and the horizontal water velocity in the waves during surf-riding, which is often cited as one of the main reasons for broaching (Faltinsen 2005), was not accounted for in the simulation model.

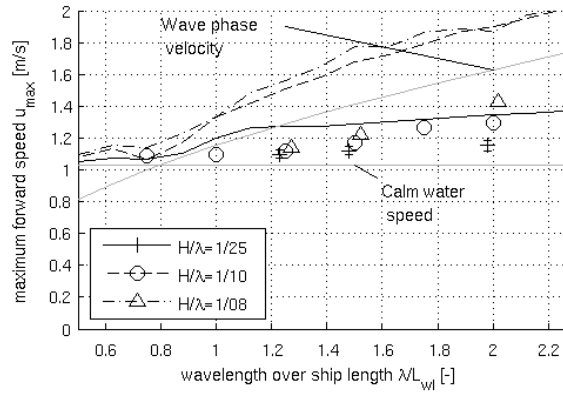
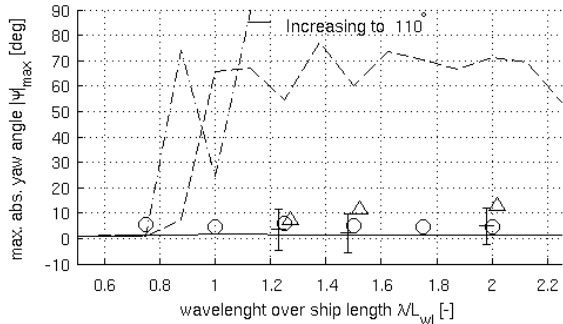


**Figure 5:** Simulated (line) and experimental (symbol) maximum ship speed  $u_{max}$  in model scale during straight line manoeuvres in following seas ( $\beta = 0^\circ$ ), for different wave steepnesses  $H/\lambda$  and different ratios of wavelength over ship length  $\lambda/L_{wl}$ . The model length between perpendiculars is 0.800m. (Thys & Faltinsen 2014).

**Figure 6:** Simulated (line) and experimental (symbol) maximum absolute yaw angle  $|\psi|_{max}$  during straight-line



manoeuvres in following seas ( $\beta = 0^\circ$ ), for different wave steepnesses  $H/\lambda$  and different ratios of wavelength over ship length  $\lambda/L_{wl}$ . Same legend as in Figure 5. (Thys & Faltinsen 2014).

## 6 CONCLUSIONS

CFD, PMM testing and simplified modular manoeuvring models are discussed. Important flow parameters and Reynolds number scaling in PMM testing are described. Results by an error analysis of PMM testing according to ITTC recommendations are presented.

A modular maneuvering model for calm-water ship manoeuvring at small and moderate Froude numbers using a combination of theory and empirical formula is described. A limited error analysis for the numerical simulation of the "MARINER" hull during 20.9 degrees starboard turn manoeuvre shows satisfactory results. The variation in the cross-flow drag coefficients has the largest influence while the influences of the wake factor

and thrust deduction factor are not large. The flow rectification factors matter. The influence in the studied variations of the wake and thrust deduction factors is negligible.

How to simulate ship maneuvering in waves by a two time-scale method using results for mean wave loads in regular waves is briefly described. It is emphasized that the effect of a seaway on ship manoeuvring is sometimes wrongly modelled because the formulations are not consistent with correct predictions of mean wave loads. Satisfactory agreement between numerical simulations and experiments of the trajectory of the SR-108 container vessel in a turning manoeuvre in regular waves is demonstrated.

Finally, we discuss by theory and experiments when the frequency of encounter between the ship and the incident waves is small and one has to solve the seakeeping and maneuvering problems simultaneously. The case is a 21m modern fishing vessel with a large ship beam-to-length ratio operating at Froude numbers up to 0.46 in following and stern quartering seas where surf-riding and broaching can occur. Improvements in the modular manoeuvring model to account for Froude number dependence is needed. Since the theoretical surge force in waves over-predicts by up to 50%, it is speculated that approximate theoretical methods does not properly account for the interaction between the steady and unsteady flow field.

## ACKNOWLEDGEMENTS

The Research Council of Norway through the Centres of Excellence funding scheme AMOS, project number 223254, supported this work.

## REFERENCES

- Ankudinov, V., Kaplan, P. & Jacobsen, B. K. (1993). 'Assessment and principal structure of the modular mathematical model for ship maneuverability prediction and real-time maneuvering simulations'. *MARSIM'93*, St. Johns, Newfoundland, Canada.
- Coleman, H. & Steele, W. (1989). *'Experimentation and Uncertainty Analysis for Engineers.'* Wiley, New York.
- Durante, D., Broglia, R., Muscari, R. & Di Mascio, A. (2010). 'Numerical simulations of a turning circle manoeuvre for a fully appended hull'. *Proc. 28th ONR Symposium on Naval Hydrodynamics*, Pasadena, 12-17 Sept.
- Ersdal, S. & Faltinsen, O. M. (2006). 'Normal forces on cylinders in near axial flow'. *Journal of Fluids and Structures*, 22, 1057-1077.
- Faltinsen, O. M., Minsaas, K., Liapis, N. & Skjørdal, S. O. (1980). 'Prediction of resistance and propulsion of a ship in a seaway'. *Proc. 13<sup>th</sup> Symposium on Naval Hydrodynamics*, Tokyo, pp 505-529.
- Faltinsen, O. M. (1990), 'Sea Loads on Ships and Offshore Structures'. Cambridge University Press.
- Faltinsen, O. M. (2005). 'Hydrodynamics of High-Speed Marine Vehicles'. Cambridge University Press.
- Faltinsen, O. M. & Timokha, A. N. (2009) 'Sloshing'. Cambridge University Press.
- Faltinsen, O. M. (2011). Keynote lecture; Modeling of manoeuvring with attention to ship-ship interaction and wind waves. *2<sup>nd</sup> International Conference on Ship Maneuvering in Shallow and Confined Water: Ship-to-Ship Interaction*. Trondheim.
- Fredriksen, A. G., Kristiansen, T. & Faltinsen, O. M. (2015). 'Wave-induced response of a floating 2D body with moonpool'. *Phil. Trans. R. Soc. A* 373.
- Fujii, H. & Takahashi, T. (1975). 'Experimental study on the resistance increase of a ship in regular oblique waves'. *Proc. 14<sup>th</sup> IITC*, Vol. 4, p.351.
- Fujii, H. & Takahashi, T. (1988). 'Practical calculation and application of added wave resistance in ship design' (In Japanese), *Journal of the Kansai Society of Naval Architects*, No.75.
- Holtrop, J. (1984). 'A statistical re-analysis of resistance and propulsion data'. *Int. Shipbuild. Progr.* 31, 1984.
- Holtrop, J. & Mennen, G. G. J. (1982). 'An approximate power prediction method'. *Int. Shipbuild. Progr.* 29.
- Ishiguro, T., Uchida, K., Manabe, T. & Michida, R. (1993). 'A study on the maneuverability of the Super Slender Twin Hull'. *Proc. FAST'93*, ed. K. Sugai, H. Miyata, S. Kubo, H. Yamata, Vol. 1, pp. 283-94, Tokyo: The Society of Naval Architects of Japan.
- ITTC (1990). 'Report of the Panel on Validation Procedures'. Nineteenth International Towing Tank Conference, Madrid, Spain.
- de Kat, J. O. & Paulling, J. R. (1989). 'The simulation of ship motion and capsizing in severe seas'. *Transactions of the Society of Naval Architects and Marine Engineers*, vol. 97, pp. 139-168.
- Maruo, H. (1960). 'Wave Resistance of a Ship in Regular Head Seas'. *Bulletin of the Faculty of Eng., Yokohama National Univ.*, Vol. 9, pp.73-91.
- Nakamura, S. & Naito, S. (1977). 'Propulsive performance of a container ship in waves'. *The Society of Naval Architects of Japan. Naval Architecture and Ocean Engineering*, Vol. 15.
- Norrbin, N. H. (1971). 'Theory and observation on the use of a mathematical model for ship maneuvering in deep and confined water'. *SSPA Report No. 68*, Gothenburg.
- Pike, D. (2004). 'Fast Powerboat Seamanship. The complete Guide to Boat Handling, Navigation, and Safety'. International Marine/ McGraw-Hill.

- Ronæss, M. (2002). 'Wave induced motions of two ships advancing on parallel course'. Dr. Ing. Thesis, Dept. of Marine Hydrodynamics, NTNU, Trondheim.
- Salvesen, N., Tuck, E. O. & Faltinsen, O. M. (1970). 'Ship motions and sea loads'. Transactions of the Society of Naval Architects and Marine Engineers, Vol. 78, pp. 250-287.
- Sarpkaya, T. (2010). 'Wave Forces on Offshore Structures'. Cambridge University Press.
- Sellmeijer, R & van Oortmerssen, G. (1984). 'The effect of mud on tanker manoeuvres'. Royal Institution of Naval Architects Transactions, Vol. 126.
- Shao, Y.L. & Faltinsen, O.M. (2012). 'Linear seakeeping and added resistance analysis by means of body-fixed coordinate system'. Journal of Marine Science and Technology.
- Skejic, R. (2008). 'Maneuvering and Seakeeping of a Single Ship and of Two Ships in Interaction'. Doctoral thesis, Department of Marine Technology, Faculty of Engineering Science and Technology, Norwegian University of Science and Technology, Trondheim, Norway.
- Skejic, R. & Faltinsen, O. M. (2008). 'A unified seakeeping and maneuvering analysis of ships in regular waves'. Journal of Marine Science and Technology, 13:371 – 394
- Søding, H. (1982), 'Prediction of ship steering capabilities'. Schiffstechnik, 29:3-29.
- Taylor, D. (1942). 'The speed and power of ships: a manual of marine propulsion'. United States Government Printing Office.
- Thys, M. (2013). 'Theoretical and experimental investigation of a free running fishing vessel at small frequency of encounter'. PhD thesis, Norwegian University of Science and Technology, Trondheim, Norway.
- Thys, M. & Faltinsen, O. M. (2014). 'Theory and experiments of a free-running fishing vessel in stern sea'. OMAE2014-2358, June 8-13, San Francisco, California, USA.
- Tuck, E. O. & Newman, J. N. (1974). 'Hydrodynamic interaction between ships'. Proc. 10th Symp. On Naval Hyd., Cambridge, Mass., USA, pp. 35-70.
- Xiang, X. (2012). 'Maneuvering of two interacting ships in waves'. Doctoral thesis, Department of Marine Technology, Norwegian University of Science and Technology, ISBN: 978-82-471-4052-9, h.
- Xiang, X. & Faltinsen, O. M. (2010). 'Maneuvering of two Interacting Ships in Calm Water'. Proc. PRADS2010, the 11th International Symposium on Practical Design of Ships and other Floating Structures, September 19-24, Rio de Janeiro.
- Xiang, X. & Faltinsen, O. M. (2011). 'Time domain simulation of two interacting ships advancing parallel in waves'. Proc. 30th Int. Conf. on Ocean, Offshore and Arctic Engineering (OMAE2011), Rotterdam, the Netherlands.
- Yasukawa, H. (2006). 'Simulations of ship maneuvering in waves (first report: turning circle maneuvers)'. (In Japanese), Paper collections of Japanese Society of Naval Architects and Marine Engineers, December.
- Yasukawa, H. (2008). 'Simulations of ship maneuvering in waves (second report: zigzag and stopping maneuvers)'. (In Japanese), Paper collections of Japanese Society of Naval Architects and Marine Engineers, June.

## **Ship Manoeuvrability, Controllability and Safety**

**Kazuhiko Hasegawa<sup>1\*</sup>**

*<sup>1</sup>Osaka University, Department of Naval Architecture and Ocean Engineering 2-1, Yamada-oka Suita, Osaka, Japan*

**Abstract:** Ship manoeuvrability, controllability and safety issues are reviewed from the author's 40-year research activities. It starts from the boom of ULCC and a question of how much large ship human operator can handle. In the research the strong relation between ship manoeuvrability and human capability is discussed using ship handling simulator and it is utilised to regulate IMO Manoeuvrability Standard. Maritime shipping industry was suffered by so-called oil-shock in 1970s, the research moves to energy saving and it forces the author to the direction of autopilot design. Cost function of autopilot is proposed and in the paper, he has also proposed a chart so-called Hasegawa chart to estimate a coefficient "Xvr" in the mathematical model. In these days many captive model experiments have been done in Japan using PMM and CMT and so-called MMG model has been established. In 1980s, the boom of first artificial intelligence raised up mainly from the U.S. with the development of workstation and various programming languages. Expert system (ES) and several paradigms including fuzzy logics (FL) and artificial neural network (ANN) etc. are also appeared. The author has participated some automatic navigation system projects in Japan and started to develop automatic collision avoidance system. The system is now available as Maritime Traffic Simulation System (MTSS) utilising ES and FL and now used for several actual projects. Automatic berthing was realised using ANN and examined by free-running experiments. Many ship accidents were analysed by the author and one of the latest one is Korean ferry "SEWOL". In the presentation these activities are introduced.

**Keywords:** ship manoeuvrability, ship controllability, ship safety, marine traffic simulation, ship accident analysis.

*(Intentionally left blank)*

## Current Status of Manoeuvring Prediction Methods, Their Mutual Pros and Cons and Ways to Quantify The Capabilities

Frans Quadvlieg<sup>1\*</sup>

<sup>1</sup>MARIN, Maritime Research Institute Netherlands, Wageningen, The Netherlands.

**Abstract:** In the paper, we make an overview of prediction techniques and some of the developments in the last years. This is done from the viewpoint of the author: as user of every technique in his daily work, and as observed of ITTC common techniques. Finally, various attempts have been made to quantify the accuracy of each prediction method. Among others the SIMMAN workshops for surface ships enabled to make an overview on the maturing of new prediction techniques.

**Keywords:** Manoeuvring; mathematical model; prediction methods.

### 1 INTRODUCTION

For manoeuvring predictions of ships and submarines, we are distinguishing the deliverable. The deliverable may be:

- Manoeuvring characteristics. What are these characteristics and what is the prediction accuracy?
- A mathematical model. This should describe the manoeuvrability? And how good is this model (and how can we quantify this?)

Sometimes, these 2 deliverables are mixed.

The prediction of *manoeuvring characteristics*, the objective is to determine several derived products from a trajectory. These characteristics may be the quantities “overshoot angles”, “advance”, “tactical diameter”, “stopping distance”. These are well defined and often asked characteristics because the IMO MSC167 requires that these characteristics are to be determined in early design stage. However, there are other characteristics that may be considered: the “maximum wind velocity” that can be withstood at a given ship speed, the “variation in heading” during course keeping in waves, or (in the case of submarines), the “time to change depth”.

For the determination of a *mathematical model*, the deliverable is different. In this case, the objective is obtain a robust mathematical model. This mathematical model has as objective that it can be implemented in a bridge simulator, or that it can be implemented in a fast time simulator. With the fast time simulator, the simulations

will be carried out using a rudder (and rpm) control and multiple calculations can be carried out (Monte Carlo simulations). Typical, the mathematical model now describes the accelerations that the ship gets as function of a state vector (6 positions, 6 velocities, rudder & control angles and rpm’s).

The deliverables of the two are quite different, this is why there is a clear difference made between these two.

In the following 2 sections, different methodologies are discussed that can deliver these deliverables. The pros and cons of the three methods are discussed. Especially in the light of the most recent developments in model testing techniques and CFD developments.

### 2 PREDICTION OF MANOEUVRING CHARACTERISTICS

For the most of the predictions, a trajectory is predicted. Data analysis of the resulting time series (data reduction) leads to the derived characteristics.

Figure 1 makes an overview of the 7 methods that we may distinguish that can deliver the manoeuvring characteristics. Of course there are eclectic mixes of these methodologies possible: for example where part of the forces are derived from CFD, while empirical methods are used to derive rudder and propeller forces.

From simple-and-low-effort to highly-complex-and-hopefully-more-accurate, we may give the overview as in Figure 2. These show our perception of the present state of reliability of the methods versus the efforts needed to run the methods.

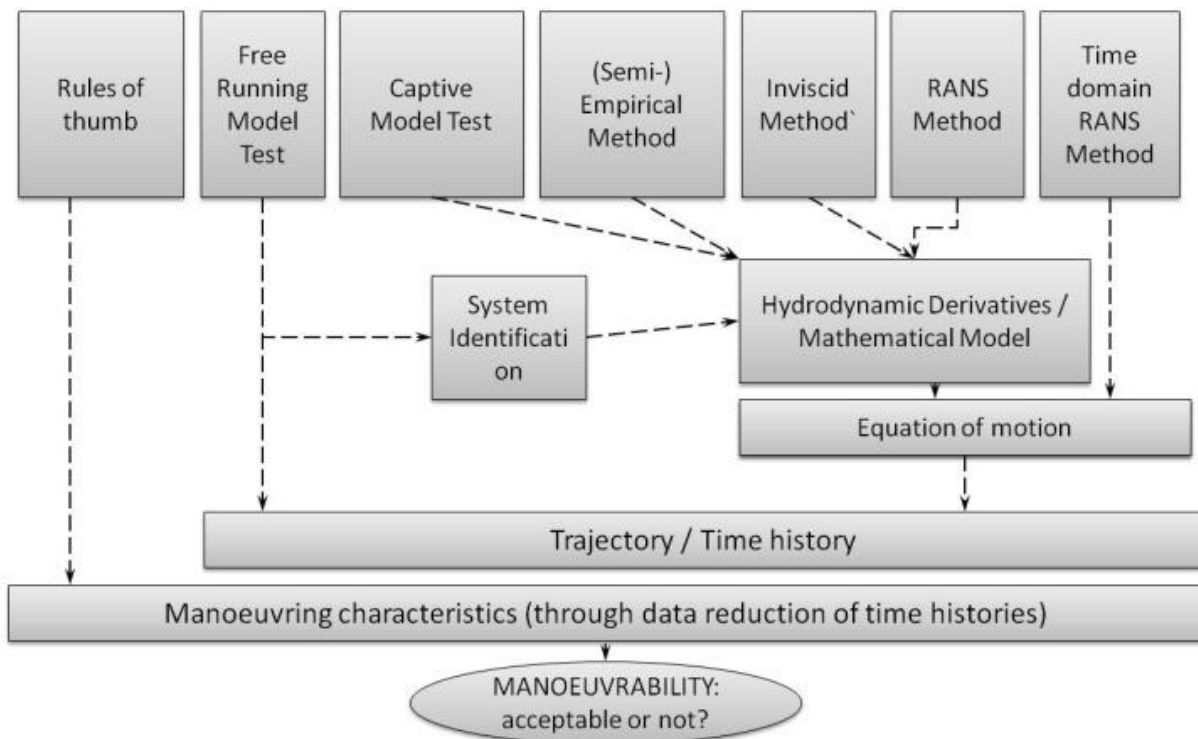


Figure 1: Overview of methods to predict manoeuvring characteristics

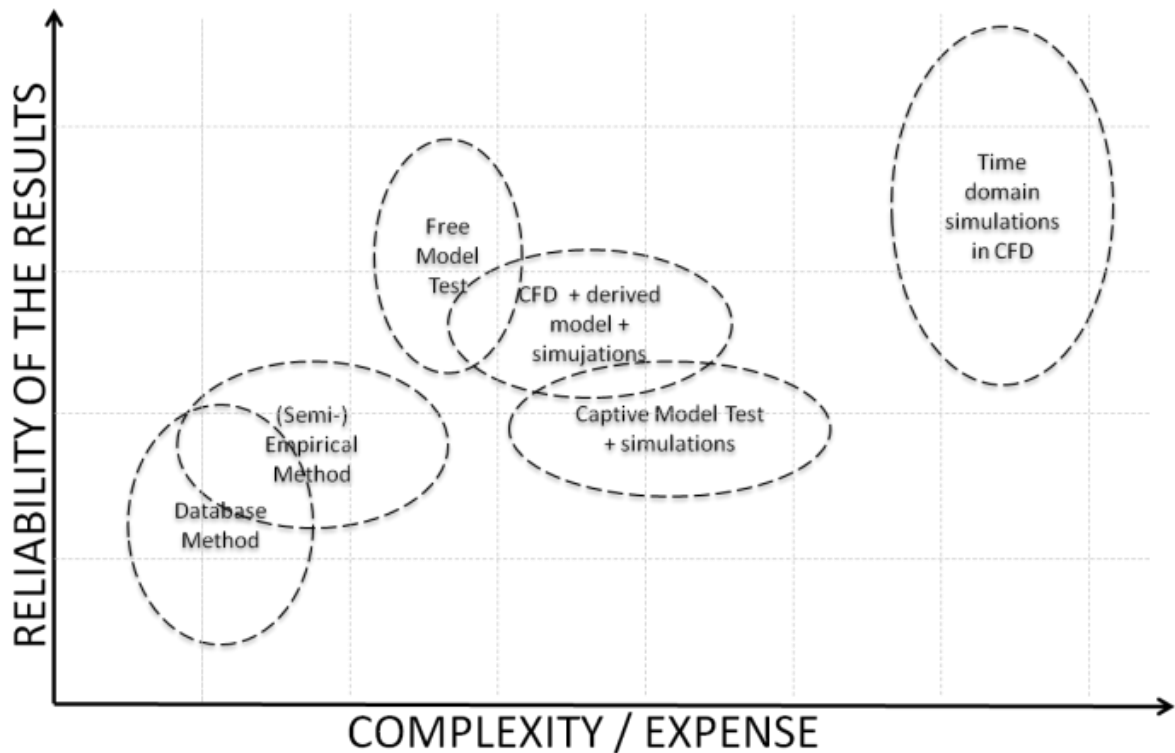


Figure 2: Different methods to predict hydrodynamic characteristics ranked in accuracy/reliability versus complexity/expense

In the following, we will detail the methods and describe the present and recent researches.

## 2.1 Rules of thumb

Rules of thumb methods can be used when tactical diameters or overshoot angles are guessed based on main particulars and rudder characteristics. The diagram of Clarke (1977) will fall under this. Based on such a diagram, it can be quickly guessed whether a ship is easily manoeuvring or not. At MARIN, this is used when the characteristics of a new designs are guessed and the main particulars of reference ships are close to a new design.

## 2.2 Semi-empirical methods

Semi-empirical methods are methods that is able to predict manoeuvring forces on the hull and rudders as function of main particulars or a minimum amount of input data. What makes this empirical is that the hydrodynamic coefficients (also called derivatives) or forces are calculated using simplified methods. Over the years, methods such as published by Clarke (1982), Ankudinov (1987, 1993), Fujino and Kijima (1993, 2003) have matured and have been in use at many cases as a first (low budget) estimate of the manoeuvrability of ships. An overview of these methods and the latest add-ons is given.

In the traditional sense, the manoeuvring coefficients are calculated based on ratios of main particulars (such as L/B and  $C_B$ ). A major step in these methods was the introduction of Oltmann and Sharma (1984) of the modular model. This allowed to describe hull forces, rudder forces, propeller forces and their mutual interactions separately. Fujino and Kijima (1996) added also some hull detail factor to this, in order to determine the manoeuvring derivatives to a higher accuracy.

The latest add-on to these methods is where these coefficients are guessed, not only based on few main particulars, but on a strip-wise description of the hull (a mix of the slender body theory and the cross flow drag theory). Although the amount of input required is more, the accuracy may also be higher (as seen in SIMMAN 2008 and SIMMAN2014).

## 2.3 Captive model tests

In the past, rotating arm and later PMM techniques have been used to derive hydrodynamic coefficients that fit in mathematical models. These techniques have been in use, and all relate to a mathematical model, which is used to carry out simulations. The paper will give an overview of the latest experimental techniques: new experimental techniques became available.

The challenge about the captive model tests, is that a dense enough matrix of test points has to be measured before a suitable mathematical model can be made.

In particular a technique that made is more affordable to perform multiple tests is the introduction of the CPMC by Grimm et al. (1977). This experimental technique allows to perform arbitrary captive trajectories through a basin. In shallow water, this was demonstrated by Eloot (1998). In deep water, this was taken to the extreme by Hallmann et al (2016). The result is that instationary captive tests are performed in a large basin (see Figure 3). With this, while sailing a track in a large basin, a combination of drift angles and turning rates can be measured during one run in the basin. This allows for an efficient use of basin time.

Nevertheless, the various stages that have to be performed while performing captive model tests is quite elaborate. This is illustrated in Figure 4. It is obvious that each of these tests have to be executed very carefully. In 2008 SIMMAN workshop, one of the conclusions was that when this complete train of steps should be well-established and regularly exercised. Only in these cases, the results of the manoeuvring characteristics are reaching a sufficiently accurate level.



Figure 3: Photograph of CPMC in MARIN's Seakeeping and Manoeuvring Basin

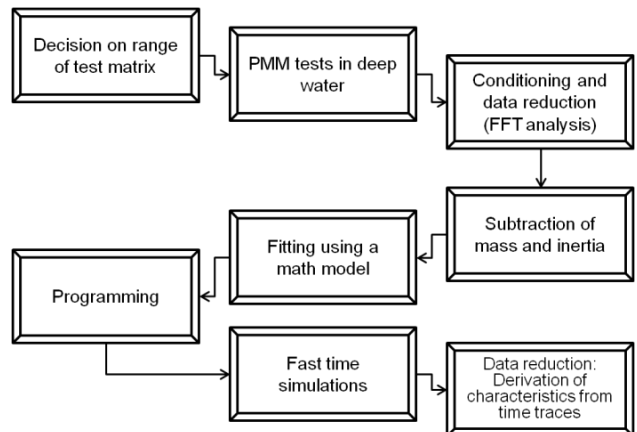


Figure 4: Steps in performing captive model tests to determine manoeuvring characteristics

Recent developments are taking place to quantify the uncertainties that may occur in all these steps. For example, for the second block, an uncertainty analysis has taken place as described by Simonsen (2004). For the 5<sup>th</sup>

block, Woodward (2013) has determined the fitting uncertainty. All these steps will be needed to determine a better understanding of the accuracy. The first block is perhaps the most important one: a suitable test matrix has to be selected that forms the basis of the model. In that stage, a range of drift angles, rudder angles, speeds, yaw rates, RPMs, etcetera need to be defined. This range needs to be rich enough to create a mathematical model that covers the state variables that the ship will encounter, and the coefficients in the mathematical model are not ill-conditioned.

#### **2.4 Inviscid methods**

Inviscid methods are typically panel methods that calculate mainly potential flow contributions. For manoeuvring related problems, the low frequent parts and the viscous parts play a role. This would mean that inviscid methods are not suitable. That is only partly correct. There are some methods in which it is possible to define the trailing vortices in these methods. With this, it is possible to use these panel methods to calculate lift. Consequently, we observe that these methods have been applied to make predictions for hydrofoil, foil assisted ships, and also for sailing yachts (in the past).

These methods are bow also explored for (very) fast ships. For very fast ships, it is namely impossible to have database methods or semi-empirical methods. In the search for a methodology that can be used in early design stage, Quadvlieg and van Walree (2015)

#### **2.5 Virtual captive tests in CFD**

In recent years, CFD has increasingly taken the place of the virtual basin, and captive tests are being replaced slowly but steadily by CFD simulations that calculate a similar large amount of individual test points. One can see in the amount of publications that this technique is becoming more and more popular. There are however still pitfalls. It is however possible to predict very good results, as demonstrated in the SIMMAN 2008 workshop by in particular Cura et al (2008).

Applications in commercial projects are nowadays becoming more common. Usually these commercial projects are not disseminated as much. But Toxopeus (2014), as shown some commercial application of this.

Points of attention to allow the practicality of this are the trade off between the need to model everything. Choices made that drive the computational efforts (and hence the cost) are

- the inclusion of free-surface or not;
- the use of wall functions or not;
- the amount of cells;
- this choice to perform URANS or steady RANS;
- the choice of the turbulence model;
- the choice of the way in which the propeller is modelled;
- the way the rudder is modelled.

Fureby et al (2016) discuss various aspects of this. The choice of LES type of turbulence model (Large Eddy Simulations) show to give better results for the detailed flow field, but will drive the amount of cells in the order of 100M. It was demonstrated that for that particular case, in order to derive global characteristics (the overall forces and moments as function of drift angle) it was sufficient to use a steady RANS. The order of magnitude of cells is approx 13M, while the calculations are taking place without wall functions.

The paragraph focuses on the ability to perform CFD instead of captive tests. In Figure 4, this means that the second block can be replaced with a set of CFD calculations. In principle, the other steps of Figure 4 remain needed in order to predict manoeuvring characteristics.

#### **2.6 Free running model tests**

The free running model tests with sufficiently large models are still in use a lot. They give the designer directly the manoeuvring characteristics. That means, that sitting on the carriage next to the model, the overshoot angles can be observed directly. In the past, manoeuvring prediction was focused on the prediction of the "directional stability" of a ship. However, since 1993 the (interim) IMO rules for manoeuvring came in the game. These caused that the focus of the prediction of surface ship manoeuvring changed from predicting directional stability towards the prediction of characteristics based on the zig-zag and turning circle tests: overshoot angles, initial turning ability, advance and tactical diameters. Free running model tests proved a very economical way to predict these quantities.

It is believed that free running model tests are the most commonly used methodology to arrive at manoeuvring characteristics. We should mention that this is also the most complete way of performing manoeuvres: no presumptions are made except the scale. For example all methods that are based on simulation—that use a mathematical model are a reflection of reality that make assumptions: for example that the added mass is constant, that the rudder has no added mass component, that

A particular point of attention is related to the scale effects. On this area, we observe the largest developments. Tonelli et al (2015) investigated the consequences of scale effects. Ueno et al (2014) have proposed an air fan on a free running model to compensate for frictional resistance in the case of very small models (scale 1:110).

The size of the model is of concern. We observe that some draw a the line that models should be larger than approximately 4 to 5 meter. Or a minimum model speed, such as at least 1 m/s. We see others that work with relatively small models. Aspects that play a role are the repeatability of the model tests, the size of propellers and rudders.

The model size alone is not the issue. There is worldwide consensus what is called the “conventional scale effect”. This is the fact that demonstrates the model scale resistance is too high, and that consequently, the propeller(s) deliver more thrust to arrive at model self-propulsion point. This would result in a too high water velocity over the rudder. On the other side, the wake fraction is higher at model scale, which results in a lower velocity over the rudder.

## 2.5 Free running, time domain CFD

The latest new kid on the block is the capability to perform 6dof RANS simulations. The equations of motions can be predicted. The latest SIMMAN 2014 workshop has demonstrated that results obtained by this method can be really good. Required computer times are still very large, but this may change in the future.

For surface ships, good correspondence is obtained, as demonstrated by Carrica et al (2012) for a surface ship and by Carrica et al (2016) for a submarine. These methods are still expensive in terms of used computer power. At present, the focus of the investigation is toward the allowable simplifications: which propeller modelling is suitable enough? Which amount of cells is needed and how large. Nevertheless, this method has received significant (academic) attention. In the international workshop on the benchmarking of ship manoeuvrability in 2008, only one submission was present that did free running manoeuvre in CFD. In the 2014 version of this workshop, there were 6 different submissions based on time domain CFD simulations.

## 3 UNCERTAINTIES

The issue at hand is: how the performance of these methods can be quantified. The following is suggested. The objective is to predict manoeuvring characteristics, and consequently, the ability to predict relevant characteristics is treated.

For each method, it is possible to define the average of the portside and starboard overshoot angles. This causes a bit of spreading in the methodology “free running model tests” (because portside and starboard are different). What is then observed is that it is possible to define an average and a standard deviation of the predictions of the overshoot angles. This is presented in Figure 5.

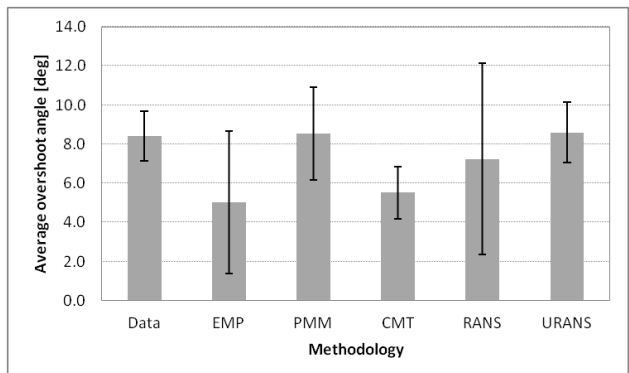


**Figure 5: Average overshoot angles, as measured during free running model tests (data) and 5 different prediction methodologies**

It is observed that the “empirical methods” show quite some spreading in the prediction, but also that it is possible that the prediction is correct. PMM tests show a larger spreading, but on average are nice. The URANS predictions (time domain RANS) are showing a very adequate average prediction, with a similar spreading. The RANS predictions (based on virtual model tests) are showing a large spreading. Also for the application of RANS combined with a mathematical model, it is clear that all steps as indicated in Figure 4 have to be performed in order to achieve a good result.

Figure 5 helps to create an overview of the relative accuracy / reliability of the methods. It should be mentioned that this is a worldwide assessment, not a judgement of individual codes or contributions. It is observed that this methodology can be used

## 4 CREATION OF A MATHEMATICAL MODEL

The previous sections are valid for the prediction of manoeuvring *characteristics*. However, for plenty of applications, the deliverable of the manoeuvring research is a mathematical model. And sometimes, the results that are achieved by using the mathematical model in a time domain simulator (monte-carlo type fast time domain simulations or bridge simulator studies).

Traditionally, simulation models are based on forces measured during (captive) model tests. However, over the past decades, more methodologies have become available.

The preferred methodology to determine a manoeuvring model is dependent on the required accuracy for the study, the risk and the reliability of the prediction for the ship type. Additionally, the environment (shallow or restricted water) and the time schedule of the customer are important considerations.

Figure 6 gives an overview of the methodologies used to arrive at simulation models for surface ships. In the schedule of Figure 6, there are two methods that are not being used (yet) commonly to create mathematical models. These are indicated by dashed lines. In addition, we may observe a similar Figure 7, which describes the cost versus the accuracy.

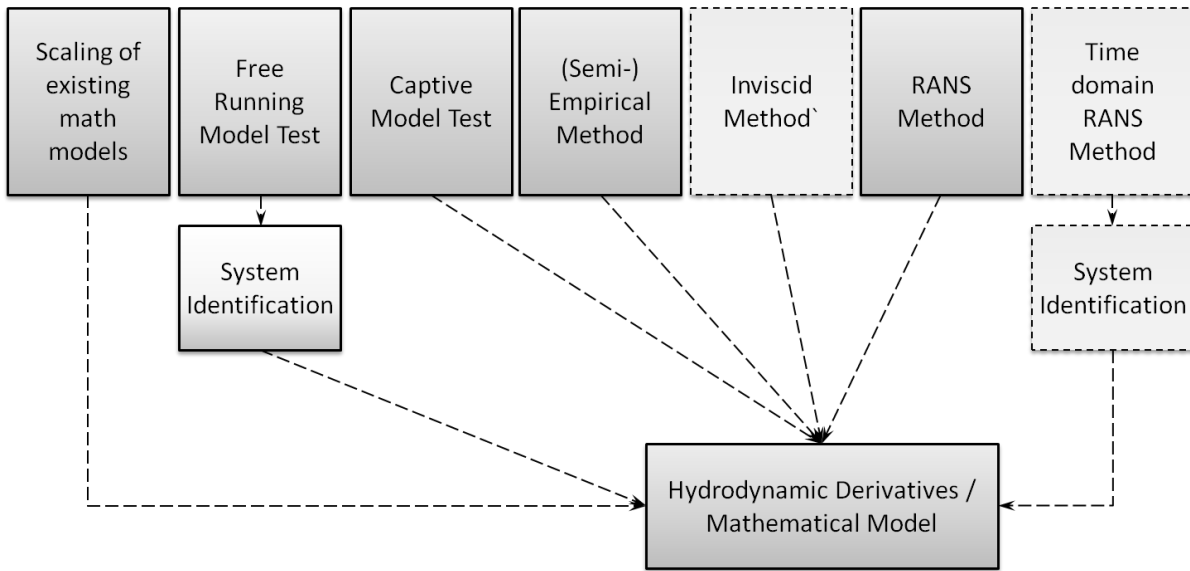


**Figure 6: Methodologies to obtain coefficients and a mathematical model**

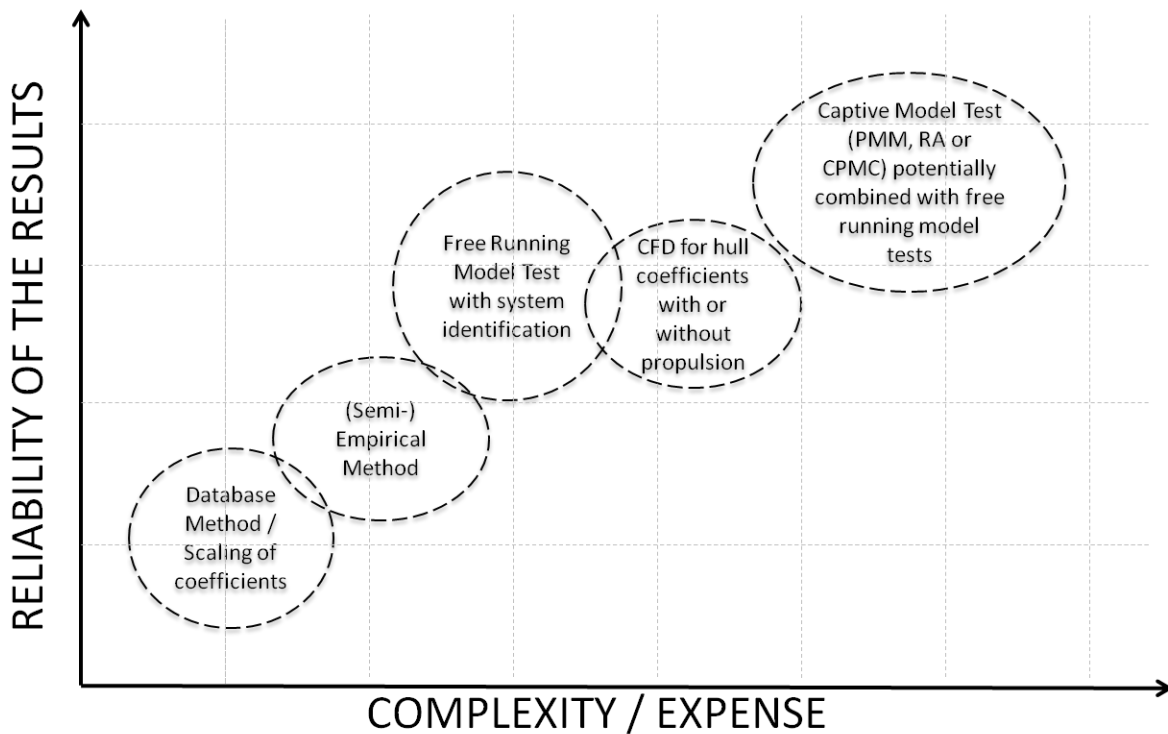


**Figure 7: Methodologies to generate mathematical models**

Next, we are treating the overview of methodologies with the practical application, the pros and cons.

- The database method uses existing, well-trusted simulation models and scales coefficients to arrive at a new simulation model. When the target ship is very close to ships for which there is already a lot of information available, the methodology is reliable, and the results can be used for feasibility studies. The advantage is that the method is very fast and can be robust. However, for the

scaling, knowledge is SME's (Subject Matter Experts) is needed.

- Semi-empirical methods are using hull, rudder and propeller data to determine manoeuvring properties. These methodologies have more flexibility: unconventional ship hulls can be addressed for example, at least as long as the shape of the hull is not too far from the data on which the semi-empirical method is based. Often, these methods are based on an eclectic blend of

slender body and cross flow drag theories, flow straightening, etcetera.

- Free running model tests are a well-known and highly reliable way of obtaining manoeuvring trajectories. In the latest development, a simulation model is created by adjusting the hydrodynamic coefficients that are calculated by semi-empirical methods by system identification using the results of the free running tests. Viviani et al (2009) successfully describes this methodology.
- CFD use for manoeuvring simulation models has been a long-term development. Recent results show that these methods are perfectly capable of achieving this goal (see Quadvlieg et al, 2015). For selected projects this is a very attractive solution (see Toxopeus et al, 2014). The future is that these methods need to be elaborated also for shallow water.
- Captive model tests have been used since the 1960s. Over the last years, MARIN has been investigating quasi-stationary tests, which have led to an efficiency gain. (see Hallmann & Quadvlieg, 2015).

## 5 UNCERTAINTIES

The challenge for these methods is that it will be necessary to define a methodology to quantify the accuracy of a mathematical model. Fuchs and Hwang (2015) make an attempt to quantify the accuracy or adequacy of a mathematical model. The quality of a mathematical model is namely the ability that the model predicts correct what it should predict. This may be divided in a set of differently and less objective quantities as the characteristics “advance” or “overshoot angle”.

The challenge in the coming years will be to quantify the adequacy of mathematical models for simulators. The guess is that after the SIMMAN 2019 workshop, this may be the next item to address by the international community.

## 5 SUMMARY AND CONCLUSIONS

This paper, in the light of recent advances of manoeuvring prediction techniques, gives an overview of the methods in place today, and their very recent developments.

One observes that in every of the methods, recent progress is booked. The availability of intense academic research in CFD has lead to a significant growth in the reliability of these methods. Still, for practical prediction of manoeuvring *characteristics*, free running model tests are a very often used method.

The paper sketched pros, cons and some challenges for the future developments in every method.

## REFERENCES

- Clarke (1977); Considerations of ship handling in hull design. Conference in ship handling, Plymouth November 1977.
- Carrica, P.M., F. Ismail, M. Hyman, S. Bhushan and F. Stern (2008), Turn and zigzag manoeuvres of a surface combatant using a URANS approach with dynamic overset grids. Proceedings of SIMMAN 2008
- Carrica, P.M., M. Kerkvliet, F. Quadvlieg, M. Pontarelli and J.E. martin (2016); CFD simulations and experiments of a manoeuvring generic submarine and prognosis for simulation of near surface operation. 31th Symposium on Naval Hydrodynamics, Monterey, CA, USA, September 2016.
- Cura, A., Vogt, M. and S. Gatchell (2008), Manoeuvring prediction for two tankers based on RANS simulation. Proceedings of SIMMAN 2008
- Eloot, K, G. Delefortrie, M. Vantorre and F. Quadvlieg (2015), Validation of Ship Manoeuvring in Shallow Water Through Free-running Tests. OMAE ASME 34th International Conference on Ocean, Offshore and Arctic Engineering, St. John's, Newfoundland, Canada, 2015
- Eloot K. and Vantorre, M. (1998); Alternative captive model tests: possibilities and limitations. International workshop on force acting on a manoeuvring vessel, September 1998, Val de Reuil, France
- Fuchs, B. and Wei-Yuan Hwang (2015); The collection of ASD tugboat operational field data and the usage for simulator modelling and validation. International Conference on Ship Manoeuvrability and Maritime Simulation (MARSIM), Newcastle, UK, 2015
- Fureby, C., Toxopeus, S.L., Johansson, M., Tormalm, M. and Petterson, K., (2016); A computational study of the flow around the KVLCC2 model hull at straight ahead conditions and at drift. Ocean Engineering, 2016
- O. Grim, P. Oltmann, S.D. Sharma, K. Wolff (1976); CPMC - A Novel Facility for Planar Motion Testing of Ship Models; 11th Symposium on Naval Hydrodynamics, April 1976
- Quadvlieg, F.H.H.A. and Brouwer, J., (2011); KVLCC2 Benchmark Data Including Uncertainty Analysis To Support Manoeuvring Predictions IV International Conference on Computational Methods in Marine Engineering (ECCOMAS MARINE), Lisbon, Portugal, 2011
- Quadvlieg, F.H.H.A., F. van Walree and V. Barthelemy (2015); Manoeuvring predictions for fast monohulls in early design stage. FAST 2015 Conference, Washington D.C., September 2015
- Quadvlieg, F.H.H.A, C.D. Simonsen, J.F. Otzen and F. Stern (2015), Review of the SIMMAN2014 Workshop on the State of the Art of Prediction Techniques for Ship Manoeuvrability. International Conference on

- Ship Manoeuvrability and Maritime Simulation (MARSIM), Newcastle, UK, 2015
- Sadat-Hosseini, H., Kim, D.-H., Toxopeus, S.L., Diez, M. and Stern, F. (2015), CFD and Potential Flow Simulations of Fully Appended Free Running 5415M in Irregular Waves World Maritime Technology Conference (WMTC), Providence, RI, 2015
- Simonsen CD (2004) PMM model test with DDG51 including uncertainty assessment. FORCE Technology report no. ONRII187, Lyngby
- Simonsen, C.D., Janne F. Otzen, C. Klimt, N.L. larsen and F. Stern (2012), Manoeuvring predictions in the early design phase using CFD generated PMM data. 29<sup>th</sup> Symposium on Naval Hydrodynamics, Gothenburg, Sweden, August 2012.
- Tonelli R. and Quadvlieg, F.H.H.A; (2015) New Benchmark Data for Manoeuvring in Shallow Water Based on Free Running Manoeuvring Tests Including Uncertainty of the Results OMAE ASME 34th International Conference on Ocean, Offshore and Arctic Engineering, St. John's, Newfoundland, Canada, 2015

- Toxopeus, S.L., Stroo, K. and Muller, B. (2013), Optimisation of Resistance and Towed Stability of an Offshore Going Barge With CFD. OMAE ASME 32nd International Conference on Ocean, Offshore and Arctic Engineering, Nantes, France, 2013
- Ueno, M. and Tsukada, Y., (2014), "Similarity of rudder effectiveness and speed response of a free running model ship", OMAE ASME 33rd International Conference on Ocean, Offshore and Arctic Engineering OMAE2014, Sane Francisco, California, USA. OMAE2014 - 23805
- Viviane, M., G. Dubbioso, C. Notaro, C. Podenzana, R. Depascale, M. Soave (2009); Application of System identification for the improvement of manoeuvrability prediction for twin screw ships. International conference on Marine Simulations and Ship Manoeuvrability MARSIM'09, Panama
- Woodward, M.D. (2013); propagation of experimental uncertainty from force measurements into manoeuvring derivatives. AMT2013, Gdansk, Poland

## The Hydrodynamics of a Spheroidal Submarine Close to the Free Surface

Ioannis K Chatjigeorgiou<sup>1\*</sup>, Touvia Miloh<sup>2</sup>

<sup>1</sup>National Technical University of Athens, School of Naval Architecture and Marine Engineering, Athens, Greece

<sup>2</sup>Tel Aviv University, Faculty of Engineering, Tel Aviv, Israel

**Abstract:** We investigate the hydrodynamics of a spheroidal submarine in an infinite liquid filed bounded from above by the free-surface. The developed methodology is analytical and results in closed-form expressions for the velocity potential and the hydrodynamic loading components. Only the diffraction problem is considered but we have to note that the multipole potentials used to formulate the diffraction component can be used to describe the radiation potentials as well. The solution method is based on the transformation of the Green's function into oblate spheroidal coordinates. That is achieved by employing a Fredholm integral equation approach of the second-kind.

**Keywords:** Submarines, oblate spheroid, hydrodynamics, diffraction.

### 1 INTRODUCTION

The method of multipoles, known also as Ursell's multipoles, was invented for the heaving problem of a half-immersed circular cylinder (Ursell, 1949; Martin, 1991). In fact, it is the direct application of the method of separation of variables and the principle of linear superposition. In contrast to "harmonics" which are the products of the separable solutions of the Laplace equation, the so-called "multipoles", aside from the field equation satisfy the boundary conditions as well. In hydrodynamics, multipole solutions are used to formulate the potential of the disturbance caused by the presence of the body into a liquid domain bounded from above by a free-surface. The nature of the disturbance can be "diffraction", "radiation", "wave resistance" and "added wave resistance". Selectively, the liquid domain can be confined by the existence of a bottom or vertical walls adding more conditions to the investigated boundary value problem, and consequently complexities.

The form of the multipole solutions follows the geometry of the solid and they are formulated by the "harmonics" which constitute the solutions of the Laplace equation in the relevant coordinate system. In fact the use of multipole solutions is the only advisable technique for achieving analytic expressions for the velocity potential (and accordingly, pressure, forces and hydrodynamic parameters) in coordinate systems for which separable solutions of the Laplace equation exist. The primary goal using this technique is the transformation of the governing Green's function into the relevant harmonics. Achieving that, the employment of the body boundary condition becomes an elementary task and it is realized through a simple derivative.

The method of multipole expansions has found a great deal of hydrodynamic applications for geometries

that allow separable solutions of the Laplace equation. Lion's share belongs to spheres for which the reported solutions became feasible after Thorn's (1953) seminal paper on the multiple expansions in the theory of surface waves. Hydrodynamic problems for spheres were exhaustively investigated by several authors (Linton, 1991 & 1993; Srokosz, 1980; Wu and Eatock Taylor, 1988 & 1990; Wu et al., 1994; Wu, 1995, 1996 & 1998a,b; Ursell, 1999a,b; Gray, 1978; Rahman, 2001; Wang, 1986). All these studies concerned fully immersed spheres while works on more difficult settings such as semi-immersed spheres are scarce (e.g., Hulme, 1982).

In contrast to spheres, fewer studies exist for more complicated geometries, such as spheroids, and nearly none on ellipsoids. Here we must distinguish between the "axisymmetric" and the "non-axisymmetric" cases of spheroids. The former and the latter cases assume that the axis of symmetry is perpendicular and parallel to the free-surface respectively. The use of multipole potentials as far as the hydrodynamics of spheroids is concerned was pioneered by Farrell (1971) & (1973). Farrell (1971) dealt with a simple application, that of the Taylor's added mass of a spheroid in an infinite medium without a free-surface. Nevertheless, in this particular study the author reported the proof of the expansion of the exponential solution of the Laplace equation in non-axisymmetric prolate spheroidal coordinates.

Accordingly, Farrell (1973) presented the exact solution of the wave resistance problem by a non-axisymmetric prolate spheroid translating with steady velocity below a free-surface in a liquid field of infinite depth. To this end Farrell (1973) used an approach based on a Fredholm integral equation of the second-kind while with his results disputed Havelock's (1931) approximation. Farrell's (1973) methodology was accordingly used by Wu and Eatock Taylor (1987) &

\* Corresponding author e-mail: chatzi@naval.ntua.gr

(1989) who tackled respectively the diffraction and the diffraction/radiation problems by immersed non-axisymmetric prolate spheroids.

Always connected with the non-axisymmetric cases of prolate spheroids, in a series of studies Chatjigeorgiou and Miloh (2013), (2014a,b) & (2015a,b) investigated all aspects associated with the linear hydrodynamics of non-axisymmetric prolate spheroids including, diffraction, radiation, wave resistance, wave resistance with forward speed, for both infinite and finite water depths. In these studies the multipole potentials were determined using the method of ultimate image singularities which proves the existence of a spheroid theorem expressed through the Miloh-Havelock integro-differential operator (Havelock, 1952; Miloh, 1974).

Finally, it should be mentioned that axisymmetric cases of spheroids were investigated by Chatjigeorgiou (2012) and (2013) who considered both oblates and prolates. To this end, the author followed a different line of approach that was based on transforming Thorne's (1953) multipole potentials, initially expressed in terms of spherical and polar coordinates, in terms of oblate and prolate spheroidal harmonics. That was achieved using proper addition theorems.

What it is missing from the literature is proper solutions for hydrodynamic boundary value problems for oblate spheroids, especially for the non-axisymmetric case of placement with respect to the free-surface. Oblate spheroids might have very valuable applications especially as modules of integrated wave energy devises. Typically, those special purpose devises rely on spheres (e.g. Greenhow, 1980) neglecting the possibility of using more complicated geometries which hopefully could be more efficient in certain applications. Non-axisymmetric oblate spheroids, based on their slendernesses, run from spheres to circular disks (in the two limiting cases), so they are quite flexible.

In the present study we tackle the diffraction problem by non-axisymmetric oblate spheroids. The method we developed is generic and could be employed for other interesting applications as well, as for example the case of a vertical wall having a circular hole, an oblate spheroid placed symmetrical on a vertical wall, etc.

In contrast to prolate spheroids, no oblate spheroid theorem exists. Therefore, for the purposes of the present contribution we apply the Fredholm integral equation approach of Farell (1973) that is based on the knowledge of the source distributions on the surface of the spheroid. The latter are obtained using the calculation formula of Lamb (1895) and the interior and exterior potentials of Hobson (1931).

## 2 THE LINEAR HYDRODYNAMIC PROBLEM

We assume an oblate spheroid that is fully immersed in a liquid field of infinite depth that is bounded from above by a free-surface. The centre of the body is situated at a distance  $f$  below the undisturbed free-surface. The orientation of the spheroid (see Figure 1) is in accord with the non-axisymmetric case, namely, horizontal semi-minor  $x$ -axis parallel to the free-surface. The semi-minor and the semi-major axis of the spheroid (along  $x$  and  $y, z$  respectively) are denoted by  $a$  and  $b$ . The semi-focal distance is  $c = \sqrt{b^2 - a^2}$  and without loss of generality we can assume that  $c = 1$ . It is also assumed that the spheroid is subjected to the action of regular incident waves, with amplitude  $A$  and circular frequency  $\omega$ , traveling at angle  $\beta$  relatively to the horizontal  $x$ -axis and undergoes small oscillatory motions with the same frequency.

In the realm of the linear potential theory, the fluid is assumed inviscid and incompressible and the flow irrotational. Flow's regime is governed by the velocity potential

$$\Phi(x, y, z; t) = Re[\phi(x, y, z)e^{i\omega t}] \quad (1)$$

where the spatial component  $\phi(x, y, z)$  should satisfy the Laplace equation

$$\nabla^2 \phi = 0 \quad (2)$$

and the linearized free-surface boundary condition

$$-K\phi + \frac{\partial \phi}{\partial z} = 0, \quad z = 0 \quad (3)$$

with  $K = \omega^2/g$  where  $g$  is the gravitational acceleration. It is understood that the velocity potential must also satisfy a proper radiation condition for outgoing waves at infinity. The total velocity potential is decomposed into the incident wave component  $\phi_I$ , the diffraction component  $\phi_D$  and the six radiation (Kirchhoff) potentials for the six modes of motion, three translational for  $j = 1, 2, 3$  (surge, sway, heave) and three rotational  $j = 4, 5, 6$  (roll, pitch, yaw) with amplitudes  $\xi_j$ . Hence

$$\phi = \phi_I + \phi_D + i\omega \sum_{j=1}^6 \xi_j \phi_j \quad (4)$$

The incident wave component is

$$\phi_I(x, y, z) = \frac{igA}{\omega} e^{Kz - iK(x \cos \beta + y \sin \beta)} \quad (5)$$

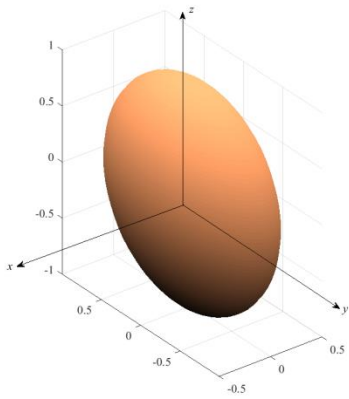


Figure 1. Non-axisymmetric oblate spheroid orientation; the free surface is considered parallel to the horizontal  $x$ -axis; the centre of the spheroid is situated at a distance  $f$  below the free-surface; the slenderness of the particular spheroid is  $a/b = 0.4$ .

The free-surface boundary condition (3), as well as the incident wave component (5), assume that the origin of the Cartesian coordinate system is fixed on the free-surface. The concerned hydrodynamic problem is completed by introducing the appropriate impermeable body boundary condition which must be satisfied separately for the diffraction and the radiation problems. These are

$$\frac{\partial(\phi_D + \phi_I)}{\partial \underline{n}} = 0 \quad (6)$$

$$\frac{\partial \phi_j}{\partial \underline{n}} = 0, \quad j = 1, 2, 3, 4, 5, 6 \quad (7)$$

where  $\underline{n} = (n_1, n_2, n_3)$  is the outward normal on the body's surface  $S$  and  $\underline{r}$  is the radius vector of a point on the surface, such that  $(\underline{r} \times \underline{n}) = (n_4, n_5, n_6)$ .

### 3 GREEN'S FUNCTION EXPANSION INTO OBLATE SPHEROIDAL HARMONICS – THE DIFFRACTION PROBLEM

Here we will investigate only the diffraction problem, noting that the radiation potentials are formulated using the same Green's function. The Green's function of a pulsating source situated at a distance  $f$  below the free-surface that satisfies the Laplace equation and the free-surface boundary condition in an infinite medium is (e.g. Wehausen and Laitone, 1960)

$$G(x, y, z; x', y', z') = \frac{1}{r} - \frac{1}{2\pi} \int_0^\infty \int_{-\pi}^{\pi} \frac{K+k}{K-k} \times e^{-2kf} e^{k(z+z') + ik[(x-x') \cos \alpha + (y-y') \sin \alpha]} d\alpha dk \quad (8)$$

$$\times e^{-2kf} e^{k(z+z') + ik[(x-x') \cos \alpha + (y-y') \sin \alpha]} d\alpha dk$$

where

$$r = \sqrt{(x-x')^2 + (y-y')^2 + (z-z')^2} \quad (9)$$

Note that the origin of the  $(x, y, z)$  system has been moved to the centre of the body.

It is now time to introduce the oblate spheroidal system. The transformation formulae between the Cartesian  $(x, y, z)$  and the oblate spheroidal  $(\eta, \theta, \psi)$  coordinates are

$$x = c \sinh \eta \cos \theta = c\mu\zeta \quad (10)$$

$$y = c \cosh \eta \sin \theta \sin \psi \\ = c\sqrt{\zeta^2 + 1}\sqrt{1 - \mu^2} \sin \psi \quad (11)$$

$$z = c \cosh \eta \sin \theta \cos \psi \\ = c\sqrt{\zeta^2 + 1}\sqrt{1 - \mu^2} \cos \psi \quad (12)$$

with  $\zeta = \sinh \eta$  and  $\mu = \cos \theta$ . Relevant relations hold for  $(x', y', z')$  using the prime symbol. The semi-major and the semi-minor axes of the spheroid are given by  $b = c\sqrt{\zeta_0^2 + 1}$  and  $a = c\zeta_0$  where  $\zeta_0 = \tanh^{-1}(a/b)$ . Accordingly, the diffraction potential (spatial only component) induced by an oblate spheroid situated in the path of a regular wave train is

$$\phi_D(x, y, z) = \int_S \frac{\sigma(x', y', z')}{r} dS \\ - \frac{1}{2\pi} \int_S \int_0^\infty \int_{-\pi}^{\pi} \frac{K+k}{K-k} \times e^{-2kf} e^{k(z+z') + ik[(x-x') \cos \alpha + (y-y') \sin \alpha]} \times \sigma(x', y', z') d\alpha dk dS \quad (13)$$

where  $\sigma(x', y', z')$  is the source strength (source distribution of the surface of the spheroid). The integration is performed over the surface of the spheroid  $S$  which for an oblate spheroid is

$$dS = b(b^2 \cos^2 \theta + a^2 \sin^2 \theta)^{1/2} \sin \theta d\theta d\psi \quad (14)$$

Substituting (13) into the boundary condition (6) results in a Fredholm integral equation of the second kind in terms of the source distribution  $\sigma(x, y, z)$  (Farell, 1973; Wu and Eatock Taylor, 1987). Further details will not be given herein since we will be using the source distribution functions in oblate spheroidal coordinates directly taken from Hobson (1931).

The incident wave potential is now transformed into

$$\phi_I(x, y, z) = \frac{igA}{\omega} e^{-Kf} e^{Kz - iK(x \cos \beta + y \sin \beta)} \quad (15)$$

where we recall that the  $z$ -axis is now fixed on the centre of the body pointing vertically upwards. Accordingly the diffraction component (13) can be considered normalized by  $igA/\omega e^{-Kf}$ .

The integration required by (13) dictates knowing the  $\sigma(x', y', z')$  on the surface of the spheroid at  $\eta = \eta_0$ . This is given by (Lamb, 1895; p.67)

$$\sigma(\eta_0, \theta, \psi) = \frac{1}{4\pi} \left( \frac{\partial \phi_{ext}}{\partial \underline{n}} - \frac{\partial \phi_{int}}{\partial \underline{n}} \right)_{\eta=\eta_0} \quad (16)$$

where  $\phi_{ext}$  and  $\phi_{int}$  denote the potentials to the exterior and to the interior of the spheroid. According to Hobson (1931), p.431, the potentials for the interior and the exterior spaces of an oblate spheroid are represented by the sum of a finite number of terms such as

$$F_n^m \frac{P_n^m(i \sinh \eta)}{P_n^m(i \sinh \eta_0)} P_n^m(\cos \theta) \begin{cases} \cos m\psi \\ \sin m\psi \end{cases}$$

$$F_n^m \frac{Q_n^m(i \sinh \eta)}{Q_n^m(i \sinh \eta_0)} P_n^m(\cos \theta) \begin{cases} \cos m\psi \\ \sin m\psi \end{cases}$$

where  $P_n^m$  and  $Q_n^m$  are the associate Legendre functions of the first and the second kind respectively and  $F_n^m$  are unknown constants associated with the degree  $n$  and the order  $m$ . Without loss of generality we will assume in the sequel that  $c = 1$  while the actual volume of the spheroid will be explicitly determined by the slenderness ratio  $a/b$ .

The source distribution over the surface of the body can be decomposed into symmetric and antisymmetric terms,  $\sigma_1$  and  $\sigma_2$ , respectively, as (Wu and Eatock Taylor, 1989)

$$\sigma = \sigma_1 + \sigma_2 \quad (17)$$

Introducing the interior and the exterior potentials into (16) immediately yields

$$\begin{aligned} & \left\{ \begin{array}{l} \sigma_1(\eta_0, \theta, \psi) \\ \sigma_2(\eta_0, \theta, \psi) \end{array} \right\} \\ &= \frac{i}{4\pi (\sinh^2 \eta_0 + \cos^2 \theta)^{1/2} \cosh \eta_0} \\ & \sum_{n=0}^{\infty} \sum_{m=0}^n \left\{ \begin{array}{l} F_n^m \\ \tilde{F}_n^m \end{array} \right\} \frac{(-1)^m P_n^m(\cos \theta)}{P_n^m(i \sinh \eta_0)} \frac{(n+m)!}{(n-m)!} \\ & \times \begin{cases} \cos m\psi \\ \sin m\psi \end{cases} \end{aligned} \quad (18)$$

The derivation of (18) was assisted by the Wronskian determinant of the associate Legendre functions [Abramowitz and Stegun, 1971; eq. (8.1.8)]

In symmetric problems about the plane  $y = 0$ , such as the wave resistance and the wave diffraction of a spheroid in head and following seas, the antisymmetric term  $\sigma_2$  is absent. In accord with the decomposition (17) we assume that

$$\phi_D = \phi_D^{(1)} + \phi_D^{(2)} \quad (19)$$

with

$$\begin{cases} \phi_D^{(1)} \\ \phi_D^{(2)} \end{cases} = \int_S \begin{cases} \sigma_1 \\ \sigma_2 \end{cases} G dS \quad (20)$$

In an approach similar to that followed by Farrell (1973) (see also Wu and Eatock Taylor, 1989) we write

$$\begin{aligned} & \int_S \begin{cases} \sigma_1(x', y', z') \\ \sigma_2(x', y', z') \end{cases} \frac{1}{r} dS \\ &= \sum_{n=0}^{\infty} \sum_{m=0}^n \left\{ \begin{array}{l} F_n^m \\ \tilde{F}_n^m \end{array} \right\} P_n^m(\cos \theta) Q_n^m(i \sinh \eta_0) \\ & \times \begin{cases} \cos m\psi \\ \sin m\psi \end{cases} \end{aligned} \quad (21)$$

Accordingly, the symmetric and antisymmetric diffraction components become

$$\begin{aligned} & \left\{ \begin{array}{l} \phi_D^{(1)}(x, y, z) \\ \phi_D^{(2)}(x, y, z) \end{array} \right\} \\ &= \sum_{n=0}^{\infty} \sum_{m=0}^n \left\{ \begin{array}{l} F_n^m \\ \tilde{F}_n^m \end{array} \right\} P_n^m(\mu) Q_n^m(i\zeta) \begin{cases} \cos m\psi \\ \sin m\psi \end{cases} \\ & - \frac{1}{2\pi} \int_0^{\infty} \int_{-\pi}^{\pi} \frac{K+k}{K-k} e^{-2kf} e^{kz+ik[x \cos \alpha + y \sin \alpha]} \times \\ & \int_S e^{kz'-ik[x' \cos \alpha + y' \sin \alpha]} \begin{cases} \sigma_1(x', y', z') \\ \sigma_2(x', y', z') \end{cases} dS d\alpha dk \end{aligned} \quad (22)$$

The next step is to express the regular terms of the right hand side of (22) with respect to oblate spheroidal coordinates. This requirement practically refers the exponential term(s). An analogous expression can be used for the incident wave component (15). The relation that transforms  $e^{kz+ik[x \cos \alpha + y \sin \alpha]}$  into prolate spheroidal coordinates has been given independently by Havelock (1954) and Farrell (1971). Here we outline the procedure that transforms the concerned term into oblate spheroidal harmonics.

First we assume that the exponential term is expressed as a series expansion of oblate spheroidal harmonics according to

$$\begin{aligned} & e^{kz+ik[x \cos \alpha + y \sin \alpha]} \\ &= \sum_{n=0}^{\infty} \sum_{m=0}^n (A_n^m \cos m\psi \\ & \quad + \tilde{A}_n^m \sin m\psi) P_n^m(\mu) P_n^m(i\zeta) \end{aligned} \quad (23)$$

where the expansion coefficients  $A_n^m$  and  $\tilde{A}_n^m$  are to be determined. Subsequently we evaluate (23) exactly on the body's surface. Hence, using (10)-(12) one gets

$$\begin{aligned} & e^{kb\sqrt{1-\mu^2} \cos \psi + ik(a\mu \cos \alpha + b\sqrt{1-\mu^2} \sin \psi \sin \alpha)} \\ &= \sum_{n=0}^{\infty} \sum_{m=0}^n (A_n^m \cos m\psi \\ & \quad + \tilde{A}_n^m \sin m\psi) P_n^m(\mu) P_n^m(i\zeta_0) \end{aligned} \quad (24)$$

By exploiting the orthogonality of  $\cos m\psi$  in the interval  $-\pi \leq \psi \leq \pi$  and the associate Legendre functions  $P_n^m(\mu)$  in the interval  $-1 \leq \mu \leq 1$  [Abramowitz and Stegun, 1970; eq. (8.14.13)] we obtain initially

$$\begin{aligned} A_s^t = & \frac{\varepsilon_t}{2\pi} \left( s + \frac{1}{2} \right) \frac{(s-t)!}{(s+t)!} \frac{1}{P_s^t(i\zeta_0)} \int_{-1}^1 e^{ika\mu \cos \alpha} P_s^t(\mu) \\ & \int_{-\pi}^{\pi} e^{kb\sqrt{1-\mu^2}(\cos \psi + i \sin \psi \sin \alpha)} \cos t\psi d\psi d\mu \end{aligned} \quad (25)$$

where  $\varepsilon_0 = 1$  and  $\varepsilon_t = 2$ ,  $t = 1, 2, \dots$ . A similar relation is obtained for  $\tilde{A}_s^t$  when applying the orthogonality of  $\sin m\psi$  in (24).

Using Havelock (1954) we know that

$$\begin{aligned} & \int_{-\pi}^{\pi} e^{kb\sqrt{1-\mu^2}(\cos \psi + i \sin \psi \sin \alpha)} \begin{Bmatrix} \cos t\psi \\ \sin t\psi \end{Bmatrix} d\psi \\ &= \pi \begin{Bmatrix} N_t(\alpha) \\ \tilde{N}_t(\alpha) \end{Bmatrix} I_t(kb\sqrt{1-\mu^2} \cos \alpha) \end{aligned} \quad (26)$$

where  $I_t$  is the modified Bessel function of the first kind and order  $t$  while it holds that

$$\begin{Bmatrix} N_m(\alpha) \\ \tilde{N}_m(\alpha) \end{Bmatrix} = \frac{(1 + \sin \alpha)^m \pm (1 - \sin \alpha)^m}{(\cos \alpha)^m} \quad (27)$$

Note that Havelock (1954) neglected to write the factor  $\pi$  in his result for (26).

Accordingly, the evaluation of the integral

$$\begin{aligned} & \int_{-1}^1 e^{ika\mu \cos \alpha} P_s^t(\mu) I_t(kb\sqrt{1-\mu^2} \cos \alpha) d\mu \\ & \left( \frac{2\pi}{z} \right)^{1/2} i^n (\sin \phi)^{v-1/2} C_n^{(v)}(\cos \phi) J_{v+n}(z) \\ &= \int_0^\pi e^{iz \cos \theta \cos \phi} \times \\ & J_{v-1/2}(z \sin \theta \sin \phi) C_n^{(v)}(\cos \theta) (\sin \theta)^{v+1/2} d\theta \end{aligned} \quad (28)$$

where  $C_n^{(v)}$  denotes the Gegenbauer polynomial. Equation (28) is valid for  $v > 1/2$  and  $n = 0, 1, 2, \dots$ . In (28) we make the following assumptions:  $\cos \theta = \mu$ ,  $\cos \phi = i\zeta_0$ ,  $v = t + 1/2$ ,  $z = -ik \cos \alpha$ . After some tedious algebra we can show that

$$\begin{aligned} & \int_{-1}^1 e^{ika\mu \cos \alpha} P_s^t(\mu) I_t(kb\sqrt{1-\mu^2} \cos \alpha) d\mu \\ &= (-1)^{t+1} i^t \left( \frac{2\pi}{k \cos \alpha} \right)^{1/2} P_s^t(i\zeta_0) I_{s+1/2}(k \cos \alpha) \end{aligned} \quad (29)$$

Therefore, the expansion coefficients  $A_s^t$  and  $\tilde{A}_s^t$  involved in (24) will be given by

$$\begin{Bmatrix} A_s^t \\ \tilde{A}_s^t \end{Bmatrix} = (-1)^{t+1} \begin{Bmatrix} i^t \\ i^{t+1} \end{Bmatrix} \frac{\varepsilon_t}{2} \frac{(s-t)!}{(s+t)!} (2s+1) \times \begin{Bmatrix} N_t(\alpha) \\ \tilde{N}_t(\alpha) \end{Bmatrix} \left( \frac{\pi}{2k \cos \alpha} \right)^{1/2} I_{s+1/2}(k \cos \alpha) \quad (30)$$

Similar relations hold for the expansion coefficients of  $e^{kz'-ik[x' \cos \alpha + y' \sin \alpha]}$  (and consequently for the incident wave potential) which are obtained by simply replacing  $\alpha$  by  $\alpha + \pi$ . Thus, assuming that

$$\begin{aligned} & e^{kz-ik[x \cos \alpha + y \sin \alpha]} \\ &= \sum_{s=0}^{\infty} \sum_{t=0}^s (B_s^t \cos t\psi + \tilde{B}_s^t \sin t\psi) P_s^t(\mu) P_s^t(i\zeta) \end{aligned} \quad (31)$$

one can show that

$$\begin{Bmatrix} B_s^t \\ \tilde{B}_s^t \end{Bmatrix} = \begin{Bmatrix} (-1)^{s+1} \\ (-1)^s \end{Bmatrix} \begin{Bmatrix} i^t \\ i^{t+1} \end{Bmatrix} \frac{\varepsilon_t}{2} \frac{(s-t)!}{(s+t)!} (2s+1) \times \begin{Bmatrix} N_t(\alpha) \\ \tilde{N}_t(\alpha) \end{Bmatrix} \left( \frac{\pi}{2k \cos \alpha} \right)^{1/2} I_{s+1/2}(k \cos \alpha) \quad (32)$$

Finally, performing the integrations over the surface of the body, we obtain the following expansions for  $\phi_D^{(1)}$  and  $\phi_D^{(2)}$

$$\begin{aligned} & \left\{ \begin{array}{l} \phi_D^{(1)} \\ \phi_D^{(2)} \end{array} \right\} \\ &= \sum_{n=0}^{\infty} \sum_{m=0}^n \left\{ \begin{array}{l} F_n^m \\ \tilde{F}_n^m \end{array} \right\} P_n^m(\mu) Q_n^m(i\zeta) \left\{ \begin{array}{l} \cos m\psi \\ \sin m\psi \end{array} \right\} \\ &+ \sum_{n=0}^{\infty} \sum_{m=0}^n \left\{ \begin{array}{l} F_n^m \\ \tilde{F}_n^m \end{array} \right\} \sum_{s=0}^{\infty} \sum_{t=0}^s \left\{ \begin{array}{l} C_{ns}^{mt} \\ \tilde{C}_{ns}^{mt} \end{array} \right\} P_s^t(\mu) P_s^t(i\zeta) \\ &\times \left\{ \begin{array}{l} \cos m\psi \\ \sin m\psi \end{array} \right\} \end{aligned} \quad (33)$$

where

$$\begin{aligned} & \left\{ \begin{array}{l} C_{ns}^{mt} \\ \tilde{C}_{ns}^{mt} \end{array} \right\} \\ &= (-1)^{n+m+t+1} i^{m+t+1} \frac{\varepsilon_t}{4} \frac{(n+m)!(s-t)!}{(n-m)!(s+t)!} \\ &\times (2s+1) \int_0^{\infty} \frac{K+k}{K-k} e^{-2kf} \int_0^{\frac{\pi}{2}} \left\{ \begin{array}{l} N_m(\alpha) N_t(\alpha) \\ \tilde{N}_m(\alpha) \tilde{N}_t(\alpha) \end{array} \right\} \\ &\times \frac{I_{s+1/2}(k \cos \alpha) I_{n+1/2}(k \cos \alpha)}{\cos \alpha} d\alpha dk \end{aligned} \quad (34)$$

which holds for  $n + m + s + t$  even, otherwise  $C_{ns}^{mt}$  and  $\tilde{C}_{ns}^{mt}$  are zero. Note that  $N_m(\alpha)$  is an even function of  $\alpha$  while  $\tilde{N}_m(\alpha)$  is an odd function of  $\alpha$ . The total diffraction potential is given by (19) while we recall that it has been considered normalized by  $igA/\omega e^{-Kf}$ . The incident wave potential (again normalized by  $igA/\omega e^{-Kf}$ ) is given by an expression similar to (31) after replacing  $k$  by  $K$  and  $\cos \alpha$  by  $\cos \beta$ . Apparently the same holds for the expansion coefficients  $B_s^t$  and  $\tilde{B}_s^t$  which in the sequel will denote the expansion coefficients of the incident wave component.

The infinite integral in (34) is divergent unless it is considered in the Cauchy Principal Value sense. In addition, in order to satisfy the far-field radiation condition the far field integral involved in the formulation of the diffraction potential(s) should be expanded in the following way

$$\int_0^{\infty} \frac{F(k)}{K-k} dk = PV \int_0^{\infty} \frac{F(k)}{K-k} dk - i\pi F(K) \quad (35)$$

The Neumann boundary condition for the diffraction problem becomes

$$\frac{\partial(\phi_D^{(1)} + \phi_D^{(2)})}{\partial \zeta} = -\frac{\partial \phi_I}{\partial \zeta}, \quad \zeta = \zeta_0 \quad (36)$$

Thus, substituting the diffraction and the incident wave components into (36) and exploiting the orthogonality relations of the trigonometric and the associate Legendre functions we obtain the following complex linear systems in terms of the unknown expansion coefficients  $F_n^m$  and  $\tilde{F}_n^m$ :

$$\begin{aligned} & \left\{ \begin{array}{l} F_s^t \\ \tilde{F}_s^t \end{array} \right\} \dot{Q}_s^t(i\zeta_0) + \dot{P}_s^t(i\zeta_0) \sum_{n=0}^{\infty} \sum_{m=0}^n \left\{ \begin{array}{l} F_n^m C_{ns}^{mt} \\ \tilde{F}_n^m \tilde{C}_{ns}^{mt} \end{array} \right\} = \\ & - \left\{ \begin{array}{l} B_s^t \\ \tilde{B}_s^t \end{array} \right\} \dot{P}_s^t(i\zeta_0) \end{aligned} \quad (37)$$

The system(s) (37) can be easily handled and can be solved using standard matrix techniques.

#### 4 HYDRODYNAMIC LOADING

The forces and moments exerted on the oblate spheroid when it is subjected the action of regular waves are obtained by integrating the hydrodynamic pressure on the surface of the spheroid. Mathematically speaking

$$F_j = -i\omega\rho \int_S (\phi_I + \phi_D) n_j dS \quad (38)$$

where  $\rho$  is the density of the liquid while  $(F_1, F_2, F_3) = (F_x, F_y, F_z)$  are the surge, sway and heave forces, and  $(F_4, F_5, F_6) = (M_x, M_y, M_z)$  are the roll, pitch and yaw moments (note that we have assumed  $c = 1$ ).

In the present section we examine the variation of the exciting forces and moments as well as the added mass and the hydrodynamic damping parameters. The exciting forces and moments are depicted in Figures 2-11 for slendernesses  $a/b = 1, 0.8, 0.4$  and  $0.2$  and three angles of heading, namely  $\beta = 0^\circ, 45^\circ$  and  $90^\circ$ . A single case of immersion is considered, that is  $f = 2b$ . The forces and moments have been normalized by  $\rho g A (ab^2)^{2/3}$  and  $\rho g A a (ab^2)^{2/3}$  respectively. The results are shown as functions of  $Kb$ . The case  $a/b \sim 1$  correspond to a sphere and the depicted results show favorable agreement with numerical data reported by other authors in the past (e.g. Linton, 1991; Wang, 1986). As expected, the surge force is increased for decreasing  $a/b$ . The same holds for the pitch and yaw moments. The opposite condition is observed for the sway and heave exciting forces. The hydrodynamic loading maxima are detected in the interval near  $Kb = 0.5$  whilst for the moments the corresponding normalized frequency approaches  $kb = 1$ .

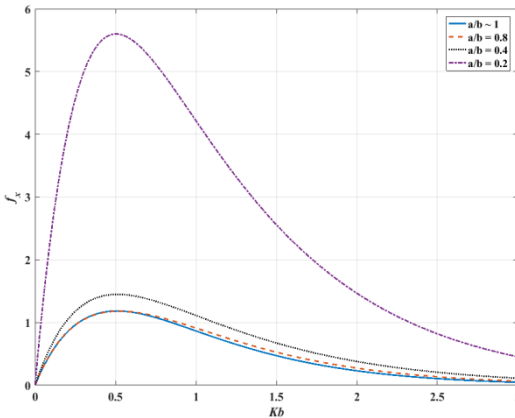


Figure 2. Magnitude of the surge force for several slenderness; the spheroid is immersed at  $f = 2b$  below the free-surface; angle of heading  $\beta = 0^\circ$ .

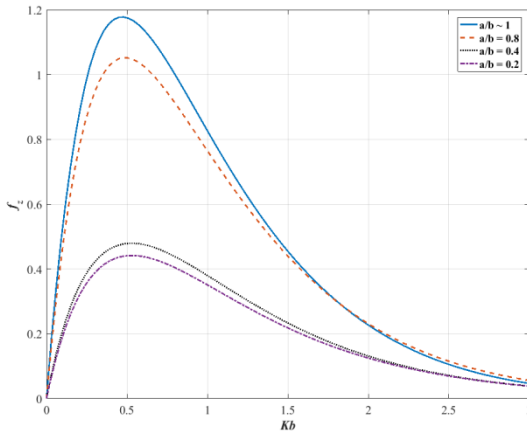


Figure 3. Magnitude of the heave force for several slenderness; the spheroid is immersed at  $f = 2b$  below the free-surface; angle of heading  $\beta = 0^\circ$ .

## 5 CONCLUSIONS

We developed an analytical methodology to solve the diffraction problem by oblate spheroidal submarines subjected to regular propagating waves with arbitrary heading angle. An oblate spheroid may have many valuable practical applications in 3D hydrodynamics as, depending on the slenderness covers geometries from a thin disk to a sphere. The adopted procedure was based on a Fredholm integral equation approach of the second kind. The source distributions needed to formulate the diffraction component were obtained using the interior and exterior potentials applied to Lamb's (1896) theorem.

We presented calculations for the exciting forces and moments applied on the spheroid which comply with the physical intuition for the problem. The surge force is increased for increasing slenderness as the spheroid approached the 2D geometry of a disk. The

same holds for both moments. In contrast, as expected, the heave and sway forces are decreased for increasing slenderness.

Exactly the same formulation can be used to properly tackle the radiation problem as well, which is left for a future endeavour. It was commented that the analytical solution presented herein can be used to deal with many interesting applications that involve an oblate spheroidal geometry, e.g. a spheroid placed symmetrically on a vertical wall, a wall that has a circular hole in it, etc.

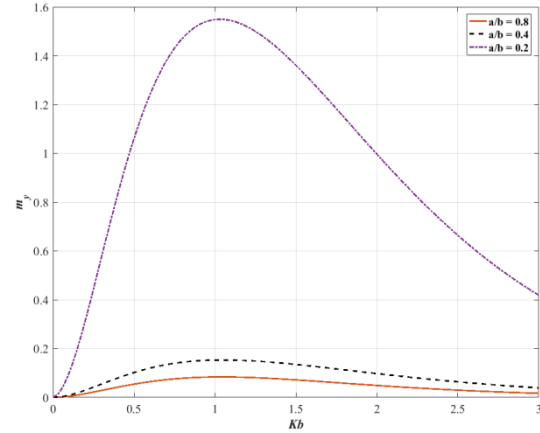


Figure 4. Magnitude of the pitch moment for several slenderness; the spheroid is immersed at  $f = 2b$  below the free-surface; angle of heading  $\beta = 0^\circ$ .

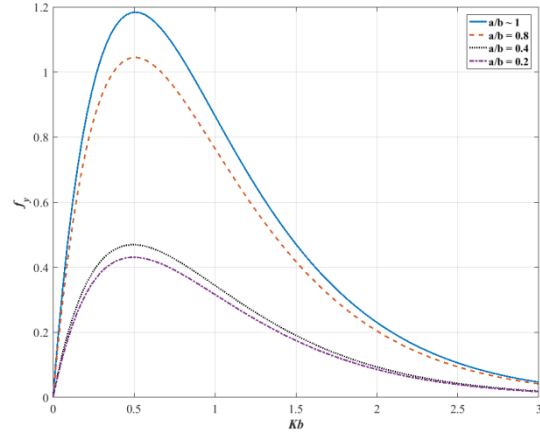


Figure 5. Magnitude of the sway force for several slenderness; the spheroid is immersed at  $f = 2b$  below the free-surface; angle of heading  $\beta = 90^\circ$ .

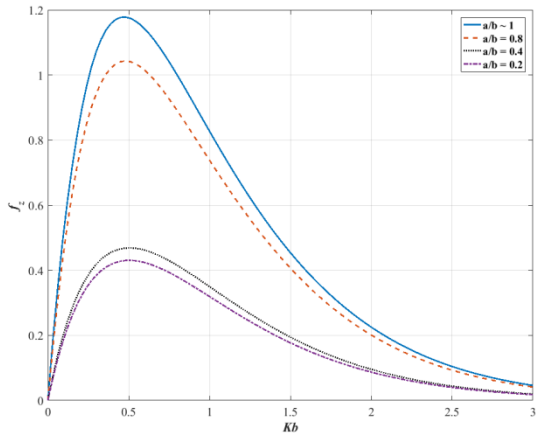


Figure 6. Magnitude of the heave force for several slenderness; the spheroid is immersed at  $f = 2b$  below the free-surface; angle of heading  $\beta = 90^\circ$ .

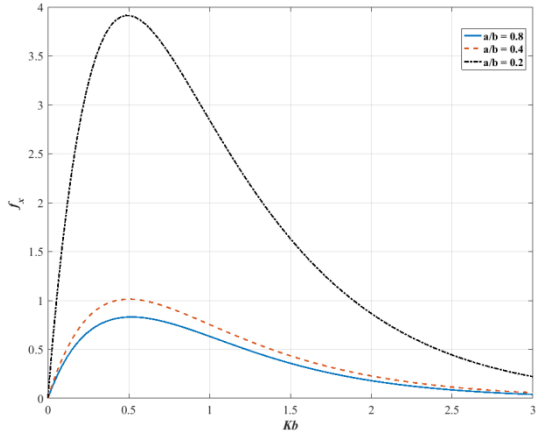


Figure 7. Magnitude of the surge force for several slenderness; the spheroid is immersed at  $f = 2b$  below the free-surface; angle of heading  $\beta = 45^\circ$ .

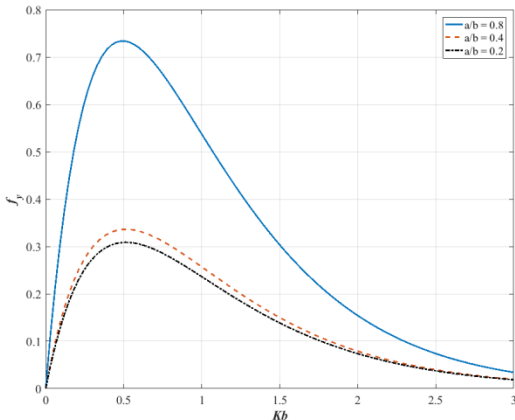


Figure 8. Magnitude of the sway force for several slenderness; the spheroid is immersed at  $f = 2b$  below the free-surface; angle of heading  $\beta = 45^\circ$ .

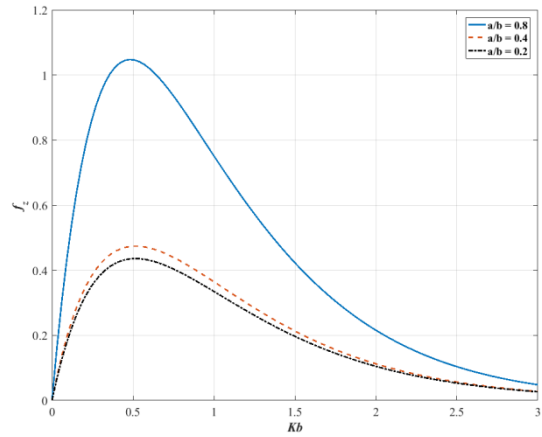


Figure 9. Magnitude of the heave force for several slenderness; the spheroid is immersed at  $f = 2b$  below the free-surface; angle of heading  $\beta = 45^\circ$ .

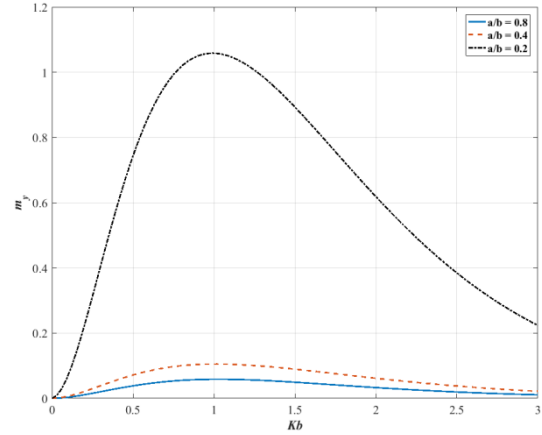


Figure 10. Magnitude of the pitch moment for several slenderness; the spheroid is immersed at  $f = 2b$  below the free-surface; angle of heading  $\beta = 45^\circ$ .

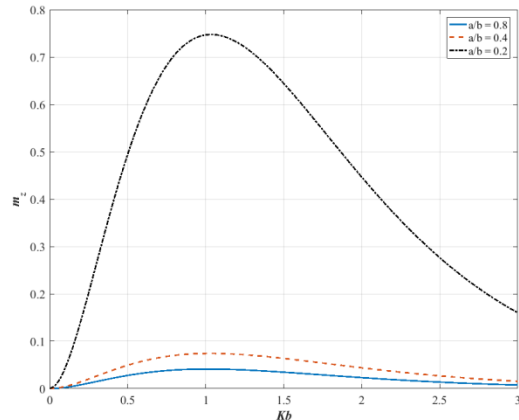


Figure 11. Magnitude of the yaw moment for several slenderness; the spheroid is immersed at  $f = 2b$  below the free-surface; angle of heading  $\beta = 45^\circ$ .

## REFERENCES

- Abramowitz, M. & Stegun, I.A. (1970). *Handbook of Mathematical Functions*. Dover Publications Inc., New York.
- Chatjigeorgiou, I.K. (2012). 'Hydrodynamic exciting forces on a submerged oblate spheroid in regular waves'. *Computers and Fluids*, **57**, pp. 151-162.
- Chatjigeorgiou, I.K. (2013). 'The analytic solution for the hydrodynamic diffraction by submerged prolate spheroids in infinite water depth'. *Engineering Mathematics*, **81**, pp. 47-65.
- Chatjigeorgiou, I.K. & Miloh, T. (2013). 'Wave scattering of spheroidal bodies below a free surface'. *Journal of Ship Research*, **57**, pp. 141-154.
- Chatjigeorgiou, I.K. & Miloh, T. (2014a) 'Free-surface hydrodynamics of a submerged prolate spheroid in infinite water depth based on the method of multipole expansions'. *Quarterly Journal of Mechanics and Applied Mathematics*, **67**, pp. 525-552.
- Chatjigeorgiou, I.K. & Miloh, T. (2014b). 'Hydrodynamics of submerged prolate spheroids advancing under waves: Wave diffraction with forward speed'. *Journal of Fluids and Structures*, **49**, pp. 202-222.
- Chatjigeorgiou, I.K. & Miloh, T. (2015a). 'Hydrodynamic wave resistance and diffraction problems of submerged prolate spheroids based on a Green's function image singularities method'. *European Journal of Mechanics/B Fluids*, **49**, pp. 184-196.
- Chatjigeorgiou, I.K. & Miloh, T. (2015b). 'Radiation and oblique diffraction by submerged prolate spheroids in water of finite depth'. *Journal of Ocean Engineering and Marine Energy*, **1**, pp. 3-18.
- Erdélyi, A. (ed.), Magnus, W., Oberhettinger, F. & Tricomi, F.G. (1953). *Higher Transcendental Functions*, Vol. II. McGraw-Hill Inc., New York.
- Farell, C. (1971). 'On the flow about a spheroid near a plane wall'. *Journal of Ship Research*, **15**, pp. 246-252.
- Farell, C. (1973). 'On the wave resistance of a submerged spheroid'. *Journal of Ship Research*, **17**, pp. 1-11.
- Gray, E.P. (1978). 'Scattering of a surface wave by a submerged sphere'. *Journal of Engineering Mathematics*, **12**, pp. 15-41.
- Greenhow, M.J.L. (1980). 'The Hydrodynamic Interactions of Spherical Wave Power Devices in Surface Seas'. In *Power from Sea Waves* (ed. B. Count), pp. 287-343, Academic Press, London.
- Havelock, T.H. (1931). 'The wave resistance of a spheroid'. *Proc Royal Society of London*, **A131**, pp. 275-285.
- Havelock, T.H. (1952). 'The moment on a submerged solid of revolution moving horizontally'. *Quarterly Journal of Mechanics and Applied Mathematics*, **5**, pp. 129-136.
- Havelock, T.H. (1954). 'The forces on a submerged body moving under waves'. *Transactions of the Institution of Naval Architects*, **96**, pp. 77-88.
- Hobson, E. (1931). *The Theory of Spherical and Ellipsoidal Harmonics*. Cambridge University Press, Cambridge; also 1955 Chelsea Publishing Co., New York.
- Hulme, A. (1982). 'The wave forces acting on a floating hemisphere undergoing forced periodic oscillations'. *Journal of Fluid Mechanics*, **121**, pp. 443-463.
- Lamb, H. 1895 *Hydrodynamics*. Cambridge University Press, Cambridge.
- Linton, C.M. (1991) 'Radiation and diffraction of water waves by a submerged sphere in finite depth'. *Ocean Engineering*, **18**, pp. 61-74.
- Linton, C.M. (1993). 'On the free-surface Green's function for channel problems'. *Applied Ocean Research*, **15**, pp. 263-267.
- Martin, P.A. (1991) Ursell's multipoles and the Rayleigh hypothesis. *Proc 6th International Workshop on Water Waves and Floating Bodies*, Cambridge, Massachusetts, Paper No 30.
- Miloh, T. (1974). 'The ultimate image singularities for external ellipsoidal harmonics'. *SIAM Journal of Applied Mathematics*, **26**, pp. 334-344.
- Rahman, M. (2001). 'Simulation of diffraction of ocean waves by a submerged sphere in finite depth'. *Applied Ocean Research*, **23**, pp. 305-317.
- Srokosz, M.A. (1980). 'Some relations for bodies in a canal, with an application to power absorption'. *Journal of Fluid Mechanics*, **99**, pp. 145-162.
- Thorne, R.C. (1953). 'Multipole expansions in the theory of surface waves'. *Proc Cambridge Philosophical Society*, **49**, pp. 707-716.
- Ursell, F. (1949). 'On the heaving motion of a cylinder on the surface of a fluid'. *Quarterly Journal of Mechanics and Applied Mathematics*, **2**, pp. 218-231.
- Ursell, F. (1999a). 'On the wave motion near a submerged sphere between parallel walls: I. Multipole potentials'. *Quarterly Journal of Mechanics and Applied Mathematics*, **52**, pp. 585-604.
- Ursell, F. (1999b). 'On the wave motion near a submerged sphere between parallel walls: II. Notes on Convergence'. *Quarterly Journal of Mechanics and Applied Mathematics*, **52**, pp. 605-621.
- Wang, S. (1986). 'Motions of a spherical submarine in waves'. *Ocean Engineering*, **13**, pp. 249-271.
- Wehausen, J.V. & Laitone, E.V. (1960). *Surface Waves*. Handbuch der Physik (eds. S Flügge, C Truesdell), Springer, Berlin.

- Wu, G.X. & Eatock Taylor, R. (1987) 'The exciting force on a submerged spheroid in regular waves'. *Journal of Fluid Mechanics*, **182**, pp. 411-426.
- Wu, G.X. & Eatock Taylor, R. (1988) 'Radiation and diffraction of water waves by a submerged sphere at forward speed'. *Proc Royal Society London*, **A413**, pp. 433-461.
- Wu, G.X. & Eatock Taylor, R. (1989). 'On the radiation and diffraction of surface waves by submerged spheroids'. *Journal of Ship Research*, **33**, pp. 84-92.
- Wu, G.X. & Eatock Taylor, R. (1990). 'The hydrodynamic forces on a submerged sphere moving on a circular path'. *Proc Royal Society London*, **A428**, pp. 215-227.
- Wu, G.X., Witz, J.A., Ma, Q. & Brown, D.T. (1994). 'Analysis of wave induced drift forces acting on a submerged sphere in finite water depth'. *Applied Ocean Research*, **16**, pp. 353-361.
- Wu, G.X. (1995). 'Radiation and diffraction by a submerged sphere advancing in water waves of finite depth'. *Proc Royal Society London*, A448, pp. 29-54.
- Wu, G.X. (1996). 'Wavemaking resistance of a group of submerged spheres'. *Journal of Ship Research*, **40**, pp. 1-10.
- Wu, G.X. (1998a) 'Wave radiation and diffraction by a submerged sphere in a channel'. *Quarterly Journal of Mechanics and Applied Mathematics*, **51**, pp. 647-666.
- Wu, G.X. (1998b). 'Wave making resistance of a submerged sphere in a channel'. *Journal of Ship Research*, **42**, pp. 1-8.

## Developments of Hydrodynamic Modeling Techniques For Underwater Vehicles

Sertaç Arslan<sup>1\*</sup>

<sup>1</sup>Roketsan A.Ş., Tactical Missile Systems Directorate,  
Şehit Yüzbaşı Adem Kutlu Sok. No:21, Elmadağ/Ankara, Turkey

**Abstract:** Hydrodynamic coefficients are one of the most important factors that strongly affect the system dynamic, performance, controllability and maneuverability characteristics of an autonomous underwater vehicle (AUV). These coefficients are generally obtained by experimental, numerical and empirical methods. Although the experimental methods are the most reliable one among these, hydrodynamic coefficients cannot usually obtain experimentally; because of financial and time related problems. Besides that, another approach by which these coefficients can be obtained in the initial design step is the numerical methods, such as computational fluid dynamics (CFD). In this study, firstly hydrodynamic equation of motion for submerged bodies is presented, then new calculation models have been constituted and verified to calculate hydrodynamic forces over submerged bodies and finally hydrodynamic coefficients of an AUV are calculated in six degree of freedom (6 DOF), by using computational and empirical methods.

**Keywords:** Underwater Hydrodynamics, CFD, Captive Model Tests, Simulation, Maneuverability.

### 1 INTRODUCTION

In last decades, intensive efforts are being concerted towards the development of underwater technologies. Autonomous Underwater Vehicles (AUVs) and Remotely Operated Vehicles (ROVs) have become main equipments for surveying below the sea in the scientific, military and commercial applications because of the significant improvement in their performance and capability. Despite the considerable improvements in AUVs performance, however, AUVs technologies are still attractive to scientist and engineers as a challenging field. Some of AUV designs, which are used for different purposes, are shown in Figure 1.



Figure 1: Types of Various AUVs (Kim and Choi 2006)

In order to design an AUV, it is usually necessary to analyze its hydrodynamics performance, maneuverability and controllability characteristics. A useful tool for determining the performance of an AUV is a dynamic simulation of the equations of the motion of the vehicle. To perform these simulations, the hydrodynamic coefficients of the vehicles must be calculated. These coefficients are specific to the vehicle and provide the description of the hydrodynamic forces and moments acting on the vehicle in its underwater environment. The hydrodynamic coefficients may be classified into two main groups. These are static and dynamic hydrodynamic coefficients. Static hydrodynamic coefficients occur while the AUV have steady cruise conditions without any

maneuvering. However, dynamic hydrodynamic coefficients are more complex than the statics, dynamic coefficients may be classified into 3 subgroups such as; linear damping coefficients (maneuvering coefficients), linear inertial force coefficients (added mass, inertia coefficients) and nonlinear damping coefficients. These coefficients may be calculated by different techniques. These are experimental, numerical and empirical methods. The most reliable one in these calculation methods is the experimental methods and it is called as Captive Model Tests. Vertical Planar Motion Mechanism (VPMM), Rotating-Arm Mechanism (RAM) and Coning Motion Mechanism (CMM) are the main Captive Model Tests to measure the hydrodynamic coefficients. VPMM, RAM and CMM are shown in Figure 2.

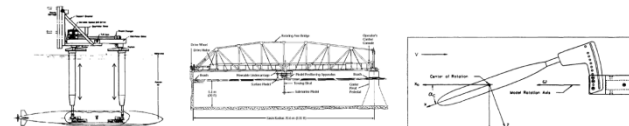


Figure 2: Rotating Arm Mechanism and VPMM (Gertler 1967).

Even if the most reliable methods to calculate the hydrodynamic coefficients are the experimental techniques, also these are the most expensive and time consuming ones to determine the hydrodynamic coefficients. Because of the reasons, experimental methods cannot be used in every design steps of the AUVs. Instead of experimental methods, numerical (computational fluid dynamics) and empirical techniques could be used in initial design steps. To calculate the hydrodynamic coefficients, new numerical calculation models and empirical methods can be developed by using

test-case documents, which have experimental data to compare and verify the solutions.

## 2 DEFINITION OF THE HYDRODYNAMICS COEFFICIENTS

In the hydrodynamic coefficients, which mostly affect the maneuverability of an AUV, are static and the linear damping coefficients. A rectangular cartesian coordinate system, attached to the center of gravity of vehicle, is used in the project. The three components of the hydrodynamic force along the directions x, y, z are denoted by X, Y, Z respectively, and the three components of the hydrodynamic moments by L, M, N. This is illustrated in Figure 3.

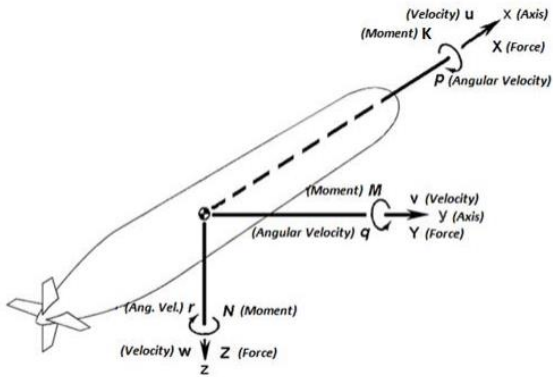


**Figure 3:** Cartesian coordinate system

In the equations of motions for underwater vehicles, the three components of force X, Y, Z and the three components of the moments L, M, N are expanded up to second order terms in the linear velocities; u, v, w and the angular velocities; p, q, r due to high nonlinearity under water motions. The expression for the yaw forces and moments are derived from “*Standard Equations of Motion for Submarine Simulations*” (Gertler 1967) and then take the form:

$$\begin{aligned} Y = & +\frac{\rho}{2} l^4 [Y_r' \dot{r} + Y_p' \dot{p} + Y_{p|p}' p |p| + Y_{pq}' pq + Y_{qr}' qr] \\ & + \frac{\rho}{2} l^3 [Y_v' \dot{v} + Y_{vq}' vq + Y_{wp}' wp + Y_{wr}' wr] \\ & + \frac{\rho}{2} l^2 [Y_r' ur + Y_p' up + Y_{|r|\delta r}' u|r| \delta r + Y_{v|r|}' \frac{v}{|v|} (v^2 + w^2)^{\frac{1}{2}} |r|] \\ & + \frac{\rho}{2} l^2 [Y_v' uv + Y_{v|v|}' v (v^2 + w^2)^{\frac{1}{2}}] \\ & + \frac{\rho}{2} l^2 [Y_{vw}' vw + Y_{\delta r}' u^2 \delta r] \\ & +(W - B) \cos \theta \sin \phi \end{aligned}$$

$$\begin{aligned} N = & +\frac{\rho}{2} l^5 [N_r' \dot{r} + N_p' \dot{p} + N_{r|r|}' r |r| + N_{pq}' pq + N_{qr}' qr] \\ & + \frac{\rho}{2} l^4 [N_v' \dot{v} + N_{vq}' vq + N_{wp}' wp + N_{wr}' wr] \\ & + \frac{\rho}{2} l^4 [N_r' ur + N_p' up + N_{|r|\delta r}' u|r| \delta r + N_{v|r|}' \frac{v}{|v|} (v^2 + w^2)^{\frac{1}{2}} |r|] \\ & + \frac{\rho}{2} l^3 [N_v' uv + N_{v|v|}' v (v^2 + w^2)^{\frac{1}{2}}] \\ & + \frac{\rho}{2} l^3 [N_{vw}' vw + N_{\delta r}' u^2 \delta r] \\ & +(x_G W - x_B B) \cos \theta \sin \phi - (y_G W - y_B B) \sin \theta \end{aligned}$$

There are many kinds of hydrodynamic coefficients in the equations of motion for underwater simulations, which could be evaluated to describe the dynamics of the vehicle. In this study hydrodynamic forces are calculated for yaw maneuver by using CFD methods and then static, linear damping, and nonlinear damping coefficients are calculated by system identification techniques and linear inertia coefficients are calculated by empirical methods.

## 3 METHODOLOGY OF THE ANALYSIS PROCESS

In this project, hydrodynamic coefficients in six degree of freedom such as surge, heave, sway forces and pitch, yaw and roll moments are calculated for different cruise conditions. In order to calculate these coefficients, linear and nonlinear steady state computational fluid dynamics (CFD) analyses are done. Firstly, CFD solution model of hydrodynamic calculations are verified, to get correct results from CFD analyses. In order to verify the solution methods of CFD calculation model, test-case documents are studied. For the verification study, hydrodynamic test results and geometry of Autosub AUV is used.

In the CFD analysis processes, 3D model is created in CATIA V5 R21 modeling software and then fluid domain is constituted. In order to constitute the grid of the AUV GAMBIT 2.4 software is used. Edge mesh, surface mesh and volume mesh of the geometry is created in GAMBIT software. Also, to define the boundary layer over the geometry TGRID 5.0 software is used. At the end of setup process, fluid domain and grid files of the AUV gets ready to perform CFD analyses in ANSYS Fluent 13.0. Some characteristic features for hydrodynamic analyses as a solver model, turbulence model, boundary conditions and Y+ values, for the solution techniques are defined in Fluent 13.0.

## 4 VERIFICATION OF HYDRODYNAMICS ANALYSIS MODEL

A comprehensive study has been performed to verify the CFD tools for the hydrodynamic analysis of underwater bodies. In order to evaluate the capabilities and accuracy of the tools used in this project, Autosub autonomous underwater vehicle (AUV) model has been selected as a test case, because of the availability of extensive validation data and geometric informations. The experimental data of Autosub AUV is generated at National Oceanography Centre, Southampton, UK.

### 4.1 Autosub Autonomous Underwater Vehicle Model

Autosub is a large AUV developed by a team of engineers and oceanographers at the National Oceanography Centre, Southampton, UK. Autosub Project was initiated firstly in 1988, in order to develop unmanned autonomous underwater vehicles for its future marine science programs and for global monitoring (Phillips and Furlong). Autosub is controlled by four movable control surface mounted at the rear of the vessel in a cruciform arrangement.

Autosub's principle dimensions and control surface hydrofoil are listed below (Phillips and Furlong).

- Length: 7 meter, Diameter: 0,9 meter
- Naca 0015 Hydrofoil;
- Chord of the hydrofoil: 0,294 meter
- Thickness of the hydrofoil: 0,02 meter

Autosub model is composed of an axisymmetric body and four appendages in plus configuration. Picture of the full model is given in Figure 4.



**Figure 4:** Autosub AUV (<http://www.noc.soton.ac.uk>)

#### 4.2 Test and Analysis Conditions

The data used in the present study are based on the experiments which were performed in the National Oceanography Centre, Southampton, UK by engineers and oceanographers at the National Oceanography Centre. Towing tank tests of Autosub are performed for 2/3 scaled model with 2.69 m/s linear velocity and between  $\pm 10$  degree angles of attacks with 2 degrees intervals. Rotating Arm tests of Autosub are also performed for 2/3 scaled model with 2.69 m/s linear velocity and for 3 different turning radius such as 13, 17.35, 26 meters. As the result of the experimental studies, drag, heave and yaw force and yaw moment of Autosub are calculated. Tests are achieved at different angle of attacks and turning radius at a model speed of 2.69 m/s which correspond to a Reynolds number of about 12 million. In the calculation of Reynolds Number, dynamic viscosity of the water is accepted as 0,001003 kg/m.s and the density is accepted as 998 kg/m<sup>3</sup>.

#### 4.3 Grid Generation of Autosub AUV

In order to perform hydrodynamic analysis, firstly fluid domains and solution grids of Autosub are created. Edge, surface and volume mesh of the geometry is created in a hierarchical order, so edge mesh of the model is constituted in first step. Grids are created in appropriate density to be use in Navier-Stokes equations. Some surface grid pictures are shown in Figure 5.

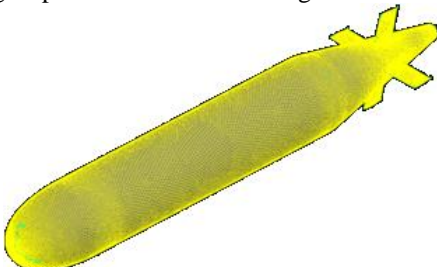


**Figure 5:** Surface grids of Autosub AUV.

Additionally to define the boundary layers over the Autosub geometry, TGRID 5.0 software is used. The boundary layer is created as two zones. These are inner zone and outer zone. To specify the zone thickness  $Y+$  is chosen as 1 and Reynolds Number is calculated as 12 million at 2,69 m/s velocity and kinematic viscosity is accepted as 1,38e-06. Boundary layers are created in compatible with turbulence models, which are used in CFD analyses. Boundary layers of Autosub model are shown in Figure 6.

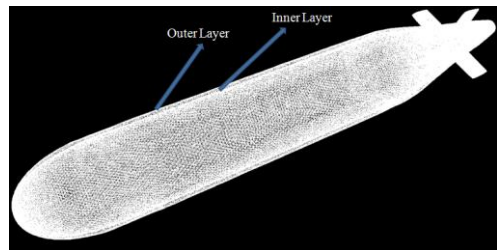


**Figure 6:** Structure of Boundary Layers of Autosub AUV.

At the end of meshing process, vehicle's grid and fluid domain's grids are completed, and the geometry gets ready to make hydrodynamic analyses in CFD software. Fluid domains are chosen large enough not to be exposed to any blockage effects. Pictures of the fluid domain are shown in Figure 7.

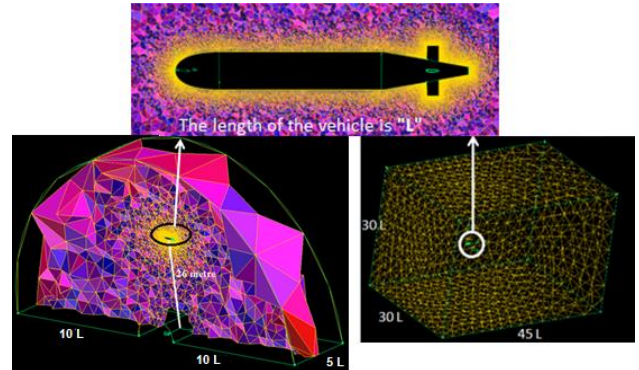


**Figure 7:** Fluid Domains of Autosub AUV.

For rotating arm simulation, circular fluid domain is defined such as in the test facilities. In the fluid domain cruise speed ( $V$ ), turning radius ( $R$ ) and angular speed ( $\omega$ ) of the AUV model can be arranged by using the following equation. As shown in the Figure 8.

$$V \text{ (m/s)} = \omega \text{ (rad/s)} \times R \text{ (m)}$$

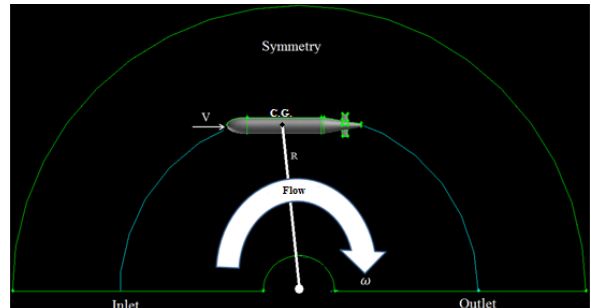


**Figure 8:** Calculation model of rotating arm facility.

#### 4.4 Results and Verification of CFD Analysis of the AUV

In the test case study of 2/3 scaled Autosub model, straight towing tank analysis results are existed for 2.69 m/s linear velocity and between  $\pm 10$  degree angle of attacks with 2 degrees intervals and Rotating Arm mechanism analyses results are existed for 2.69 m/s linear velocity for 3 different (13, 17.35, 26 m) turning radius. So that, Autosub hydrodynamic analyses are performed in the same condition with test case document. Comparisons are accomplished with dimensionless terms. Hydrodynamic forces and moments are converted to dimensionless form with length of the model (L), velocity of the vehicle (V) and the density of the fluid ( $\rho$ ).

In this study, hydrodynamic modeling infrastructure is setup by using Pressure-based solver model, and Navier-Stokes Equations are solved in implicit, steady conditions. Moreover in hydrodynamic analyses,  $K-\epsilon$  turbulence model is used in Realizable, Enhanced Wall Treatment turbulence conditions. Some nondimensionalized terms are provided in the below.

$$w' = \frac{w}{U} \quad (1)$$

$$C_D = \frac{\text{Drag Force}}{1/2\rho V^2 L^2} \quad (2)$$

$$C_Z = \frac{Z}{1/2\rho V^2 L^2} \quad (3)$$

$$C_M = \frac{M}{1/2\rho V^2 L^2 L} \quad (4)$$

For the straight towing tank simulation, comparative graphics of the experimental and CFD results of drag and heave force coefficients are shown in Figure 9 and 10.

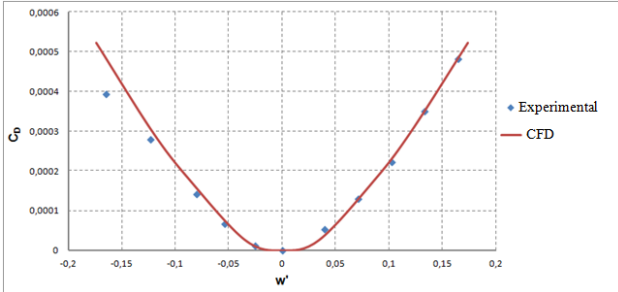


Figure 9: Variation of Drag Force Coefficients vs.  $w'$  (Phillips and Furlong).

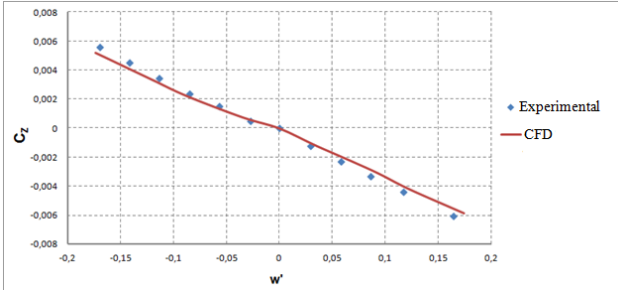


Figure 10: Variation of Surge Force Coefficients vs.  $w'$  (Phillips and Furlong).

As shown in the figures, CFD analyses result are compatible with experimental results for surge and heave force with the change of angle of attack. Moreover, in the Rotating Arm (RA) simulations rotational flow is defined into fluid domain by using the same solver and turbulence models with the straight towing tank simulation. For the rotational flow, Moving Reference Frame module in Fluent is used and the desired rotational flow is defined. AUV model is attached to the RA mechanism by the center of gravity in the simulations. One of the rotational speed, turning radius and cruise speed parameters can be adjust by setting the other ones constant. Fluid domain is constituted in 5 million mesh and the analyses are converged after the 1500 iterations.

Analyses results of the RA simulation for different turning radius are given in Table 1 and the comparative graphics of the experimental and CFD results of yaw

moments with respect to yaw angular speed is shown in Figure 11.

Table 1 : Rotating arm simulation analyses results

| Velocity<br>(m/s) | Turning<br>Radius (m) | Yaw rate<br>(rad/s) | Yaw moment<br>(Nm) |
|-------------------|-----------------------|---------------------|--------------------|
| 2,69              | 13                    | 0,2069              | -1082              |
| 2,69              | 17,36                 | 0,155               | -803,65            |
| 2,69              | 26                    | 0,1035              | -528,46            |

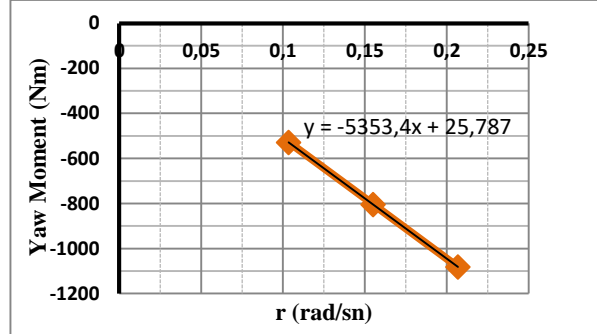


Figure 11: Yaw moments vs. yaw rate in RA test (Phillips and Furlong).

The graphic shows the change of yaw moment with respect to yaw angular velocity. The change of the moment is linear and so the derivative of the line gives the dimensionalized  $N_r$  value. When  $N_r$  get nondimensionelized,  $N_r'$  coefficient can be calculated.

$$N_r = -5353,4 \rightarrow N_r' = \frac{N_r}{\left(\frac{1}{2}\rho u l^3\right)} \rightarrow N_r' = -0,00513 \quad (5)$$

According to experimental result, value of the  $N_r'$  coefficient is -0,00540 and so the comparison table is given in the below.

Table 2: Results of the RA verification study (Phillips and Furlong).

| $N_r'$ (CFD) | $N_r'$ (Experimental) | Error  |
|--------------|-----------------------|--------|
| -0,00513     | -0,00540              | % 4,94 |

As shown in Table 2, experimental results and the numerical result are so close to each other, the difference is just the % 4,94. This situation shows us, numerical methods can be used to calculate linear maneuvering coefficients instead of experimental techniques in conceptual and initial design steps. Moreover, velocity contour of the RA calculation domain is given in the Figure 12. As expected, speed of the flow changes due to turning radius used in RA simulation.

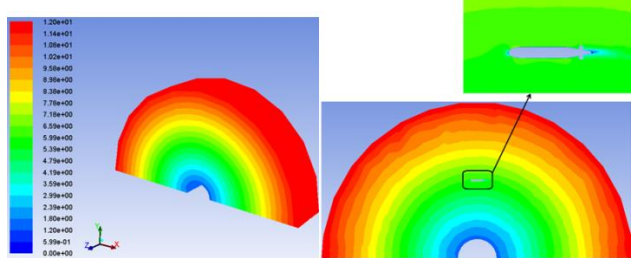


Figure 12: Solution domain and velocity contour of the RA numerical analyses.

This RA simulation is verified for the yaw plane however, this calculation method can also be used for the pitch plane analyses.

In the RA verification study propeller effects do not included in the RA analyses, but according to additional analyses which is done for examination of underwater dynamics, propeller effects can also be included in the RA analyses.

In this part, verification of hydrodynamic analysis model for the calculation of static and linear dynamic hydrodynamic coefficients for underwater vehicles is performed. Through this verification study, basic hydrodynamic coefficients of AUVs can be determined by computational methods, in initial design steps. In the next step, hydrodynamic database of Autosub is constituted in six degree of freedom by using verified hydrodynamic analysis model however, yaw plane hydrodynamic analyses results are shared.

## 5 HYDRODYNAMICS DATABASE OF AUTOSUB AUV

In this study, a comprehensive study has been made to constitute hydrodynamic database of Autosub AUV in six degree of freedom (6DOF) by using verified numerical methods but, yaw plane results are just shared. Different static and dynamic hydrodynamic analyses are performed for different cruise conditions. In static hydrodynamic analyses cruise speeds, control surface deflections and angle of attacks are variable parameters. In addition to this, rotational and acceleration maneuvering conditions are also simulated in dynamic hydrodynamic analyses. In dynamic analyses turning radius, sideslip angle and control surface deflections are the variable parameters. Calculated hydrodynamic forces and moments can be used in conceptual design process of Autosub AUV model however, in order to calculate the hydrodynamic coefficients in the equations of motion, system identification methods must be used using the calculated forces and moments.

### 5.1 Analysis Conditions of Autosub AUV

In the present study, X, Y, Z forces and K, M, N moments of Autosub is calculated for different maneuvering conditions. Velocity levels in the analyses are 5, 10, 15, 20 and 25 Kts. The analyses are performed for nine different sideslip angles ( $\beta$ ); these are -10, -7, -5, -2, 0, 2, 5, 7, and 10 degrees. Also Autosub's hydrodynamic analyses are performed for nine rudder deflection angles ( $\delta_r$ ) configurations 0,  $\pm 5$ ,  $\pm 10$ ,  $\pm 15$ ,  $\pm 20$  degrees. Additionally, dynamic hydrodynamic analyses are performed for 24 different maneuvering conditions such as; three different turning radius 20, 30, 40 meters and four different cruise speed 10, 15, 20, 25 Kts for positive and negative yaw maneuvers. Operating Reynolds Number is changed between  $1,27e+07$  and  $6,52e+07$ . In these hydrodynamic analyses, kinematic viscosity of the water is accepted as  $1,38e-06$ .

### 5.2 Hydrodynamic Analysis Results of Autosub AUV

In this scope firstly, drag forces of Autosub is calculated for different velocities. The calculated drag force versus velocity graphic is shown in Figure 13. In the graphic, units of the velocities are knot and it is seen that, increment of drag force is compatible with velocities.

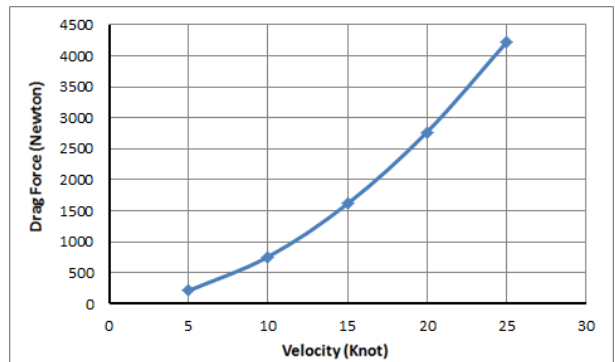


Figure 13: Drag Forces vs. Velocity Graphics of Autosub.

Axial forces are also calculated for different angle of attacks in different velocities, as shown in Figure 14. In the graphic, units of the velocities are knots and it is seen that, increment and decrement of axial forces are compatible with angle of attack and cruise velocity. Variation of the axial forces with angle of attacks is too much in high speeds and very little in low speeds.

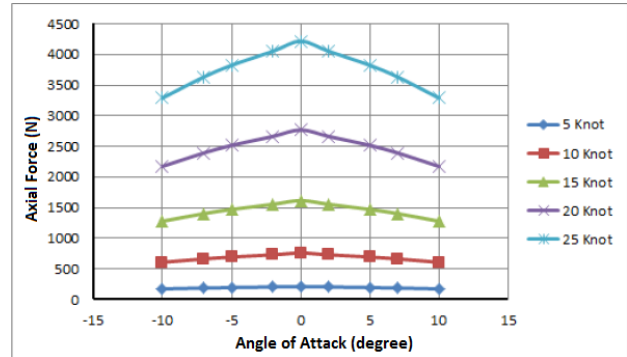


Figure 14: Axial Forces vs. AOA for Different Velocities.

In addition to axial forces, yaw forces of Autosub are investigated. Variation of yaw force versus sideslip angle at different velocities graphics are shown in Figure 15.

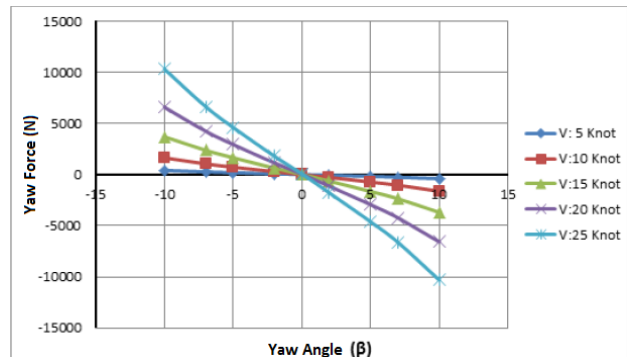
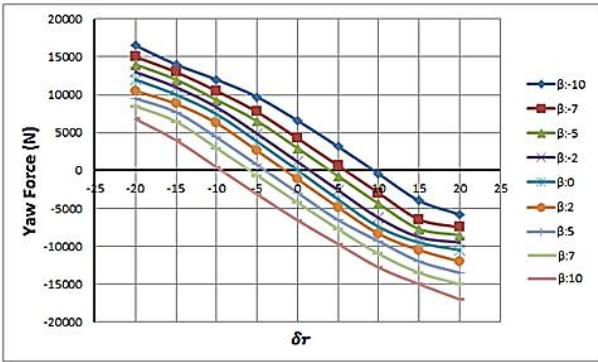


Figure 15: Yaw Force vs. Sideslip Angle for Different Velocities.

As shown in the graphics, yaw force increases with sideslip angle in negative direction for different velocities. In hydrodynamic simulation and modeling calculations, square of the vehicles length is accepted as a reference area and the length of the vehicle is accepted as a reference length.

In the yaw maneuvering analyses, change of yaw forces with respect to control surface deflections for different sideslip angles are examined at 20 Kts speed. This graphic gives us the trim points of Autosub for continuous yaw

maneuvering conditions at 20 Kts. In the equilibrium points, yaw force equals to zero for continuous maneuvers.



**Figure 16:** Yaw forces vs.  $\delta_r$  @  $V = 20$  Kts

In the equilibrium point the change of yaw force with respect to control surface deflection is also important so, this change of yaw force is examined for different velocities in the Figure 17.

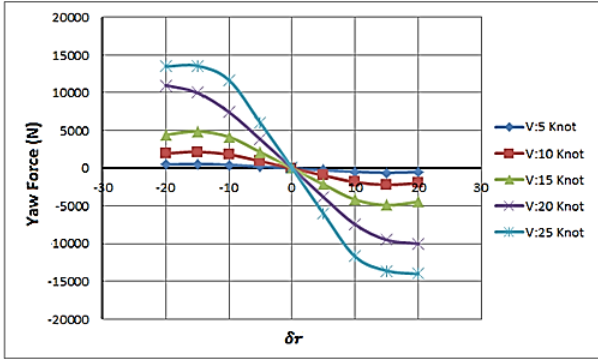


**Figure 17:** Yaw forces vs.  $\delta_r$  for different velocities

As shown in the Figure 17, change of yaw force with respect to control surface deflection is linear but, this regime changes for high deflections because of the loss of lift over the control surface. Linear graphics give opportunities to calculate the desired interval values due to interpolation.

For dynamic analyses in the Rotating Arm simulation, change of yaw moment with respect to yaw rate for different cruise velocities is examined.

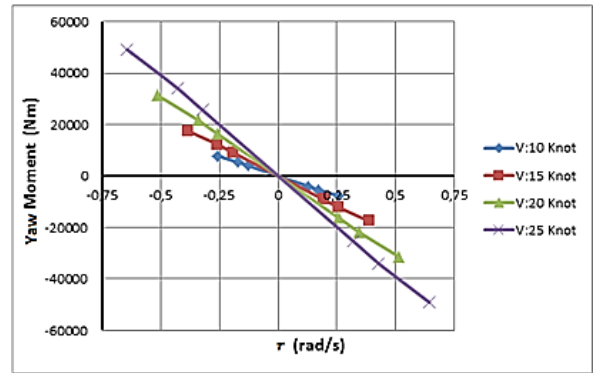


**Figure 18:** Yaw moment vs.  $r$  for different velocities

As shown in the Figure 18 yaw moment changes linearly with respect to yaw rate and the slopes of the graphics are changed by velocity. The slopes of the lines in Figure 18 give the  $N_r$  dimensional value. When the slope of the graphics get nondimensionalized as told in 4.4 section,

$N_r'$  coefficient can be calculated.  $N_r'$  coefficient is the damping coefficient of yaw maneuver.

$$N = N_r \cdot r \quad (6)$$

$$N_r = N_r' \cdot u \cdot \frac{\rho}{2} l^4 \quad (7)$$

$$N = N_r' \cdot r \cdot u \cdot \frac{\rho}{2} l^4 \rightarrow N_r' = \frac{N_r}{u \cdot \frac{\rho}{2} l^4} \quad (8)$$

**Table 3:**  $N_r'$  coefficients vs. velocities

| $V$ (Kts) | $N_r$  | $N_r'$   |
|-----------|--------|----------|
| 10        | -30950 | -0,00491 |
| 15        | -46475 | -0,00491 |
| 20        | -61968 | -0,00491 |
| 25        | -77590 | -0,00491 |

In Table 3, values of  $N_r'$  coefficients do not changed with respect to velocity. This situation is valid for underwater linear and nonlinear maneuvering coefficients. So that, when all the hydrodynamic coefficients get calculated in system simulation studies, any desired analyses can be performed in a velocity. One of the other important parameter is Yaw Force when the vehicle has yaw maneuvering. Yaw force has been examined for different yaw rates and cruise speeds. Pitch plane effects do not included in the yaw maneuvering analyses. Regime of the yaw force for yaw maneuvering is shown in the Figure 19.

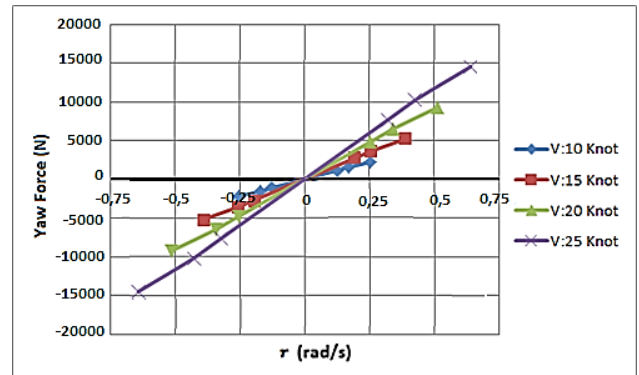


**Figure 19:** Yaw force vs.  $r$  for different velocities

Yaw forces changes linearly with respect to yaw rates for different velocities. However, slope of the lines in the graphics are changed for velocities. When these slopes get nondimensionalized  $Y_r'$  coefficient can be calculated.  $Y_r'$  is also one of the damping coefficients of yaw maneuvers.

$$Y = Y_r \cdot r \quad (9)$$

$$Y_r = Y_r' \cdot u \cdot \frac{\rho}{2} l^3 \quad (10)$$

$$Y = Y_r' \cdot r \cdot u \cdot \frac{\rho}{2} l^3 \rightarrow Y_r' = \frac{Y_r}{u \cdot \frac{\rho}{2} l^3} \quad (11)$$

**Table 4:**  $Y_r'$  coefficients vs. cruise velocities

| $V$ (Kts) | $Y_r$  | $Y_r'$   |
|-----------|--------|----------|
| 10        | -9110  | -0,01025 |
| 15        | -13783 | -0,01025 |
| 20        | -18449 | -0,01025 |
| 25        | -23148 | -0,01025 |

In Table 4, values of  $Y_r'$  coefficients do not changed with respect to velocity. As it mentioned before, this situation is valid for underwater linear and nonlinear maneuvering coefficients.

For the underwater maneuverings, roll moment is very dominant due to propeller effects and nonlinearity of hydrodynamics, so roll moments cannot be neglected. Roll moment coefficients and cross flow coefficients interaction with the roll motion must be calculated and included in the equations of motions.

In order to calculate the roll moments and cross coupled terms interaction with the roll motion in the captive model tests, Coning Motion Mechanisms are used. However, roll moments of Autosub and the effects of the roll rates to the yaw moments are studied by CFD methods for 5, 10, 15, 20 RPM roll rates and 10, 20 Kts velocities. For the roll motion definition in the CFD analyses, a cylindrical fluid domain is used and the roll rate ( $p$ ) is defined around the X axis. Coning angle and roll angle can also be defined to Autosub in the fluid domain however, in this analysis the model has no coning angle, roll angle and coning angle deflection. The cylindrical fluid domain is shown in the Figure 20.

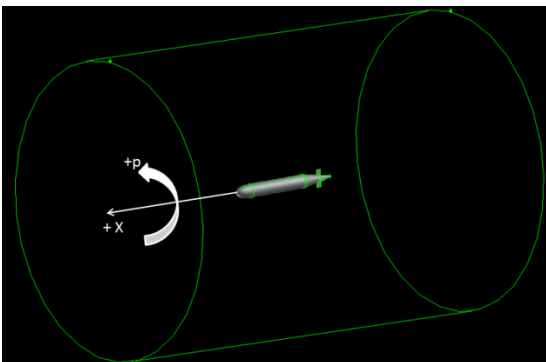


**Figure 20:** The cylindrical fluid domain for roll Analyses

In Figure 21, roll moments values with respect to roll rate for different cruise velocity is shown.

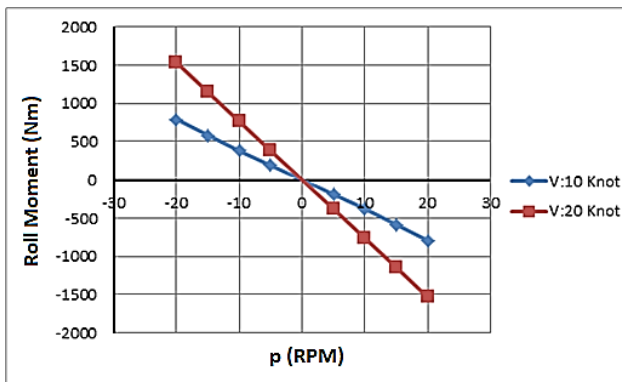


**Figure 21:** Roll moments vs. roll rates for different V

Roll moments increases linearly with roll rates in negative direction for different velocities and the slopes of the lines in the graphics are changed for velocities. When these slopes get nondimensionalized  $K_p'$  coefficient can be calculated.  $K_p'$  is the damping coefficient of roll moments.

$$K = K_p \cdot p \quad (12)$$

$$K_p = K_p' \cdot u \cdot \frac{\rho}{2} l^4 \quad (13)$$

$$K = K_p' \cdot p \cdot u \cdot \frac{\rho}{2} l^4 \rightarrow K_p' = \frac{K_p}{u \cdot \frac{\rho}{2} l^4} \quad (14)$$

$K_p'$  coefficient has quite significant role for yaw maneuvers due to cross coupled effects. These effects occur under water especially due to fluid density and propeller effects. So that, roll moments effects cannot be neglected and must be included in 6DOF system simulation analyses.

**Table 5:**  $K_p'$  coefficients vs. V

| V (Kts) | $K_p$   | $K_p'$   |
|---------|---------|----------|
| 10      | -39,123 | -3,1E-06 |
| 20      | -76,493 | -3,1E-06 |

One of the other significant parameter for an underwater vehicle which has yaw maneuver is the change of yaw moment with respect to roll rate because, underwater vehicles have significant amount of roll motions in the yaw maneuvers. So, change of yaw moments with respect to roll rate are examined for different velocities.

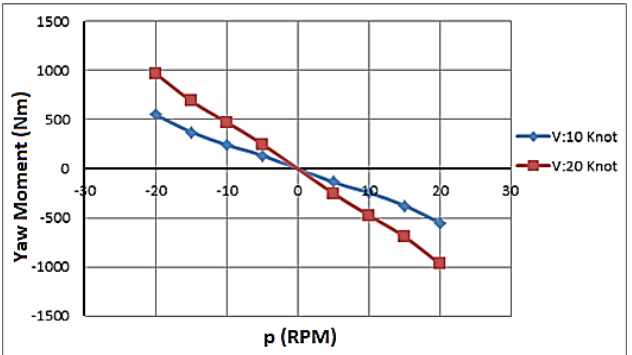


**Figure 22:** Yaw moments vs. roll rates for different V

Yaw moments increases linearly with roll rates in negative direction for different velocities and the slopes of the lines in the graphics are changed for velocities. When these slopes get nondimensionalized  $Y_p'$  coefficient can be calculated.

$$N = N_p \cdot p \quad (15)$$

$$N_p = N_p' \cdot u \cdot \frac{\rho}{2} l^4 \quad (16)$$

$$N = N_p' \cdot p \cdot u \cdot \frac{\rho}{2} l^4 \rightarrow N_p' = \frac{N_p}{u \cdot \frac{\rho}{2} l^4} \quad (17)$$

$Y_p'$  is one of the significant coupled coefficient that occurs when the combined yaw and roll maneuvers and used in the system simulations analyses in 6 DOF.

**Table 6:**  $N_p'$  coefficients vs. V

| V (Knot) | $N_p$   | $N_p'$     |
|----------|---------|------------|
| 10       | -26,288 | -2,086E-06 |
| 20       | -52,50  | -2,086E-06 |

Roll rate does not affect the pitch plane maneuvers as much as yaw plane so the roll motions especially examined in the yaw maneuvers analyses. Essentially, for underwater maneuvers roll motion is undesired affect and inserted to system as a disturbance so, underwater vehicles must deflect control surfaces to cover this disturbance. For the better and efficient designs, roll motion affects must be minimized.

One of the significant output of this analysis, maneuvering coefficients do not depend on the cruise

speed and so, these coefficients can be used in every velocity steps in the simulation studies.

In the accelerated motions, inertia force coefficients has occurred such as added mass and added inertia coefficients. These coefficients do not occur in the steady maneuvering conditions however, when the vehicle has acceleration in the cruise conditions added mass and when the vehicle has accelerated maneuvers added inertia coefficients has occurred. 36 different coefficients exist in the added mass matrix but the most sensitive for the system dynamics and those are included in the equations of motions are the diagonal terms in the added mass matrix. Added mass and added inertia coefficients of Autosub for the diagonal terms and value of the inertia terms those occur over Autosub are shared in Table 7.

**Table 7:** Diagonal elements of added mass matrix of Autosub

| Added mass or inertia coeff. | Value of the coefficient | Value of the inertia terms |
|------------------------------|--------------------------|----------------------------|
| $X_u'$                       | -6,12E-04                | -104,75 Kg                 |
| $Y_v'$                       | -2,02E-02                | -3457,37 Kg                |
| $Z_w'$                       | -2,02E-02                | -3457,37 Kg                |
| $M_q'$                       | -7,37E-04                | -6180,99 Kg.m <sup>2</sup> |
| $N_r''$                      | -7,37E-04                | -6180,99 Kg.m <sup>2</sup> |
| $K_p'$                       | -5,20E-06                | -43,61 Kg.m <sup>2</sup>   |

These inertia coefficients works as damping terms in the motions. Added mass coefficients are just dependent on the geometric specification of the vehicles. So that, when Autosub has accelerated motions, it has significant amount of added mass and added inertia moment, due to volume of it. These terms are significant enough to be included in the system simulation analyses.

## 6. CONCLUSIONS

In this paper firstly, underwater hydrodynamics, new generation underwater vehicles and usage area of these vehicles have explained. In order to design a desired underwater vehicle, the main significant parameters are hydrodynamic coefficients and the equations of motions are mentioned. Calculation methods of hydrodynamic coefficients such as experimental, numerical, empirical and advantages and disadvantages of them are defined. Although the experimental methods are the most reliable ones to calculate hydrodynamic characteristics, this method is also the most expensive and time consuming one to determine the hydrodynamic coefficients. For this reason, new numerical calculation techniques have developed.

Benchmark study of Autosub AUV which was prepared in the National Oceanography Centre, Southampton, UK by engineers and oceanographers at the National Oceanography Centre is used to verify developed numerical calculation techniques. Straight towing tests results are used in static analyses and rotating arm test results are used for dynamic analyses. After the verification of CFD modelling methods, 6DOF hydrodynamic database of Autosub is constituted however, only yaw plane analyses are shared in this paper. In addition to this, effects of roll motions to the yaw maneuvering and diagonal terms of added mass

matrix of Autosub are also studied. In this paper, some hydrodynamic coefficients are calculated by nondimensionalizing the slope of the analyses graphics. However, in 6DOF system simulations, all hydrodynamic coefficients are calculated via system identification techniques and CFD analyses results used as hydrodynamic test results.

In conclusion, hydrodynamic coefficients are the main significant parameters that affect the maneuverability characteristics of underwater vehicles. Hydrodynamic coefficients in the equations of motions are independent on cruise velocities so that, these coefficients are characteristic for a vehicle and can be used for different cruise conditions. Numerical and empirical techniques can be used to calculated hydrodynamic characteristics and define basic configurations of underwater vehicles especially for initial design steps. However, in the detail and final design phases, underwater test mechanisms and sea-trial test techniques must be used to finalize the hydrodynamic design and generate the final hydrodynamic databases.

## 7 REFERENCES AND CITATIONS

- Phillips, A., Furlong, M., Turnock, S. R., The Use of Computational Fluid Dynamics to Determine the Dynamic Stability of an Autonomous Underwater Vehicle, National Oceanography Center, Southampton, England.
- Fossen, T., I., 1994: Guidance and Control of Ocean Vehicles, Wiley, H., Sons, 5-90.
- Gertler, M., 1967: The DTMB Planar Motion Mechanism System, Naval Ship Research and Development Center.
- Gertler, M., Grant, R. H., 1967: Standard Equations of Motion for Submarine Simulations, Naval Ship Research and Development Center.
- Jones, D. A., Clarke, D. B., Brayshaw, I. B., Barillon, J. L, and Anderson B., 2002: The Calculation of Hydrodynamic Coefficients for Underwater Vehicles, Maritime Platforms Division/Platform Sciences Laboratory, Australia.
- Jun, B. H., Park, J. Y., Lee, F. Y., Lee, P. M., Lee, C. M., Kim, K., Lim, Y. Y. and Oh, J. H. (2009). Development of the AUV ISIMI and a free running test in an Ocean Engineering Basin, Ocean Engineering Research Department, Republic of Korea.
- Kim, K. and Choi, H., S. (2006). Analysis on the controlled nonlinear motion of a test bed AUV-SNUUV I, Department of Naval Architecture and Ocean Engineering, Seoul National University, Republic of Korea.
- <http://www.noc.soton.ac.uk>
- <http://web.mit.edu/towtank/>
- <http://www.km.kongsberg.com>

## A Mathematical Model for Studying Maneuvering Motions and Course Instabilities of Sailing Yachts

**Manolis Angelou<sup>1\*</sup>, Kostas J. Spyrou<sup>1</sup>**

<sup>1</sup>National Technical University of Athens (NTUA), Faculty of Naval Architecture and Marine Engineering

**Abstract:** Towards creating capability for analyzing course instabilities of sailing yachts in waves, the authors are at an advanced stage of development of a mathematical model of maneuvering motion comprised of two major components: an aerodynamic, focused on the calculation of the forces on the sails, taking into account the variation of their shape under wind flow; and a hydrodynamic, handling the movement of the hull with appendages in water. The fluid-structure interaction problem of the sails is tackled using a 3d approach where the aerodynamic component of the model involves the application of the steady form of the Lifting Surface Theory, in order to obtain the force and moment coefficients, while the deformed shape of each sail is obtained using a Shell Finite Element formulation. The hydrodynamic part consists of modeling hull reaction, hydrostatic and wave forces. A Potential Flow Boundary Element Method is used in order to calculate the Side Forces and the Added Masses of the hull and its appendages. The calculation of resistance is performed through a standard formulation. Wave excitation is currently limited to Froude - Krylov loads.

**Keywords:** Sailing Yachts.

### NOTATION

|             |   |                      |   |
|-------------|---|----------------------|---|
| $A$         | Cross sectional area ( $\text{m}^2$ )               | $\vec{n}_P$          | Panel normal vector (Body Fixed System)                   |
| $A_{ij}$    | Matrix of influence coefficients                    | $p$                  | Roll velocity (rad/sec)                                   |
| $A_R$       | Aspect ratio  | $P, E_{\text{Main}}$ | Principal dimensions of Main sail                         |
| $B$         | Beam (m)  | $q$                  | Pitch velocity (rad/sec)                                  |
| B.E.M.      | Boundary Element Method                             | $\vec{q}_{\Gamma}$   | Vortex induced velocity                                   |
| $C_D$       | Drag Coefficient                                    | $r$                  | Yaw velocity (rad/sec)                                    |
| $C_L$       | Lift Coefficient                                    | $\vec{r}_C$          | Distance to a point "C" (m)                               |
| $C_F$       | Force Coefficient                                   | $\vec{r}_P$          | Panel moment vector arm (Body Fixed System)               |
| $D$         | Drag force (N)                                      | $S_i$                | Surface of "i" component ( $\text{m}^2$ )                 |
| DoF         | Degrees of Freedom                                  | $T$                  | Draft (m)   |
| F.E.M.      | Finite Element Method                               | $u$                  | Surge velocity (m/sec)                                    |
| $F_i$       | Force or moment due to "i" excitation               | $v$                  | Sway velocity (m/sec)                                     |
| $F_N$       | Froude Number                                       | V.L.M.               | Vortex Lattice Method                                     |
| $g$         | Gravity acceleration ( $\text{m/sec}^2$ )           | $V_{\text{AW}}$      | Apparent Wind speed (m/sec)                               |
| $h$         | Wave steepness ratio                                | $V_B$                | Yacht Speed (m/sec) (m/sec)                               |
| $I_{J,Jib}$ | Principal dimensions of Jib sail                    | $V_T$                | Transverse velocity (m/sec)                               |
| $I_X$       | Moment of Inertia around X axis ( $\text{kg m}^2$ ) | $V_t$                | Tangential velocity (m/sec)                               |
| $I_Y$       | Moment of Inertia around Y axis ( $\text{kg m}^2$ ) | $V_{\text{TW}}$      | True Wind speed (m/sec)                                   |
| $I_Z$       | Moment of Inertia around Z axis ( $\text{kg m}^2$ ) | $\nabla \Phi$        | Potential velocity (m/sec)                                |
| $k$         | Wave number (rad/m)                                 | $w$                  | Heave velocity (m/sec)                                    |
| L.S.T.      | Lifting Surface Theory                              | $x_{\text{CG}}$      | Longitudinal center of gravity (m)                        |
| $L_i$       | Lift force of "i" component (N)                     | $x_{\text{CEFF}}$    | Longitudinal center of effort (m)                         |
| $L_{WL}$    | Length of waterline (m)                             | $y_{\text{CEFF}}$    | Transverse center of effort (m)                           |
| $m$         | Yacht mass (kg)                                     | $z_{\text{CG}}$      | Vertical center of gravity (m)                            |
| $m_X$       | Surge added mass (kg)                               | $z_{\text{CEFF}}$    | Vertical center of effort (m)                             |
| $m_{YY}$    | Sway added mass (kg)                                | $z_P$                | Vertical distance of panel center to mean water level (m) |
| $\vec{n}$   | Normal vector                                       | $\alpha$             | Angle of attack (rad)                                     |

|               |  |
|---------------|--|
| $\alpha_R$    | Effective rudder angle of attack (rad) |
| $\alpha_{TW}$ | True Wind angle (rad)                  |
| $\alpha_{AW}$ | Apparent wind angle (rad)              |
| $\beta$       | Drift angle (rad)                      |
| $\Gamma$      | Vortex strength (1/sec)                |
| $\delta$      | Rudder deflection delta angle (rad)    |
| $\zeta$       | Local water surface elevation (m)      |
| $\theta$      | Pitch angle (rad)                      |
| $\lambda$     | Wave length (m)                        |
| $\mu$         | Ship-wave incident angle (rad)         |
| $\mu_{YY}$    | Sway sectional added mass (kg)         |
| $\rho$        | Density of water (kg/m <sup>3</sup> )  |
| $\sigma$      | Source strength                        |
| $\varphi$     | Roll angle (rad)                       |
| $\varphi_0$   | Incident wave potential                |
| $\varphi_P$   | Perturbation potential                 |
| $\psi$        | Yaw angle (rad)                        |
| $\omega$      | Ship-wave frequency of encounter       |

## 1 INTRODUCTION

In the literature of sailing yacht modeling and dynamic behavior, one comes across several significant studies focusing on the detailed calculation of the hydro/aero-dynamic flow and the sails' structural behavior (e.g. Jones, 2001, Kagemoto, 2000). On the other hand, the course stability of sailing yachts has not attracted similar attention as a topic for scientific investigation. Historically, several records exist describing broaching-to incidents of ships with sails, dating back to the early modern period when sails were the main means of propulsion (Spyrou, 2010). Occurrences of broaching-to continue to be reported till our days, often concerning racing or cruising sailing yachts (Lloyd, 1988). The present study is a step towards setting up a framework for the systematic study of such course instability phenomena of sailing yachts operating in strong wind and waves. As will be described next, a mathematical model is under development, consisted of: an aerodynamic component, addressing the forces on the sails and the variation of their shape due to wind flow; and a hydrodynamic, addressing the dynamic behavior of the hull and its appendages.

## 2 MATHEMATICAL MODELLING

### 2.1 Equations of Motions and Coordinate Systems

As the model is intended for performing course stability analysis, both upwind and downwind cases should be under consideration. The model is built for simulating ship motions in 6 degrees of freedom. Three different coordinate systems are used: an earth-fixed, non-rotating, coordinate system  $(x_O, y_O, z_O)$ ; a wave-fixed system that is used for studies in monochromatic waves and it travels with the wave celerity  $(x_W, y_W, z_W)$ ; and a body-fixed

$(x, y, z)$  system with its origin located on the midship point where the centerplane and the waterplane intersect (Figure 1). The systems are in accordance with the right-hand rule where 'x' axis points positive forward, having on its right the positive 'y' axis, while positive 'z' axis points downwards.

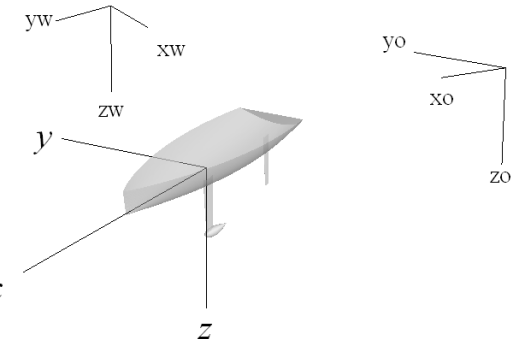


Figure 1 – Coordinate Systems.

Assuming the hull as a rigid body, the equations of motions for the 6 DoF, as they accrue from application of Newton's law, obtain the following form (SNAME 1950):

$$m \left[ \dot{u} + qw - rv - x_{CG} (q^2 + r^2) + z_{CG} (pr + \dot{q}) \right] = X - mg \sin \theta \quad (1.1)$$

$$m \left[ \dot{v} + ru - pw + z_{CG} (qr - \dot{p}) + x_{CG} (qp + \dot{r}) \right] = Y + mg \sin \varphi \cos \theta \quad (1.2)$$

$$m \left[ \dot{w} + pv - qu - z_{CG} (p^2 + q^2) + x_{CG} (rp - \dot{q}) \right] = Z + mg \cos \varphi \cos \theta \quad (1.3)$$

$$I_X \dot{p} - mz_{CG} (\dot{v} + ru - pw) - mx_{CG} z_{CG} (\dot{r} + pq) = K \quad (1.4)$$

$$\begin{aligned} I_Y \dot{q} + (I_X - I_Z) rp + mz_{CG} (\dot{u} + qw - rv) \\ - mx_{CG} (\dot{w} + pv - qu) + mx_{CG} z_{CG} (p^2 - r^2) \\ = M - mx_{cg} g \cos \varphi \cos \theta \end{aligned} \quad (1.5)$$

$$\begin{aligned} I_Z \dot{r} + (I_Y - I_X) pq + mx_{cg} (\dot{v} + ru - pw) \\ + mz_{CG} x_{CG} (rq - \dot{p}) = N \end{aligned} \quad (1.6)$$

The right-hand-side of the above equations, containing forces and moments, can be expanded in modular form for each equation mode  $i$  as

$$F_i = F_{HS} + F_{HR} + F_R + F_S + F_W \quad (1.7)$$

where the subscripts indicate force contribution from **HydroStatic**, **Hull Reaction**, **Rudder**, **Wave** and **Sails** respectively, in accordance with the excitation being of hydrodynamic or aerodynamic origin.

### 3 SAILS MODEL

Sail excitation is calculated allowing for the deformation of sail surface due to pressure's variation, using as input parameter the relative-to-the-sail(s) wind direction. Modeling effort is hence split towards creating an aerodynamic and a structural module. The integration of the aerodynamic and structural models with a hydrodynamic model of vessel's movement in waves is the focus of the current paper and hence, only simple steady methods of sail modeling will be applied.

#### 3.1 Upwind Case

The small thickness of the sails makes them ideal for being modeled with a potential flow method, such as the one using the Lifting Surface Theory (L.S.T.) which is usually applied through a numerical scheme based on the Vortex Lattice Method (V.L.M.). While the lifting surface bears minimal computational cost, it requires that the flow always remains attached to the surface, thus restraining L.S.T.'s applicability to a relatively small range of fluid inflow angles. The structural part is treated using simple flat shell elements. The sail system is considered to consist of a main and jib sail. Upon the calculation of the apparent wind angle and velocity the forces and moments for each sail expressed in the body fixed system are (Figure 2):

$$X_S = L_S \cdot \sin(a_{AW}) - D_S \cdot \cos(a_{AW}) \quad (1.8)$$

$$Y_S = L_S \cdot \cos(a_{AW}) + D_S \cdot \sin(a_{AW}) \quad (1.9)$$

$$K_S = -Y_S \cdot z_{CEFF} \quad (1.10)$$

$$N_S = Y_S \cdot x_{CEFF} + X_S \cdot y_{CEFF} \quad (1.11)$$

where

$$L_S = \frac{1}{2} \rho C_L V^2 a_{AW} S \quad (1.12)$$

$$D_S = \frac{1}{2} \rho C_D V^2 a_{AW} S \quad (1.13)$$

are the lift and drag forces for the sails respectively and their calculation is discussed in the next section.

##### 3.1.1 Aerodynamic Part

The L.S.T. is actually a linearized Boundary Element Method (B.E.M.) offering a formulation that allows the effects of camber and thickness to be decoupled, and the no-entrance boundary condition to be transferred to the mean camber line of a surface. The Vortex Lattice Method is a numerical scheme that discretizes a surface into a series of rectangular panels, allowing so the real flow to be approximated by placing a series of discrete lines of vorticity instead of a continuous distribution along the field. In terms of the Lifting Surface Theory, a system of constant strength horseshoe vortices is placed on every panel.

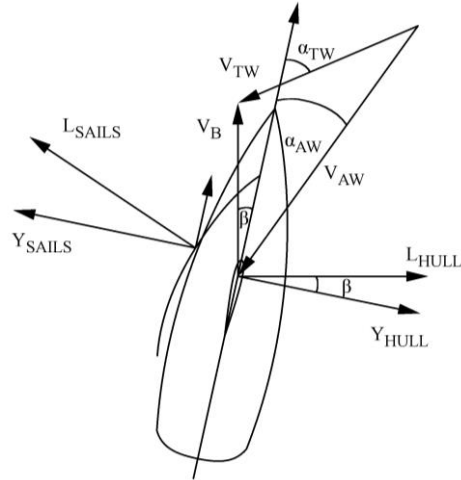


Figure 2 – Horizontal Plane Upwind Yacht Dynamics.

The vortex consists of a parallel to the leading panel edge filament and two trailing filaments that run towards the trailing edge, where the Kutta condition is satisfied, and further to the wake. As the wake is a free shear layer, it can only carry vorticity. The flow being steady, it allows a first approximation for the free vortex sheet, with the vortex lines aligned with the initially undisturbed flow (frozen wake propagating aft on the direction of the free stream). The induced velocity of every horseshoe vortex  $j$  to every point  $i$ , accounted-for by the respective Biot-Savart Type Velocity Integral, is represented by a matrix of influence coefficients and the no-entrance boundary condition  $\{\nabla\Phi \cdot \vec{n} = 0\}$  reduces to a system of linear equations  $A_{ij}\Gamma_j = V_{\infty i} \cdot \vec{n}_i$ .

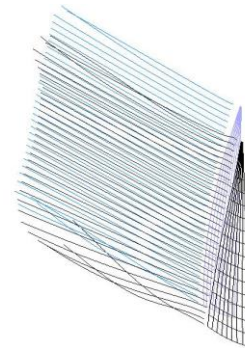


Figure 3 – Two sails system – flying shapes and wakes.

Once the coefficient matrix has been calculated, the linear system is solved for the strength of the horseshoe vortices and subsequently the total velocities are calculated. The wake vortex lines are then rotated in order to be aligned with the local total velocity vectors and to apply the force free condition, providing so the roll-up of the wake. Finally, the lift forces on the sail are calculated using the Kutta - Jukowski theorem

$$\vec{L} = \rho \cdot \vec{V}_t \times \vec{\Gamma} \quad (1.14)$$

where  $\vec{V}_t$  is the tangential velocity. The forces are then directed as input to the structural part, to calculate the nodal displacements. The deformed surface is returned to

the Lifting Surface module and the procedure commences iteratively until the aerodynamic forces have converged. The number of necessary iterations for convergence is increasing in respect of the relative wind inflow angle, and reaches 25-30 iterations for large angles. An example of converged shapes appears in Figure 3.

### 3.1.2 Aeroelastic Part (static aeroelasticity)

The variation of the sail shape is tracked using flat triangular shell elements, consisting of a membrane (Constant Strain Triangles) and a bending part (Discrete Kirchhoff Triangles). The elements are thus developed by superimposing the stiffness of the membrane and the bending components.

The membrane contribution to the shell element is provided by the Constant Strain Triangle under plane stress conditions. As in Zienkiewicz (2000a and 2000b), the element is considered to be a flat triangle with three nodes and two degrees of freedom per node, i.e., in the two planar directions. For the plate bending part the adapted formulation is the one of Batoz (1980) and consider the Discrete Kirchhoff Triangle, an element with three nodes and three degrees of freedom per node; that being the normal to the triangle displacement and the rotations around the  $x$  and  $y$  axis respectively.

The authors acknowledge that the structural formulation implemented so far is simplistic; the solution is linear, as membrane and bending contributions are solved independently. Additionally, the current method is appropriate only for small displacements. However, as most non-linear models known to the authors tackle the large displacement behavior implicitly (considering a single time step, the exciting load is applied incrementally in sub-steps), the simulations are carried out in the same context.

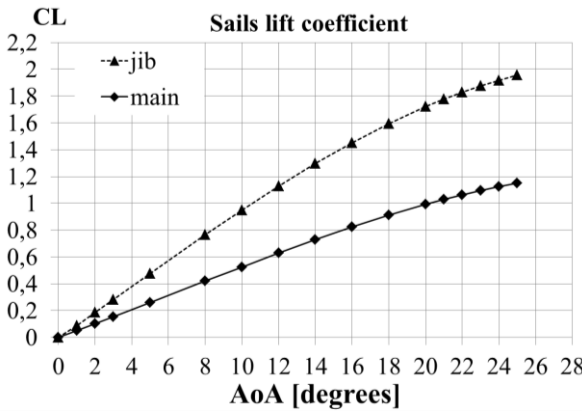


Figure 4 – Two sails system – Lift Coefficients (graph from Angelou & Spyrou 2016).

The angle of attack was considered as for airfoils; i.e. it is the relative angle between the incoming flow and a line segment connecting the leading and trailing edge of the camber line.

### 3.1.3 Results

Lift and drag coefficients for a system of two sails, a

main and a jib, are calculated for a small range of incoming flow angles ( $0^\circ$  -  $25^\circ$ ) and the Lift curves are presented in Figure 4 (Drag values were insignificant). The sails are assumed to be made of Kevlar and exhibit isotropic behavior, while their principal dimensions are:

$$I_{\text{jib}} = 13.0 \text{ m}, J_{\text{jib}} = 5.0 \text{ m} , \quad \text{for the Jib}$$

$$P_{\text{main}} = 15.0 \text{ m}, E_{\text{main}} = 6.0 \text{ m} , \quad \text{for the Main.}$$

### 3.2 Downwind Case

To examine numerically the behavior of a sail in a wider operational range where drag effects become dominant, the use of viscous flows methods such as RANSE or LES solvers may be unavoidable. In the context of the authors' progress so far, in a recent paper (Angelou and Spyrou, 2015) the sails model was expanded from the outskirts of upwind sailing, to beam and fully downwind cases. The method was a pseudo-3d approach, based on the evaluation of the flow field characteristics around certain cross sections of the sails.

The 2-d fluid domain per section was obtained by solving the non-conservative Vorticity Transport and Stream Function Equations, using the Finite Volume method. The deformed shape of each section was obtained using a finite element formulation for flexure elements.

Apart from ignoring any 3-dimensional cross flow effects, the method also suffered from some numerical diffusion making its' applicability questionable. Moreover, the induced computational cost prohibited the simultaneous solution of the method along with the hydrodynamic model. Although the method was not promoted for longer term use, it could still serve a purpose. As the long term objective is to perform directional stability analysis using 6 degrees of freedom while taking into account the instant position and shape of the sail(s), this method proved useful as an intermediate step towards a Lagrangian "free" vorticity formulation, where remeshing of the domain and the large computational cost would be avoided.

In the Lagrangian approach a B.E.M. solves for the surface vorticity distribution around the sail. The vorticity is then shed to the domain by assigning its strength to newly created numerical quantities (vortex blobs) that are allowed to convect and diffuse according to the Vorticity Transport Equation. The numerical solution of the latter is dictated by the viscous split technique where the convection and diffusion terms are treated separately.

Convection was treated in a time marching scheme with the addition of mollifier terms to regularize the vortex kernels and desingularize the velocity near the vortex core, while diffusion was modeled implicitly. Vorticity values were not actually changed and the diffusion effects were introduced by small perturbations of the translational displacements of the blobs by application of the random walk method. At the time this paper is written, the aforementioned method is still under

development and, so far, only moderate inflow angles have been treated successfully (Figure 5).

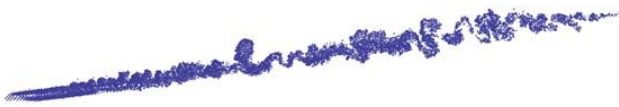


Figure 5 – Numerical Vortex blobs evolution behind a sail chord line.

Since there are no result yet available to the authors for purely downwind cases, the driving coefficients were adopted from available literature. Lasher et al (2003), measured lift and drag coefficients for a series of investigated spinnakers (Figure 6).

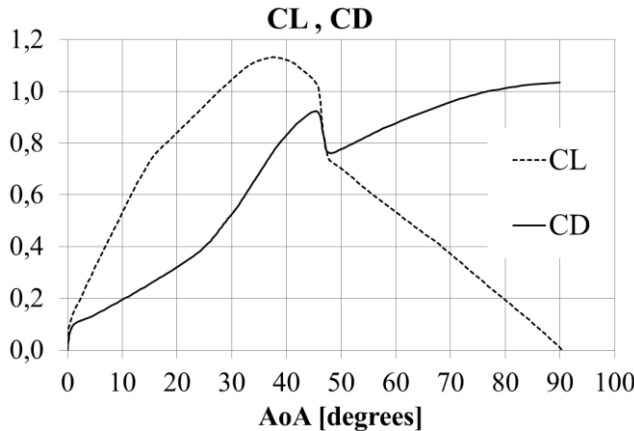


Figure 6 – Lift and Drag coefficients for a spinnaker. Curves are recreated based on data from Lasher (2003).

The sail forces and moments for the downwind case, where the yacht is sailing equipped with a spinnaker sail are:

$$X_S = L_S \cdot \sin(a_{AW}) + D_S \cdot \cos(a_{AW}) \quad (1.15)$$

$$Y_S = D_S \cdot \sin(a_{AW}) + L_S \cdot \cos(a_{AW}) \quad (1.16)$$

$$K_S = -Y_S \cdot z_{CEFF} \quad (1.17)$$

$$N_S = Y_S \cdot x_{CEFF} + X_S \cdot y_{CEFF} \quad (1.18)$$

## 4 HULL MODEL

### 4.1 Hydrostatic Forces and Moments

In order to calculate the hydrostatic pressure terms, the hull is discretized into rectangular panels (Figure 7) each of which has its submergence evaluated during every time step. Numerical integration of below expressions (1.19) and (1.20) for the static pressure sustained by the submerged panels, either on still water or on wavy conditions, provides the instant values of hydrostatic forces and moments.

$$\vec{F}_{HS} = -\rho g \iint_S (z_p + \zeta) \cdot \vec{n}_p \, dS \quad (1.19)$$

$$\vec{M}_{HS} = -\rho g \iint_S (z_p + \zeta) \cdot (\vec{r}_p \times \vec{n}_p) \, dS \quad (1.20)$$

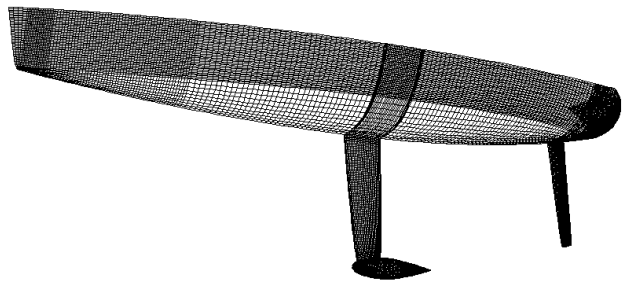


Figure 7 – Hull Paneling (graph from Angelou & Spyrou 2016).

### 4.2 Hull Reaction Forces and Moments

Following the approach of Oltmann and Sharma (1985), the terms involved with the hydrodynamic reaction of the hull and the appendages are distinguished to *Ideal Fluid*, *Cross-Flow* and *Lifting* effects.

$$\vec{F}_{HR} = \vec{F}_{IF} + \vec{F}_{CF} + \vec{F}_L \quad (1.21)$$

The first two contributions are treated by a strip theory method, in contrast to the third which is obtained from a 3-dimensional method.

#### 4.2.1 Ideal fluid effects

Following Yuanxie (1986) the acceleration terms of the linear hydrodynamic derivatives on sway and yaw modes can be calculated in terms of a strip-theory type formulation by integrating the sectional sway added mass dependent kernels.

$$Y_{\dot{V}} = m_{yy} = - \int_{-L/2}^{L/2} \mu_{yy} \, dx \quad (1.22)$$

$$N_{\dot{r}} = - \int_{-L/2}^{L/2} x^2 \cdot \mu_{yy} \, dx \quad (1.23)$$

$$Y_{\ddot{r}} = N_{\dot{v}} = - \int_{-L/2}^{L/2} x \cdot \mu_{yy} \, dx \quad (1.24)$$

Moreover, assuming that surge and sway velocities, as also yaw acceleration, are independent of the longitudinal position of the hull section, the velocity related terms are calculated from the expressions:

$$Y_V = \int_{-L/2}^{L/2} \frac{\partial \{\mu_{yy}(x)\}}{\partial x} \, dx \quad (1.25)$$

$$N_V = \int_{-L/2}^{L/2} x \frac{\partial \{\mu_{yy}(x)\}}{\partial x} \, dx \quad (1.26)$$

$$Y_r = - \int_{-L/2}^{L/2} \left[ x \frac{\partial \{\mu_{yy}(x)\}}{\partial x} + \mu_{yy}(x) \right] \, dx \quad (1.27)$$

$$-m_x \cdot v_0$$

$$N_r = - \int_{-L/2}^{L/2} x \left[ x \frac{\partial \{\mu_{yy}(x)\}}{\partial x} + \mu_{yy}(x) \right] \, dx \quad (1.28)$$

The method is straightforward once the sectional sway added mass is known. The latter is calculated by a simple 2-D panel method under the assumptions (Angelou & Spyrou, 2016):

- 1) of a body moving inside a large volume of inviscid, incompressible and irrotational fluid where the fluid velocity can be described by the gradient of a scalar harmonic potential  $\phi$  and
- 2) of the motion being a pure drift motion of zero frequency.

A representation for the associated potential is obtained by distributing a series of singularities, in this case source and sinks  $\{\sigma\}$ , on each section and reducing to a system of linear equations by enforcing the Neumann boundary condition. The potential and the corresponding perturbation velocities induced from these panel singularities on a random field point P are given by Katz and Plotkin (2001):

$$\varphi_P = -\frac{1}{4\pi} \int_{L_{per}} \left( \frac{\sigma}{r} \right) ds, \nabla \varphi_P = -\frac{1}{4\pi} \int_{L_{per}} \nabla \left( \frac{\sigma}{r} \right) ds \quad (1.29)$$

and the sectional added mass by Newman (1977):

$$\mu_{ij} = \rho \int_{Y_B} \varphi_i \frac{\partial \varphi_j}{\partial n} ds \quad (1.30)$$

They are treated for the influence of the instantaneous submerged section under wave conditions in a similar manner to Tsigas and Spyrou (2012).

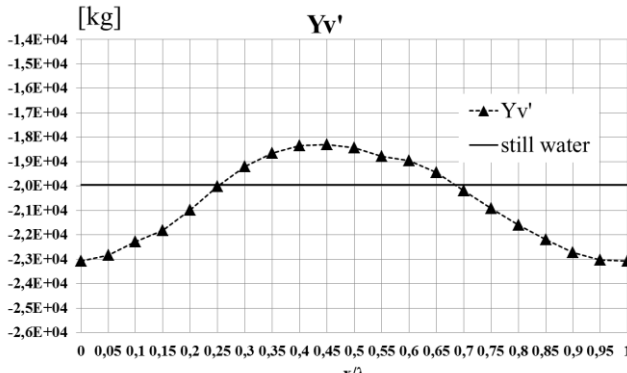


Figure 8 – Variation of  $Y_v'$  with ship position on wave

(graph from Angelou & Spyrou 2016).

The variation of the acceleration derivatives due to purely following sea waves of harmonic type, characterized by a length of  $\lambda = 2.0 \cdot L_{WL}$  and a steepness of  $h = 1/50$ , is depicted in Figure 8 for different relative hull-wave positions. The vertical axis provides the value of the force, while the horizontal axis represents the relative position of the hull scaled to the wave length.

#### 4.2.2 Cross-Flow effects

The cross-flow terms are the outcome of local transverse velocity on the hull, as the latter commences a turn or while sustaining a considerable drift angle. If  $v_T = (v + r \cdot x)$  is the transverse velocity at the position of a section, then a hull of length  $L$  sustains, due to cross

flow effects, a sway force and a yaw moment equal to:

$$Y_{CF} = -\frac{\rho}{2} \int_{-L/2}^{L/2} \{A(x, T) \cdot C_D(x, T, v_T) v_T |v_T| \cos \phi\} dx \quad (1.31)$$

$$N_{CF} = -\frac{\rho}{2} \int_{-L/2}^{L/2} \{A(x, T) \cdot C_D(x, T, v_T) v_T |v_T| \cdot x \cos \phi\} dx \quad (1.32)$$

where  $A(x, T)$  is the cross sectional area of a section at longitudinal position  $x$  and instant draft  $T$ ,  $C_D(x, T, v)$  is the cross-flow drag coefficient for that section as a function also of the transverse velocity defining laminar or turbulent flow behavior.

This coefficient can be approximated from published in the literature results that concern equivalent ellipsoidal or triangular two-dimensional shapes, mainly from Hoerner (1965). However, extracting values, for quantitative use, from an old, low resolution, printed source, entails the possibility of large inaccuracy in the prediction of  $C_D$ . This comes in contrast to the 2<sup>nd</sup> optional method of using state-of-the-art viscous flow CFD solvers that can provide  $C_D$  values, in principle with good accuracy.

It should be noted that this coefficient involves information about the viscous-pressure drag of the section. However the potential influence of the cross-flow drag has already been implemented inside the velocity derivatives of the *ideal-fluid effects* sub-model. This introduces a problem of finding a representation regarding the purely viscous portion of  $C_D$ , as adopting values for it from either proposed methods will lead to loss of the wave-variation character of the velocity derivatives.

That being the case, the choice was made to use commercial RANSE software to calculate the total drag coefficient of a series of double bodies of sections of representative shape and for a range of drafts and then subtract the pressure component. The obtained purely viscosity-based terms for each section and instant position were fitted for a range of velocities using functions of  $f(v) = a \cdot v^b$  form (Figure 9).

The calculations were performed in ANSYS Fluent, incorporating the Spallart – Almaras turbulence model, and in an effort to create meshes that would allow wall  $y^+$  values to retain a magnitude of less than unity during the solution. It should be mentioned that there were cases where this was very difficult to achieve and the drag might have been underestimated.

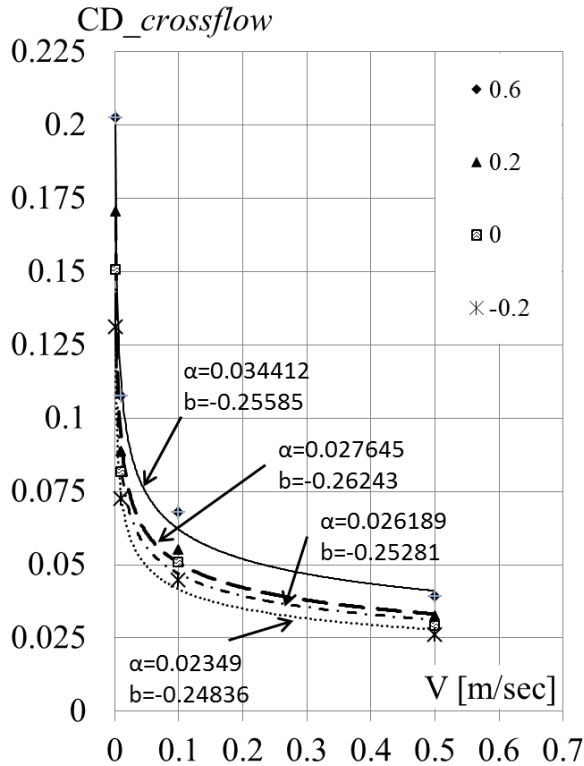


Figure 9 – Cross-flow drag coefficient vs. velocity and fitting functions for a section with keel, with parameter section's draft. Markers and numbers in legend represent emergence (negative) or submergence (positive) deflection from design draft (graph from Angelou & Spyrou 2016).

This raises a question regarding the accuracy of the method. However, the sections resemble bluff bodies, where the pressure drag is expected to dominate in magnitude, over its viscous counterpart. Indeed, the overall influence of the developed viscous forces was of very small order and losses in accuracy may not be too important. Moreover, calculating the viscous force for a very large set of combinations of draft and heel angles for every section, would involve a huge computational load of pre-runs in order to equip the model.

#### 4.2.3 Lifting effects

Due to their slenderness, the keel and the rudder of the hull can have their lift and lift-induced drag calculated using the horseshoe vortex lifting surface method, as done for the sails (Figure 10).

For the canoe body of the hull though, the method falls short in applicability, because thickness effects cannot be disregarded. Its shape being far from slender, makes the treatment even with the thickness corrected version of the lifting surface method unsuitable. However, it can be approximated as a very low aspect ratio  $\{A_R\}$  airfoil with a round planform. This configuration is characterized by a strong dependence to non-linear lift and according to Hoerner (1985) it may be approximated by (Figure 10):

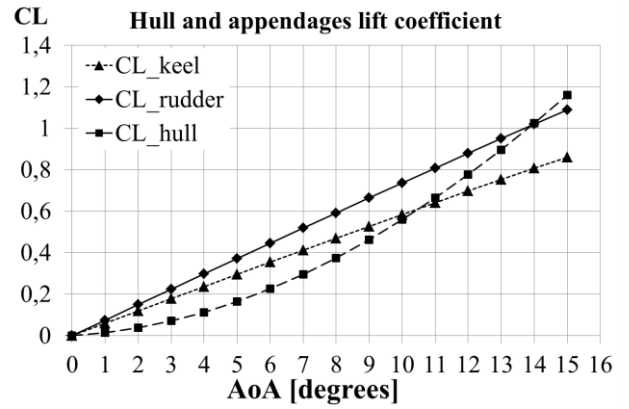


Figure 10 - Lift coefficient for underwater surfaces (graph from Angelou & Spyrou 2016).

$$C_L = 0.5 \pi \sin a \cos a (A_R + a) \quad (1.33)$$

In the same context, the lift induced drag is approximated by Hoerner (1965):

$$\begin{aligned} C_{DL} &= C_{L\_linear} \tan(0.5a) + \Delta C_{L\_non-linear} \tan a \\ &= 0.5 \pi \sin a A_R \tan(0.5a) + k \sin^2 a \tan a \end{aligned} \quad (1.34)$$

where  $k \approx 1.25$  and  $A_R \approx 0.045$  for the wetted part of the canoe body. The lift and drag forces of the keel, are functions of drift angle ( $\beta$ ) and their contribution on the equations of motions is obtained as:

$$L_{KEEL} = \frac{1}{2} \rho C_{L\_K}(\beta) V_B^2 S_K \quad (1.35)$$

$$D_{KEEL} = \frac{1}{2} \rho C_{D\_K}(\beta) V_B^2 S_K \quad (1.36)$$

$$X_{KEEL} = L_{KEEL} \sin(|\beta|) - D_{KEEL} \cos(\beta) \quad (1.37)$$

$$Y_{KEEL} = -L_{KEEL} \cos(\beta) \operatorname{sign}(\beta) - D_{KEEL} \sin(\beta) \quad (1.38)$$

$$N_{KEEL} = Y_{KEEL} \cdot xcef_{KEEL} \quad (1.39)$$

$$K_{KEEL} = -Y_{KEEL} \cdot zcef_{KEEL} \quad (1.40)$$

Similar are the equations for the contribution of the hull.

At the time this paper is written and in terms of calculating the lifting forces on the appendages, the authors are evaluating the influence that the thickness effects terms of the lifting surface theory induce, as also the extent of their applicability. Moreover the canoe body lift contribution is approximated using a horizontal strip theory approach (i.e. waterlines instead of sections) and the aforementioned vortex particles implementation.

#### 4.2.4 Additional terms

- a) The resistance term  $R$ , involved only in the surge equation of motion (1.1), can be decomposed to **viscous**,

**induced** and **wave-making** parts. The **induced** terms are actually the lifting terms that were already addressed in the maneuvering *Hull Reaction* terms. The **Viscous** terms are calculated as in Oossanen (1993) with some modifications regarding the contribution of the bulbous part of the keel, where a form factor has been implemented for the keel-bulb, as in Nesteruk & Cartwright (2011). The **wave-making** resistance is calculated as in Pascual (2007) by an approximation based on the sectional areas of the yacht. Wherever included in the above formulation, the wetted surface is calculated from the summation of the areas of the hull panels (Figure 7) that are immersed at that instant, taking into consideration waves, heave, heel, pitch and yaw.

b) A damping coefficient for roll is implemented using an approximation as in Masuyama (2011):

$$K_{\phi} = -2(a_0 + 0.4Fn)mg GM \left( \frac{T}{2\pi} \right)^2 \quad (1.41)$$

where  $a_0$  was estimated from roll tests of similar yachts.

#### 4.3 Rudder Forces and Moments

Since the calculations were performed considering a steady state mode, the influence of the trailing vortex sheet of the keel onto the rudder is not included. There is a need so, to introduce a correction factor and treat these effects implicitly. Thus the angle of attack  $a_R$  on the rudder is provided by:

$$a_R = \delta - \gamma_R \cdot \beta \quad (1.42)$$

where  $\delta$  is the rudder deflection angle, while  $\gamma_R$  is the decreasing ratio of inflow angle (Masuyama and Fukasawa, 2011). The rudder contributions on the equations of motions are:

$$L_{RUD} = \frac{1}{2} \rho C_{L\_R}(a_R) V_B^2 S_R \quad (1.43)$$

$$D_{RUD} = \frac{1}{2} \rho C_{D\_R}(a_R) V_B^2 S_R \quad (1.44)$$

$$X_{RUD} = -L_{RUD} \sin(|a_R|) - D_{RUD} \cos(a_R) \quad (1.45)$$

$$Y_{RUD} = -L_{RUD} \cos(a_R) \text{sign}(a_R) - D_{RUD} \sin(a_R) \quad (1.46)$$

$$N_{RUDDER} = Y_{RUD} \cdot xcef_{RUD} \quad (1.47)$$

$$K_{RUDDER} = -Y_{RUD} \cdot zcef_{RUD} \quad (1.48)$$

#### 4.4 Wave Excitation Forces and Moments

Considering an undisturbed pressure field around the yacht, the wave excitation is limited to Froude-Krylov forces and moments. These are calculated by integrating the unit potential  $\varphi_0$  (Angelou & Spyrou, 2016) on every immersed panel of the hull up to the elevated running waterline, after the panel coordinates have been transformed suitably for the relative position of the hull on the encountered wave.

$$\varphi_0 = \frac{g}{\omega} i \exp(k\zeta - i(x \cos \mu + y \sin \mu)) \quad (1.49)$$

$$\vec{F}_W = \text{Re} \left\{ -i\omega e^{i\omega t} \zeta \iint_S \varphi_0 \vec{n}_p \, dS \right\} \quad (1.50)$$

#### 5 CASE STUDIES – EARLY RESULTS

In this section we present the outcome of two simulations; an upwind case where the yacht performs a multiple tacking maneuver in head sea waves and a downwind case where the transitional behavior from asymmetrical surging to surf-riding is examined.

The equation of motions ode's are solved using the 4<sup>th</sup> order Runge-Kutta method. All calculations involving numerical loops on hull panels and strip theories are performed using the OpenMP implementation of the Intel Fortran compiler on Linux Opensuse.

##### 5.1 Upwind Simulation

In the first scenario the yacht commences a tacking maneuver with and without the presence of head sea waves of  $\lambda=1.0$   $LWL$  and steepness of  $h=1/50$ . Using a simple PD controller for course-keeping, the yacht performs tacking maneuvers around earth fixed Y axis and is ordered to keep a heading angle of 20°. When the distance of the trajectory from the Y axis reaches a threshold (set here on 40 meters) the controller orders the yacht to reach a heading of -20° until the bilateral distance criteria is met (Figure 11).

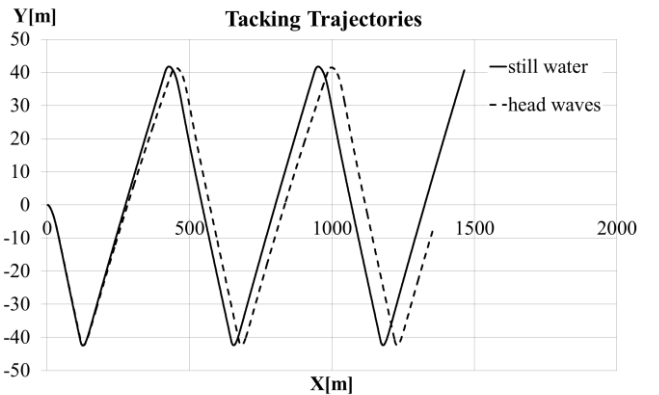


Figure 11 – Tacking Trajectory on calm and wavy seas (graph from Angelou & Spyrou 2016).

The yacht experiences a surging behavior, however speed losses appear small (Figure 12) and are more easily apprehended by considering the difference in the total track covered by the yacht.

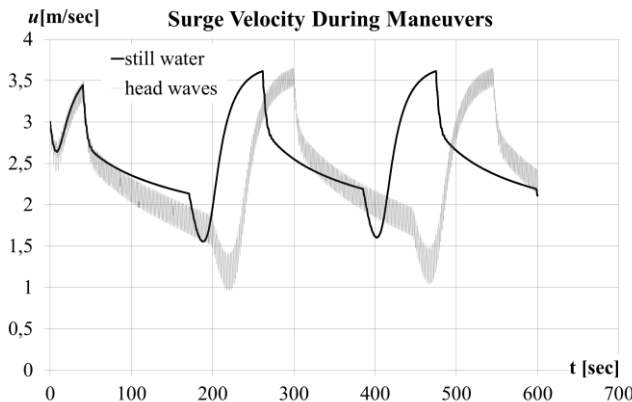


Figure 12 – Surge velocity during tack (graph from Angelou & Spyrou 2016).

## 5.2 Downwind Simulation

In the second scenario the yacht is sailing under the influence of a purely following true wind ( $0^\circ$  off the stern) of constant speed of 10 knots. The yacht is considered to carry a cruising symmetric spinnaker of area  $S_{SPIN}=70 \text{ m}^2$ .

Simultaneously it is excited by following harmonic waves of  $\lambda=2.0 \text{ L}_\text{WL}$  and steepness of  $h=1/50$ . As shown in Figure 13, the yacht experiences surging, which becomes asymmetric if the wave steepness is increased ( $h=1/35$ ). If the incident waves steepness reaches the threshold of  $h=1/30$  the yacht adopts surf-riding behavior and oscillates around the wave celerity.

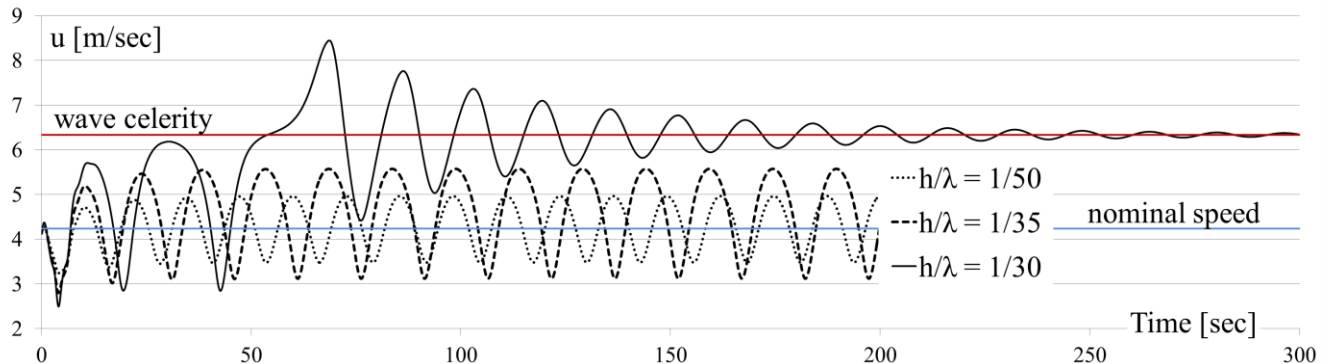


Figure 13 – Asymmetrical Surging and Surf-riding on following waves (graph from Angelou & Spyrou 2016).

## 6 CONCLUSIONS

This study covered the development of a mathematical model for course-keeping and maneuvering studies of sailing yachts in waves. The character of this tool is modular, providing all parts with a potential for growth in terms of modeling complexity. The model is still under development. Admittedly, some of the sub-models have not had their contribution strongly justified as they are intended to be replaced soon by more sophisticated versions, having been implemented in their current form for the sake of overall model completeness. First trials on instability phenomena, covered in the literature only for motorboats, show qualitatively reasonable predictions.

Along with the addition of transient and more detailed formulations regarding the excitations of the sails, as also the implementation of added mass and potential damping terms regarding all modes of motions, validation and verification with experimental and computational data is due to follow. It is the authors' intention to increase the complexity of the implemented sub-models, as also to broaden the model's overall applicability, while retaining the focus on the propensity of sailing yachts for instability phenomena that compound their performance and safety.

## REFERENCES

- Angelou M., Spyrou, K.J., "Simulations of Sails of a Yacht using a Fluid-Structure Interaction Model", 10<sup>th</sup> HSTAM International Congress on Mechanics, Chania, Greece, 2013.
- Angelou M., Spyrou, K.J., "Modeling Sailing Yachts' Course Instabilities Considering Sail Shape Deformations", Proceedings of the 12<sup>th</sup> International Conference on the Stability of Ships and Ocean Vehicles, Glasgow, UK, 2015.
- Angelou M., Spyrou, K.J., "Towards a New Mathematical Model for Investigating Course Stability and Maneuvering Motions of Sailing Yachts", The 22nd Chesapeake Sailing Yacht Symposium Annapolis MD, USA 2016.
- Batoz J.L., Bathe K.J., Ho L.W., "A Study of Three-Node Triangular Plate Bending Elements". International Journal for Numerical Methods in Engineering, Vol. 15. 1771-1812, 1980.
- Hoerner, S.F., "Fluid-Dynamic Drag", Hoerner Fluid Dynamics, 2<sup>nd</sup> edition, USA, 1965.
- Hoerner, S.F., "Fluid-Dynamic Lift", Hoerner Fluid Dynamics, 2<sup>nd</sup> edition, USA, 1985.
- Jones, P., Korpus,R. "International America's Cup Yacht Design Using Viscous Flow CFD", Proceedings of the 15<sup>th</sup> Chesapeake Sailing Yacht Symposium, Annapolis, MD, January 2001.
- Katz J., Plotkin A., "Low Speed Aerodynamics", Cambridge University Press, Second Edition, Cambridge, 2001.

- Kagemoto, H., Fujino, M., Kato, Takayoshi, K., Wu, Ch.T., "A Numerical and Experimental Study to Determine the Loads on a Yacht Keel in Regular Wave", Proceedings of the 7<sup>th</sup> International Conference on the Stability of Ships and Ocean Vehicles, Australia, 2000.
- Lasher, W.C., Sonnenmeier, J.R., Forsman, D.R., Zhang, C., White, K., "Experimental Force Coefficients for a Parametric Series of Spinnakers", Proceedings of the 16<sup>th</sup> Chesapeake Sailing Yacht Symposium, Annapolis, MD, March 2003.
- Lloyd, B., "Guide to Avoid Broaching", The New York Times, July 11, 1988.
- Masuyama, Y. and Fukasawa T., "Tacking Simulation of Sailing Yachts with New Model of Aerodynamic Force Variation During Tacking Maneuver", SNAME Journal of Sailboat Technology, 2011.
- Melliere, R.A., "A Finite Element Method for Geometrically Non-linear Large Displacement Problems in Thin, Elastic Plates and Shells", Doctoral Dissertation, Missouri University of Science and Technology, Paper 2102, 1969.
- Nesteruk, I. and Cartwright, J.H.E., "Turbulent Skin-Friction Drag on a Slender Body of Revolution and Gray's Paradox", 13th European Turbulence Conference (ETC13), Journal of Physics: Conference Series 318, 2011.
- Newman, J.N., "Marine Hydrodynamics", The MIT Press, 9<sup>th</sup> edition, 1977.
- Oltmann, P., Sharma S.D., "Simulation of Combined Engine and Rudder Maneuvers Using an Improved Model of Hull-Propeller-Rudder Interactions", The 15<sup>th</sup> Symposium of Naval Hydrodynamics, National Academy Press, 1985.
- van Oossanen, P., "Predicting the Speed of Sailing Yachts," SNAME Transactions, Vol. 101, 1993.
- Pascual, E., "Revised Approached to Khaskind's Method to Calculate the WaveMaking Resistance Depending on the Sectional Area Curve of the Ship", Journal of Ship Research, Vol. 51, September 2007, pp. 259-266, 2007.
- SNAME, "Nomenclature for Treating the Motion of a Submerged Body Through a Fluid" SNAME Transactions, 1950.
- Spyrou, K.J., "Historical Trails of Ship Broaching-To", The Transactions of the Royal Institution of Naval Architects: Part A - International Journal of Maritime Engineering, 152, Part A4, pp. 163-173, 2010.
- Tigkas, I., Spyrou, K.J., "Continuation Analysis of Surf-riding and Periodic Responses of a Ship in Steep Quartering Seas", Proceedings of the 11<sup>th</sup> International Conference on the Stability of Ships and Ocean Vehicles, Athens, Greece, 2012.
- Yuanxie, Zhao., "Calculation of Ship Manoeuvring Motions in Shallow Water", Schiffstechnic Bd. 33 1986.
- Zienkiewicz O.C., Taylor R.L., "The Finite Element Method, Volume 1 : The Basis", Butterworth – Heinemann, Fifth Edition, Oxford, UK, 2000.
- Zienkiewicz O.C., Taylor R.L., "The Finite Element Method, Volume 2 : Solid Mechanics", Butterworth – Heinemann, Fifth Edition, Oxford, UK, 2000.

## The Gate Rudder Application to Improve Poor Course Keeping Ability of Ships

**Serkan Turkmen<sup>1\*</sup>, Noriyuki Sasaki<sup>1</sup>, Mehmet Atlar<sup>2</sup>, Adrian Miles<sup>3</sup>, Toshifumi Takeda<sup>4</sup>**

<sup>1</sup>Newcastle University, Newcastle Upon Tyne, UK

<sup>2</sup>University of Strathclyde, UK

<sup>3</sup>Stone Marine Propulsion Ltd, Birkenhead, UK

<sup>4</sup>Yamanaka Zosen Co. Ltd., Japan

### **Abstract:**

“Gate rudder” is a term describing the special arrangement of a twin rudder and propeller system where two rudder blades with asymmetric cross sections are placed aside the propeller. The main advantage of this propulsion system is its energy saving feature. This originates in the rudder thrust induced by the cambered twin rudder blades and the propeller, acting as an efficient accelerating ducted propeller.

A recent study of the gate rudder (Sasaki et al. 2015) revealed that this innovative system has a remarkable flap effect which can be effective for efficient manoeuvring of ships by exploiting the interaction between the twin rudder blades and the ship stern. This phenomenon can be seen already, to a certain extent, in conventional rudder systems and has been introduced in the theoretical model of Manoeuvring Modelling Group (MMG) as a rudder force increase factor ( $a_H$ ). Average values of  $a_H$  for conventional rudders vary in general between 0.1 -0.2. However the  $a_H$  value for the gate rudder can be as high as 0.4 and hence presenting an excellent potential for a superior course keeping ability for ships.

A vessel with extreme stern fullness suffers from poor course keeping ability and improvement of this setback using a gate rudder system is the main focus of the current study which presents the comparative simulation results for the course keeping ability of such vessel equipped with a conventional rudder and gate rudder system. In the study a modified MMG model was employed to simulate the manoeuvring performance of different hull forms to demonstrate the effectiveness of the gate rudder system to improve the poor course keeping ability of the vessels with extreme stern fullness.

**Keywords:** Twin Rudder, Gate Rudder, Duct Effect, Energy Saving Devices, Manoeuvrability,

### **1. Introduction**

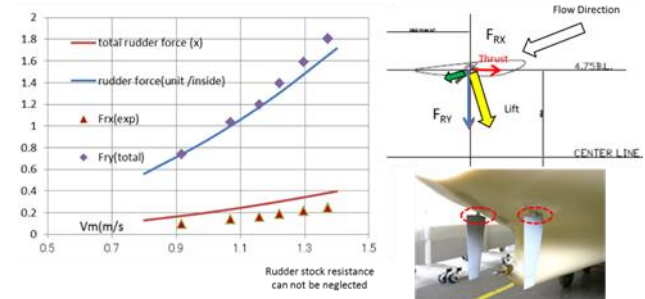
While a conventional rudder (CR) is essential to manoeuvre the ship, it also has the following disadvantages:

- increase of appendage drag,
- necessary modifications to the stern arrangement to accommodate the rudder that enforces restriction not only to the propeller aperture but also to the engine room arrangement,
- a non-uniform flow imposed on the propeller plane that can easily increase the vibration and noise originating not only from the propeller but also from the combination of the propeller with the rudder,
- Cavitation erosion on the rudder highly problematic for high speed vessels.
- Poor course keeping for ships with a displacement ( $\nabla$ ) to length ( $L$ ) ratio ( $\nabla^{1/3}/L > 0.2$ , DNV (1995).

In most cases it might be required to install Energy Saving Devices (ESD) and high-lift rudder area to overcome the above mentioned disadvantages. An alternative solution to this can be the “Gate Rudder” (GR) concept which was

introduced by (Sasaki, 2013). The GR is a twin rudder system with two asymmetric rudders at each side of a propeller (see Figure 1). One main advantage of this system is its energy saving potential which is based on the rudder thrust (duct effect) induced by the cambered twin rudder blades and efficiently accelerated propeller flow.

Figure 1. Gate Rudder of NOAH Project (Sasaki 2013)



A recent study of the GR reveals that this innovative rudder system has a remarkable “flap effect” which can be effective for efficient manoeuvring of ships by exploiting the interaction between the twin rudder blades and the ship

stern (Sasaki et al, 2015). Equation 1 explains the flap effect in terms of the total side force ( $F_T$ ).

$$F_T = F_Y(1+a_H) \quad (1)$$

$$F_Y = F_N \cos \delta \quad (2)$$

where  $F_Y$  is the side force generated by the rudder and  $a_H$  is the so-called ‘‘rudder force increase factor’’.  $F_N$  is the rudder normal force and  $\delta$  is the rudder angle.  $a_H$  is also the ratio of the hydrodynamic force induced on the ship hull by the rudder action.  $a_H$  can be expressed as a function of the distance between the rudder, hull form and the overall hull-propeller-rudder arrangement (Hirano 1981, Gong et al. 1995, Molland 2011). This phenomenon can already be seen to a certain extent in the case of conventional rudders and was introduced in the theoretical model of Manoeuvring Modelling Group (MMG) by the above described the rudder force increase factor ( $a_H$ ). The MMG standard method was proposed by the Japan Society of Naval Architects and Ocean Engineers to standardize the mathematical model for ship manoeuvring predictions (Yasukawa, 2015). Average values of  $a_H$  for conventional rudders vary between 0.1-0.2 in general (Hirano 1981, Gong et al. 1995).

In a recent study the MMG model was further developed for the GR simulations (Carchen et al. 2016) where it was found that the  $a_H$  values for the GR can be as high as 0.4. Hence presenting an excellent potential for superior course keeping ability for ships. In the same study, the results of the previously conducted towing tank and cavitation tunnel experiments were used to validate the modified MMG model for the GR application.

Although the recent activity in (Carchen et al, 2016) explored various manoeuvring aspects of the GR application using the enhanced MMG model, the main objective of the current study was the application of the CR and GR systems to different hull forms in order to evaluate the course keeping performances by using the enhanced MMG model. Hull derivatives were partly adopted from the studies of (Sasaki et al., 2015), (Yasukawa, 2015) and (Hirano, 1981).

The remaining sections of this paper describes the GR concept in details (in Section 2), the MMG model (in Section 3), results of the MMG simulations (in Section 4) and conclusions drawn from the study (in Section 5).

## 2. Development of The Gate Rudder concept

The main motivation behind the innovative twin rudder system was the development of Energy Saving Devices (ESD). This is an important area in Energy Efficiency Design Index (EEDI) and Ship Energy Efficiency Management Plan (SEEMP), mainly focusing on the reduction of carbon emission due to shipping transport. There are different ESDs based on various hydrodynamic principles (Sasaki et al. 2015).

Within the context of the energy saving the key aspect of the GR is that it can be used to steer ships effectively as well as to save energy as an ESD. The GR generates lateral forces to steer a vessel like a CR. Additionally the GR creates induces axial velocity in the propeller plane,  $v_i(0, y_0, z_0)$ , generates an extra thrust, due to the so-called the duct effect. As illustrated in Figure 2. the induced velocity generates circulation,  $\Gamma(z)$ , around the GR based on the Biot-Savart law. The circulation, in turn, can be related to the lift force,  $L(z)$ , on the rudder surface according to the Kutta-Joukovski law.

$$v_i(0, y_0, z_0) = \int_{z_B}^{z_T} \frac{\Gamma(z)}{2\pi r} dz \quad (3)$$

$$L(z) = \rho V(z) \Gamma(z) \quad (4)$$

The additional thrust generated improves the propulsive efficiency. Moreover, the improvement of the stern flow can reduce the flow noise and vibration, and shifting the rudder engine room forward increases the cargo space whilst decreasing the ship length (Sasaki et al. 2015).

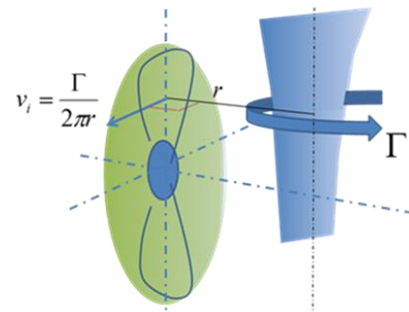


**Figure 2. Induced velocity in a propeller plane originated from gate rudder**

A single rudder stock was used for early application of the GR. This was later replaced by two stocks driving two individual, asymmetric blade system to improve manoeuvrability, as well as the duct effect. This concept provides also extra features such as stopping ability, berthing performance (in crabbing mode), and reduction of the rolling motion by controlling the rudder angles individually. Figure 3 shows the target position of the GR compared to other control devices in terms of its development strategy. The development strategy of the GR aims to improve the energy saving capability as well as to maintain safe ship manoeuvrability. Therefore, the GR was proposed as a new ESD to combine simultaneously a better propulsive performance with strong manoeuvrability.

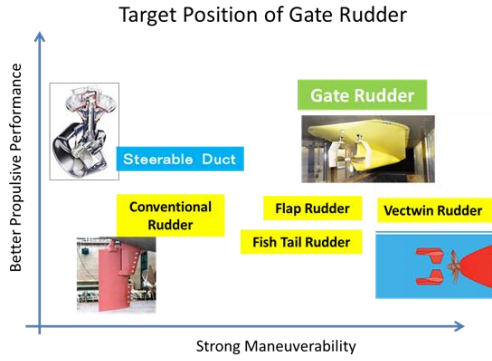


**Figure 3. Target position of Gate Rudder in ESD development strategy**

### 3. Methodology

In order to predict the course keeping ability, a modified MMG model was used. The main difference from the original MMG model is a prediction procedure of rudder forces. As the gate rudder has two blades beside a propeller, the flow fields depend not only on the rudder angle but also on the propeller rotation direction as illustrated in Figure 4 .

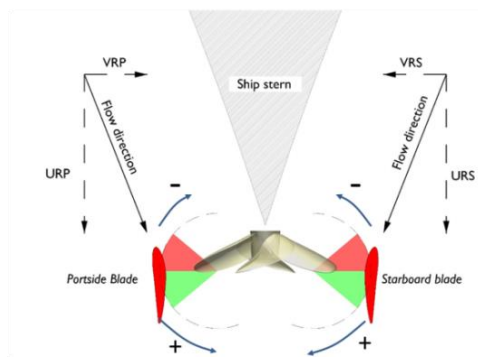


**Figure 4. Definitions of rudder angles and flow**

The simplification of the flow field around the hull and gate rudder system provided a modelling challenge. The prediction of this flow field by CFD based on the Navier-Stokes equation solver be seen as a possible solution including the propeller action. The propeller performance characteristics (thrust, torque, advance speed) were introduced in the CFD model as a momentum source. To decrease the calculation time, simplifications were made such as the free surface and the existence of rudders was neglected. Therefore, the interaction between the rudders, propeller and ship was not included in the CFD calculation.

Numerically calculated velocities ( $U$  and  $V$ ) around the GRs position , shown in Figure 4, were averaged along the virtual span of the GR for the range of effective inflow angle to rudder (port side blade  $50 \leq \alpha_R \leq 130$  and starboard side blade  $230 \leq \alpha_R \leq 310$ ) at each drift angle( $\beta$ ) from 0 to 35 degree. Multiple regression analysis was used to

estimate normalized velocities as a function of the drift angle  $\beta$  and  $\alpha_R$ . The estimated function was then employed in the MMG model to determine forces generated by the GRs (Carchen et al. 2016).

A flow chart presenting the principal features of the methodology, using numerical method and hydrodynamic derivatives from experiment for the computation, is shown in Figure 5.

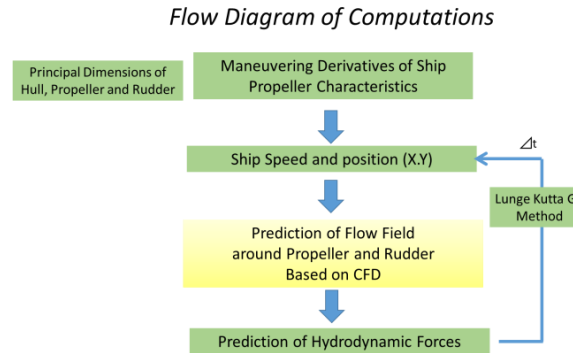


**Figure 5. Flow diagram of computations**

### 4. Case studies

In order to demonstrate the strong flap effect of the GR three different hull types, listed in Table 1, were investigated. Figure 6 shows that the indexes of fullness of these vessel are scattered and the fullness of the Bulk Carrier is remarkably larger than of the other two vessels. The most important manoeuvrability feature of a beamy vessel, such as this bulk carrier, is the course keeping ability. IMO introduced a regulation, Standards for Ship Manoeuvrability, to approve this ability by the maximum overshoot angles of zig-zag tests as shown in Table 2.

From a practical point of view, designers have been using an unstable loop width instead of the over shoot angle as described in Yoshimura (1998). Sasaki (2013) presented a simple prediction method of unstable loop width. In the prediction method, two parameters are used, i.e. the fullness parameter ( $\gamma A$ ) and the form factor  $K$ . The fullness parameter represents two-dimensional fullness of the vessel and  $K$  represents the effect of the strength of the longitudinal vortex which can suppress the two-dimensional separation by stimulating the three-dimensional separation. This longitudinal vortex can maintain the pressure recovery of the stern part which can be seen in the fine vessels. Figure 6 shows the relationship between  $K$  and  $\gamma A$  for the hullforms under investigations. As shown in Figure 6 the bulk carrier is clearly the unstable one amongst the three hullforms investigated.

**Table 1. Principal dimensions of Vessels equipped with Gate Rudder**

| Ship type                       | Bulk    |       | Domestic       |      | Feeder        |      |
|---------------------------------|---------|-------|----------------|------|---------------|------|
|                                 | Carrier | Cargo | Container      |      |               |      |
| Lpp (m)                         | 225     |       | 68.6           |      | 101.9         |      |
| B (m)                           | 48.8    |       | 12             |      | 17.8          |      |
| d (m)                           | 13.4    |       | 4.19           |      | 5.25          |      |
| Design Speed kn                 | 14.5    |       | 12.8           |      | 15.5          |      |
| Rudder type                     | Conv.   | GR    | Fish Tail type | GR   | Flap type     | GR   |
| Propeller Dia. (m)              | 6.4     | 6.4   | 2.4            | 2.4  | 3.4           | 3.3  |
| Pitch Ratio                     | 0.75    | 0.9   | 0.7            | 0.8  | 0.7           | 0.85 |
| Rudder Projected Area ( $m^2$ ) | 73.2    | 45    | 4.87           | 3.45 | 8.77          | 5.4  |
| Rudder Height (m)               | 10.5    | 9.8   | 2.86           | 3    | 3.7           | 3    |
| Additional study                |         |       | Stern end Bulb |      | Pre Swirl Fin |      |

**Table 2 IMO Manoeuvering Standard (IMO 1993)**

| Measure of Maneuverability                            | Criteria and Standard                             | Maneuver           | IMO Standard                      |
|---|---|--------------------|-----------------------------------|
| Required for Optional Class Notation                  |   |                    |                                   |
| Turning Ability                                       | Tactical Diameter                                 | Turning Circle     | $TD < 5L$                         |
|   | Advance   |                    | $Ad < 4.5L$                       |
| Course Changing and Yaw Checking Ability              | First Overshoot Angle                             | 10/10 Zig-zag test | $\alpha_{10_1} \leq f_{101}(L/V)$ |
|   | Second Overshoot Angle                            |                    | $\alpha_{10_2} < f_{102}(L/V)$    |
|   | First Overshoot Angle                             | 20/20 Zig-zag test | $\alpha_{20_1} \leq 25$           |
| Initial Turning Ability                               | Distance traveled before 10-degrees course change | 10/10 Zig-zag test | $\ell_{10} \leq 2.5L$             |
| Stopping Ability                                      | Track Reach                                       | Crash stop         | $TR < 15L^{(1)}$                  |
|   | Head Reach  |                    | None                              |
| Recommended, Not Required for Optional Class Notation |   |                    |                                   |
| Straight-line Stability and Course Keeping Ability    | Residual turning rate                             | Pull-out test      | $r \neq 0$                        |
|   | Width of instability <sup>(2)</sup> loop          | Simplified spiral  | $\alpha_U \leq f_u(L/V)$          |

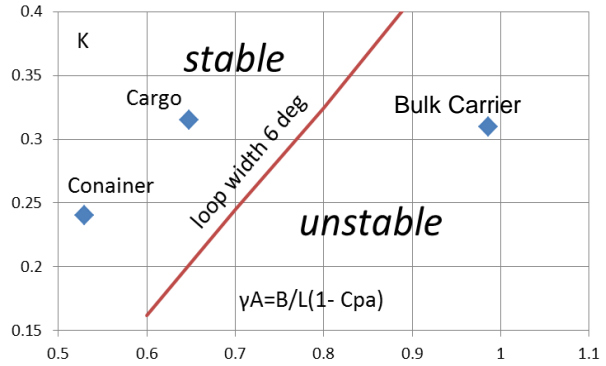


**Figure 6. Quick Cart of Course Keeping Ability**

The manoeuvring performances of the subject three hullforms were simulated by using the modified MMG model in the following sub-section of the paper.

#### 4.1 Domestic Cargo

This vessel was studied in details not only from the propulsive performance point of view but also from the manoeuvring performance (Turkmen et al. 2015, Carchen et al. 2016). The captive and free running model tests with this vessel were recently conducted at the Kyushu University of Japan. The instrumentation used for the manoeuvring tests are shown in Figure 7. Due to the space restriction, the rudder control system was installed only on the starboard side. The simulations were thus conducted for two cases. The first case was the same condition as the model test. The second case was the simulation of the result of a combined twin rudder system in normal operation.

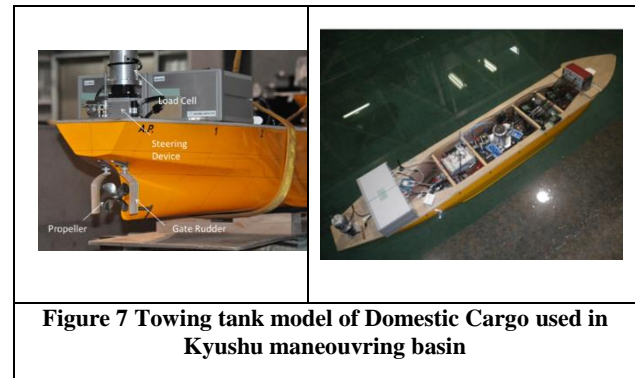


**Figure 7 Towing tank model of Domestic Cargo used in Kyushu manoeuvring basin**

The flow fields were estimated by CFD as reviewed in Section 3 and in (Carchen et al. 2016). Figure 8 shows the velocity contours behind the vessel. This velocity distribution was used to determine the forces generated by the rudder in the MMG software. Figure 9 and Figure 10 show the comparison of the towing tank test and MMG simulation for 35 degree turning circle test and 20 degree zig-zag tests that are the IMO requirements. Both simulation and experiments satisfied the standards for the Gate Rudder.

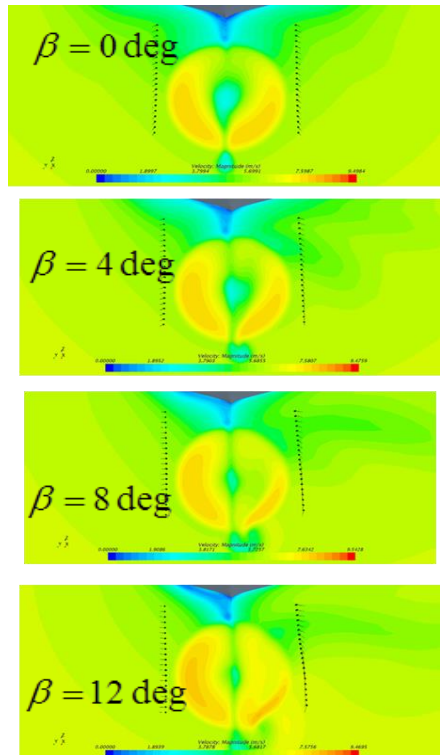


**Figure 8** The flow field characteristics behind the stern for different drift angles

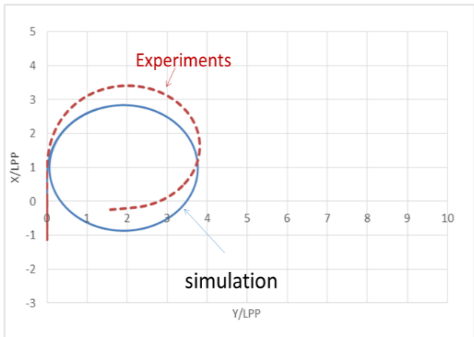


**Figure 9.** Starboard 35deg turning circle test: ship track

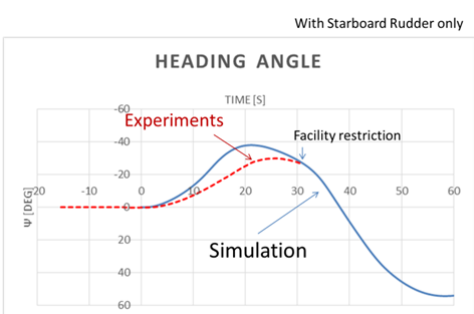


**Figure 10.** Time series of heading angle during Port 20 deg zig-zag test

12 present the Zig-Zag manoeuvres simulation for  $\pm 10$  degree and  $\pm 20$  degree, respectively. The improvement on the course keeping can clearly be detected in the  $\pm 20$  degree Zig-zag tests as shown in Figure 12. The remarkable GR contribution to the Turning circle test outperformed the CR as shown in Table 5.

10 to STARBOARD Z-TEST      10 to PORT Z-TEST

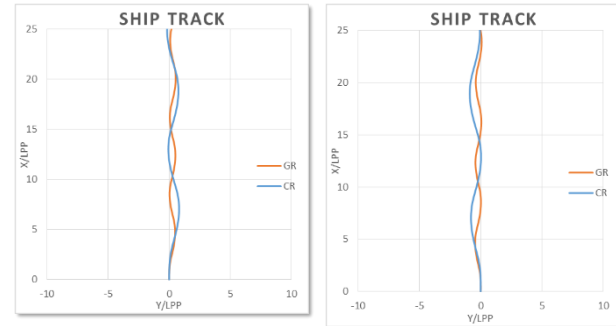


**Figure 11.** Zig-Zag manoeuvres  $\pm 10$  degree

The IMO standard was verified by using the MMG model. Table 3, Table 4 and Table 5 show that both the CR and GR satisfy the IMO criteria.

20 to STARBOARD Z-TEST      20 to PORT Z-TEST

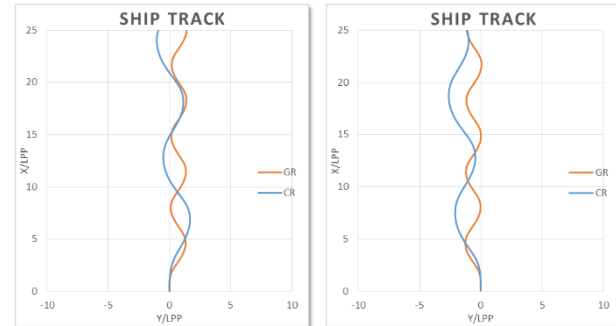


**Figure 12.** Zig-Zag manoeuvres  $\pm 20$  degree

**Table 3** Z-TEST Overshoot angle  $\pm 10$

|        | CR      | GR      | CR      | GR      |
|--------|---------|---------|---------|---------|
| 10°    | 1st OSA | 1st OSA | 2nd OSA | 2nd OSA |
| +10(S) | 2.9     | 2.3     | 4.2     | 2.4     |
| -10(P) | 2.9     | 2.1     | 3.6     | 2.8     |
| MEAN   | 2.9     | 2.2     | 3.9     | 2.6     |

The MMG model was further employed to investigate the course keeping ability of CR and GR. Figure 11 and Figure

**Table 4. Z-TEST Overshoot angle  $\pm 20$**

|        | CR      | GR      | CR      | GR      |
|--------|---------|---------|---------|---------|
| 20°    | 1st OSA | 1st OSA | 2nd OSA | 2nd OSA |
| +20(S) | 7.2     | 12.6    | 13.8    | 12.2    |
| -20(P) | 11.3    | 12.0    | 8.4     | 12.4    |
| MEAN   | 9.3     | 12.3    | 11.1    | 12.3    |

**Table 5. Turning circle test Advance and Diameter**

|        | CR     | GR     | CR      | GR      |
|--------|--------|--------|---------|---------|
| 35°    | Adv./L | Adv./L | Tact./L | Tact./L |
| +35(S) | 4.4    | 2.8    | 5.4     | 3.8     |
| -35(P) | 4.0    | 2.9    | 4.7     | 3.8     |
| MEAN   | 4.2    | 2.8    | 5.0     | 3.8     |

#### 4.2 Feeder Container

The second case is the Container Vessel. A GR was designed and optimized for this vessel to investigate its energy saving performance. Figure 13 shows the actual vessel and the GR model. The manoeuvring performance of the vessel with the CR and the GR was simulated with the MMG model. The simulation results are presented in Figure 14 and Figure 15 for the  $\pm 10$  degree and  $\pm 20$  degree Zig-Zag manoeuvres simulation. The overshoot angle and turning circle test results are given in Table 6, Table 7 and Table 8. All results are below the IMO limits. The vessel with the GR performs better than with the CR at the Z tests for overshoot angle  $\pm 10$ .



**Figure 13 Feeder Container vessel and GR model**

20 to STARBOARD Z-TEST      20 to PORT Z-TEST

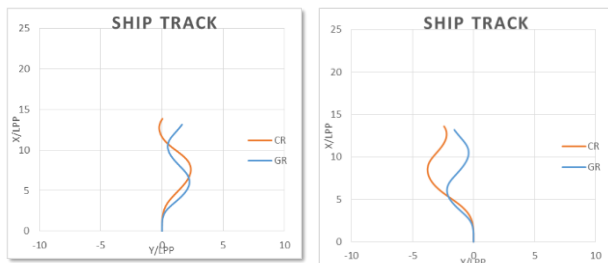


**Figure 15 Zig-Zag manoeuvres  $\pm 20$  degree**

**Table 6. Z-TEST Overshoot angle  $\pm 10$**

|        | CR      | GR      | CR      | GR      |
|--------|---------|---------|---------|---------|
| 10°    | 1st OSA | 1st OSA | 2nd OSA | 2nd OSA |
| +10(S) | 5.5     | 4.0     | 18.0    | 4.9     |
| -10(P) | 8.3     | 3.7     | 6.9     | 5.6     |
| MEAN   | 6.9     | 3.9     | 12.4    | 5.2     |

**Table 7. Z-TEST Overshoot angle  $\pm 20$**

|        | CR      | GR      | CR      | GR      |
|--------|---------|---------|---------|---------|
| 20°    | 1st OSA | 1st OSA | 2nd OSA | 2nd OSA |
| +20(S) | 14.2    | 20.8    | 24.2    | 15.9    |
| -20(P) | 26.8    | 20.3    | 14.1    | 15.7    |
| MEAN   | 20.5    | 20.6    | 19.2    | 15.8    |

**Table 8. Turning circle test Advance and Diameter**

|        | CR     | GR     | CR      | GR      |
|--------|--------|--------|---------|---------|
| 35°    | Adv./L | Adv./L | Tact./L | Tact./L |
| +35(S) | 4.4    | 3.4    | 4.0     | 4.2     |
| -35(P) | 4.1    | 3.4    | 3.6     | 4.2     |
| MEAN   | 4.2    | 3.4    | 3.8     | 4.2     |

#### 4.3 Bulk Carrier

The MMG model was further used for the Bulk Carrier vessel to investigate the GR application for a typical hull form with large beam and block coefficient. Figure 16 and Figure 17 present the CR and GR  $\pm 10$  and  $\pm 20$  Zig-Zag manoeuvres simulations. Table 9, Table 10 and Table 11 show the over shoot angle and turning circle test results to compare with the IMO requirements. The vessel with the CR shows poor course keeping performance for particularly  $\pm 20$  Z test. The main reason, as indicated in the introduction, is the fullness of the Bulk Carrier with a high block coefficient and the low length to volume ratio. Improvements take place when the GR system is used. This improvement can be seen in the results of the turning circle test as well. IMO criteria were satisfied for both the CR and the GR.

10 to STARBOARD Z-TEST      10 to PORT Z-TEST

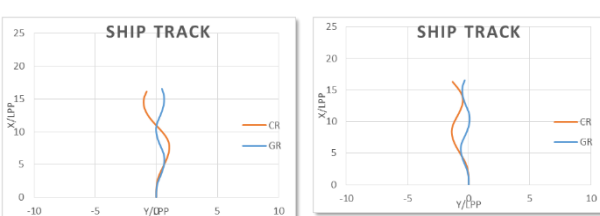


**Figure 14 Zig-Zag manoeuvres  $\pm 10$  degree**

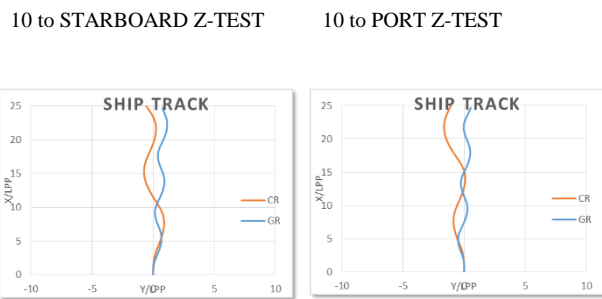


**Figure 16** Zig-Zag manoeuvres  $\pm 10$  degree

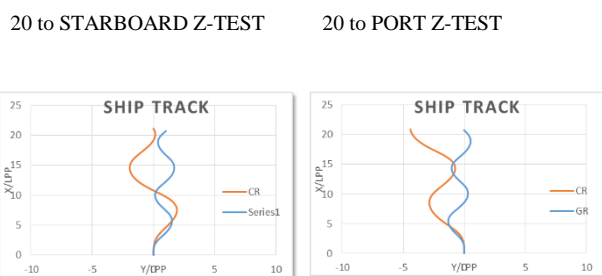


**Figure 17** Zig-Zag manoeuvres  $\pm 20$  degree

**Table 9.** Z-TEST Overshoot angle  $\pm 10$

|        | CR      | GR      | CR      | GR      |
|--------|---------|---------|---------|---------|
| 10°    | 1st OSA | 1st OSA | 2nd OSA | 2nd OSA |
| +10(S) | 3.1     | 4.6     | 10.2    | 4.1     |
| -10(P) | 3.1     | 3.0     | 4.4     | 6.2     |
| MEAN   | 3.1     | 3.8     | 7.3     | 5.1     |

**Table 10.** Z-TEST Overshoot angle  $\pm 20$

|        | CR      | GR      | CR      | GR      |
|--------|---------|---------|---------|---------|
| 20°    | 1st OSA | 1st OSA | 2nd OSA | 2nd OSA |
| +20(S) | 8.2     | 10.7    | 26.6    | 10.7    |
| -20(P) | 16.3    | 8.6     | 12.5    | 13.2    |
| MEAN   | 12.3    | 9.7     | 19.6    | 12.0    |

**Table 11.** Turning circle test Advance and Diameter

|        | CR     | GR     | CR      | GR      |
|--------|--------|--------|---------|---------|
| 35°    | Adv./L | Adv./L | Tact./L | Tact./L |
| +35(S) | 4.5    | 3.2    | 4.5     | 3.5     |
| -35(P) | 4.1    | 3.6    | 4.0     | 4.1     |
| MEAN   | 4.3    | 3.4    | 4.2     | 3.8     |

## 5. Conclusions

By employing the well-established MMG model this study compared the course keeping performance of different hull forms with a CR and a GR system. Three vessels were used to simulate their manoeuvring capabilities. The flow field behind the hulls was calculated with the CFD approach and

IMO criteria checked for each hull case. Based on the simulation results, the following conclusions can be drawn:

1. The CFD approach can satisfactorily calculate the velocity distribution around the rudder including the action of the propeller in a simplified manner. Estimated velocities can be presented as function of the drift angle and the effective inflow angle.
2. All three cases showed that the modified MMG program can predict the manoeuvrability of the vessel with the GR as well as with the CR.
3. Each hull had unique hull derivatives which were rudder-type independent. Therefore course keeping improvement depended on the rudder and the operation condition. The applications showed that the GR system is able to improve the vessel's course keeping ability. The remarkable flap effect ( $a_H$ ) of the GR increased the lateral forces and the yaw moment. This led to a good course keeping ability.
4. The flap effect of the GR is the most significant factor for a Bulk Carrier that has the highest fullness. The findings highlight the significance of the GR and suggest that the GR system can be recommended for similar types of vessel.

Taken together, these findings strengthen the idea that the GR system is an innovative, advanced application to improve ship manoeuvring capabilities, while it can also be used as an energy saving device.

## REFERENCES

- Carchen, A., Shi, W., Sasaki, N. and Atlar, M. (2016) A prediction program of manoeuvrability for a ship with a gate rudder system. A. Yücel Odabaşı Colloquium Series - 2nd International Meeting on Recent Advances in Prediction Techniques for Safe Manoeuvring of Ships and Submarines. Istanbul, Turkey. November 2016.
- DNV (1995). Ship manoeuvrability: Guidelines for rudder area. Casualty Information.
- Hirano, M., A. (1981). A Practical Calculation Method of Ship Manoeuvring Motion at Initial Design Stage. Naval Architecture and Ocean Engineering 19: 68-80.
- IMO. Interim Standards for Ship Manoeuvrability Resolution A.751 (18), Dec. 1993.
- Molland, A., F. & Turnock, S., R. (2011) Marine rudders and control surfaces. 1st ed. Butterworth-Heinemann
- Sasaki, N., Atlar, M. & Kuribayashi, S. (2015). Advantages of twin rudder system with asymmetric wing section aside a propeller. J Mar Sci Tecnol., 10.1007/s00773-015-0352-z
- Sasaki, N. (2013). ZEUS and NOAH projects of NMRI. 3rd international symposium on marine propulsions.

- Sasaki, N., Atlar, M. & Kuribayashi, S. (2015). Advantages of twin rudder system with asymmetric wing section aside a propeller. *Journal of Marine Science and Technology*: 1-12.
- Turkmen, S., Carchen, A., Sasaki, N. & Atlar, M. (2015). A New Energy Saving Twin Rudder System-Gate Rudder. SCC 2015, Intl Conference on Shipping in Changing Climate, Glasgow, 24-26 November
- Yasukawa, H. & Yoshimura, Y. (2015). Introduction of MMG standard method for ship maneuvering predictions. *Journal of Marine Science and Technology* 20(1): 37-52.
- Yoshimura, Y. (1998) Prediction of ship manoeuvrability of SR221 series model with full load and ballast conditions. Proceedings of Workshop on Ship Manoeuvrability in Kyushu University.

## A Prediction Program of Manoeuvrability for a Ship with a Gate Rudder System

**Alessandro Carchen<sup>1\*</sup>, Weichao Shi<sup>1</sup>, Noriyuki Sasaki<sup>1</sup>, Mehmet Atlar<sup>2</sup>**

<sup>1</sup>*School of Marine Science and Technology, Newcastle University, Newcastle Upon Tyne, UK*

<sup>2</sup>*Department of Naval Architecture, Ocean & Marine Engineering, Strathclyde University, UK*

**Abstract:** The Gate Rudder is a special twin rudder system with two rudder blades placed aside of a propeller. Main advantage of this system is the energy saving originated from the rudder thrust which is induced by the two cambered rudder blades comparably efficient to ducted propellers. However, as any rudder's prime task, the performance of manoeuvrability is critical to the Gate Rudder too. With the currently available Manoeuvring Modelling Group (MMG) simulation programs, the simulation is only applicable to the traditional single rudder located behind the propeller. Therefore, how to predict the manoeuvring performance for the gate rudder is the focus of this paper.

On the other hand, a recent study of the Gate Rudder reveals that this innovative system has remarkable flap effect which is well known as a manoeuvring interaction between rudder blades and ship stern. This phenomenon has been observed in the case of conventional rudder and introduced into an MMG-based theoretical model as interaction factor  $aH$ . However, the average values of  $aH$  for conventional rudder is between 0.1–0.2 in general whilst the  $aH$  value for the Gate Rudder is more than twice as much, showing a superior course keeping ability of the Gate Rudder.

The paper presents the manoeuvrability simulation method of a ship with this Gate Rudder system and introduces some examples of comparisons between the model tests and free running tests which was conducted with 2.5 m ship model in the manoeuvring tank at Kyushu University, Japan.

**Keywords:** Gate Rudder, course keeping ability, flap effect, MMG model, CFD simulation

### 1 INTRODUCTION

#### 1.1 Gate Rudder concept application

The demand for improvements in ship energy efficiency is still a paramount in mitigating CO<sub>2</sub> emissions from shipping in spite of low fuel oil price. Consequently, substantial amount of Energy Saving Devices (ESDs) have been proposed, but so far only cost-effective proposals could survive. In this paper a new ESD, known as “Gate Rudder”, will be introduced as applied on a 499 tonnes domestic cargo ship.

The Gate Rudder concept originated from twin rudder systems located aside a propeller. By replacing the conventional rudder by this novel system, many advantages can be gained as shown in Table 1.

Whereas the studies on the propulsive performance of Gate Rudder have been already presented, e.g. Sasaki et al (2015), Turkmen et al (2015), the manoeuvring performance of the gate rudder including a theoretical analysis has not been deeply investigated.

**Table 1. Pros and Cons of Gate Rudder**

| Name                  | Conventional Rudder | High Lift Rudder    | Gate Rudder       |
|-----------------------|---------------------|---------------------|-------------------|
| Energy saving         | base                | Equivalent or worse | 3-5% better       |
| Turning at Navigation | base                | Superior            | Better            |
| Course keeping        | base                | Better              | Better            |
| Turning at port       | base                | Superior            | Better            |
| Stopping              | base                | Better              | Better            |
| Berthing              | base                | Equivalent          | Superior          |
| Noise and Vibration   | base                | Better              | Superior          |
| Cost                  | base                | Slightly worse      | Depends on design |
| Impact on Design      | base                | Equivalent          | Superior          |

**Table 2. Steering Modes of Gate Rudder**

| Name            | Functions  | Rudder angle         |
|-----------------|--|----------------------|
| Economy mode    | The most efficient operation at calm sea condition       | + 3 ~ + 5 deg.       |
| Rough sea mode  | The propeller speed can be increased by accelerated flow | + 0 ~ + 2 deg.       |
| Steering mode   | Normal steering (change the course)                      | Example -10 & +10dg. |
| Circle mode     | Emergency steering (circle motion)                       | -30 & +35 deg.       |
| Crash Stop mode | Emergency steering (crash stop)                          | -30 & -30 deg.       |
| Crabbing mode   | Berthing & de-berthing motion                            | +110 & +60 deg.      |

This paper therefore focuses on the manoeuvrability prediction method for the Gate Rudders. The program was established by modifying the hydrodynamic forces of propeller and rudder, considering the interaction as explained in the following sections.

The unique manoeuvring modes of the Gate Rudder described in The Gate Rudder concept originated from twin rudder systems located aside a propeller. By replacing the conventional rudder by this novel system, many advantages can be gained as shown in Table 1.

Whereas the studies on the propulsive performance of Gate Rudder have been already presented, e.g. Sasaki et al (2015), Turkmen et al (2015), the manoeuvring performance of the gate rudder including a theoretical analysis has not been deeply investigated.

**Table 2** show superior manoeuvrability with various modes to operate the vessel. Each of the twin rudder blades can be helmed from forward to afterward. The most efficient rudder mode will be crabbing mode which can be seen in Figure 1 (bottom right). This mode promises strong side forces aiding the ship berthing. Table 3 shows an overview of the research programs related to the manoeuvrability investigation of the Gate Rudder.

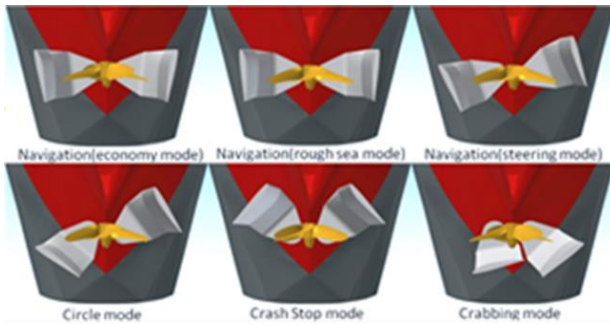


Figure 1. Steering Modes of Gate Rudder

Table 3. Research on manoeuvrability of Gate Rudder

| Name             | Contents   | Facility etc.                                    |
|------------------|--|--|
| Tank Tests       | Rudder Force Measurements with 6m Large Ship Model (without yaw angle)<br>Hull Force Measurements with 2 m Ship Model<br>Captive Tests and Free Running Tests with 2.5m Ship Model | NMRI<br>FEL<br>Kyushu Uni.                       |
| Simulation       | Development of Simulation Program based on MMG model<br>Rudder Control System  | Newcastle Uni. & Kamome Propeller<br>Tokyo Keiki |
| Full Scale Tests | Maneuvering Tests at Sea Trial<br>Monitoring at After Delivery   | Yamanaka Ship Yards<br>Newcastle Uni.            |

## 1.2 The MMG standard prediction method

The MMG standard prediction method is a nonlinear ship manoeuvring mathematical model based on the concept developed by the Japanese Manoeuvring Modelling Group (Ogawa *et al.*, 1977) and later unified by the Japan Society of Naval Architects and Marine Engineers (*Report of Research committee on standardization of mathematical model for ship maneuvering predictions*, 2013). The standard is composed by four parts, namely:

- Mathematical manoeuvrability model
- Procedure to conduct the required captive model tests
- Procedure to analyse the model tests
- Full-scale manoeuvrability prediction method

Whilst details of the latter three parts can be found in Ogawa *et al.* (1977) and in the *Report of Research committee on standardization of mathematical model for ship maneuvering predictions* (2013), recalling the fundamentals of the first fits within the scope of this work.

The reference coordinate system adopted by the MMG is introduced as reported in (Yasukawa and Yoshimura, 2015):

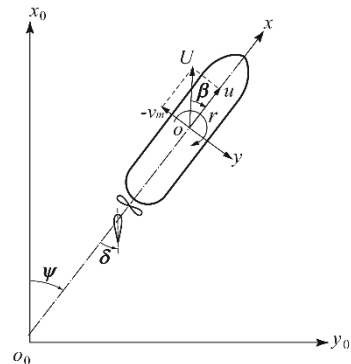


Figure 2. Reference coordinate system (Yasukawa and Yoshimura, 2015)

Where  $x_0$  and  $y_0$  lay on the still water surface,  $o$  coincides with the midship point,  $u$  and  $v_m$  are the components of the ship velocity  $U$  along the ship axis,  $r$  is the yaw rate and  $\beta, \delta, \psi$  the drift, rudder and heading angles respectively. According to the model, the acting forces are subdivided by reason of their source:

$$\begin{cases} X = X_H + X_R + X_P \\ Y = Y_H + Y_R \\ N = N_H + N_R \end{cases}$$

where subscript H, P and R refer to Hull, Propeller and Rudder, respectively.

Hull forces are addressed as functions of the velocity  $U$  of the vessel, its drift angle  $\beta$  and yaw rate  $r$  with uncoupled and coupled terms up to the third order:

$$\begin{cases} X_H \\ Y_H \\ N_H \end{cases} = f(U, \beta, \dot{\beta}, \ddot{\beta}, r, \dot{r}, \ddot{r}, \beta r, \beta r r, \dots)$$

The relationships with these variables depend on the geometry of the vessel and it's therefore recommended to carry out captive model tests to obtain the manoeuvrability derivatives. Where this is not possible, statistical regressions may be used for common hull forms such as in (Yamaguchi *et al.*, 2009).

Propeller forces are considered in the longitudinal direction only. The usual representation for the propeller characteristics is used to calculate the propeller thrust  $K_T$  keeping into account the change in wake fraction  $w_P$  and thrust due to the manoeuvring motion. The function  $K_T = f(J_P)$  is represented by a second order polynomial.

The hydrodynamic rudder forces are presented as sum of two fundamental components, namely the lift force acting on the rudder itself and the lift force induced on the hull caused by the so-called flap effect, i.e. the interaction between rudder and hull.

$$\begin{cases} X_R = -(1 - t_R)F_N \sin \delta \\ Y_R = -(1 - a_H)F_N \cos \delta \\ N_R = -(x_R + a_H x_H)F_N \cos \delta \end{cases}$$

where  $F_N$  represents the rudder normal force,  $t_R$  the change in drag due to rudder-propeller interaction,  $a_H$  the magnitude of the flap effect,  $x_R$  and  $x_H$  respectively the rudder and flap force centroid from mid-ship. The rudder normal is also defined as:

$$F_N = 0.5\rho A_R U_R^2 f_\alpha \sin \alpha_R$$

With  $A_R$  being the rudder projected area,  $f_\alpha$  the rudder lift coefficient,  $U_R = \sqrt{u_R^2 + v_R^2}$  and  $\alpha_R$  respectively the inflow velocity and angle at the rudder, as it can be seen in Figure 3.

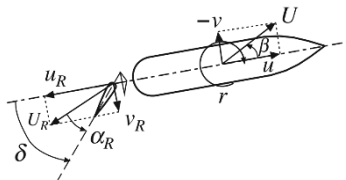


**Figure 3. Rudder and ship velocities and angles (Yasukawa and Yoshimura, 2015)**

It is worth recalling that in the MMG model the definition of the inflow characteristics comes with consideration of the complex flow straightening phenomena related to the hull/propeller slipstream during any manoeuvre.

Owing to the characteristics described above and the limited number of variables, the MMG standard prediction method thus lends itself to be implemented in a manoeuvrability simulation program.

### 1.3 Problem definition

Nevertheless, the particular geometry and location of the Gate Rudder, demands additional considerations. A first effect of its uncommon features can be seen in the water flow on the Gate Rudder, due to the closer proximity to the hull and the propeller disc. This also affects the interaction

with the hull during turning manoeuvres, as it will be seen in the following sections. Finally, because of its unique mechanism many steering modes can be explored and the relative helm control thus has to be defined.

## 2 CFD SIMULATIONS

Commonly, it is acknowledged that the marine rudders are generally positioned behind the propellers at the after end of the marine vessel, whilst the Gate Rudders are set aside the propeller. The Gate Rudder's conceptual design intends to take advantage of the duct effect to produce additional thrust forces. As mentioned earlier, this greatly complicates the flow conditions of the Gate Rudders.

As it has been reviewed in the standard MMG method (Yasukawa and Yoshimura, 2015), the flow velocity for a traditional rudder is basically determined by the effective wake with propeller operating under various heading conditions. However, rare experimental or numerical studies have been conducted to investigate the effective wake aside of the propeller, let alone under various heading conditions.

Therefore, the first task within this study is to understand and predict the flow velocity distribution for the Gate Rudders. In order to perform this task, a simplified full-scale computational fluid dynamics (CFD) model has been established in this chapter.

### 2.1 Numerical modelling methodology

The numerical model in this paper is built in the commercial CFD software Star-CCM+ to solve the incompressible Reynolds Averaged Navier–Stokes (RANS) equations with Shear Stress Transport (SST) turbulence models. The simulation has been conducted for the target vessel with a full-scale 68m long numerical model. Due to the limitations of computational power and for the purpose to achieve a quick prediction of the velocity distribution aside the propeller, the simulations have been conducted without the free surface to neglect its limited impact on the effective wake.

**Table 4. CFD simulation conditions**

|                    |   |
|--------------------|---|
| Ship length        | 68m                                     |
| Ship speed         | 12.81 knots                             |
| Propeller diameter | 2.5m                                    |
| Propeller thrust   | 96.985 kN                               |
| Propeller RPS      | 3.5 to 3.8 RPS<br>(Constant thrust)     |
| Drift angles       | 0° to 16° (2° intervals)<br>25° and 35° |

However, the flow induced by the propeller cannot be ignored during the effective wake prediction and a virtual disc model at the propeller position has been included to simulate the effect of propellers, where the virtual disc can simulate the propeller flow without an actual propeller modelling. By providing the propeller open water curve, the program can automatically match the correct operating

condition in order to maintain the required thrust to overcome the vessel's resistance. The conditions of the CFD simulation are specified in Table 4 and represent an actual operational profile. The layout of the Gate Rudders arrangement is presented in Figure 4.

## 2.2 Mesh generation and boundary condition definition

Trimmer mesh generator in Star-CCM+ has been used with prismatic boundary layer mesh control and volumetric mesh control. Mesh overview has been presented in Figure 5. Local mesh refinement has been specified especially in the propeller position and near the bulbous bow as it can be seen Figure 6. In total, 2 million cells have been used in the computational domain.

During the simulation,  $k-\omega$  Shear Stress Transport (SST) turbulence model has been preferred. Velocity inlet with oblique flow angle and pressure outlet have been applied for the inlet and outlet boundary conditions, while a free-slip wall condition is applied to the bottom boundary.

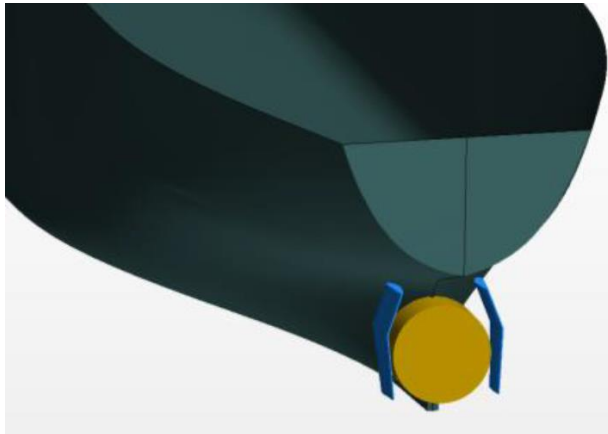


Figure 4. Positions of virtual disc and Gate Rudders

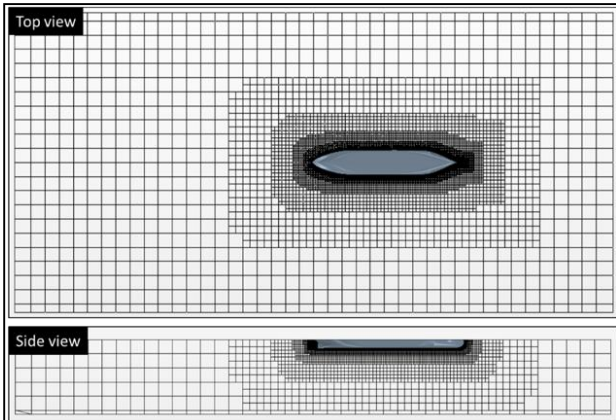


Figure 5. Mesh overview

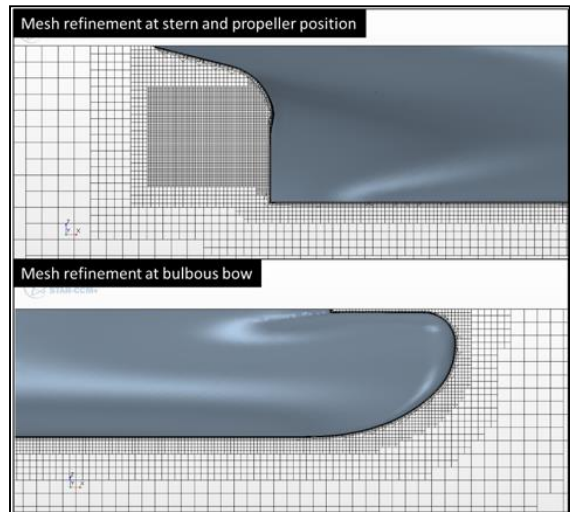


Figure 6. Mesh refinement at stern and bow

## 2.3 Simulation results and analysis

Based on the above setup, the flow velocity distribution in the Gate Rudder position can be achieved. As shown in Figure 7, the velocity distribution of the section at the propeller position and together with the vector at the Gate Rudder position have been displayed when the oblique (drift) angle is  $0^\circ$ . As it can be seen, the flow is nearly symmetric to the mid-ship but not exactly, due to the rotational effect of this right-handed propeller model. It can also be seen in Figure 8 from the top view of the shaft line section.

Another example of result has been presented is the case of  $16^\circ$  of drift. The same post analysis has been conducted, which has been presented in Figure 9 and Figure 10. Because of the oblique flow angle, the velocity distribution is strongly biased, especially for the starboard side.

Based on the above results, it was possible to parametrise the flow velocity components in the  $x$  and  $y$  directions for each of the two blades and every rudder angle. Using a powerful statistical software, the velocities were expressed as polynomial functions of the drift and rudder angle in order to be easily calculated inside the simulation program.

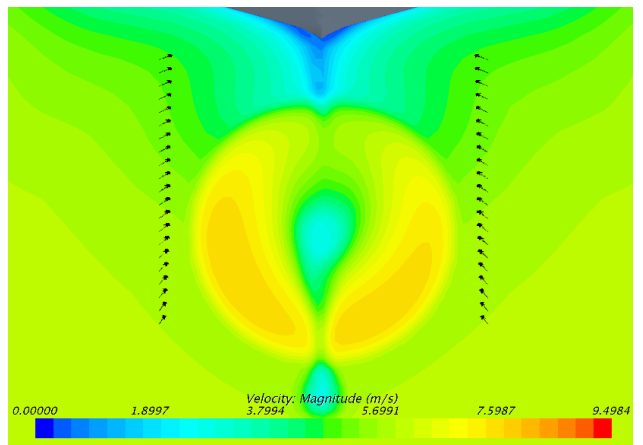
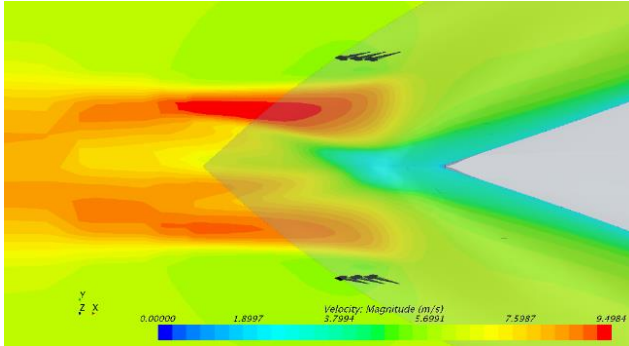
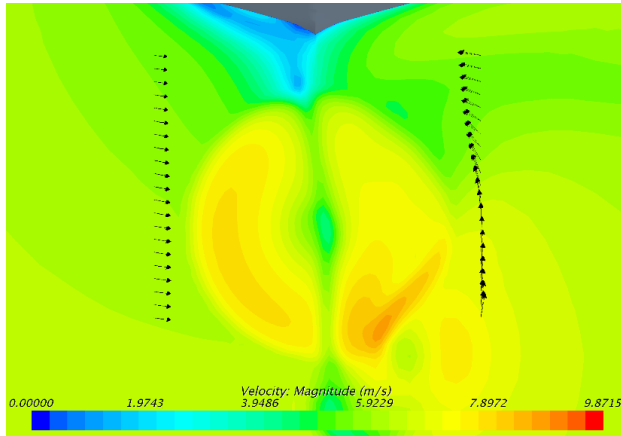


Figure 7. Velocity and vector distribution at  $0^\circ$  oblique angle (aft view)



**Figure 8.** Velocity and vector distribution at 0 degree oblique angle (top view)



**Figure 9.** Velocity and vector distribution at 16 degree oblique angle (aft view)

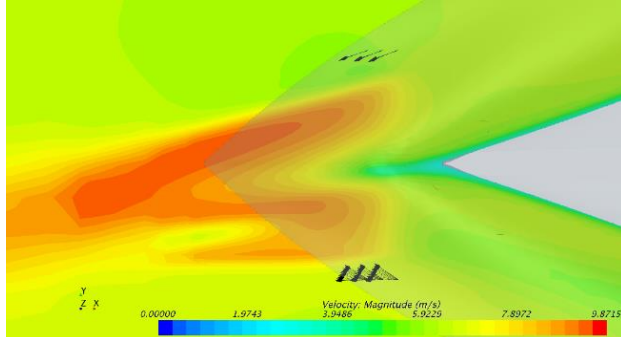


**Figure 10.** Velocity and vector distribution at 16 degree oblique angle (top view)

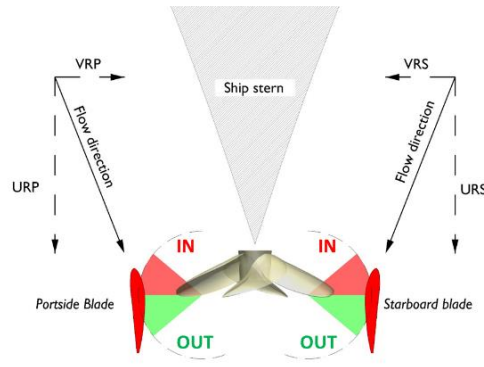


**Figure 11.** Inflow parameters for the Gate Rudder

### 3.1 Determination of the hydrodynamic forces

The different hydrodynamic conditions at which the Gate Rudder is subjected had to be initially addressed. Firstly, new parameters were defined to address the inflow components and the peculiar rudder angles assumed by the Gate Rudder as in Figure 11. For convention, rudder angles closer to the hull (*in*) are negative, those farther from the hull (*out*) are positive. In second place, the inflow velocity components need to be determined in order to calculate the inflow angle and, in turn, the rudder force. Whereas for a conventional rudder the velocity components are determined using standard approximation formulas, in this study they could be expressed according to the CFD results as:

$$UR_{\sigma} = A_0 + A_1 \delta_{\sigma} + A_2 \beta_R + A_3 \beta_R^2 + \dots + A_n \beta_R^{n-1}$$

$$VR_{\sigma} = B_0 + B_1 \delta_{\sigma} + B_2 \beta_R + B_3 \beta_R^2 + \dots + B_n \beta_R^{n-1}$$

Where  $\sigma$  identifies either the Port (*P*) or the Starboard side (*S*) blade and  $\beta_R$  is the local drift angle at the rudder defined as the algebraic sum of the ship drift angle  $\beta$  and that locally induced by the ship's yaw motion:

$$\beta_R = \beta - \ell'_R r'$$

With  $\ell'_R$  obtained from the captive model tests and  $r'$  being the ship's yaw rate (Yasukawa and Yoshimura, 2015). From the above, it is possible to calculate the inflow angle on each blade as:

$$\alpha_{R,\sigma} = \delta_{\sigma} - \tan^{-1} \left( \frac{VR_{\sigma}}{UR_{\sigma}} \right)$$

Therefore, the normal force on each blade can be found:

$$F_{N,\sigma} = 0.5 \rho A_R (UR_{\sigma}^2 + VR_{\sigma}^2) f_{\alpha} \sin \alpha_{R,\sigma}$$

Owing to the wide variation of relative position between rudder blades and hull and the significant consequence on the flap effect, it was seen as necessary to specify different flap effect coefficients depending on whether the blades are closer or farther from the hull. Therefore,  $a_{H(in)}$  and  $a_{H(out)}$  were defined, with each blade assuming at every calculation step the relative value in accordance with its position. The total rudder forces and moments are thus calculated as:

$$\begin{cases} X_R = X_{RP} + X_{RS} \\ Y_R = Y_{RP} + Y_{RS} \\ N_R = N_{RP} + N_{RS} \end{cases}$$

### 3 MANOEUVRABILITY PREDICTION PROGRAM

The manoeuvrability program has been built in Excel environment using VBA to code the MMG prediction model and it aims to simulate the standard ITTC Z-Tests and Circle Test for both conventional and Gate Rudders.

The program comprises an Excel user interface for data input and output analysis and an integrated VBA code handling the iterative solution of the fundamental equations. The first core part of the code is concerned with the determination of the hydrodynamic forces acting on Hull, Propeller and Rudder. The second handles the initialization, a Runge-Kutta discretization method and the controls of simulation and virtual ship.

where:

$$\begin{aligned} X_{RP} &= -(1 - t_R)F_{NP} \sin \delta_P \\ X_{RS} &= -(1 - t_R)F_{NS} \sin \delta_S \\ Y_{RP} &= -(1 - a_{HP})F_{NP} \cos \delta_P \\ Y_{RS} &= -(1 - a_{HS})F_{NS} \cos \delta_S \\ N_{RP} &= -(x_R + a_{HP}x_H)F_{NP} \cos \delta_P \\ N_{RS} &= -(x_R + a_{HS}x_H)F_{NS} \cos \delta_S \end{aligned}$$

### 3.2 Manoeuvre and simulation controls

The input data are initialised from the user interface depending on whether the rudder mode is set to simulate a conventional or Gate Rudder. As mentioned earlier, the program is built so as to simulate generally 4 zig-zag tests and 2 circle tests; however, in the case of conventional rudder these are set to the standard ITTC cases, i.e.  $\pm 10^\circ$ ,  $\pm 20^\circ$  and  $\pm 35^\circ$ . The required inputs thus pertain:

- Hull dimensions and geometric coefficients
- Hull derivatives and added masses
- Propeller dimensions and performance coefficients
- Rudder dimensions and coefficients
- Gate Rudder initial helm controls for each test and each blade
- Ship speed and propeller rate of revolutions
- Time discretization settings

The hydrodynamic equations are calculated inside a Runge-Kutta loop controlled by the simulation length, time step size and output time set by the user. An integrated autopilot function controls the ship manoeuvre during the zig-zag tests in accordance with the IMO requirements.

Three additional add-ins allow the execution of simple animations, the automatic calculations of propeller speed and to obtain the hull derivatives using Kijima's regression formulas (Yamaguchi *et al.*, 2009).

### 3.3 Simulation settings

The data used in the simulation of the Gate Rudder manoeuvrability performance are here reported. The principal ship characteristics are listed in Table 5. In addition:

- The Hull derivatives were derived from captive model tests results.
- From the same test  $\ell'_R = -1$ ,  $a_{H(in)} = 0.4$ ,  $a_{H(out)} = 0$  and  $x_H = -0.45$ .
- The Gate Rudder lift coefficient was derived from tests in the Emerson Cavitation Tunnel of Newcastle University, UK as being  $f_\alpha = 1.4\pi$ .
- The model speed was set  $V_s = 0.48 \text{ m/s}$ .
- Simulation was run with a time step of  $0.05\text{s}$  and an output time of  $0.5\text{s}$  for  $200\text{s}$ .
- The propeller Open Water characteristics were also evaluated in the Emerson Cavitation tunnel and the quadratic equations are:

$$K_T = -0.25J^2 - 0.4J + 0.343$$

$$10K_Q = -0.25J^2 - 0.65J + 0.518$$

To match the experimental validation settings, the Gate Rudder helm angles listed in Table 6 were used.

### 4 MANOEUVRING TEST VALIDATION

To verify the simulation program, captive tests and free running tests were conducted at the manoeuvring and sea-keeping tank of Kyushu University. Pictures of the tank and of the 2.5m wooden model are shown in Figure 12 and Figure 13, respectively. Table 6 shows the test matrix of the manoeuvring tests conducted with the model. Two kind of test were conducted; captive tests and free running tests with the Gate Rudder.

**Table 5. Main particulars of the case study ship**

| Variable            | Symbol               | Value | [m]               |
|---------------------|----------------------|-------|-------------------|
| Length              | <i>Lpp</i>           | 2.50  |                   |
| Breadth             | <i>B</i>             | 0.44  | [m]               |
| Draft               | <i>d</i>             | 0.15  | [m]               |
| Block Coefficient   | <i>Cb</i>            | 0.714 |                   |
| Centre of Buoyancy  | <i>lcb</i>           | -1.81 |                   |
| Prop. Diameter      | <i>Dp</i>            | 0.09  | [m]               |
| Rudder Area (1 bl.) | <i>AR</i>            | 0.005 | [m <sup>2</sup> ] |
| Rudder Span (1 bl.) | <i>H<sub>R</sub></i> | 0.117 | [m]               |

**Table 6. Simulation test matrix**

| Test        | Port blade | Starboard blade |
|-------------|------------|-----------------|
| +10 zig-zag | 0          | -10             |
| -10 zig-zag | 0          | 10              |
| +20 zig-zag | 0          | -20             |
| -20 zig-zag | 0          | 20              |
| +35 circle  | 35         | -30             |
| -35 circle  | -30        | 35              |

During the captive tests, the rudder forces of the starboard side rudder were measured simultaneously with the 3 components of the hull forces. During the free running tests, the ship motion was captured by optical means without touching the ship to allow the purest free motion from the carriage.

There were two restrictions for free running tests given by the tank length and the measurement instruments. Due to the length of the tank it was not possible to cover the 2<sup>nd</sup> overshoot angle. Another restriction was the size of rudder

steering instruments. As the space was not enough to install two sets of this instrument at the stern (shown in Figure 14), only one side of the Gate Rudder could be controlled. Therefore, some results are predicted by the simulation by superposing the rudder forces which was measured independently.



**Figure 12. Model basin of Kyushu University**

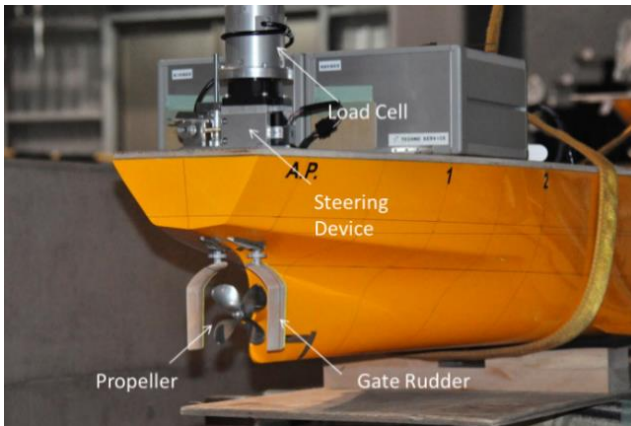


**Figure 13. 2.5m wooden model**



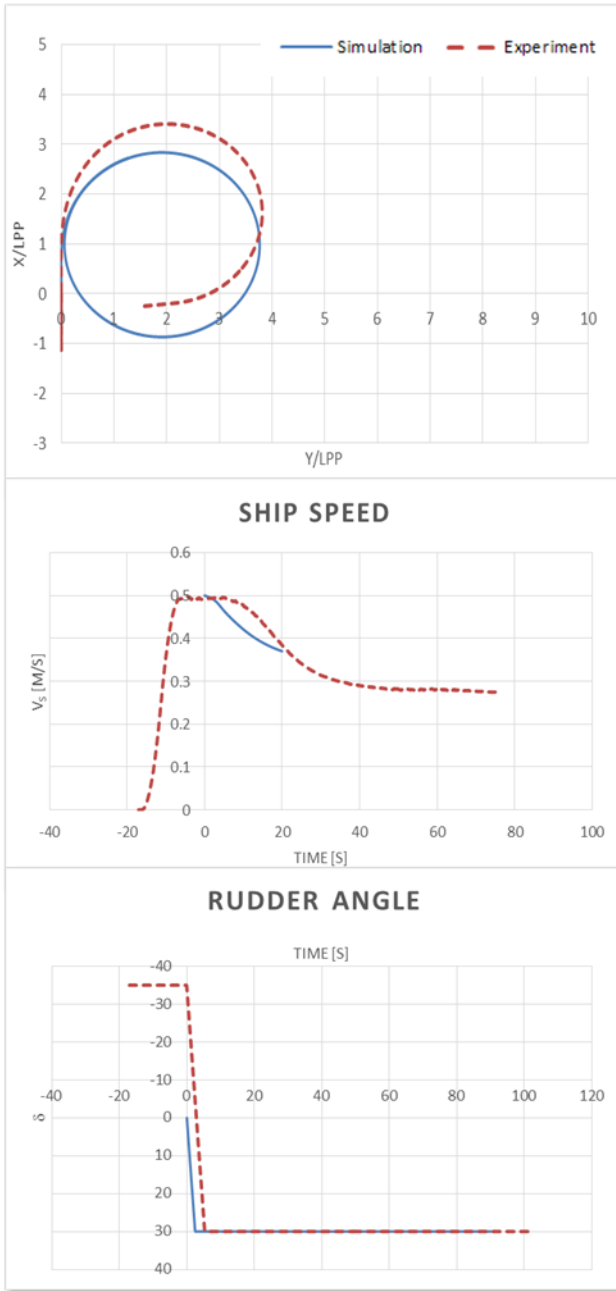
**Figure 14. Setup of the manoeuvring test**

#### 4.1 Test results and comparison with simulations

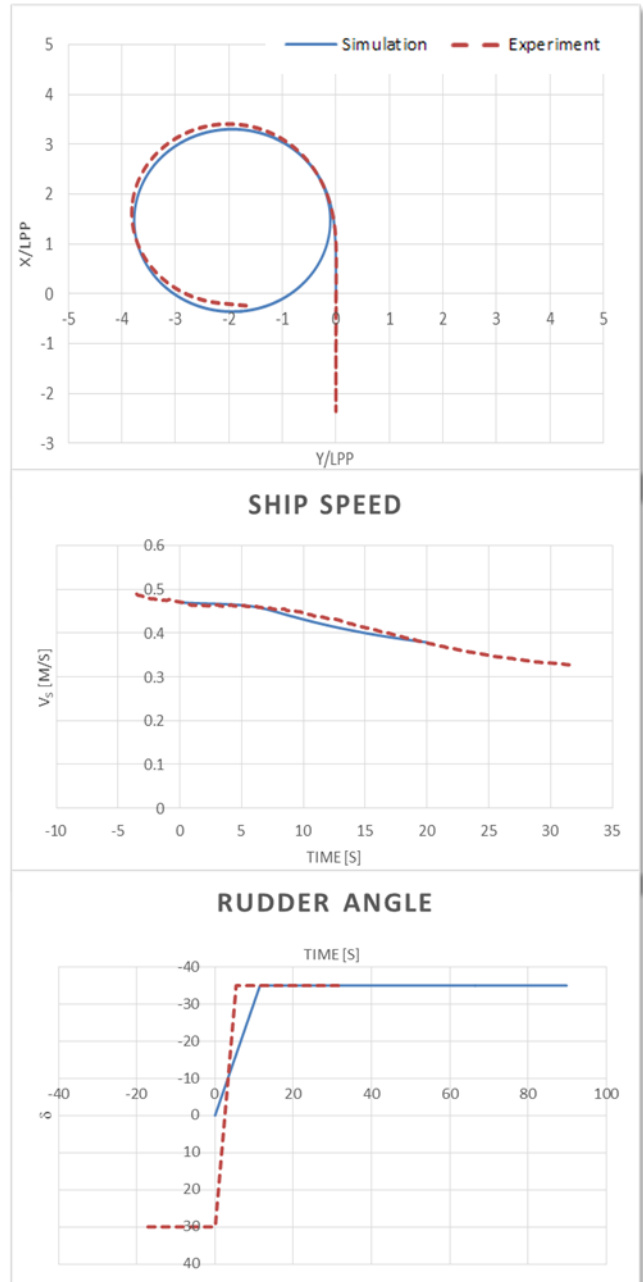
The results from the simulation and the free-running test were compared and they are presented in Figure 15 through Figure 18. The blue line represents the simulated results,

the red dashed line the experimental measurements. Due to the facilities limitations, the Portside rudder blade was fixed on 35deg (Starboard turn) and 30deg (Port turn) whilst the only Starboard blade was remotely controlled. The computation closely agrees with the experimental measurements and captures the trajectory of the vessel during the manoeuvre, the differences stemming mainly from particular experimental limitations that could not be reproduced in the simulation.

Figure 15 and Figure 16 show comparisons between the simulated and experimental results for standard 35deg circle tests, with values agreeing particularly for the Portside manoeuvre. This is likely due to the the strong asymmetries in the velocity gradients on the two rudder blades caused by the action of the propeller.



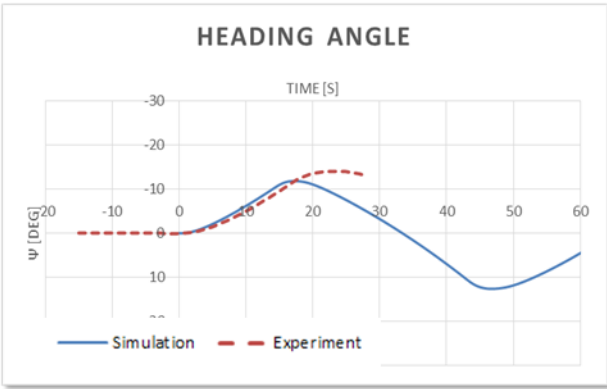
**Figure 15.** Starboard 35deg circle test: ship track (a), rudder angle (b) and ship speed (c) time series



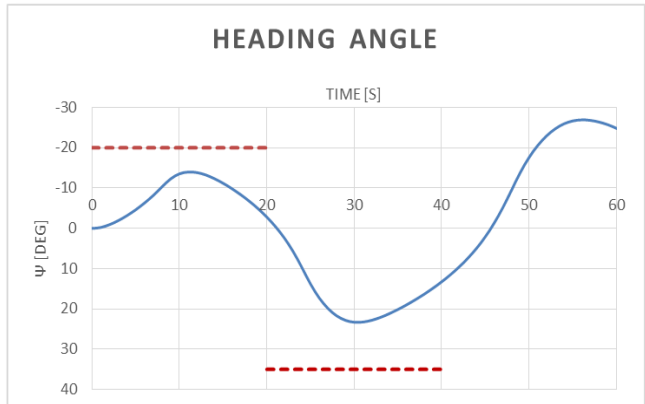
**Figure 16.** Port 35deg circle test ship track (a), rudder angle (b) and ship speed (c) time series

Figure 17 and Figure 18 plot the time series of the heading angle during two representative zig-zag manoeuvres, -10 and -20. In this case, the Port rudder blade was locked on 0 deg angle with the only Starboard rudder blade changing position. Considering such limitation in the experimental facility, the simulations and experimental measurements agree within reason, despite the evident of slower response of the vessel to the change in helm angle during the model testing.

Figure 19 through to Figure 22 present the heading time series for all the conducted zig-zag tests against the IMO requirements, showing a good performance of the Gate Rudder within the standards.



**Figure 17.** Time series of heading angle during Port 10deg zig-zag test



**Figure 20.** Time series of heading angle during Port simulated 10deg zig-zag test

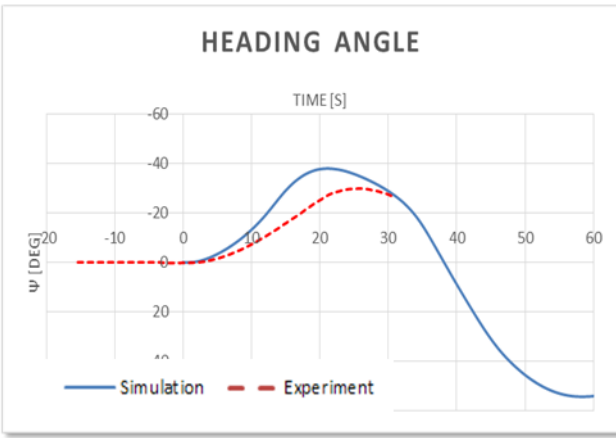


**Figure 18.** Time series of heading angle during Port 20deg zig-zag test

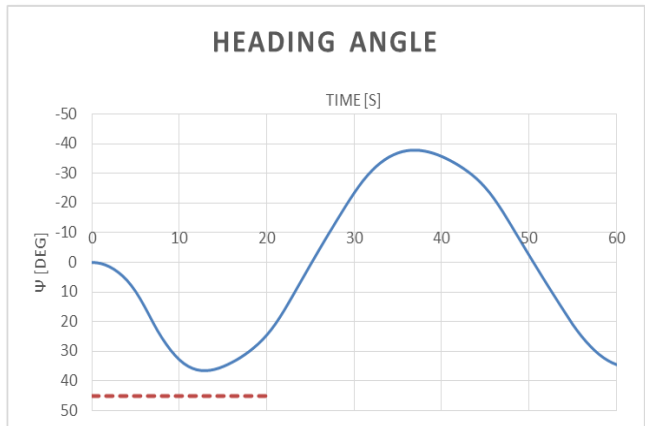


**Figure 21.** Time series of heading angle during Starboard simulated 20deg zig-zag test

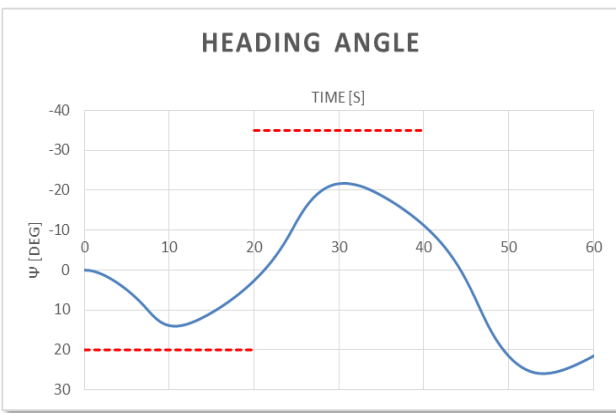


**Figure 19.** Time series of heading angle during Starboard simulated 10deg zig-zag test

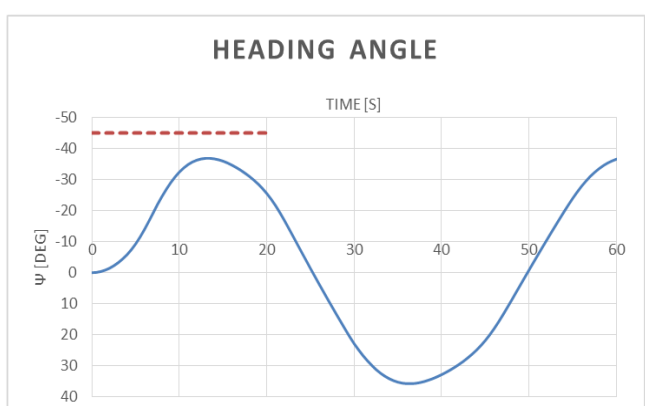


**Figure 22.** Time series of heading angle during Port simulated 20deg zig-zag test

## 5 CONCLUSIONS

This paper attempted to address the manoeuvring performance prediction of the conceptual Gate Rudder. The MMG standard prediction method was reviewed and chosen to conduct further development for the Gate Rudders. Considering the interaction between the hull and the propeller, by using the CFD simulations, a detailed analysis were conducted to achieve the flow velocity around the

Gate Rudders. Based on this analysis, the MMG standard method was tailored in the environment of a simulation program to predict the manoeuvring performance of the Gate Rudder as per the standard ITTC recommended procedures. Finally, Free-running manoeuvring tests were conducted in Kyushu University to validate the program prediction with encouraging results. The project confirmed that the simulation program can simulate fairly well the motions of a vessel equipped with a Gate Rudder and that it can be useful for preliminary manoeuvring performance predictions.

#### **ACKNOWLEDGEMENTS**

The Authors would like to thank Kamome Propellers for the support given to the advancement of the Gate Rudder project. They also thank the members of Kyushu University for conducting the manoeuvrability tests composing an essential part of this work.

#### **REFERENCES**

- Sasaki, N. Atlar, M. and Kuribayashi, S. (2015), 'Advantages of twin rudder system with asymmetric wing section aside propeller', Journal of Marine Science and Technology, DOI 10.1007/s00773-015-0352-z
- Turkmen, S., Carchen, A., Sasaki, N. and Atlar, M. (2015), 'A new energy saving twin rudder system – Gate rudder', SCC 2015, Intl Conference on Shipping in Changing Climate, Glasgow, 24-26 November
- Ogawa, A., T., K. and Kijima, K. (1977) MMG report-I, on the mathematical model of Ship manoeuvring.
- Report of Research committee on standardization of mathematical model for ship maneuvering predictions (2013) (P-29). Japan Society of Naval Architects and Ocean Engineers.
- Yamaguchi, Y., Furukawa, Y., Mutuo, H. and Kijima, K. (2009) 'Study on prediction method of hydrodynamic derivatives for full ships'.
- Yasukawa, H. and Yoshimura, Y. (2015) 'Introduction of MMG standard method for ship maneuvering predictions', Journal of Marine Science and Technology, 20, pp. 37-5

## **Towards Establishing Minimum Installed Power for safe Manoeuvring of Ships in Adverse Environmental Condition**

**Emmanuel Irimagha<sup>1\*</sup>, Richard Birmingham<sup>1</sup>, Michael Woodward<sup>2</sup>, Zhiqiang Hu<sup>1</sup>**

<sup>1</sup>Newcastle University, School of Marine Science and Technology

<sup>2</sup>University of Tasmania

**Abstract:** This research study is to provide tools for establishing a minimum installed power that will allow a ship, in its in-service condition, to meet within a given confidence interval for minimum safe manoeuvring performance at design stage. To achieve the set objective a reasonable minimum manoeuvring performance criteria for extreme adverse environmental conditions will be defined. Some Expressions will be applied to definition extreme adverse environmental conditions including Wind, Ocean current and a waves. There will be the development of a fast-time and efficient Program that can be used to simulate the manoeuvring performance of a given ship when attempting the defined criteria manoeuvres in the identified conditions. The program will be written to include a batch-file algorithm for running repeated scenarios using the derived simulation tool, subject to irregular inputs and capable of outputting a pass-or-fail based on the identified criteria. The output will be evaluated in comparison to known statistical distributions with the aim of identifying a confidence interval for the results.

**Keywords:** Manoeuvring; EEDI, Environment, Minimum Power.

### **INTRODUCTION**

Traditionally, the design and production of ships have been driven by cost, customer requirements, reliability and efficiency while ensuring that environmental regulations are considered. Today, the need for environmental protection is a principal factors and rules are getting more stringent – A Drive towards “Green Ship”. In its 62nd Session, held from 11th to 15th July 2011, the International Maritime Organisation adopted Mandatory Measures to reduce Greenhouse gas (GHG) emission from International Shipping. In this respect, there was an amendment which added a new Chapter 4 to MARPOL Annex VI (Regulation for the Prevention of Air Pollution From Ships) Regulation on Energy efficiency, For Ships to make Mandatory the Energy Efficiency Design Index (EEDI) for New Ships. (see also MGN 462 (M+F))

In respect of the above, there was some Agreed Work Plan in which the Marine Environmental Protection Committee (MEPC) was tasked with amongst others, further improving:

- Draft Guidelines on the method of calculation of the EEDI for new ships;
- Draft interim Guidelines for determining minimum propulsion power and speed to enable safe manoeuvring in adverse weather conditions or sea state.

To clarify this last point, the need to install minimum power is very useful in reducing environmental pollution but this in itself might end up creating other problems. For example,

- A vessel may not be able to meet with the need to manoeuvre in certain possible adverse weather condition normally encountered in service.
- Routes of Vessel might change in the course of its lifetime and vessel may operate in areas with different environmental conditions at some point in their service life.
- As the vessel ages, it requires more power for meeting design speed and engine performance generally reduces.
- reduced speed, then the risk of hull fouling is increased, hence, efficiency quickly drops, leading again to increased emissions for given distance, however, this last point will not be detailed in this research

Hence, there is need to develop some fast and efficient tools for establishing an acceptable risk level for ship in anticipated adverse weather conditions in terms of a minimum installed power; both for design and for the evaluation of existing ships intending to undergo modifications to make them meet with the requirement.

This tool can be applied to substantially narrow down the number of experimental or CFD runs, where greater accuracy is required.

RASHIDUL (2011), investigated the impact of EEDI on ship design and the hydrodynamics. In order to find the impact on ship design and hydrodynamics, parametric analyses of ship is accomplished for different ship types such as Bulk Carrier, Tanker, Container vessel etc. He used the Holtrop & Mennen, 1982 method to predict the main engine power after calculating the resistance and finally calculated EEDI with the current IMO formulation.

Ming-Chung Fang, et al (2005) developed a simplified six degrees of freedom mathematical model encompassing calm water manoeuvring and traditional seakeeping theories to simulate ship turning circle test in regular waves

In his PhD thesis, DG Trodden (2014) proposed a propeller selection method that is most suited to ships which are susceptible to relatively large drift angles and/or relatively high installed power requirements. He suggested that the EEDI in its present implementation discourages design for in-service conditions. The value for the EEDI that the ship attains is verified from sea trials (in calm water). A ship optimised for service conditions will not be optimal when run in trial conditions, and thus may even fail the EEDI requirement, however in real working conditions the design may surpass the EEDI requirement.

During an international conference on the Influence of EEDI on Ship Design organised by the Royal Institute of Naval Architect (RINA – 2014) in London<sup>1</sup>; contributors, Ryuji Miyaki Etal, Nippon Kaiji Kyokai (Class NK) Japan, presented a paper titled “Verification Methods for Speed Trial and Minimum Propulsion Power for EEDI”. In the paper, Issues bordering on Amendments to Marpol Annex VI, which has made Energy Efficiency Design Index (EEDI) and Ship Energy Efficiency Management Plan (SEEMP) compulsory were discussed and it was noted that ClassNK has developed a software called “PrimeShip-Green/MinPower” used for the assessment of minimum propulsion power. The verification for methods of speed trials and minimum propulsion power for EEDI, and the software developed by ClassNK were introduced. In same conference, P. P. Dallinga Et al in their paper “Impact of Power Reduction on Sustained Speed and Reliability”, contributed their view on the impact of the EEDI power reduction on the operational performance of a tanker. Based on an estimate of the evolution in hull form, the resistance and propulsion characteristics, the related increase in added resistance and the impact of the increased speed loss on the trip duration and reliability were quantified on a typical European coastal route.

Edward Lewis (1990), The principles of Naval Architecture Vol. III, chapter IX, gave an in-depth explanation of controllability of Ships; derived mathematical expressions that define the criterion for stability and the practical conditions that will affect the said criteria.

L. Letki and DA Hudson (2005) in their work, presented the principle of unified mathematical model and the principle of the time simulation and its implementation.

Zafer Ayaz, obtained an improved numerical model for capsizing involving all degrees of freedom.

This work will produce a program that can be used to establish a safe lower limit for the manoeuvring performance in adverse environmental conditions that the ship might reasonably encounter in operation, during its design stage and also when it is required for a ship to be modified to improve its efficiency.

## Mathematical Model

A modular approach does describe the individual elements, such as hull, rudder, propeller etc., as separate modules which will be incorporated within the overall system. The forces and moments contained within each module will be constructed with reference to the particular physical processes involved. This thesis will adopt the modular approach as this will better fit into real life situation.

The effects of these forces and moments on a moving ship are to be determined in six degrees of freedom motion due to the fact that environmental disturbances does relatively increase effect of the other three degrees of freedom (roll, pitch and heave which are traditionally assumed as negligible in manoeuvring studies. For the starting part of this work, we will consider four degrees-of-freedom; i.e. Surge (X); Sway(Y) and Yaw (N) and roll as coupled since the experimental data available for ease of verification. Once the program is up and running, then the remaining two degrees of freedom will be inputted using Charts and formulae from recognised Authors.

It is worthy to note that the essential consideration that will be analysed in details for purpose of making decision for this work will be on the Forward and Roll motion effects.

In a body-fixed coordinates system with the origin lying in the mid-ship point assuming the ship to be symmetrical about its longitudinal centre-plane, implying that  $y_G = 0$ , i.e. the centre of gravity has coordinates  $(x_G, 0, z_G)$ , and  $I_{xz}$   $I_{yz}$ ,  $I_{xy}$  i.e. Products of inertia about the body axis system are ignored; the six degrees of freedom equation motion, as is in Fossen, is

$$\text{Surge, } X = m[(\dot{u} - vr + wq) - x_G(q^2 + r^2) + z_G(pr - \dot{q})]$$

$$\text{Sway, } Y = m[(\dot{v} - wp + ur) + z_G(qr - \dot{p}) + x_G(qp - \dot{r})]$$

$$\text{Heave, } Z = m[(\dot{w} - uq + vp) - z_G(p^2 + q^2) + x_G(rp - \dot{q})]$$

$$\text{Roll, } K = I_x \dot{p} + (I_z - I_y)qr + m\{-z_G(\dot{v} - wp + ur)\}$$

$$\text{Pitch, } M = I_y \dot{q} + (I_x - I_z)pq + m\{z_G(\dot{u} - vr + wq) - x_G(\dot{w} - uq + vp)\}$$

$$\text{Yaw, } N = I_z \dot{r} + (I_y - I_x)pq + m\{x_G(\dot{v} - wp + ur)\} \quad (1)$$

Where  $x_G$ ,  $y_G$ ,  $z_G$  are Coordinates of the centre of gravity in the body axis system,

$u$ ,  $v$ ,  $w$ , are surge, sway and heave velocity components of the velocity of the chosen ship origin O in the horizontal longitudinal and transversal directions x, y and z of the coordinate system, respectively,

$p$ ,  $q$  and  $r$  are the roll, pitch and yaw rates.

The letters with ‘dot’ represents the rate of change with respect to time.  $I_x$ ,  $I_y$ ,  $I_z$  are Moments of inertia about the body axis system

The forces and moments acting on a Ship during manoeuvring in adverse weather are:

- i. Inertial reaction forces caused by Ship's acceleration,
- ii. Hydrodynamic forces acting on the hull and appendages due to ship velocity, acceleration, propeller rotation and rudder deflection
- iii. Environmental forces due to wind, waves and currents
- iv. External forces from Tugs, Thrusters etc.
- v. Shallow water effects
- vi. Bank effects
- vii. Stabiliser forces.

The Forces to be discussed and applied in details in this work are those that relate to the first three items.

$$X = X_H + X_P + X_R + X_E$$

$$Y = Y_H + Y_P + Y_R + Y_E$$

$$Z = Z_H + N_E$$

(2)

$$K = K_H + K_P + K_R + K_E$$

$$M = M_H + M_E$$

$$N = N_H + N_P + N_R + N_E$$

Where X, Y, Z, K, M, and N represents the Surge, Sway, Heave, Roll, Pitch and Yaw F respectively, and Subscripts H, P, R and E are used to represent Hydrodynamic, Propeller, Rudder and Environmental (Wind Wave, Ocean Current) effects

### Hydrodynamic forces

Hydrodynamic forces are those that arise from the hull velocity through the water, which are Damping Forces, and those due to the acceleration of the hull through water (Added mass Forces).

Considering the effect steering and roll motion of a container ship, the force and moments above, including those caused by the action of the Rudder was obtained using known non-dimensional hydrodynamic derivatives, the equations was given by SON and NOMOTO (1981) as follows:

$$X = X_{uu}u^2 + (1 - t)X_{vr}vr + X_{vv}v^2 + X_{rr}r^2 + X_{\phi\phi}\phi^2 + x_p + X(\delta) + c_{RX}F_N \sin \delta + (m + m_y)vr$$

$$Y = Y_vv + Y_rr + Y_pp + Y_{\phi\phi}\phi + Y_{vvv}v^3 + Y_{rrr}r^3 + Y_{vvr}v^2r + Y_{vrr}vr^2 + Y_{vv\phi}v^2\phi + Y_{v\phi\phi}v\phi^2 + Y_{rr\phi}r^2\phi + (1 + a_H)F_N \cos \delta - (m + m_x)ur$$

$$\begin{aligned} K &= K_vv + K_{vvv}v^3 + K_{vvr}v^2 + K_rr + K_{rrr}r^3 + K_{\phi\phi}\phi^2 \\ &\quad + K_{\phi\dot{\phi}} + K_{\dot{\phi}\phi} + K_{vv\phi}v^2\phi + K_{v\phi\phi}v\phi^2 \\ &\quad + K_{r\phi\phi}r\phi^2 - (1 + a_H)z_RF_N \cos \delta \\ &\quad + m_xI_rur - W(GM)\phi \end{aligned}$$

$$\begin{aligned} N &= N_vv + N_rr + N_pp + N_{\phi\phi} + N_{vvv}v^3 + N_{rrr}r^3 \\ &\quad + N_{vvr}v^2r + N_{vrr}vr^2 + N_{vv\phi}v^2\phi \\ &\quad + N_{v\phi\phi}v\phi^2 + N_{rr\phi}r^2\phi + N_{r\phi\phi}r\phi^2 \\ &\quad + (x_R + a_Hx_H)F_N \cos \delta \end{aligned}$$

(3)

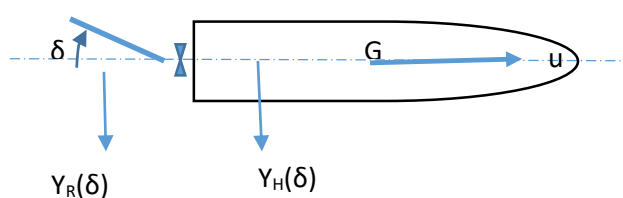
where X, Y, Z, are Hydrodynamic force components along body axes, and K, M, N, Hydrodynamic moment components along body axes,  $Y_v, Y_{vv}, \dots N_v, N_{rr}, \dots$ etc are hydrodynamic derivatives.  $\psi$  is the yaw angle: bow to starboard positive,  $\phi$  is roll angle: starboard down positive  $a_H$  is Rudder to hull interaction coefficient,  $F_N$  Normal force action on the rudder,  $z_R$  is the z - coordinate of point on which rudder force,  $Y_\delta$  acts,  $x_R$  is the x - coordinate of point on which rudder force  $Y_\delta$  acts,  $x_H$  is the x - coordinate of point on which normal force FN acts

$m_j$  and  $m_i$  are the mass and individual added masses in the jth component of the ship. The added masses can be derived by a combination of methods of Strip Theory and Lewis Conformal Mapping as in *Do & Tran (2016)*. The hydrodynamic coefficients can be estimated at design stage with Ship's dimensions. However, for the purpose of this research, one used derivative obtained from experiments based on an existing ship that has been subjected to extensive research by several Scholars with parameters in *SON and NOMOTO (1981)*. This was done for ease of verification of functionality of program and results.

Edward Lewis (1990) gives equations for the rate of change of surge, sway and Yaw velocities these are used to calculate the surge velocity u, sway velocity by Using Euler Integration in time steps. It is also used to find the roll rates p, roll angle  $\phi$ , heading angle  $\psi$ , position in x direction, position in y direction, rudder deflection angle  $\delta$ , and n (the actual shaft velocity) by a specified time step and then added to the initial and subsequently, previous value of the variable.

### Rudder

The rudder forces and moments are calculated as follows:



$$X_R = -(1 - t_R)F_N \sin \delta$$

$$\begin{aligned}
Y_R &= -(1 + a_H) F_N \cos \delta \cdot \cos \phi \\
K_R &= z_{HE} (1 + a_H) F_N \cos \delta \\
N_R &= -(x_R + a_H x_H) F_N \cos \delta \cdot \cos \phi
\end{aligned} \tag{4}$$

The Rudder normal force is given by

$$F_N = \left( \frac{6.13\Lambda}{\Lambda+2.25} \right) \left( \frac{A_R}{L^2} \right) V_R^2 \sin(\alpha_R) \tag{5}$$

Where  $V_R$  is the Effective rudder inflow velocity,  $\alpha_R$ , the Effective rudder inflow angle,  $\delta$ , the Rudder angle in radians,  $V$  Initial velocity of ship,  $\rho$  Mass density of sea water,  $L$  is the Ship length between perpendiculars (LBP),  $\Lambda$  is the Rudder aspect ratio,  $A_R$ , the Rudder area, while  $u_R$  and  $v_R$  are components of rudder effective inflow velocity

### Propeller Force and the Shaft Speed Feedback Control

The total longitudinal force generated by the propellers is given by

$$X_p = (1 - t) \sum(T_p) \tag{6}$$

$$T_p = \rho * D_p^4 * K_T * n^2 \tag{7}$$

$$\text{And } J = u \cos \beta (1 - w_p) / (n \cdot D_p) \tag{8}$$

and using a Propeller characteristics expression from Kupier 1992,

$$K_T = 0.294 - 0.247J - 0.227J^2 + 0.0693J^3 \tag{9}$$

Ferial El-Hawary (2001) expressed the Propeller thrust as a function of propeller power and Torque

$$T_a = \text{sgn}(n) \frac{\rho^{\frac{1}{3}} D^{\frac{2}{3}} K_T h_T (1-t_d)}{(2\pi K_Q h_Q)^{\frac{2}{3}}} \cdot P_a^{2/3} \tag{10}$$

Given the specified command  $T_{ref}$ , the corresponding reference (commanded) speed in the propeller,  $n_{ref}$ , is found by the function

$$n_{ref} = g_{n0}(T_{ref}) = \text{sgn}(T_{ref}) \sqrt{\left| \frac{T_{ref}}{\rho D^4 K_{T0}} \right|} \tag{11}$$

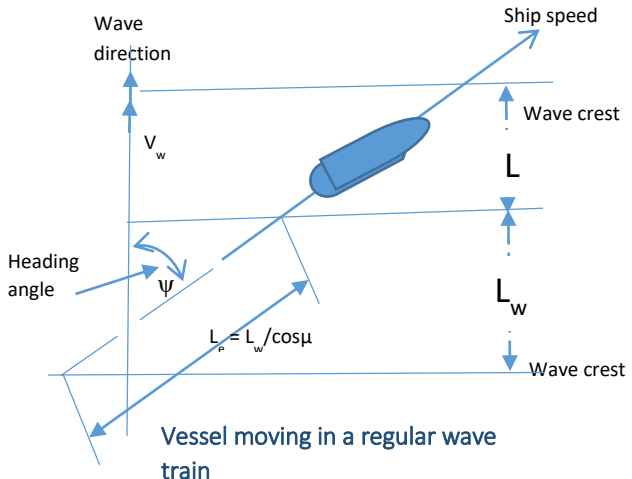
Where  $K_T$  is the Thrust coefficient,  $J$  is Advance coefficient,  $n$  is Number of propeller revolutions per second,  $D$  is Propeller diameter,  $w_p$  is the Effective propeller wake fraction.

### Wave Forces

In the implementation of the wave force, Froude Krylov Force and Diffraction Forces are to be taken into consideration. The Froude Krylov force equations are used on the assumption that the wave shape is not destroyed with the existence of the ship hull. For the derivation of the wave forces one applied some formulae as in Motorki Araki (2012), for the Froud Krylov Force and the Diffraction Force.

For this work, the wave encounter angle is assumed to be same as the wind encounter angle (and fixed to the initial wind angle).

The wave height is kept constant at the initial stage of developing the program and then there will be some modification to make the wave irregular



$$\text{Rameswar (1978) shows that the frequency of encounter } \omega_e = \omega_w \left( 1 - \frac{\omega_w V}{g} \cos \psi \right) \tag{12}$$

Where  $\omega_w$  is the wave frequency and  $\psi$  is the Ship's heading angle,  $L_w$  is the wavelength,  $V_w$  is the wave velocity.

Motoki Araki (Dec 2012), Gave the following equations for the Froude-Krylov and the Diffraction Forces:

$$\begin{aligned}
X_{FK} &= -\rho g \zeta_w k \cos \psi \cdot \sqrt{F_c^2 + F_s^2} + \sin(k \xi_G + \varepsilon_F) \\
Y_{FK} &= \rho g \zeta_w k \sin \psi \cdot \sqrt{K_c^2 + K_s^2} + \sin(k \xi_G + \varepsilon_F) \\
K_{FK} &= \rho g \zeta_w k \sin \psi \cdot \sqrt{F_c^2 + F_s^2} + \sin(k \xi_G + \varepsilon_F) \\
N_{FK} &= \rho g \zeta_w k \sin \psi \cdot \sqrt{N_c^2 + N_s^2} + \sin(k \xi_G + \varepsilon_F)
\end{aligned} \tag{13}$$

And

$$\varepsilon_F = \tan^{-1} \left( \frac{F_s^2}{F_c^2} \right), \tag{14a}$$

$$\varepsilon_k = \tan^{-1} \left( \frac{K_s^2}{F_c^2} \right), \tag{14b}$$

$$\varepsilon_N = -\tan^{-1} \left( \frac{N_s^2}{N_c^2} \right) \tag{14c}$$

Where  $X_{FK}$  and  $Y_{FK}$  are Froude-Krylov forces in surge and sway respectively,  $K_{FK}$  and  $N_{FK}$  are Froude-Krylov moments in roll and yaw respectively,  $\zeta_w$  is the wave amplitude,  $k$  is the wave number,  $\psi$  is the Ship's course,  $F_c$ ,  $F_s$ ,  $K_c$ ,  $K_s$ ,  $N_c$ ,  $N_s$  are functions defined in Motoki Araki (Dec 2012).

In the implementation of the Diffraction Force, the ship is assumed to be generally slender, thus the surge component was neglected and approximate formulae for estimating the diffraction forces of the other modes are applied and expressed as:

$$\begin{aligned}
Y_W^{Diff}(u, \xi_G, /, \lambda, \psi) &= \\
\zeta_w \omega \omega_e \sin \psi \int_{AE}^{FE} \rho S_y(x) e^{-\frac{kd(x)}{2}} \sin k(\xi_G + x \cos \psi) dx. \\
K_W^{Diff}(u, \xi_G, /, \lambda, \psi) &= \\
-\zeta_w \omega \omega_e \sin \psi \int_{AE}^{FE} \rho S_y(x) e^{-\frac{kd(x)}{2}} \sin k(\xi_G + x \cos \psi) dx. \\
N_W^{Diff}(u, \xi_G, /, \lambda, \psi) &= \\
\zeta_w \omega \omega_e \sin \psi \int_{AE}^{FE} \rho S_y(x) e^{-\frac{kd(x)}{2}} x \sin k(\xi_G + x \cos \psi) dx. \\
(15)
\end{aligned}$$

Details can be seen in Motoki Araki (Dec 2012).

Simulating the wave force is a major challenge in this work as most available expressions including the one represented above deal with regular waves and a lot others are programmed into CFD based software. The expression above or other suitable one will be modified using some mathematical function in the program to make it such that the wave amplitude and the frequency of encounter will alter as a function of time in a manner that brings it closer to the form of irregular wave as possible.

So far, work on Wave force computation is still being put together. Verification of Wave load will be done using WASIM software.

### Wind Force

The force due to the wind is assumed to be unidirectional. And for the purpose of this research, the vessel would be simulated to turn into head wind. The expressions below are applied to obtain the Wind force

$$\begin{aligned}
F_x &= C_x \times q A_T \cos \gamma \\
F_y &= C_y \times q A_L \sin \gamma \\
N &= C_N \times q L A_L \sin \gamma \\
K &= C_K \times q A_L H_L \sin \gamma
\end{aligned}
(16)$$

Where  $H_L = A_L/L$

$A_T$  is Transverse projected area,  $A_L$  is Longitudinal projected area

$$V_h = v_{ref} \left( \frac{h}{h_{ref}} \right)^{1/n} \quad (17)$$

$V_h$  = wind velocity at elevation  $h$  above the mean sea level [m/s];  $v_{ref}$  is wind velocity at the reference height;  $h_{ref}$  is reference height (10 m or 33ft in API standard);  $1/n$  is exponent of the velocity profile

According to Turk and Prpić-Oršić (2009), the instantaneous wind pressure is given by

$$q = \frac{1}{2} \rho |v_z + u - \dot{x}| (v_{mw} + \dot{x}) \quad (18)$$

Where  $u$  is the wind velocity,  $v_{mw}$  the mean velocity, and  $\dot{x}$  the instantaneous velocity of the structural member.

[Blenderman \(1994\)](#), provides coefficients of lateral and longitudinal resistance, cross-force and rolling moment

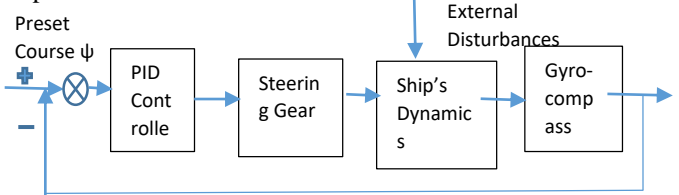
### Simulation and Controls

A fast time Simulation model code will be written in a compiler based software such as Fortran. This will incorporate the propeller thrust force and a rudder control algorithm which will tend to correct deviations and keep the vessel on course.

SOLAS II-1/29.3 requires that The main Steering Gear be capable of putting the rudder over from  $35^\circ$  on one side to  $35^\circ$  on the other side with the ship at its deepest seagoing draught and running ahead at maximum ahead service speed and under the same conditions, from  $35^\circ$  on either side to  $30^\circ$  on the other side in not more than 28 s; for all ships operated by power unit.

To this end the minimum rate of turn ( $\dot{\delta}$ ) for the rudder when using the steering gear should be  $65^\circ/28s = 2.321^\circ/s$ . However, for the purpose of this work a rate of  $2.5^\circ/sec$  shall be applied.

The Automatic control of a Ship's system can be represented as follows:



The expression of algorithm of a PID controller in continuous time is given by

$$u(t) = K_p \left[ e(t) + \frac{1}{T_i} \int_0^t e(t) dt + T_d \frac{de(t)}{dt} \right] \quad (19)$$

Where  $K_p$  is proportional factor;  $T_i$  is integral time constant;  $T_d$  is the derivative time constant

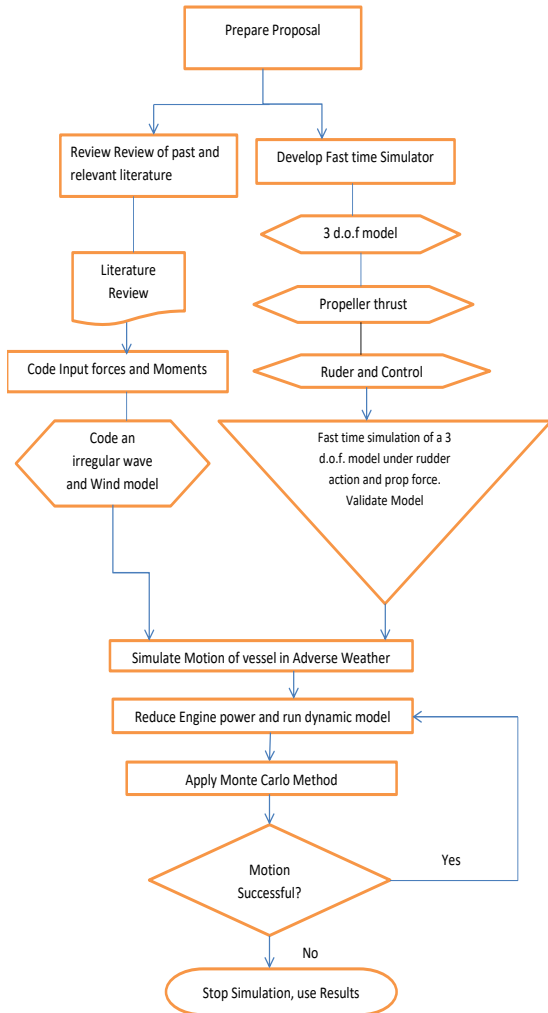
$$T_E \dot{\delta} = \delta_E - \delta \quad (20)$$

$T_E$  is the time constant of the steering gear and  $\delta_E$  is the command rudder angle.

The program will be such that the vessel, which is assumed to be a rigid body can be steered. Start the Simulation with the Ship headed to the sea into head wind and waves. The simulation will be looped to run through a specified number of times (say a thousand times) to ensure repeatable success.

Then reduce the installed power and the above process repeated, until a point where the simulation stops under some defined criteria, i.e. when with a reduced installed power, the Vessel slows down substantially or not able to turn into the wave. Results will be drawn from this outcome and appropriate recommendations made.

Below is a flow Chart showing the plan of activities:



## Discussion

The simulation of a container ship manoeuvring in calm water was done using Microsoft Excel, this was used to execute a turning circle manoeuvre, and however, the spreadsheet gets complicated as one adds the environmental forces and the control algorithms. Hence, the work so far done is being written in FORTRAN. However, it is worthwhile to note that FORTRAN program does not have its own plotting utility hence an open source program called GNU Plot will be applied for plotting the motions.

## Conclusion

The expected outcome, relevant equations, method of application and the overall plan have been explained. For this research, a Ship with known experimental data is being used but there is need for future work to be done especially in the area of improving on the empirical formulae for manoeuvring derivatives using Ship's basic dimensions so that this program will be less tasking to use.

At a minimum, it is necessary to establish a safe lower limit for the manoeuvring performance in adverse environmental conditions that the ship might reasonably

encounter. This would then enable a prospective ship buyer or a regulatory authority to readily make a quick decision. Nevertheless, when establishing the safe lower limit for installed power, a realistic assessment of the in-service performance should be included, based on realistic estimations of hull condition.

## REFERENCES

- Anton Turk and Jasna Prpić-Oršić (2009): Estimation of Extreme Wind Loads on Marine Objects
- David George Trodden 2014, Optimal Propeller Selection when Accounting for a Ship's Manoeuvring Response due to Environmental Loading
- Do Thanh Sen & Tran Canh Vinh (2016): *Determination of Added Mass and Inertia Moment of Marine Ships Moving in 6 Degrees of Freedom*
- Edward V. Lewis (1990). Principles of Naval Architecture; Published by The Society of Naval Architects and Marine Engineers.
- Ferial El-Hawary (2001): The Ocean Engineering Handbook Ferial El-Hawary; December 28, 2000 by CRC Press
- Fossen, Thor I., (1994): Guidance and control of ocean vehicles
- Holtrop, J. and Mennen, G.G.J. (1982): An Approximate Power Prediction Method. International Shipbuilding Progress, 29(335), 166–170.
- KUIPER, G. 1992. The Wageningen propeller series, MARIN Publication 92-001, Wageningen.
- Kyoung-Ho SON", and Kensaku NOMOTO (J.S.N.A, Japan, Vol .150, Dec. 198I): On the Coupled Motion of Steering and Rolling Motion of a High-speed Container Ship.
- L. Letki and DA Hudson (2005): Simulation of Ship Manoeuvring Performance in Calm Water and Waves.
- Maritime and Coastguard Agency MGN 462 (M+F) Pollution - Entry into Force of the Energy Efficiency Design Index. 2013
- Ming-Chung Fang, et al; A Nonlinear Mathematical Model for Ships Turning Circle Simulation in Waves (Journal of Ship Research, Vol. 49, No. 2, June 2005, pp. 69-79)
- Motoki Araki, (Dec 2012): Ship Manoeuvring Mathematical model Using System Identification Technique with Experimental and CFD Free Running Trials in Calm Water and Astern Waves.
- Note by the International Maritime Organization to the thirty-fifth session of the Subsidiary Body for Scientific and Technical Advice (SBSTA 35), Nov 2011 (<http://www.imo.org/en/OurWork/Environment/PollutionPrevention/AirPollution/Documents/COP%202017/Submiss>

ions/Final%20SBSTA%20EEDI%20SEEMP%20COP17.pdf).

Rameswar Bhattacharyya (1978), Dynamics of Marine Vehicles Royal Institute of Naval Architect (RINA) Conference in London, 24/25th September 2014 - (Ryuji Miyake, Takeshi Shimada, M. Abdul Rahim, A. Asok Kumar, Nippon Kaiji Kyokai (ClassNK), Japan) Influence of EEDI on Ship Design: Verification Methods for Speed Trial and Minimum Propulsion Power For EEDI. R. P. Dallinga, R. Grin – (MARIN, G.v.d.Bles, J.J.Nieuwenhuis – CONOSHIP) : Impact of Power Reduction on Sustained Speed and Reliability. (<http://www.rina.org.uk/hres/EEDI%20brochure%20WEB.pdf>)

S. M. RASHIDUL HASAN, 2011. – Impact of EEDI on Ship Design and Hydrodynamics (A Study of the Energy Efficiency Design Index)

W. Blödermann: Wind Loading of Ships – Collected Data from Wind Tunnel Tests in Uniform Flow, Institut für Schiffbau der Universität Hamburg, Bericht No 574, pp.

53 (1996).

Zafer Ayaz (2003). Manoeuvring Behaviour of Ships in Extreme astern Seas.

D Vassalos , N Umeda, M Hamamoto and M Tsangaris – THE ROYAL INSTITUTION OF NAVAL ARCHITECTS (1999), Modelling Extreme Ship Behaviour In Astern Seas ([http://legacy.sname.org/committees/planninggroup/astern\\_seas.pdf](http://legacy.sname.org/committees/planninggroup/astern_seas.pdf))

Edward M. Lewandowski: The Dynamics of Marine Craft, Manoeuvring and Seakeeping (Advanced Series on Ocean Engineering, Volume 22).

Gerritsma, J “Experimental Determination of Damping, Added Mass and Added Mass Moment of Inertia of a Ship Model” International Shipbuilding Progress 1957.

H. Yasukawa ; Y. Yoshimura, Introduction of MMG standard method for ship maneuvering predictions (Journal of Marine Science and Technology, (2015)20:37-52.

International Towing Tank Conference - Guideline on Use of RANS Tools for Manoeuvring Prediction (<http://ittc.sname.org/CD%202011/pdf%20Procedures%202011/7.5-03-04-01.pdf>)

J.M.J. Journée : User Manual of SEAWAY Release 4.19 (12-02-2001) Report 1212a February 2001

Kotas J. Spyrou, I. Tigas, and A. Chatzis (Journal of Research. May 2007): Dynamics of a ship steering in wind revisited

Masaru Tsujimoto, Kazuya Shibata, Mariko Kuroda, Ken Takagi: A practical correction method for Added resistance in waves

Masayoshi HIRANO (J.S.N.A. Japan Vol.147, June 1980): A Practical Calculation Method of Ship Manoeuvring at Initial Design Stage

Michael Metcalf and John Reid: Fortran 90/95 explained second edition

Michael Woodward: Lecture Notes on Manoeuvring 2014.

Xiao Chen, 2013: Real-time Physics Based Simulation for 3D Computer Graphics. PhD thesis at Georgia State University.

Yang Xingyan, Chen Min: Discussion on Calculation Method of windage Area of (Ships <http://www.doc88.com/p-2028118000929.html>).

*(Intentionally left blank)*

## On the State-of-Art for Hydrodynamic Assessment of Offshore Heavy Lift & Installation Vessels DP Systems

Zafer Ayaz<sup>1\*</sup>,

<sup>1</sup>Saipem Ltd., London, United Kingdom

**Abstract:** This paper discusses the current industry-practice on the hydrodynamic analysis of offshore heavy lift and installation vessels DP systems. The review of the analytical models, introduction of advanced numerical models i.e. CFD, and model tests/field experiences from the literature are added. The conclusions from a recent JIP focusing on improving the understanding of thruster interactions for various types of offshore vessels and developing advance allocation algorithms for the DP systems are also summarized.

**Keywords:** Offshore heavy lift vessels, hydrodynamic assessment, DP Systems.

### 1 INTRODUCTION

The Dynamic Positioning (DP) systems for offshore vessels have been evolved considerably since their introduction in early 70s as the operational activities move to harsher environments and ultra-large offshore vessels being constructed to increase the operational capacity to meet growing energy demand.

Dynamic positioned vessel (or DP Vessel) is described as a unit or vessel which automatically maintains its position (fixed location or predetermined track) by means of thruster force (IMCA 2003). This definition includes remaining at a fixed location, precision manoeuvring, tracking and other specialist positioning abilities. The shift towards the DP vessels from traditional vessels with passive mooring systems started due to the increased activities in deeper waters (i.e. greater than 300m) which prohibits the use of the conventional mooring systems (Nienhuis 1983), (Terwesga et al 2001). The flexibility and mobility of DP systems led to its exploitation of marginal oil fields, with added advantage that assistance of anchor handling vessels is no longer necessary. There is also additional advantage of using the systems with cable or pipelay vessel with dynamic tracking (DT) systems. Furthermore, the potential risk of damaging subsea facilities or pipelines by use of the anchors can be avoided as well. While the DP vessel was initially the preferred option for the deep water applications, thanks to the experience gained over the years and more sophisticated control systems, it is also a preferred cost-effective alternative to moored vessels in shallow water operations i.e. dredging (Ayaz & Macdonald 2011).

The complete installation necessary for dynamically positioning a vessel comprises following subsystems; i) Power system ii) Thruster system and iii) DP control system. While the power system is an important element of the DP system, this paper exploits the current practices and state-of-art for modelling and operating the latter two subsystems.

### 2 THE DP SYSTEM

A schematic diagram of a modern DP system is shown in Figure 1.

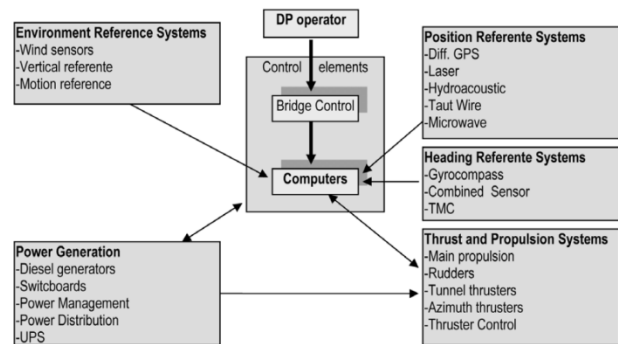


**Figure 1. Schematic Diagram of a DP System (IMCA 2003)**

The general arrangement of a DP system on an offshore vessel is shown in Figure 2.

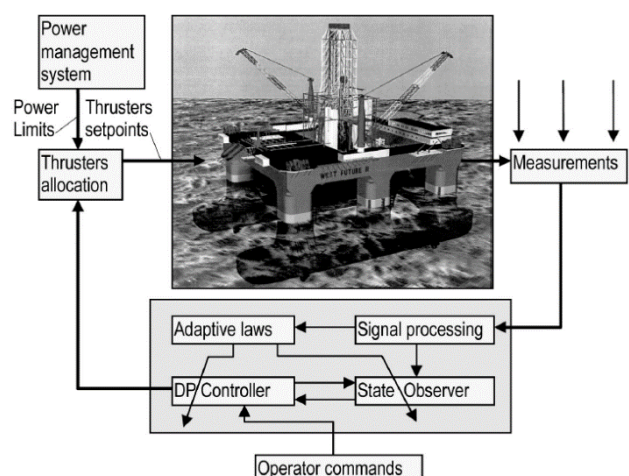


**Figure 2. The general arrangement of a DP system (Chas & Ferreiro 2008)**

Any vessel can move in six degrees of freedom; three rotations (roll, pitch and yaw) and three translations

\* Corresponding author e-mail: zafer.ayaz@saipem.com

(surge, sway and heave). Dynamic positioning conventionally is concerned with the automatic control of surge, sway and yaw. Surge and sway are related to the position of the vessel, whilst yaw is defined by the vessel heading.

Every vessel is subjected to forces from wind, waves and tidal movements (currents) as well as forces generated from the propulsion system and other external elements i.e. cranes, lifted cargo, pipelay residue tension etc. The movement of the vessel changes of position and heading is the result to these forces. Position is measured by position reference systems, while heading information is provided from gyrocompasses. The vessel must be able to control position and heading within acceptable limits facing the external forces. If these forces measured directly, the control computers (Figure 1) can apply immediate compensation. The DP control system calculates the offsets between the measured values of position and heading and the required values, and after that it calculates the forces that the thrusters must generate in order to reduce the errors to minimum (ideally zero). This mechanism is illustrated for a DP pipelay installation vessel as given in Figure 3.

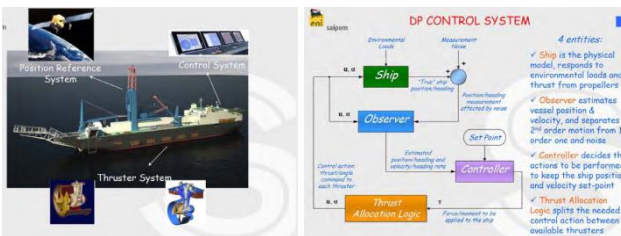


**Figure 3. DP operating philosophy for pipelay installation vessel (courtesy of Saipem Ltd.)**

The operating principle of a modern state-of-art DP system, therefore, have two important components; handling of environmental and external forces in relation to vessel motions/position and determining thruster forces in relation to a control system. This is also illustrated in Figure 4.

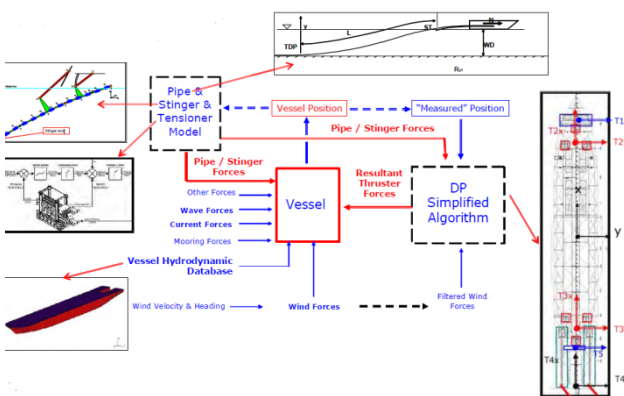


**Figure 4. A modelling of DP system on pipelay installation vessel (courtesy of Saipem Ltd.)**

The modelling and estimation of the environmental and operation components are described in the following sections.

### 3 MODELLING OF THE DP SYSTEM

A mathematical model of a DP system (with corresponding axis system) is shown in Figure 5.

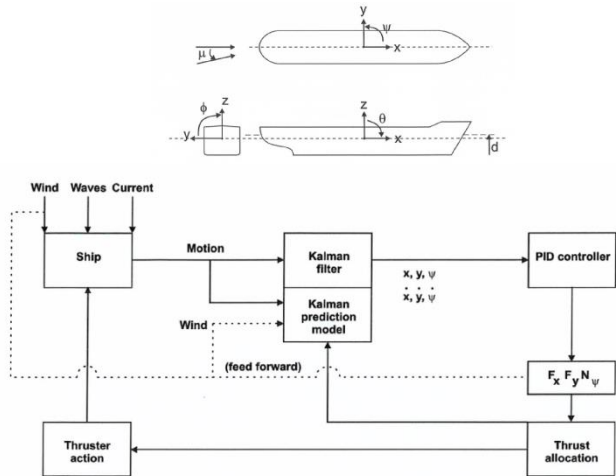


**Figure 5. DP mathematical model**

The control loop shown in Figure 5 (and also illustrated in Figures 1 to 4) is the main part of the DP system. The principal features are the algorithms that compute the position correction measures on the basis of the measured reference point errors.

#### 3.1 Mathematical Model of A DP Ship

The motions of a ship can be described by a set of differential equations. For DP Control, only the low frequency (drift) motions in horizontal plane are considered. The excitation of motions is caused by second order effects, wind and current, while the low frequency motions themselves induce fluid reaction forces.

The mathematical model of behaviour of a ship under the influence of a wind, wave drift and current is given by (MARIN 2013). Incorporation of thruster action leads to the following equations of motion:

$$M(\ddot{x}^{LF} + D(\dot{x}^{LF})\dot{x}^{LF}) = X_{HD} + \sum_i X_{EXT,i} \quad (1)$$

Where  $x^{LF}$  = low frequency motions of surge, sway and yaw;  $X_{HD}$  = second order hydrodynamic reaction forces; and  $X_{EXT}$  = other low frequency varying exciting forces (i);  $M$  = mass/inertia matrix of surge, sway and yaw;  $A$  = coupled low frequency added mass matrix of surge, sway and yaw included in  $M$ ;  $D$  = damping matrix due to coupling.

The mathematical model of the ship motions in horizontal plane is used in the Kalman filter. The filtering of position measurements contain noise and wave frequency modulations upon the low frequency drift motions.

In the state-of-art modelling systems (See Section 3.3), Kalman filters are now extended to adaptive control system in which the control updates are included in the recursion scheme. The adaptive control systems can be linear or non-linear by applying quadratic cost functions for the adaptation of the control coefficients and they assume a typically Gaussian process.

In the Kalman filter, the mathematical model of a ship motions is used to make a prediction of ship position on the next time step. The prediction is compared with the forthcoming measurement, and the weighted result is used to steer the thrusters. Discrepancies between the measurement and the prediction are used to update the parameters in the mathematical model and improve the next prediction. Since the prediction and update steps can be carried out in one sample cycle of typically less than 1 second prototype time, the phase lag problem is quite significantly reduced.

For an extended Kalman filter, most widely used in the current DP systems, the non-linear parts are linearised, typically using Taylor-series expansion, and the coefficients thereof are included in the parameter update step of the process. The low frequency linearised state space model for extended Kalman filter is:

$$\begin{aligned} x_{k+1} &= A_k x_k + \Gamma_k + FW_k \\ y_k &= Cx_k + V_k \end{aligned} \quad (2)$$

Where the first line describes the prediction of the low frequency position and heading and their derivatives  $x$  on time step  $k+1$  from the status on time step  $k$  and  $\Gamma_k$ ; the second line represents the position measurements at time step  $k$ . In both equations the noise in the process is incorporated;  $W_k$  = noise due to inaccuracy in the mathematical model ;  $V_k$  = noise in the measurement. Both noise functions are assumed to have a Gaussian distribution with zero mean; and  $F$  and  $C$  = matrices representing the transfer of  $W$  and  $V$  to the dimensions of the vectors  $x$  and  $y$ , respectively.

### 3.2 Environmental Forces

The environmental forces acting on a DP ship are due to current (including ship's own speed if required), wind and waves.

A good knowledge of the environmental forces will improve the position predictions of the model shown in Section 3.1. If an environmental force is unknown the model shown in Section 3.1 will make an estimate of the total environmental forces from the discrepancies between predicted motion and measured motion. The estimated environmental force is typically assumed to be caused by a steady condition. However, the wave drift forces and wind forces may vary strongly due to wave groups and wind gusts. This leads to inaccuracies in the predictions.

Therefore, the estimation of wind and wave drift through actual wind measurement and wave drift force measurement on the ship will improve the accuracy. This method is called 'feed forward' i.e. wind feed forward or wave drift force forward are regularly applied on the DP systems. It is also necessary to provide feed forward signal to the mathematical model given in Equation (2) in order to provide proper position estimates.

The wind feed forward is very straight forward and uses the actual wind speed and direction measured on-board to calculate the wind forces and moment on the vessel.

The wave feed forward requires more detailed calculations. As explained in Section 3.1, the first order wave motions are not strictly necessary for a DP system. However, the inclusion of high frequency motions will improve the filtering. If the 6-DOF equations of motion are included in the mathematical model so that Karman filter are able to compare the total motions with the measured total motions. The better agreement between mathematical model and measurement allows better tuning of the Kalman filter and the resulting estimate of the low frequency motion components. The current state of the art for the estimation of high frequency motions include estimating the wave and estimating of wave drift forces.

The wave feed calculation is performed either i) by numerical integration of the low pass filtered pressure from the relative motion squared along the waterline or ii) based on wave direction measurement (assuming wave groups) and using drift force transfer functions. The comparison of real time wave drift force measurements with theoretical wave drift force calculations is given in Figure 6 (Aalbers 2004).

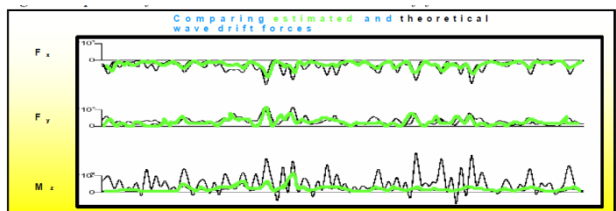


**Figure 6. Comparison of real-time environmental force estimator (RTEFE) versus the theoretical wave drift force calculations (Aalbers 2004)**

Other external forces such as pipe lay tension for pipelay installation vessels or crane /rigging force measurements are also fed into the system in real-time in similar manner.

The recent projects considered the use of a number of relative motion sensors around the ship to make an estimate of the wave drift forces and the wave direction. Neural network techniques were tested to derive a robust estimate from the input signals, in such a way that malfunctioning of one (or more) probes can be dealt with (Naaijen & Huijmans 2010).

An extension to 'feed forward' system is the development of on-board wave and motion measurement systems using remote measurement of short crested waves by the X-band radar as shown in Figure 7 (Naaijen & Huijmans 2010), (Dannenberg et al 2010), (Hertzberger 2013).

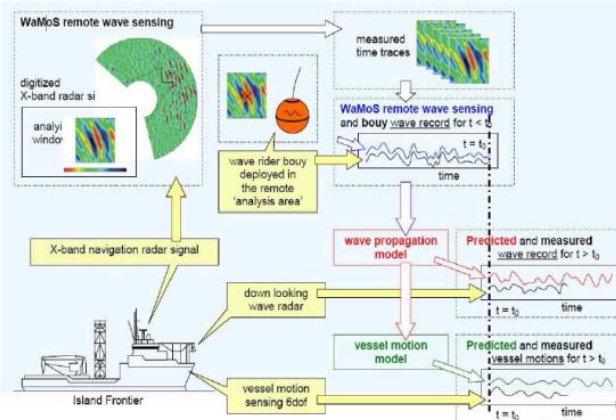


**Figure 7. On board wave and motion estimator (Dannenberg et al 2010)**

### 3.3 Thruster Forces and Thruster Degradation

The thrusters on the ship generate the restoring and damping forces required to keep the ship on station. Some of the thruster systems available on the latest generation of heavy lift and installation vessels and important hydrodynamic issues are shown in Table 1 and Figure 8. From hydrodynamic point of view, the force generated at the thruster shaft is not identical to the resultant force acting on the ship. The presence of the ship hull and the flow around the ship (due to motions, current or flow from another thruster) will lead to induced forces or loss of effectiveness or so-called ‘thruster interaction effects’.

**Table 1. Typical thrusters and hydrodynamic mechanism for offshore vessels**

| Type                               | Action   | Mechanism  |
|------------------------------------|--|--|
| Tunnel Thruster                    | Side force                                       | Suction flow and jet induced flow  |
| Azimuthing thruster (retractable)  | All directions force                             | Jet flow friction and jet induced flow interaction on hull/thrusters                         |
| Normal propellers / Active Rudders | Longitudinal force / Force directions in segment | Suction flow interaction on hull in forward thrust mode, strong jet flow interaction on hull |
| Podded propellers                  | All directions force                             | Jet flow friction and jet induced flow interaction on hull/thrusters                         |

Also, the thruster set points may not coincide with the required set points such as thruster angle, number of revolutions and pitch due to the limited rate of change of these quantities (Nienhuis 1986).

For the actual set points, the total forces exerted by all propulsors are calculated as (Nienhuis 1986):

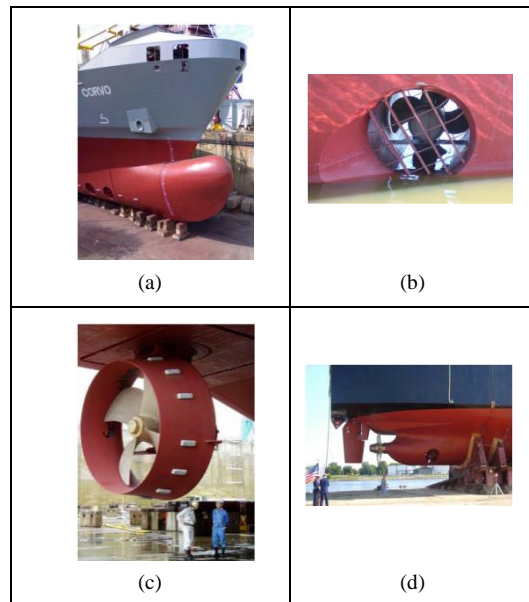


**Figure 8. Example of different thrust type, (a) tunnel thruster at bow , (b) closed tunnel thruster, (c) azimuthing thruster (d) main propeller/rudder at stern**

$$F_t(x, \dot{x}, t) = F_{az}(x, \dot{x}, t) + F_t(x, \dot{x}, t) + F_m(x, \dot{x}, t) \quad (3)$$

Where  $F_{az}$  = the total induced force of all azimuthing thrusters;  $F_t$  = the force exerted by tunnel thrusters; and  $F_m$  = the force of main propeller arrangement.

All of the above forces are divided into a thrust and an induced hull force. The thrust force is calculated from typical open water  $K_T/K_Q$  (Propeller force/Torque) diagrams/calculations. The characteristic of tunnel thruster is derived based on tunnel configuration. The forces exerted by an arbitrary arrangement of azimuthing thrusters are calculated by:

$$F_{az}(x, \dot{x}, t) = \sum_{i=1}^{n_{az}} T_{az,i} C_{hi} l_i \quad (4)$$

Where  $l_i$  = depends on the thruster angle and the considered mode (surge, sway, yaw);  $T_{az,i}$  = thrust of azimuthing thruster  $i$  including interaction caused by other azimuthing thrusters and  $C_{hi}$  = the correction factor for thruster/hull interactions, function of the thrust  $T_{az,i}$ , the thruster angle and the current speed, as well as its direction.

The thrust  $T_{az,i}$  may be influenced by one or more other azimuthing thrusters which generate a velocity field at thruster  $i$  in Eq. (4). The total axial velocity at the location of thruster  $i$  is used to calculate the thrust with the open-water diagrams. This velocity is determined by:

$$v_i = U_{\infty i} + \sum_{k=1, k \neq i}^{n_{az}} \Delta v_{ki} \quad (5)$$

Where  $U_{\infty i}$  = the inflow caused by flow (i.e. current),  $\Delta v_{ki}$  = the extra induced velocity at thruster  $i$  caused by thruster  $k$ , function of prevailing average flow, thrust, torque and presence of vessel hull.

As the Equations (3) to (5) indicate thruster interaction effects are parameter of thruster-hull, thruster-thruster and thruster-inflow (current, wave etc.). In modern DP system modelling, there are well-established methods which have been evolved since the early days of the operation of DP

systems that take into account all of the aforementioned interaction effects (Nienhuis 1986, Lehn 1992, Dexter 1997 and IMCA 2003).

Thruster hull interactions are based on the forces induced on the hull by the suction flow and the jet induced flow. These forces maybe viscous of origin or potential pressure origin or caused by blockage effects. The type of thruster and its location on the vessel greatly determines the thruster hull interaction effects (Figure 9).

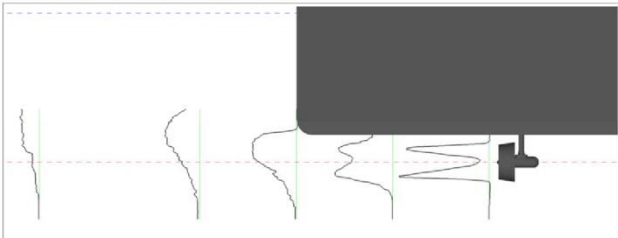


**Figure 9. Measured Wake Velocities for a Thruster Under a Barge (Cozijn et al 2010)**

Thruster-thruster interactions mostly lead to degradation and caused, similarly, by the blockage effects and loss of efficiency. It is a major design aspect and this ultimately limits the feasibility of thruster arrangements. Thruster-current interaction effect, on the other hand, may be small compared to others for azimuthing and main thrusters, except tunnel thrusters, in normal offshore conditions. However, it could be detrimental in very high current conditions such as ‘loop currents’ observed in Gulf of Mexico.

The assessment of these effects has mainly been performed using the model tests and/or the experience obtained over the years from the operations and the ‘full-scale’ measurements. The information is then fed into to the most of the modern-day DP system mathematical modelling described in Section 3.1. However, the published data are often too general or not applicable to the specific design consideration. Model tests, on the other hand, do provide detailed results, but are relatively expensive. And test results often become available relatively late in the design process, making it difficult to incorporate in the design. Computational Fluid Dynamics (CFD) is increasingly becoming an alternative method, but there is still relatively little experience in the application of CFD as an engineering tool for thruster-interaction effects (Cozijn & Hallmann 2012).

A dedicated Joint Industry Project (JIP) was run between 2010-2014 which included different stake holders from offshore industry (i.e. thruster/DP manufacturers, shipyards, vessel operators, design houses, research institutes etc.) and the academia (Cozijn & Hallmann 2012). The JIP aimed at increasing the insight in the physical phenomena, quantifying thruster interaction effects and investigating possibilities for improvement.

For this purpose, dedicated thruster-interaction model tests were performed using the state-of-art PIV measurement tools for several configurations of increasing complexity (Figure 10).

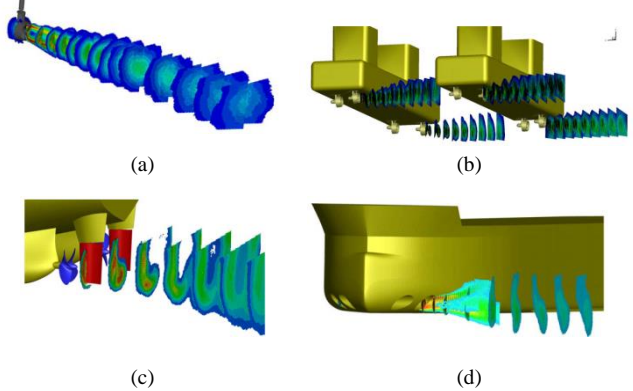


**Figure 10. Measured Wake Velocity Field** (a) Open Water Thruster (b) Semi-submersible (c) Drill ship rudder/main propeller (d) Drill Ship Bow Thruster (Cozijn & Hallmann 2012, 2013, 2014)

PIV measurements indicated that (Cozijn & Hallmann 2012, 2013, 2014):

- The wake flow behind azimuthing thruster shows circular pattern in the measured cross sections. The wake flow horizontally for ‘Normal’ thrusters and is directed slightly downwards for the ‘Tilted’ thrusters. The presence of the hull above the hull, inevitably, affects the shape of the wake for ‘Normal’ thrusters while this is much less pronounced for the ‘Tilted’ thrusters (Figure 11)
- The presence of ‘beam on current’ increases the observed thruster-hull interaction effects on a semi-submersible type vessel while ‘head on’ currents affects the shape of wake, as well as its path (Figure 12)
- ‘Tilted’ thruster can also reduce thruster-thruster effects
- The wake of two main propellers merges into single wake at some distance down-stream from the vessel stern (Figure 13). The highest axial velocities in the wake found are near the free surface. A rudder angle up to 10° causes wake flow to deflect, but the overall patterns in wake flow remain similar to wake flow in case of a rudder angle of 0°.
- The measurements provide valuable insights for the flow patterns of thruster wake while they can provide good benchmark cases for CFD analysis.

Subsequently, the detailed CFD analyses were performed using the three different methods established for the analysis of thruster interactions in recent years:

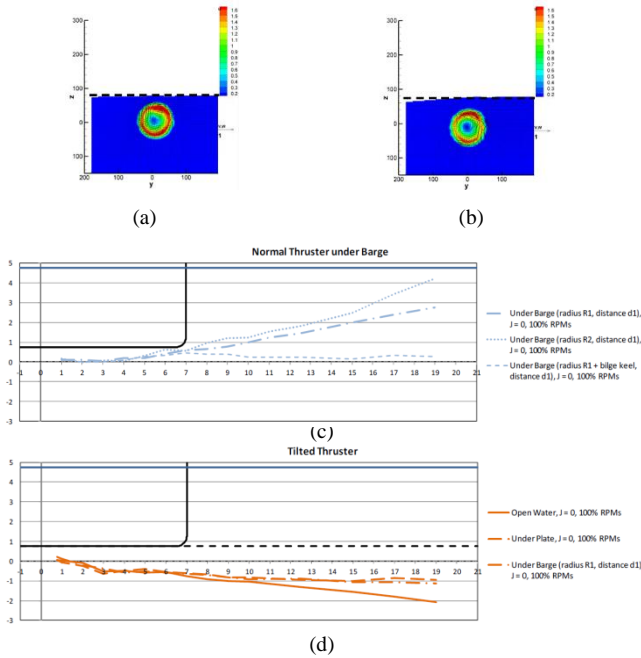


**Figure 11. Measured Wake Velocity Field** (a) ‘Normal’ thruster under barge  $x/D=1$  (b) ‘Tilted’ thruster under barge  $x/D=1$  (c) ‘Normal’ thruster under barge (d) ‘Tilted’ thruster under barge (Cozijn & Hallmann 2012)

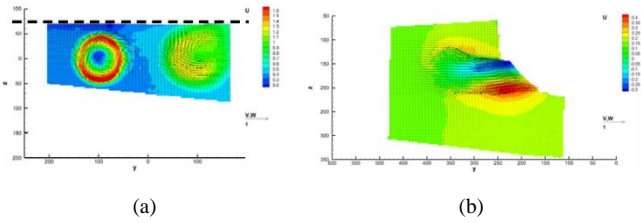


**Figure 12. Measured Wake Velocity Field** (a) ‘Normal’ thruster, semi-submersible in between pontoons under beam-on current (b) Head-on current for the centre of aft/bow tunnel thruster (Cozijn & Hallmann 2013, 2014)

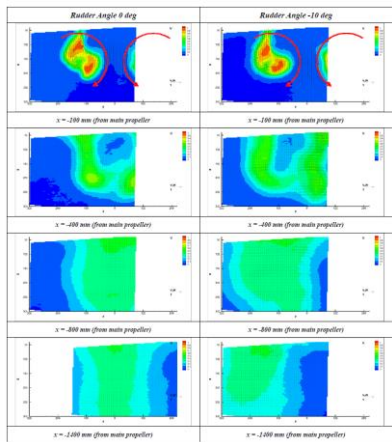


**Figure 13. Measured Wake Velocity Field** (a) ‘Normal’ thruster, semi-submersible in between pontoons under beam-on current (b) Head-on current for the centre of aft/bow tunnel thruster (Cozijn & Hallmann 2014)

- **Actuator Disk (AD):** This model substitutes propeller blades with an ‘equivalent’ body-force distribution, approximately distributed over the volume cut out by the blades. The body-force distribution is an input of the model, therefore a priori knowledge or an estimation of this distribution is required. This method is not good to capture flow fields close to the AD however preferable, with small computation effort, in downstream (wake trajectory), (Maciel et al 2013).
- **Moving Reference Frame (MRF) or Frozen Rotor:** Vessel and the propeller are treated as two separate domains. For both domains, RANS equations are solved using an absolute formulation, steady flow approach. If the incoming flow is uniform, this method is ideal and it can be regarded as a ‘tuned’ AD method, (Maciel et al 2013).
- **Sliding Interfaces (SI):** The most physically complete approach, where no approximation is made to the interaction of the vessel and the propeller flow. RANS domains are solved by unsteady calculations using a moving grid approach where the grid moves arbitrarily inside the fluid domain, following the movement of boundaries. The calculations, inevitably, computationally expensive (Maciel et al 2013).

The validation of CFD results with the PIV tests indicated relatively qualitative agreement in most cases. While, the SI is numerically most advanced method, in terms of accuracy for downstream wake flow trajectory which is also highly relevant to thruster-hull and thruster/thruster interaction problems both MRF and AD methods also have satisfactory agreement with the PIV results. (Figures 14, 15 and 16).

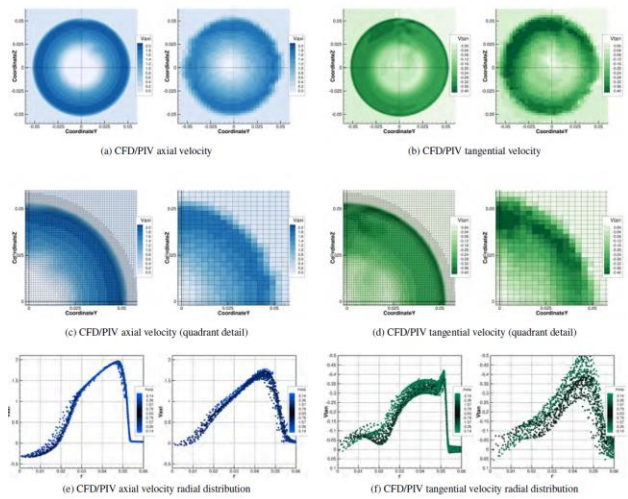


**Figure 14. Comparison of axial and tangential velocity components in the vicinity of an open water thruster** (Maciel et al 2013)

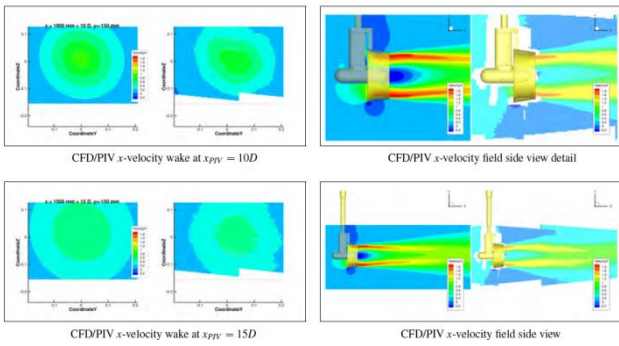


**Figure 15. Comparison of velocity field along the thruster wake, far downstream (Maciel et al 2013)**

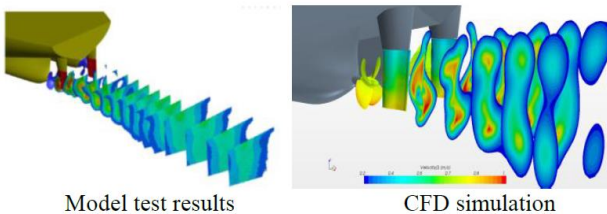


**Figure 16. Comparison of CFD flow field with PIV for a DP shuttle tanker (Lu & Wang 2014)**

The results obtained from the extensive PIV tests and CFD analyses were provided to a dedicated DP capability analysis tool developed as part of the JIP. The parameters from some of well-known methodologies for thruster interaction effects which are widely used in most DP software (i.e. Nienhuis 1986, Lehn 1992) were revised based on the analysis and PIV results in the new software. Furthermore, ‘forbidden zones’ which restrict a thruster’s azimuthing angle due to interaction effects with other azimuthing thrusters on the vessel were re-defined as a results of the analyses and PIV tests (Figure 17).

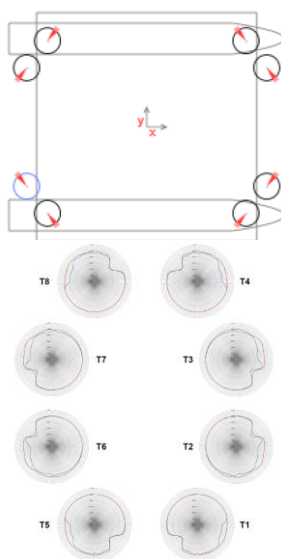


**Figure 17. Forbidden zones and corresponding thruster-hull interaction coefficients for a semi-submersible (courtesy of TRUST JIP)**

### 3.4 DP Control System

The positioning accuracy of a DP vessel under the environmental conditions and the influence of thruster-interaction effects depends on a number of aspects:

- The severity of environmental conditions
- The influence of external forces i.e. pipe residual lay tension, mechanical connection through rigging/crane etc.
- The amount of saturation of the thrusters
- The performance of thrusters
- The accuracy of position estimate on basis of Kalman model prediction and possible reference measurement
- The adequacy of selected control coefficients
- The adequacy of selected heading set point

The DP control systems is regarded as the weakest point in the chain (Holvik, 1998) meaning that the systems for Thrusters, Generators, Power Management, Sensors and Reference System have to have certain standard and accuracy in order to be able to Position a DP vessel accurate and safe.

The thruster allocation is essential part of this control system in which the required forces and moments as calculated by the control algorithm are translated into thruster commands in efficient manner as shown in Figure 18:

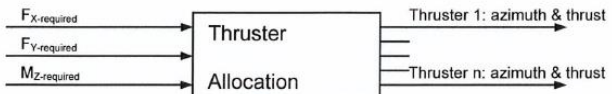


**Figure 18. Thruster allocation mechanism (MARIN 2013)**

The total consumed power in bollard pull condition can be calculated by the following relation (MARIN 2013):

$$P = \sum_{i=1}^N P_{Max,i} \cdot \left( \frac{F_i}{F_{max,i}} \right)^k \quad (6)$$

Where  $N$  = total number of thrusters;  $P_{Max,i}$  = Maximum consumed power of thrusters;  $F_i$  = Thrust delivered by thrusters  $i$ ;  $F_{max,i}$  = Maximum delivered thrust of thruster ‘ $i$ ’ in bollard pull condition,  $k$  = exponent (normally 3/2 meaning thrusters are more power efficient at low thrust settings).

Optimisation technique, then, is applied for thruster allocation establishing a relation between delivered thrust and consumed power (also called ‘Cost Function’). The most widely used technique is to apply Lagrange multipliers which are then used with adaptive control system incorporating thrust saturation, forbidden zones and thrust degradation effects as outlined in Sections 3.1 and 3.3 (MARIN 2013).

As part of TRUST JIP, enhancing the thruster allocation algorithms was also investigated. The one of methods developed was Sequential Quadratic Programming (SQP) based on optimisation focusing on azimuthing thrusters-interaction effects (Arditti et al 2014). A schematic of SQP optimisation is shown in Figure 19.

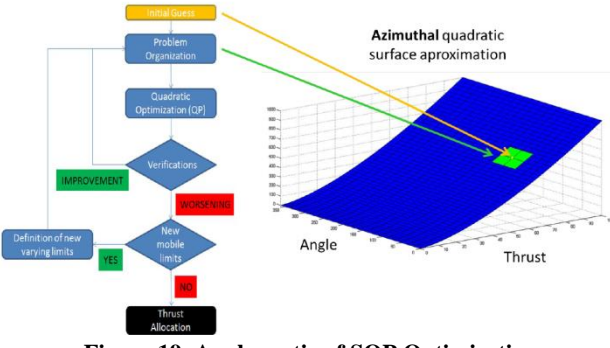


**Figure 19. A schematic of SQP Optimisation**

The allocation algorithm consists of two parts; a general optimisation with saturation constraints based on the SQP, and a binary search based saturation treatment with a special heuristic acceleration to achieve near-optimal solution which saturates almost all thrusters in worst the case (Figure 19). One of the important outcomes of the SQP technique is to utilise thruster interaction effects without applying constraints of forbidden zones (i.e. near-optimal saturation of all thrusters is sought). The agreement between the SQP method and forbidden zone (denoted FZ) is very good with the SQP method can further utilise thruster efficiency providing operational and cost gains, Figure 20 (Arditti et al 2014).

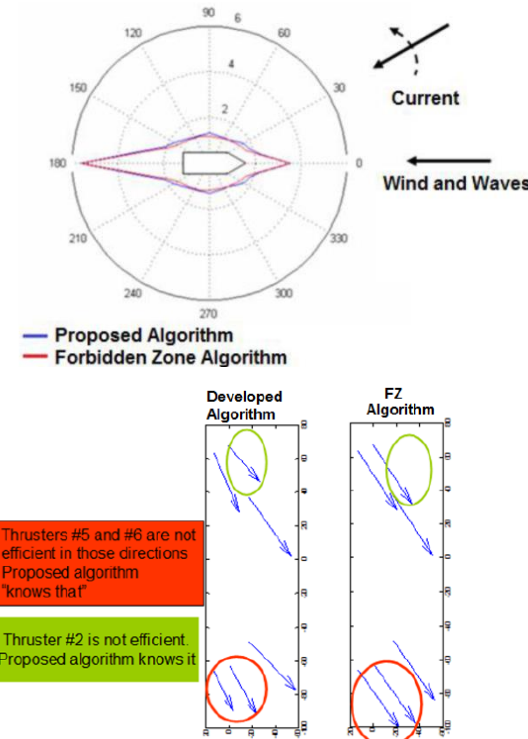


**Figure 20. Maximum current capability plot of DP vessel with SQP Optimisation and Forbidden Zone (FZ) algorithm and Numerical Comparison between the allocation algorithm (Arditti et al 2014)**

Other methods such as evolutionary algorithms using population sampling, probabilistic methods and response surface models were also investigated.

## 4 DP ASSESSMENT AND SIMULATIONS

For an early design stage and during the initial offshore field assessment the DP capability plots are the most established presentation of the vessel's DP performance. This method is also very suitable for comparing different designs provided the method of calculation is the same. The calculation of forces are quasi-static (i.e. mean static forces are applied) usually at most onerous condition (i.e. all environment forces are co-directional). Furthermore, the redundancy in the DP system is checked by analysing the worst case scenario identified, typically, from the Failure Modes and Effects Analysis (FMEA) as a class/regulatory body requirement. A typical DP capability plots is shown in Figure 21.

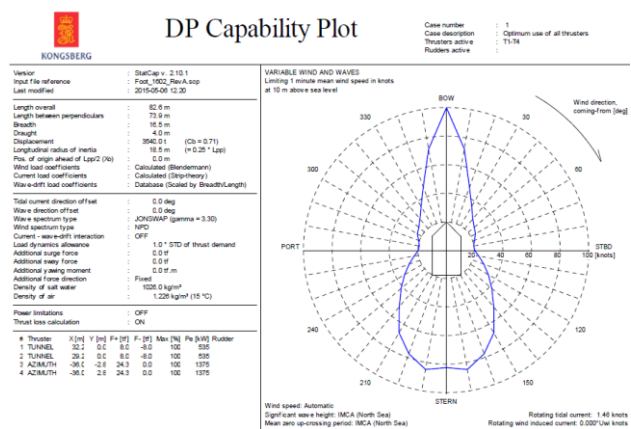


**Figure 21. A typical DP capability plot (courtesy of Kongsberg)**

However, the DP capability plots do not give an answer to positioning accuracy or they do not determine if the vessel actually be able to maintain position in a given limit sea state. This is crucial for many critical offshore operations such as vessel-to-vessel transfer, DP pipe lay positioning or trenching operations. Therefore, a time domain based method, as illustrated in Figure 4, will be more accurate. This will be also a replica of what an on-board DP system produce offshore (DP 'footprint' or time-series). However, they could be expensive in terms of running time and they will require complex modelling, as outlined in Section 3.1, for the design stage assessment. An alternative in recent years, is to introduce a 'Dynamic' DP capability analysis in which 'feed forward' time series of wind and wave drift (as explained in Section 3.2) are introduced to the modelling along with the adaptive allocation algorithms and thruster interaction effects described in the previous sections (Van't Veer & Gachet 2011). A comparison of static and dynamic capability plots is shown in Figure 22.

In Figure 22, dynamic capability and actual time domain analysis indicate wind speed in static capability analysis using the mean drift force are larger than the vessel can cope with in sea state in which the wave drift load and wind load vary in time.

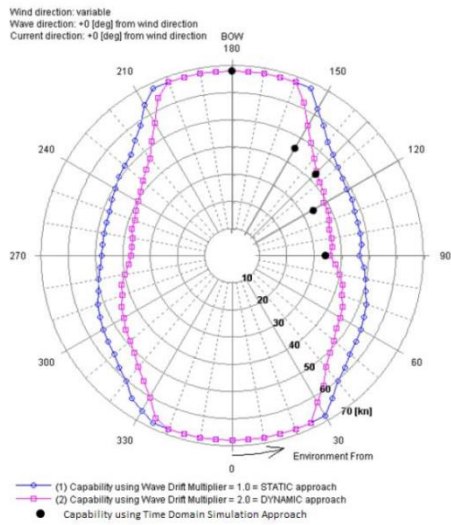


**Figure 22. DP capability plot (Van't Veer & Gachet 2011)**

## 5 CONCLUSIONS

The current practises of hydrodynamic analysis of offshore heavy lift and installation vessel DP behaviour and the modelling of control mechanisms and thruster interactions were reviewed.

The inclusion of some of the recent developments in wave and wind feed forward (prediction) and adaptive control algorithms has improved the prediction accuracy.

A recent JIP conducted by different industry partners on thruster interactions effects concluded that CFD methods and advanced allocation algorithms can be used in the engineering stage of the DP system design.

The current work in this field focuses on establishing the vessel's DP capability limits based on the motion and operational limits (i.e. DP foot print, excursion or external forces applied through the motion of crane/stinger etc.) rather than a set of prescriptive environmental limits identified in quasi-static analysis commonly used in the industry for the DP capability assessment.

## 6 DISCLAIMER

The views, opinions, findings, conclusions or recommendations expressed in this paper are strictly those of the author. They do not necessarily reflect the views of the Saipem Ltd. (affiliate of Saipem S.p.A). Saipem Ltd. (affiliate of Saipem S.p.A) takes no responsibility for any errors or omissions in, or for the correctness of, the information contained in the paper:

## REFERENCES

- Aalbers, A.B. (2004). 'Wave Feed Forward DP and the Effect on Shuttle Tanker Operation'. *Proceedings of the Dynamic Positioning Conference*, Houston, USA.
- Arditti, F., Souza, F.L., Martins, T.C. & Tannuri, E.A. (2015). 'Thruster Allocation Algorithm with Efficiency Function Dependent on the Azimuth Angle of Actuators' *Offshore Engineering* 105(1), pp.206-216.
- Ayaz, Z. & Macdonald, R. (2011). 'The Assessment of Ploughing Operations with DP Vessels in Shallow Water'. *Proceedings of International Conference on Offshore Pipeline Technology*, Amsterdam, the Netherlands.
- Chas, C.S. & Ferreiro, R. (2008). 'An Introduction to Ship Dynamic Positioning Systems'. *Journal of Maritime Research* 5(1), pp.79-96.
- Cozijn, H., Hallmann, R. & Koop, A. (2010). 'Analysis of Velocities in the Wake of Azimuthing Thrusters, using PIV Measurements and CFD Calculations'. *Proceedings of the Dynamic Positioning Conference*, Houston, USA.
- Cozijn, H. & Hallmann, R. (2012). 'The Wake Flow Behind; Measurements in Open Water, Under A Plate and Under A Barge'. *Proceedings of the 31st International Conference on Ocean, Offshore and Arctic Engineering*, Rio de Janeiro, Brazil.
- Cozijn, H. & Hallmann, R. (2013). 'Thruster-Interaction Effects on A DP Semi-Submersible and Drill Ship – Measurement and Analysis of The Thruster Wake Flow'. *Proceedings of the 32nd. International Conference on Ocean, Offshore and Arctic Engineering*, Nantes, France.
- Cozijn, H. & Hallmann, R. (2014). 'Thruster-Interaction Effects on A DP Shuttle Tanker – Measurement of The Main Propeller and Bow Tunnel Thrusters'. *Proceedings of the 33rd. International Conference on Ocean, Offshore and Arctic Engineering*, San Francisco, USA.
- Dannenberg, J., Naaijen, P., Hessner, K., Van den Boom, H. & Reichert, K. (2010). 'The On board Wave and Motion Monitor OWME'. *Proceedings of the 29th International Conference on Ocean, Offshore and Arctic Engineering*, Shanghai, China.
- Deter, D. (1997). 'Principal Aspects of Thruster Selection'. *Proceedings of the Dynamic Positioning Conference*, Houston, USA.
- Hertzberger , G.M. (2013). *The influence of wave fields descriptions on real time deep water drift forces*. MSc. Thesis, Delft University of Technology, the Netherlands.
- Holvik, B. (1998). 'Basics of Dynamic Positioning'. *Proceedings of the Dynamic Positioning Conference*, Houston, USA.
- IMCA (2003). *Guidelines For Design & Operation of Dynamically Positioned Vessels*. <http://www.imca-int.com>.
- Lehn, E. (1992). 'Practical Methods for Estimation of Thrust Losses'. Marintek, Norway Research Report, Doc. No: 513003.00.06.
- Lu, P. & Wang, S. (2014). 'CFD Simulation of Propeller and Tunnel Thruster Performance'. *Proceedings of the 33rd. International Conference on Ocean, Offshore and Arctic Engineering*, San Francisco, USA.

- Maciel, P., Koop, A. & Vaz, G. (2013). ‘Modelling Thruster-Hull Interaction with CFD’. Proceedings of the 32<sup>nd</sup>. International Conference on Ocean, Offshore and Arctic Engineering, Nantes, France.
- MARIN, Netherlands (2013). Hydrodynamics of Floating Offshore Structures. Course Notes.
- Naaijen, P. & Huijsmans, R.H.M. (2010). ‘The Real Time Prediction of Second Order Wave Drift Forces for Wave Feed Forward in DP’. Proceedings of the 29th International Conference on Ocean, Offshore and Arctic Engineering, Shanghai, China.
- Nienhuis, U. (1986). ‘Simulation of Low Frequency Motions of Dynamically Positioned Offshore Structures’. Proceedings of Royal Institute of Naval Architects, UK.
- Van den Boom, H.J.J. & Nienhuis, U. (1983). ‘Hydrodynamic Analysis of Dynamically Positioned Vessels’. Proceedings of International Workshop on Ship and Platform Motions, Berkeley, USA.
- Van’t Veer, V. & Gachet, M. (2011). ‘Dynamic Positioning – Early Design, Capabilities , Offsets – A Novel Approach’. Proceedings of the 30th International Conference on Ocean, Offshore and Arctic Engineering, Rotterdam, the Netherlands.
- Van Terwisga, T., Quadvlieg, F. & Valkhof, H. (2001). ‘Steerable Propulsion Units: Hydrodynamic Issues and Design Consequences’. Proceedings of 80<sup>th</sup>. Anniversary Conference of Schottel GmbH & Co, Germany.

## **Design and Development of a New Free-Running Manoeuvring test Facility at ITU**

**Cansın Özden<sup>1\*</sup>, Sertaç Kurdoğlu<sup>1</sup>, Ersin Demir<sup>1</sup>**

*<sup>1</sup>Istanbul Technical University, Faculty of Naval Architecture and Ocean Engineering, 34469 Maslak-Istanbul, Turkey*

**Abstract:** Free running manoeuvring test systems present an efficient way of estimating manoeuvring characteristics for surface vessels and submarines. Many towing tanks and research institutes around the world are equipped with such facilities with varying characteristics. Within the framework of a recent research development programme a new Free Running system, designated as Takip Modlu Manevra Deney Sistemi has been designed to be used at ITU Lake in Istanbul Technical University (ITU). This paper describes the main characteristics of the system and explains the design procedure.

**Keywords:** manoeuvring, free running test, hydrodynamic derivatives.

### **1 INTRODUCTION**

Pioneering studies about Free Running systems are carried out in David Taylor Model Basin. Hoffman explains in detail in his report “A Radio Control and Powering System for Free-Running Models of Surface Ships” (Hoffman, 1960) the system for free running models which dimensions extend up to 10m and which are propelled in the manoeuvre basin with the dimensions 80x120m. The models displacements of which change from 65 kg to 2 tons with powers up to 3 HP are propelled with two motors in ahead or sternway. The need for rudder torque is approximately 12 Nm for two different rudders which angular velocity is for each 4 to 40 deg/s. In this report information about how the manoeuvring trajectories are assigned is not given. Despite that in another report (Gover, 1960) which is also prepared in DTMB by Gover, it is explained that for the quality of ship maintenance for captains focused on human and machine the system which is reported by Hoffman is used. In this report it is mentioned that the manoeuvring trajectory is determined from the data collected from the filming of three different cameras in the J-shaped manoeuvring basin in DTMB.

Beside this it is seen that pmm systems especially in wide model basins with the use of relative positioning transducers named as tracking lag can be used as free running systems. In a system explained by Grim et.al. the model in the manoeuvring basin in HSVA is attached to the towing carriage by a cord for transfer the power needed to command the rudder and the propulsion motor. The three digital transducers on the tracking lag of the free running model are producing the input signals so that the carriage can automatically follow the model in three degrees of freedom (Grim et.al. 1976).

All motions of the experimental system which is following the model are recorded and from this data the manoeuvring

trajectory of the model is determined. Nowadays such systems are also used. The system developed for model basins for the topic shallow water and interaction with other ships by Vankerhove et.al. in Ghent University and Flanders Hydrolic Research Center has an autopilot which enables collision, stop, zigzag, acceleration and static tests (Vankerhove et al, 2009).

Besides the free running manoeuvring experimental facilities in the IHHR model basin in Iowa University can track the model without contact. The system follows the LED lights on the model with 0.1mm precision and transmit the data in 6 channels for 6 degrees of freedom. A 7th channel gives signals on the instant motion of the model and enables that the carriage follows the model (Hyunse, 2009)

All in all, free running manoeuvring test systems present an efficient way of estimating manoeuvring characteristics for surface vessels and submarines. Many towing tanks and research institutes around the world are equipped with such facilities with varying characteristics. Within the framework of a recent research development programme a new Free Running system, designated as Takip Modlu Manevra Deney Sistemi has been designed to be used at ITU Lake in Istanbul Technical University (ITU). This paper describes the main characteristics of the system and explains the design procedure.

### **2 DESCRIPTION OF THE SYSTEM**

ITU FreeRunning test system is a modular system which can fit ship models to run them for standard ship manoeuvring tests. System consist of two main stations, one is the shore station and the other is the mobile unit. In the shore station, there are the stationary unit of Real Time Kinetic GPS system, GPS control unit, a portable

\* Corresponding author e-mail: ozden@itu.edu.tr

computer, WiMAX ruggedcom shore module and Omni antennas and radio control handset. While the mobile unit consist of battery package, IMU (Inertial Measurement Unit), GPS Heading unit and dual antennas, a PLC (Programmable Logic Controller) for the control of the system, up to four servo motors and their drive systems for propulsion and up to four servo motors and drive systems for rudders or steering devices, WiMAX ruggedcom mobile unit and Omni antennas. These systems can be collected in five main groups such as;

- Main electric system
- Device control system
- Signal measurement system
- Communication system
- Model ship

## 2.1 Main Electric System

Free running system is a semi-autonomous vehicle which can operate by itself in accordance with the preprogrammed tasks. For all the mobile equipment, there need to be stored energy which can endure along the tests. Therefore, a 48V battery pack is designed as a part of the mobile unit. However GPS, IMU and WiMAX systems require 12VDC and servo drives run at 220V AC, so there will be DC-DC converters and DC-AC invertor which also will be parts of the electric system.



Figure 1: Demonstration of a test scene

## 2.2 Device Control System

Free running model is planned to be controlled by a PLC in two modes; remotely operated and semi-autonomous mode. Remote operate mode will be selected prior and after the tests to bring the model to test area from shore and vice versa. Also remotely operated mode is an emergency mode, if any unexpected situation or an error occur during the tests, operating mode will be changed accordingly. In remotely operated mode, test personnel on shore operate the boat as it is RC hobby boat using the RC handset. RC receiver on deck, receives the signals and sends PWM signals to PLC and the later one produces the position

signals for servo motors for both main propulsion and rudder deflections.

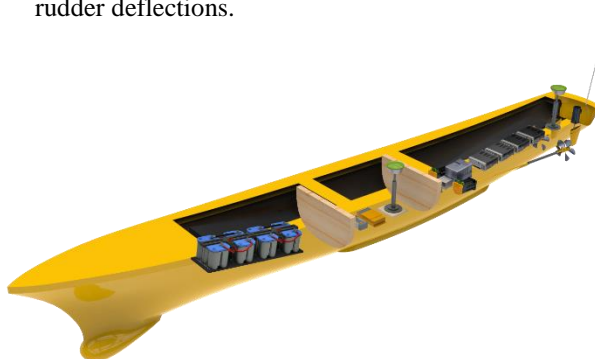


Figure 2: Illustration of the mobile unit of the free running system

On the other hand, for semi-autonomous mode; after the test personnel bring the boat to test field on RC mode than switch the operation mode to test mode from the free running test user display running at portable PC on shore. Using this display, user can select the test mode such as turning, zigzag etc., can select the test speed or RPM of the propulsion motors or rudder deflections for the current real time position or the required input for the zigzag tests.

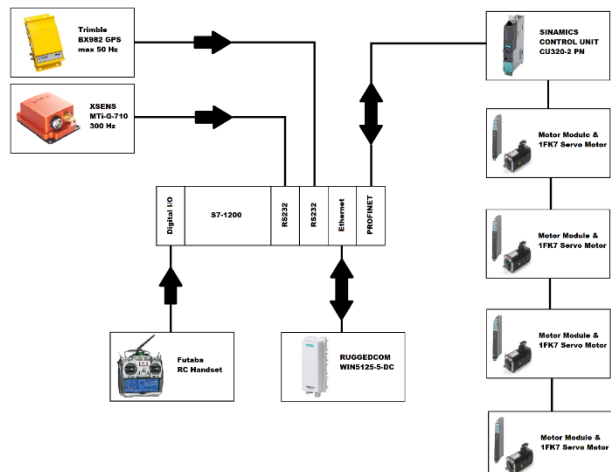


Figure 3: Control system connections of the Free Running system

Thus, as the control system, PLC is handling the real time user signals or runs the predefined test procedures. But when it is executing the predefined it generates servo positions or RPMs with the inputs coming from IMU and GPS Heading.

## 2.3 Signal Measurement System

The main idea of the free running system is to precisely implement propeller rotations and rudder deflections in accordance with the standard manoeuvres and simultaneously measure the ship motions such as GPS coordinates, heading and roll, pitch, heave data if required.

In ITU Free running test setup; an RTK (Real Time Kinetic) GPS system is planning to be used for precisely collect the position and heading data. Trimble BX982 Heading Rover and Trimble R10 modules are selected for this purpose and can produce 8mm and 0.09 degree accurate position and heading data, respectively. R10 system will be positioned at the shore and BX982 will be on deck with two antennas which will be located as far as possible. An IMU system, possibly an Xsens MTI-G-710 will be mounted at center of gravity in order to measure heave, pitch and roll data. Finally, servo motor RPM and positions are measured by their encoders. All these data are collected and combined by PLC, and send to shore station. Connections of the control and measurement system can be seen in Figure 3 and 4.

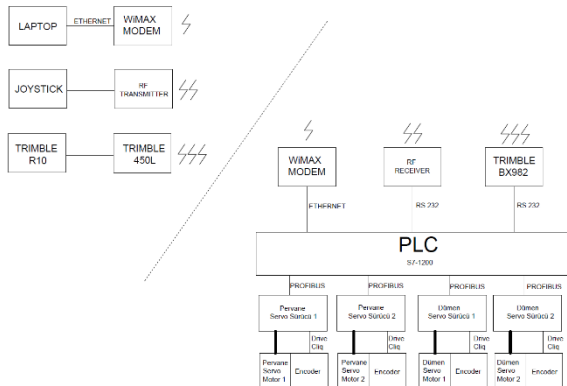


Figure 4: System communication diagram

#### 2.4 Communication System

Communication of the free running system has two separate methods for different equipment. Radio communication is used only in remote control mode via RC handset and receiver in one way communication. The main data communication is done with WiMAX Ruggedcom units. A Win5125 mobile unit and two Omni antennas will be on deck at all times to send data to shore which is packed by PLC provided from GPS, IMU and servo encoders. Mobile unit also receives data from shore such as user inputs via user display such as operating mode, test modes and other inputs. Shore part of the WiMAX system is the 7225 unit which is connected to portable computer which runs the user display and also stores the data provided by the PLC via WiMAX system. Selected WiMAX system is able to provide communication up to 5km range.

The connections of sub systems between PLC will be through additional modules on PLC. GPS, IMU systems will be connected with RS232 serial connectors, WiMAX systems will be Ethernet connected. RC receivers will be 0-5V digital I/O connected, while servo drive modules use PROFINET protocol.

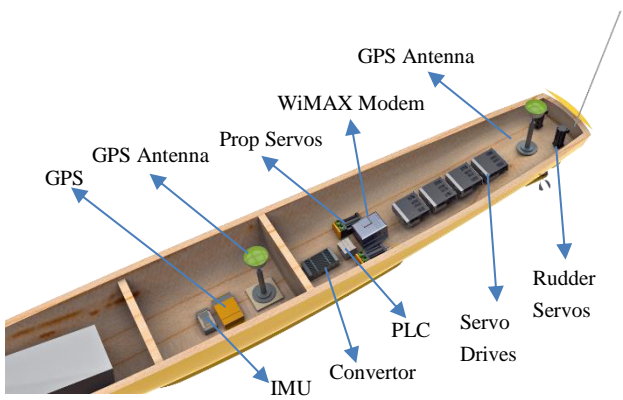


Figure 5: Close look of the inner units of free running system

#### 2.5 Ship Model

Free running system will be mounted on the ship model which's manoeuvring performance desired to be evaluated. All above described systems will be in IP68 covers which provide splash and dust protection suitable for use outside.

As the initial model, DTMB 5415 is selected due to available data for the validation of the procedure. All the systems Ship models for the free running tests will be machined at ITU Ata Nutku Ship Model Basin's 5 axis milling machine and tests are planned to be performed in the small lake which is a few hundred meters away from the Basin.

### 3 CONCLUSION

Main specifications and thoughts for the selection of the equipment for the designed to build free running system of Istanbul Technical University Naval Architecture and Ocean Engineering Faculty is described. Properties, limitations and accuracy of the systems are listed.

### 4 ACKNOWLEDGEMENTS

This research was sponsored by the Undersecretariat for Defense Industries under Grant 991-LST00-0090-001-000-0. Authors would like to thank Prof. Dr. Ömer Gören and Prof. Dr. Kadir Sarıöz for their support, guidance and patience since the very beginning of the project. Authors wish to thank ADIK Shipyard for their support and would also wish to acknowledge Mr Azmi Ak and Mr Sinan Burunsuz of DATUM – Denizaltı Teknolojileri ve Uygulamalı Müh Company for their valuable help during design and construction of the systems.

## REFERENCES

- Deakin, B. and Buckland, D. 2010, "Recent advances in radio controlled model testing", The 2nd Chesapeake power boat symposium Annapolis, Maryland, USA, 2010
- Gover, S.C. – "Free-Running Model Techniques for the Evaluation of Ship-Handling Qualities", DTMB Report, Maryland, USA, 1960
- Grim, O., Oltman, P., Sharma, S.D., Wolff K. (1976). 'CPMC - A Novel Facility for Planar Motion Testing of Ship Models'. Hamburg, Technische Universität Hamburg-Harburg, Bericht Nr 345.
- Hoffman, C. W. – "A Radio Control and Powering System for Free-Running Models of Surface Ships", DTMB Report, Maryland, USA, 1960
- Hyunse, Y. - Phase-Averaged Stereo-PIV Flow Field and Force/Moment/Motion Measurements for Surface Combatant in PMM Maneuvers, PhD Thesis, University of Iowa, USA, 2009
- Im, N., Seo, J.H. – "Ship Manoeuvering Performance Experiments Using a Free Running Model Ship", International Journal on Marine Navigation and Safety of Sea Transportation V4. N.1, 2010
- Vankerkhove, G., Vantorre, M. and Delefortrie, G. - "Advanced model testing techniques for ship behaviour in shallow and confined water", Advanced Model Measurement Technology for EU Maritime Industry – AMT'09, France, 2009

## Numerical Investigation of Viscous Effects on the Static PMM Tests of Ships

Suleyman Duman<sup>1\*</sup>, Sakir Bal<sup>2</sup>

<sup>1</sup>*Yildiz Technical University, Faculty of Naval Architecture and Maritime, 34349 Besiktas -Istanbul, Turkey*

<sup>2</sup>*Istanbul Technical University, Faculty of Naval Architecture and Ocean Engineering, 34469 Maslak-Istanbul, Turkey*

**Abstract:** The main objective of this study is to investigate the viscous effects on the static PMM (Planar Motion Mechanism) tests of ships numerically. RANS and Euler approaches have been employed in order to calculate hydrodynamic forces and moments acting on the well-known naval surface combatant DTMB 5415 hull. Several computational fluid dynamics (CFD) analyses have been carried out using a commercial code based on finite volume method (FVM). The flow is considered as 3-D, incompressible, transient and fully turbulent in order to solve RANS (Reynolds Averaged Navier-Stokes) equations. First, the code has been validated with the available experimental data in literature. After validation of the method, static PMM tests have been applied for both viscous and inviscid cases. Hydrodynamic analyses have been carried out for a fixed Froude number. During the analyses, the free surface effects have been taken into account and the hull is considered as fixed. The results of viscous model have been compared with those of inviscid case, via forces and moments acting on the hull. In addition, wave deformations along the hull have been investigated by considering both the viscous and inviscid results.

**Keywords:** PMM simulation, ship maneuvering, CFD, viscous effects, wave deformation.

### 1 INTRODUCTION

Predictions of ship-maneuvering performance have been a vital subject for decades in the last century. The prediction of ship maneuvering performance in the early design stage has a significant role to know the adequacy of ship's controllability. In order to estimate the ship-maneuvering performance, experimental, numerical and empirical methods have been widely used. As known, the experimental methods are expensive and time consuming. Meanwhile, computational fluid dynamics (CFD) methods have become increasingly important and is now an essential part of ship design. CFD methods are cost effective as compared with the experiments and are quick-responding methods. In addition, CFD methods can be employed both simulating viscous and inviscid flows.

Typically, inviscid free-surface approaches based on the boundary element method (BEM) are used to analyze the forebody, especially for the interaction of bulbous bow and forward shoulder “(Bertram 2012)”, where viscous flow codes focus on the aft body or appendages. BEM techniques (panel methods) are used for potential flows and cannot be used to solve RANS or Euler equations. However, the applications of both viscous and inviscid models in flow codes are widely used. For potential flows, the integrals over the whole fluid domain can be transformed to integrals over the boundaries of the fluid domain. “Bal (2008)” used an iterative boundary element method (IBEM) to predict the wave pattern and wave resistance of surface piercing bodies. An iterative boundary element method was developed to predict the flow characteristics such as; wave drag and lift, for both 2-

D and 3-D cavitating hydrofoils and ship-like bodies moving with constant speed under or on the free surface “(Uslu & Bal 2008)”.

Nowadays, viscous CFD codes became more reliable and efficient to use on ship maneuvering problems. “He et al (2016)” have applied CFD techniques to predict the maneuvering performance of MOERI KVLCC2. “Sakamoto et al (2012)” have used URANS approach to simulate the static and dynamic maneuverings of the well-known surface combatant DTMB 5415.

Static and dynamic maneuvers have been investigated extensively by using CFD based methods “(Simonsen & Stern 2003)”, “(Bhushan et al 2007)”, “(Kim et al 2015)”, “(Sakamoto et al 2012)” and “(Dogrul & Celik 2016)”. The CFD simulations provide more insights to the entire flow structure around the hull, and the simulation results can be used to compute the forces and moments acting on the hull and then to determine hydrodynamic derivatives “(Yoon 2009)”. There are some difficulties along with the advantages of URANS method such as, the implementation of complex geometries, solving 6-DOF (Degrees of Freedom) ship motions (needs huge computing capability) and environmental effects etc. Moreover, RANS methods are required to be verified and validated “(Stern et al 2001)” to be reliable and accepted by end-users as a solution tool for use in industry or the navy.

Recently, international workshops are organized via collaboration of related institutions to meet the demand for EFD (Experimental Fluid Dynamics) validation data. Researches about ship maneuvering have focused on

modern tankers (KVLCC1 and KVLCC2), Kriso Container Ship (KCS), and US Navy surface combatant (DTMB 5415), which is currently used in this study. In the Gothenburg 2000 Workshop, "Larsson et al (2003)" and "Kim et al (2001)" provided steady-flow data for KCS and KVLCC2. For DTMB 5415, data procurement has been part of an international collaboration between IIHR (Iowa Institute of Hydraulic Research), INSEAN (Italian Ship Model Basin) and DTMB (David Taylor Model Basin), for more than 10 years "(Yoon 2009)". After the Gothenburg Workshop, SIMMAN 2008 and SIMMAN 2014 Workshops were organized to discuss more recent studies.

Experimental ship model tests can be separated into free running model tests and captive model tests "(Lewis 1989)". In all types of model tests, free-running test is the closest to the reality, due to the fact that there is no mathematical modeling or assumption to simplify the problem. However, the individual maneuvering factors, e.g., changes of sway forces according to the steering angle, cannot be obtained from this type of tests due to providing only the final results/information. System Identification (SI) method is used in recent studies to obtain more information from free-running tests "(Oltmann 2000)", "(Viviani et al 2003)", "(Yoon & Rhee 2003)". Besides to SI method, Artificial Neural Networks (ANNs) is applied to maneuvering problems "(Moreira & Soares 2003)".

The other ship model test so-called captive model testing technique comprises planar motion mechanism (PMM) "(Gertler 1967)", "(Strom-Tejsen & Chislett 1966)", rotating arm test (RAT) or circular motion test (CMT) "(Gertler 1966)" and oblique towing test.

A commonly used method to predict ship maneuvering performance is to use equations of motions with experimentally or numerically determined maneuvering coefficients proposed "by Abkowitz (1964)." Once these coefficients are determined for a specific ship, the equations of motions are solved simultaneously to simulate the dynamic behavior of the ship. Maneuvering coefficients can be obtained from static and dynamic PMM tests.

In this study, static drift PMM simulations have been applied for a fixed Froude number to calculate some of the maneuvering coefficients by using both URANS and Euler approaches. The results of viscous model have been compared with those of inviscid case, via forces and moments acting on the hull.

## 2 COMPUTATIONAL METHOD

All computations reported in this study are performed using the RANSE solver software Star-CCM+ from CD-adapco. The software is based on a finite volume (FV) methods. Appropriate initial and boundary conditions and a number of discrete approximations are needed to obtain an algebraic equation system solvable on a computer. First, the computational domain is subdivided into a finite number of control volumes (CVs) which have a hexahedral

shape in this study. The time interval is also subdivided into time steps of appropriate size.

The fluid flow is considered as 3-D, incompressible and fully turbulent. Hydrodynamic analyses have been carried out for a fixed Froude number. During the analyses, the free surface effects have been taken into account and hull is considered as fixed. The flow is assumed to be governed by the RANS equations, in which turbulence effects are included via two-equation model. Thus, the continuity equation, three momentum equations and two equations for turbulence are solved. The conservation law must be satisfied as well.

The free surface flow problem is included to the CFD simulations by using volume of fluid (VOF) method which is utilized by Eulerian fluid approach. The VOF method developed "by Hirt & Nichols (1981)" is fixed mesh technique designed for two or more fluids, where in each cell of a mesh it is necessary to use only one value for each dependent variable defining the fluid state "(Fonfach 2010)".

The segregated flow solver is used to solve the Navier-Stokes equations in an iterative method. After the volume fraction and turbulence quantities are solved, the procedure is repeated until all non-linear and coupled equations are satisfied within a prescribed tolerance. Then, the process advances to the next time level.

### 3.1 Governing Equations

Considering the flow incompressible with constant viscosity and assume that there are no body forces acting on the hull, the averaged continuity and momentum equations may be written in tensor form and Cartesian coordinates as follows "(Ferziger & Perić 2002)":

$$\frac{\partial(\rho\bar{u}_i)}{\partial x_i} = 0 \quad (1)$$

$$\frac{\partial(\rho\bar{u}_i)}{\partial x_i} + \frac{\partial(\rho\bar{u}_i\bar{u}_j + \rho\bar{u}_i\bar{u}_j)}{\partial x_j} = -\frac{\partial\bar{p}}{\partial x_i} + \frac{\partial\bar{\tau}_{ij}}{\partial x_i} \quad (2)$$

in which  $\bar{\tau}_{ij}$  are the mean viscous stress tensor components, as shown below:

$$\bar{\tau}_{ij} = \mu \left( \frac{\partial\bar{u}_i}{\partial x_j} + \frac{\partial\bar{u}_j}{\partial x_i} \right) \quad (3)$$

and  $p$  is the mean pressure,  $\bar{u}_i$  is the average Cartesian components of the velocity vector,  $\rho\bar{u}_i\bar{u}_j$  is the Reynolds stresses,  $\rho$  is the fluid density and  $\mu$  is the dynamic viscosity coefficient.

### 3.2 Choice of Time Step

The Courant number (CFL) is the ratio of the physical time step ( $\Delta t$ ) to the mesh convection time scale, which is typically calculated for each cell.

$$CFL = \frac{U\Delta t}{\Delta x} \quad (4)$$

For numerical stability, the Courant number should be equal or less than 1. For transient ship resistance computations "ITTC (2011)" proposes the formulae

$\Delta t = 0.005 - 0.01L/U$ , where L is the length between perpendiculars and U is the ship advance speed, for the choice of time step.

### 3.2 Grid Resolution and Boundary Conditions

The computational domain and boundary conditions are illustrated as follows ("Figure 1" and "Figure 2").

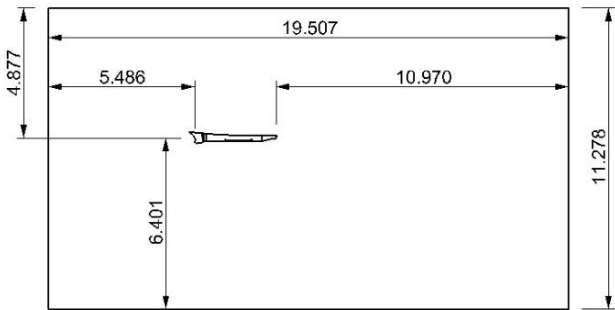


Figure 1 Computational domain.

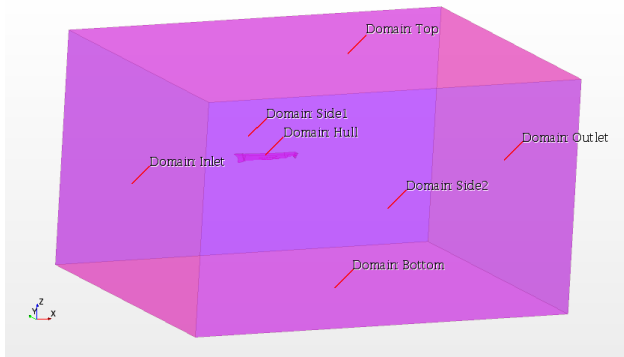


Figure 2 Boundary conditions.

The origin of the coordinate system is the intersection point of forward perpendicular and base line. Ship boundaries are identified as no-slip walls where the normal component of the velocity is to be zero. Front, top and bottom faces of the computational domain are defined as velocity inlets. Side faces are assigned as symmetry-planes and the back face is defined as pressure outlet. Symmetry type boundary condition enables to reduce the computational domain size and mesh number by half. In order to calculate the free surface deformations at the interaction of two phases (air and water), the free surface is defined as calm water initially.

Table 1 Computation domain dimensions.

| Domain dimensions (m) |            |         |        |
|-----------------------|------------|---------|--------|
| Upstream              | 1.8LBP     | 5.486m  |        |
| Downstream            | 3.6LBP     | 10.973m |        |
| Boundaries            | Top        | 1.6LBP  | 4.877m |
|                       | Bottom     | 2.1LBP  | 6.401m |
|                       | Transverse | 2.4LBP  | 7.315m |

The computational domain dimensions are given in "Table 1". Upstream is in the negative and downstream is in the positive x-direction. The top boundary distance indicates the distance between top of domain and the origin of coordinate system.

Finite element method is used to discretize the computational domain. Hexahedral elements are used in order to generate the computational grid. Volumetric controls have been used to refine the grid around the hull, bow and stern, free surface and wake zone.

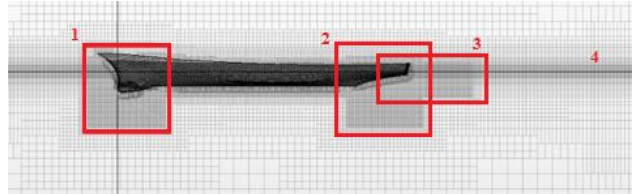


Figure 3 Grid topology: profile view.

At the bow and the wake zone some refinements are also applied, since the flow has complex behavior at these zones. A boundary layer is placed near the hull by using 6 prism layers. Numbers 1 and 2 in the "Figure 3" represent the bow and stern mesh refinements. In the wake zone of the ship model, a cylindrical volumetric control represented with number 3 is created to capture the free surface deformations well.

Number 4 in the "Figure 3" indicates the free surface mesh refinement to capture the Kelvin waves properly. There are two geometries that can be used to refine the mesh around the free surface. These are triangular ("Figure 4") and rectangular volumetric controls ("Figure 5"). The triangular mesh refinements can also be called as Kelvin waves adopted grid.

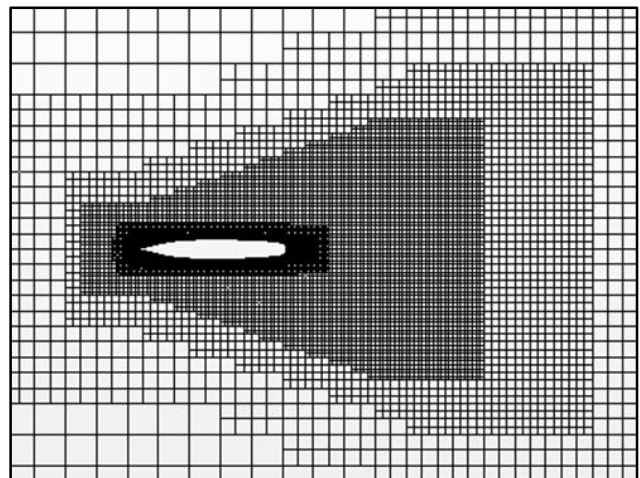


Figure 4 Grid topology: top view, triangular.

The main idea of using triangular volumetric controls is to reduce the computational costs. Since the Kelvin waves have a specific spreading angle ( $19^\circ 28'$ ), it makes sense to transform the rectangular refinements to triangular ones to reduce the computational cell numbers. Details can be found in "Duman (2016)".

A study has been made to compare the effects of triangular and rectangular mesh refinements around the free surface.

It is seen that triangular mesh refinements give almost the same results as the rectangular ones. The order of error is approximately around  $10^{-4}$ .

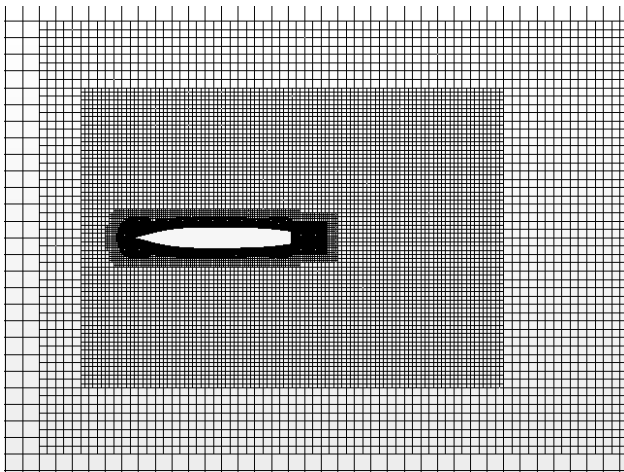


Figure 5 Grid topology: top view, rectangular.

The grid is reduced about  $8.4 \times 10^4$  cell numbers in Kelvin waves adopted grid. Due to the computational capability, triangular volumetric controls are used for the simulations.

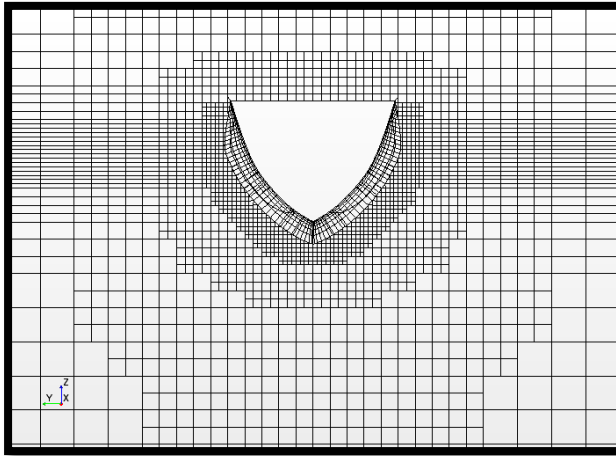


Figure 6 Grid topology:  $x/L=0.2$ .

### 3 COMPUTATIONAL RESULTS

The well-known naval surface combatant DTMB 5415 has been chosen for the investigation of viscous effects on static PMM tests of ships. The ship includes both a sonar dome and a transom stern. The model is un appended except for port and starboard bilge keels, i.e., not equipped with shaft, struts, propellers, or rudders for static drift simulations. The 3-D view of the ship model with a sonar dome and a transom stern including bilge keels is represented in "Figure 7".



Figure 7 3-D view of 5415 "(Duman 2016)".

The model scale is  $\lambda=46.588$ , which is also entitled as DTMB 5512 in literature. The principal particulars of the ship are given in "Table 2".

Table 2 Principal particulars of 5415 "(SIMMAN 2014)"

|               | Model  | Ship          |
|---------------|--------|---------------|
| $\lambda$     | 46.588 | -             |
| $L_{BP}$ (m)  | 3.048  | 142.00        |
| $LWL$ (m)     | 3.052  | <b>142.18</b> |
| $B_{WL}$ (m)  | 0.409  | 19.06         |
| $B_M$ (m)     | 0.429  | 20.00         |
| $T_M$ (m)     | 0.132  | 6.15          |
| $S$ ( $m^2$ ) | 1.370  | 2972.60       |
| ( $m^3$ )     | 0.084  | 8424.40       |
| $C_B$         | 0.507  | 0.507         |
| $C_M$         | 0.821  | 0.821         |
| $F_n$         | 0.280  | 0.280         |

Standard PMM tests consist of both static and dynamic captive model tests "(Gertler 1967)". Static PMM tests are divided into a series of parametric tests, e.g., static drift, static rudder and drift and rudder. The static drift tests have been simulated in this study. Drift angle is changed from 0 to 20 degrees in both viscous and inviscid analyses. The hull is considered as fixed throughout the simulations as in the experiment "(Yoon 2009)". Hydrodynamic analyses have been carried out for a fixed Froude number.

### 3.1 Validation of Forces and Moments

Forces and moments acting on the gravity center of ship are computed for each case. The mean values of these quantities are obtained from time-averages of numerical results. The averaging operations are performed within the quasi-steady state interval.

In order to generalize the problem, it is convenient to make non-dimensionalize the ship-maneuvering motion equations. The procedure follows the prime system of SNAME "(Nomenclature 1952)". According to this system,  $L$ ,  $L/V$  and  $1/2\rho L^2 T$  are used as the dimensions for length, time and mass, respectively, where the  $L$ ,  $V$ ,  $\rho$  and  $T$  are the ship length, ship speed, water density and draft of the ship, respectively.

Table 3 Viscous simulation results.

| Drift angle (°) | X'      | Y'      | N'      |
|-----------------|---------|---------|---------|
| 0               | 0,01722 | 0,00000 | 0,00000 |
| 2               | 0,01726 | 0,01124 | 0,00517 |
| 6               | 0,01812 | 0,03211 | 0,01566 |
| 9               | 0,01934 | 0,04688 | 0,02400 |
| 10              | 0,02001 | 0,05183 | 0,02664 |
| 11              | 0,02043 | 0,05754 | 0,02902 |
| 12              | 0,02122 | 0,06303 | 0,03106 |

|    |         |         |         |
|----|---------|---------|---------|
| 16 | 0,02611 | 0,09372 | 0,03881 |
| 20 | 0,03244 | 0,13059 | 0,04650 |

The viscous and inviscid simulation results are compared with EFD results (“Yoon 2009”) (“Table 3”, “Table 4”) and plotted in comparison with EFD data (“Figure 8”, “Figure 9”, “Figure 10”).

Table 4 Errors between viscous model and EFD results.

| Drift angle<br>(°) | % $\epsilon_X$ | % $\epsilon_Y$ | % $\epsilon_N$ |
|--------------------|----------------|----------------|----------------|
| 0                  | 7,62%          | 100,00%        | 100,00%        |
| 2                  | 6,85%          | 26,97%         | 12,48%         |
| 6                  | 4,43%          | 11,87%         | 4,41%          |
| 9                  | 4,81%          | 0,38%          | 3,89%          |
| 10                 | 6,42%          | 4,55%          | 1,68%          |
| 11                 | 4,48%          | 9,96%          | 3,26%          |
| 12                 | 5,86%          | 12,64%         | 5,46%          |
| 16                 | 9,46%          | 10,61%         | 13,56%         |
| 20                 | 17,96%         | 9,09%          | 15,91%         |

Forces and moments are given in the ship-fixed coordinate system. X', Y' and N' indicate the surge force (resistance), sway force and yaw moment, respectively.

Table 5 Inviscid simulation results.

| Drift angle (°) | X'      | Y'      | N'      |
|-----------------|---------|---------|---------|
| 0               | 0,00658 | 0,00000 | 0,00000 |
| 2               | 0,00687 | 0,00896 | 0,00511 |
| 6               | 0,00768 | 0,02732 | 0,01532 |
| 9               | 0,00904 | 0,04130 | 0,02346 |
| 10              | 0,01021 | 0,04655 | 0,02577 |
| 11              | 0,01094 | 0,05268 | 0,02847 |
| 12              | 0,01234 | 0,05885 | 0,03066 |
| 16              | 0,01939 | 0,08671 | 0,03779 |
| 20              | 0,02438 | 0,11561 | 0,05044 |

Table 6 Errors between inviscid model and EFD results.

| Drift angle<br>(°) | % $\epsilon_X$ | % $\epsilon_Y$ | % $\epsilon_N$ |
|--------------------|----------------|----------------|----------------|
| 0                  | 58,88%         | 100,00%        | 100,00%        |
| 2                  | 57,46%         | 1,20%          | 11,02%         |
| 6                  | 55,72%         | 4,80%          | 2,13%          |
| 9                  | 50,99%         | 11,55%         | 1,55%          |
| 10                 | 45,72%         | 14,28%         | 1,65%          |
| 11                 | 44,04%         | 17,56%         | 5,11%          |
| 12                 | 38,47%         | 18,43%         | 6,66%          |

|    |        |        |        |
|----|--------|--------|--------|
| 16 | 18,70% | 17,30% | 15,83% |
| 20 | 11,36% | 19,52% | 8,79%  |

The inviscid model is insufficient to calculate surge forces (“Table 6”). Viscous model gives better results that are compatible with the EFD data (“Figure 8”).

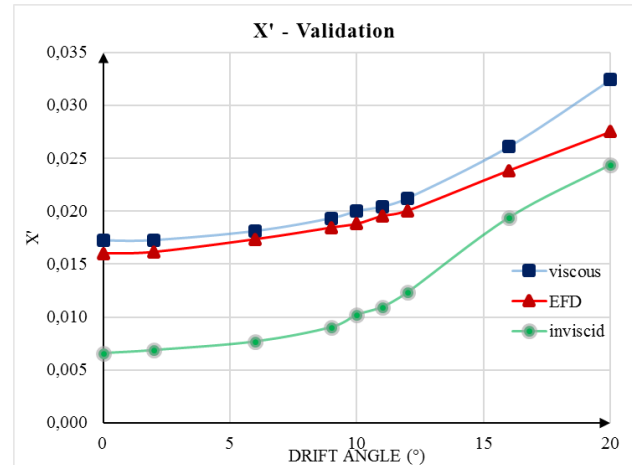


Figure 8 Comparison of X' (surge forces).

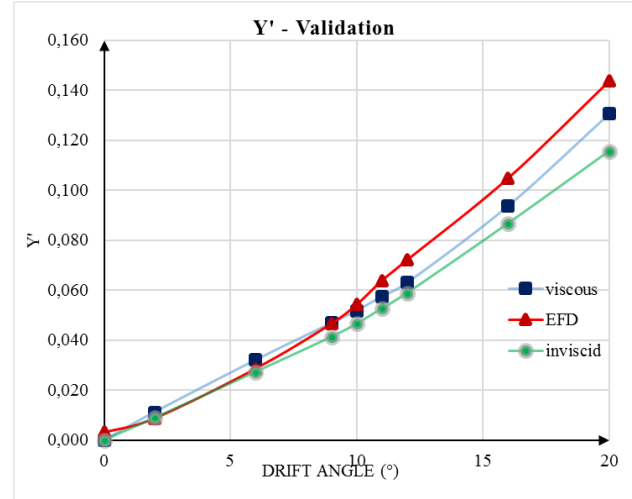


Figure 9 Comparison of Y' (sway forces).

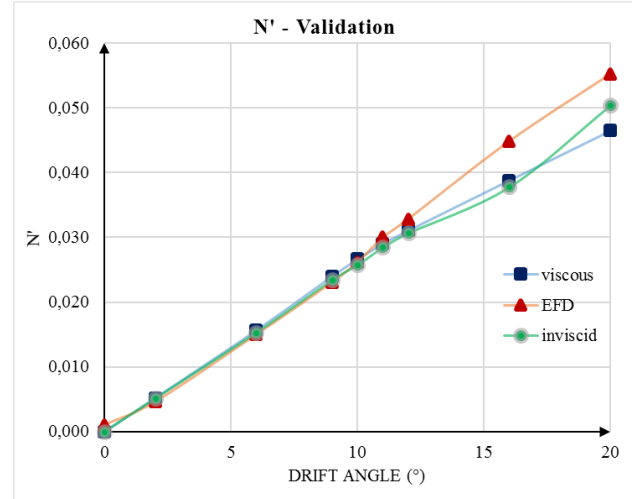


Figure 10 Comparison of N' (yaw moments).

The non-dimensional pressure coefficient  $C_p$  distributions are given in “Figure 11” and “Figure 12”.

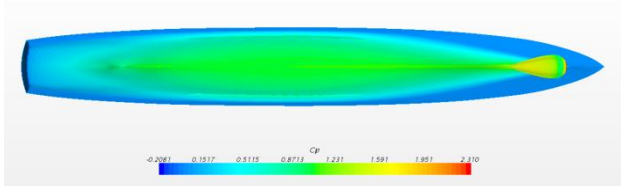


Figure 11 Cp distribution: bottom view.

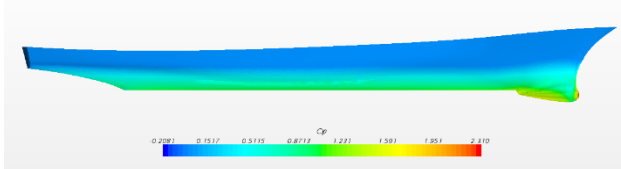


Figure 12 Cp distribution: starboard side view.

The Kelvin wave pattern is given in “Figure 13” for straight-ahead condition.

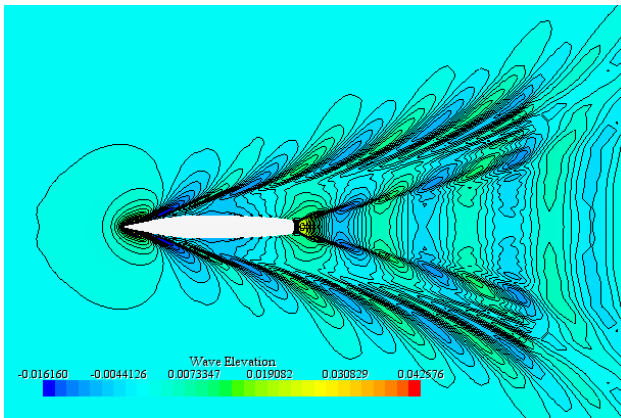


Figure 13 Kelvin wave pattern.

### 3.2 Free Surface Deformations

As known, nonlinearities and flow separations increase at high drift angles. The free surface deformations for several static drift cases are investigated and compared with the available experimental data for both viscous and inviscid models.

The first case is straight-ahead condition. The free surface deformations obtained from numerical analyses are compared with the EFD validation data (“Bhushan et al 2015”) in “Figure 13” by taking a particular section along the hull at  $y/L=0.082$ . The x-axis is non-dimensional x-position and y-axis is non-dimensional wave elevation in “Figure 14”. In this comparison the locations of wave crest and wave trough, are important. It can be said that the general trend of free surface waves can clearly be seen to be compatible with the EFD results.

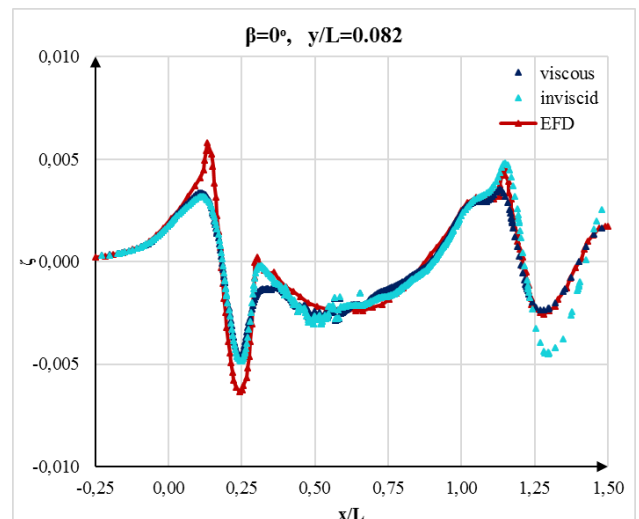


Figure 14 Wave elevations at  $x/L=0.082$  for  $\beta=0^\circ$ .

The wave profile at  $x/L=0.082$  is investigated for finer and coarser grids (“Figure 15”). It can be seen that coarser grid is not capable to capture the free surface deformations than medium and fine grids.

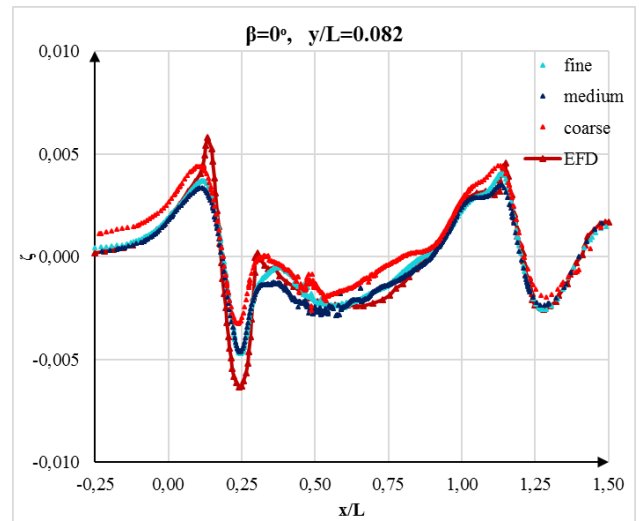


Figure 15 Wave profiles for different grid types.

The next case is  $\beta=2^\circ$  static drift condition. Two sections are taken from the free surface along both leeward and windward sides of the hull at  $y/L=0.212$  (leeward side) and  $y/L=-0.222$  (windward side). The wave profiles on this section are plotted and compared for viscous and inviscid models (“Figure 16”, “Figure 17”).

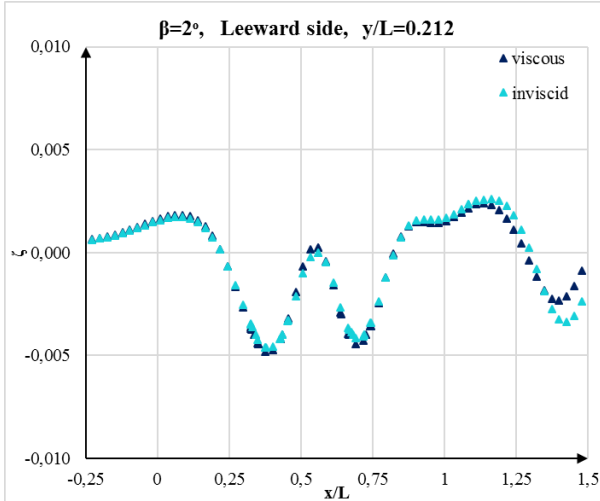


Figure 16 Wave profiles at  $y/L=0.212$  (leeward side).

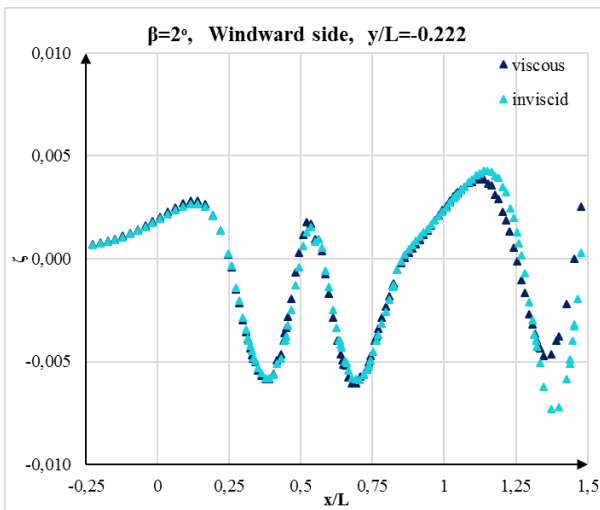


Figure 17 Wave profiles at  $y/L=-0.222$  (windward side).

The trend of the wave profiles of viscous and inviscid models on the leeward and windward sides are agreeable. However, in the wake zone inviscid wave amplitudes are larger than viscous ones, since there is a damping caused by the viscosity.

### 3.3 Comparison of Maneuvering Coefficients

The static drift simulation results are used to calculate the maneuvering coefficients, then are compared with the EFD (“Yoon 2009”) results (“Table 7”).

Table 7 Maneuvering coefficients of viscous and inviscid models in comparison with the EFD results.

|       | Yoon    | URANS   | $\% \epsilon$ | Euler   | $\% \epsilon$ |
|-------|---------|---------|---------------|---------|---------------|
| X*'   | -0,0170 | -0,0175 | 2,94%         | -0,0067 | 60,59%        |
| Xvv'  | -0,1528 | -0,1743 | 14,07%        | -0,1926 | 26,05%        |
| Yv'   | -0,2961 | -0,3389 | 14,45%        | -0,2236 | 24,48%        |
| Yvvv' | -1,9456 | -2,1010 | 7,99%         | -0,4076 | 79,05%        |
| Nv'   | -0,1667 | -0,1580 | 5,22%         | -0,1825 | 9,48%         |
| Nvvv' | -0,4355 | -0,1973 | 54,70%        | -0,8256 | 89,58%        |

Although the inviscid model can capture the free surface waves in a satisfactory manner, the estimation of forces is

not satisfactory as expected. The surge forces are quite different from the EFD data. The sway forces and yaw moments results seem to be close to viscous results and this may mislead one about the applicability of inviscid model in ship maneuvering problems. However, if the maneuvering coefficients obtained from the numerical analyses are considered, it is clearly seen that viscous model gives better results than the inviscid model.

### 3.4 Fast Time Simulation of Ship Maneuvering

A computer program called as DYNEQNOMS has been developed “by Duman (2016)” to solve the differential equations of ship maneuvering motion simultaneously according to the Abkowitz’s mathematical model.

The hydrodynamic derivatives calculated from the numerical analyses are put into the ship maneuvering simulator to simulate the turning maneuver. Besides the hydrodynamic derivatives, rudder deflection angles and principal particulars of the ship are used as inputs.

Motion equations are written in matrix form and solved via Gauss-Jordan Elimination method. The simple Euler method is used to calculate each velocity component for the next time step. The time step is chosen as  $2 \times 10^{-2}$ . Since the linear and angular velocity terms are known for each time step, the yaw angle, drift angle, turning circle diameter, tactical diameter, advance and transfer distances are calculated.

The turning maneuvering of 5415 is simulated by DYNEQNOMS and the trajectory of the ship is presented in “Figure 18”, where the x-axis and y-axis are the surge and sway directions in meters, respectively. The yaw rate, sway velocity and drift angle converged to constant values, which means the ship turns on a steady turning circle. The steady turning radius is presented with the linear model approximation and several empirical formulas. The tactical diameter is compared with the experimental and numerical validation data (“Table 8”).

Table 8 Turning maneuver simulation results

|                     | Steady turning<br>radius (m) | Tactical<br>diameter<br>(m) |         |
|---------------------|------------------------------|-----------------------------|---------|
| Non-linear<br>model | 0.87LPP                      | DYNEQNOMS                   | 4.79LPP |
| Linear<br>model     | 1.25LPP                      | FORCE PMM                   | 4.05LPP |
| Thieme              | 0.26LPP                      | MARIN-Free<br>sailing       | 4.55LPP |
| Schoenherr          | 2.61LPP                      | MARIN–<br>SurSim            | 2.6LPP  |
| Lyster &<br>Knight  | 2.46LPP                      | IOWA-RANS<br>Cst RPM        | 4.6LPP  |

The nonlinear model estimates the steady turning diameter lower than linear model. The chosen empirical formulas

were proposed for cargo ships and not suitable for warships. As seen, the tactical diameter obtained numerically is compatible with the available validation data.

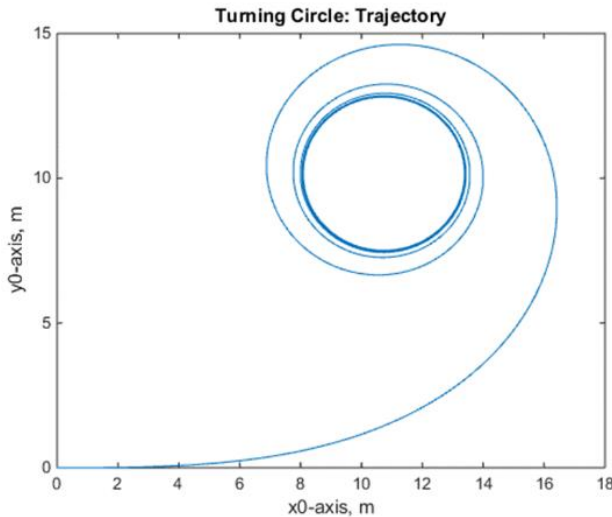


Figure 18 Trajectory of the ship during the turning motion.

#### 4 CONCLUSIONS

The nature of ship maneuvering problems is highly complex and nonlinear. Viscosity has a significant role in order to estimate the ship-maneuvering performance. The computational results of both URANS and Euler approaches are compared with each other and available experimental data. It is shown that viscous results have been in good agreement with the EFD data. The inviscid method is not sufficient to estimate the surge forces, but can be used to capture the free surface deformations in a satisfactory manner. Since there is no damping caused by viscosity, inviscid model is insufficient for capturing the wave deformations in the wake zone and for positive drift angles it may also be insufficient along the hull.

The inviscid sway forces and yaw moments results seem to be close to viscous results and this may mislead one about the practical applicability of inviscid model in ship maneuvering problems in a positive manner. However, if the maneuvering coefficients obtained from the numerical analyses are considered, it can be clearly seen that the viscous model gives better results than the inviscid model. The hydrodynamic derivatives obtained from viscous analyses are estimated in a satisfactory manner for practical applications. The viscous model is found to be suitable for the presented ship maneuvering problem considering the overall table.

In addition, the turning maneuvering motion is simulated by DYNEQNOMS. The turning diameter is compared with the linear model and the empirical formulas. The tactical diameter is compared with the available validation data. The hydrodynamic coefficients are used as in the literature. The ship maneuvering simulator is found to be successful in solving the ship maneuvering equations.

In the future studies, the dynamic PMM tests will be simulated with URANS method and maneuvering coefficients will be calculated including acceleration and angular velocity terms. The heel effect on the turning maneuver will be taken into account. The computational grid quality will be increased. In addition, the definite maneuvers, e.g., turning maneuver, the zig-zag, spiral and pull-out maneuvers, will be simulated with using the determined maneuvering coefficients as inputs to the ship maneuvering simulator. The maneuvering performance of multihull vessels such as; catamaran, trimaran, will be investigated.

#### REFERENCES

- Abkowitz, M.A., (1964). Lectures on ship hydrodynamics – Steering and maneuvering (No. Hy-5). Hydro & Aerodynamic Laboratory, Lyngby, Denmark.
- Bal, S., (2008). Prediction of wave pattern and wave resistance of surface piercing bodies by a boundary element method. *Int. J. Numer. Methods Fluids* 56, 305–329. doi:10.1002/fld.1527
- Bertram, V., (2012). *Practical ship hydrodynamics*, 2. ed. ed. Elsevier, Oxford.
- Bhushan, S., Xing, T., Carrica, P., Stern, F., (2007). Model-and Full-scale URANS/DES Simulations for Athena R/V Resistance, Powering, and Motionos. *Numer. Ship Hydrodyn. Conf. II*, 122–142.
- Bhushan, S., Yoon, H., Stern, F., Guilmeneau, E., Visonneau, M., Toxopeus, S., Simonsen, C., Aram, S., Kim, S.-E., Grigoropoulos, G., (2015). CFD VALIDATION FOR SURFACE COMBATANT 5415 AT STRAIGHT-AHEAD AND 20 DEGREE STATIC DRIFT CONDITIONS (Technical Report No. 493). University of Iowa, IIHR-Hydroscience & Engineering.
- Dogrul, A., Celik, F., (2016). AN EXPERIMENTAL AND NUMERICAL INVESTIGATION OF RESISTANCE COMPONENTS AND FREE SURFACE DEFORMATIONS FOR A MEDIUM SPEED DISPLACEMENT VESSEL. *Brodogradnja* 47–65. doi:10.21278/brod67204
- Duman, S., (2016). INVESTIGATION OF THE TURNING PERFORMANCE OF A SURFACE COMBATANT WITH URANS (Master's Thesis). Istanbul Technical University.
- Ferziger, J.H., Perić, M., (2002). *Computational methods for fluid dynamics*, 3., ed. ed. Springer, Berlin.
- Fonfach, J.M.A., (2010). Numerical study of the hydrodynamic interaction between ships in viscous and inviscid flow (PhD Thesis). Universidade de Lisboa.
- Gertler, M., (1967). THE DTMB PLANAR-MOTION-MECHANISM SYSTEM (TEST AND EVALUATION REPORT No. AD659053). *Naval Ship Research and Development Center*, Washington, DC.

- Gertler, M., (1966). Cooperative Rotating-arm and Straight line Experiments with ITTC Standard model (Mariner type Ship) (No. 2221). David Taylor Model Basin.
- He, S., Kellett, P., Yuan, Z., Inceciik, A., Turan, O., Boulogeoris, E., (2016). Manoeuvring prediction based on CFD generated derivatives. *J. Hydron. Ser B* 28, 284–292. doi:10.1016/S1001-6058(16)60630-3
- Hirt, C., Nichols, B., (1981). Volume of fluid (VOF) method for the dynamics of free boundaries. *J. Comput. Phys.* 39, 201–225. doi:10.1016/0021-9991(81)90145-5
- ITTC, (2011). Practical Guidelines for Ship CFD Applications. Presented at the Proceedings of 26th ITTC, Hague.
- Kim, H., Akimoto, H., Islam, H., (2015). Estimation of the hydrodynamic derivatives by RaNS simulation of planar motion mechanism test. *Ocean Eng.* 108, 129–139. doi:10.1016/j.oceaneng.2015.08.010
- Kim, W.J., Van, S.H., Kim, D.-H., (2001). Measurement of Flows Around Commercial Ship Models. *Exp. Fluids* 31, 567–578.
- Larsson, L., Stern, F., Bertram, V., (2003). Benchmarking of Computational Fluid Dynamics for Ship Flows: The Gothenburg 2000 Workshop. *J. Ship Res.* 47, 63–81.
- Lewis, E.V. (Ed.), (1989). Motions in waves and controllability, 2. revision, 1. print. ed, Principles of naval architecture. Society of Naval Architects and Marine Engineers, Jersey City, NJ.
- Moreira, L., Guedes Soares, C., (2003). Dynamic model of manoeuvrability using recursive neural networks. *Ocean Eng.* 30, 1669–1697. doi:10.1016/S0029-8018(02)00147-6
- Nomenclature for Treating the Motion of a Submerged Body through a Fluid (Technical and Research Bulletin No. 1–5), (1952). SNAME.
- Oltmann, P., (2000). 25 years Computerized Planar Motion Carriage at HSVA – A resume. Presented at the International Workshop on Ship Maneuvrability at the Hamburg Ship Model Basin, Hamburg.
- Sakamoto, N., Carrica, P.M., Stern, F., (2012). URANS simulations of static and dynamic maneuvering for surface combatant: part 1. Verification and validation for forces, moment, and hydrodynamic derivatives. *J. Mar. Sci. Technol.* 17, 422–445. doi:10.1007/s00773-012-0178-x
- SIMMAN, (2014). Geometry and Conditions of US Navy Combatant [WWW Document]. simman2014.dk. URL <http://simman2014.dk/ship-data/us-navy-combatant/geometry-and-conditions-us-navy-combatant/>
- Simonsen, C.D., Stern, F., (2003). Verification and validation of RANS maneuvering simulation of Esso Osaka: effects of drift and rudder angle on forces and moments. *Comput. Fluids* 32, 1325–1356. doi:10.1016/S0045-7930(03)00002-1
- Stern, F., Wilson, R.V., Coleman, H.W., Paterson, E.G., (2001). Comprehensive Approach to Verification and Validation of CFD Simulations—Part 1: Methodology and Procedures. *J. Fluids Eng.* 123, 793. doi:10.1115/1.1412235
- Strom-Tejsen, J., Chislett, M.S., (1966). A Model Testing Technique and Method of Analysis for the Prediction of Steering and Manoeuvering Qualities of Surface Vessels (No. Hy-7). Hydro & Aerodynamic Laboratory, Lyngby, Denmark.
- Uslu, Y., Bal, S., (2008). Numerical Prediction of Wave Drag of 2-D and 3-D Bodies under or on a Free Surface. *Turk. J. Eng. Environ. Sci.* 32, 177–188.
- Viviani, M., Depascale, R., Sebastiani, L., Bonvino, C.P., Dattola, R., Soave, M., (2003). Alternative Method for the Identification of Hydrodynamic Coefficients from Standard Manoeuvres. Presented at the MARSIM'03, p. RC-5.
- Yoon, H., (2009). Phase-averaged stereo-PIV flow field and force/ moment/motion measurements for surface combatant in PMM maneuvers (PhD Thesis). University of Iowa.
- Yoon, H.K., Rhee, K.P., (2003). Identification of hydrodynamic coefficients in ship maneuvering equations of motion by Estimation-Before-Modeling technique. *Ocean Eng.* 30, 2379–2404. doi:10.1016/S0029-8018(03)00106-9

*(Intentionally left blank)*

## **Design and Implementation of a Planar Motion Mechanism at ITU Ship Model Basin**

**Cansın Özden<sup>1\*</sup>, Sertaç Kurdoğlu<sup>1</sup>, Ersin Demir<sup>1</sup>**

<sup>1</sup>*Istanbul Technical University, Faculty of Naval Architecture and Ocean Engineering, 34469 Maslak-Istanbul, Turkey*

**Abstract:** Planar Motion Mechanisms (PMM) present an efficient way of estimating manoeuvring derivatives required to solve the equations of motion for surface vessels and submarines. Many towing tanks and circulating water channels around the world are equipped with such facilities with varying characteristics. Within the framework of a recent research development programme a new PMM system, designated as ITU-PMM, has been designed to be installed in the Ata Nutku Ship Model Basin (ANSMB) at Istanbul Technical University (ITU). Prior to the implementation of the main PMM, a smaller version was designed, constructed and installed at the circulating water channel (ITU-CWC-PMM), in order to test the viability of the main PMM system to be installed at the towing tank. This paper describes the main characteristics both systems and explains the design procedure.

**Keywords:** manoeuvring, planar motion mechanism, hydrodynamic derivatives.

### **1 INTRODUCTION**

A common way of describing hydrodynamic forces acting on a surface vessel or submerged body is to employ the idea of hydrodynamic (or manoeuvring) 'derivatives'. Consequently, in order to solve the equations of motion for any given configuration it is necessary to know these coefficients with reasonable accuracy. Many attempts have been made in the past to fulfil this requirement by utilizing various experimental techniques, such as wind tunnels and the rotating arm facilities. However, Planar Motion Mechanism (PMM) systems incorporate in one device a means for experimentally determining all of the hydrodynamic coefficients required in the equations of motion for surface vessels and submerged bodies (Gertler 1967).

The concept of PMM first developed by A. Goodman for use in determining lateral stability of aircraft. The first application of PMM systems, as a captive manoeuvring test technique, was initiated at David Taylor Model Basin and the DTMB PMM system was placed into regular service in 1957 (Gertler 1967). This was followed by similar devices all over the world, including but not limited to: University of California, Berkeley (1962), Institute für Schiffbau, Hamburg (1963), Technological University Delft (1963), Hydronautics (1963), Bassin d'Essais des Carennes (1964), University of Tokyo (1965), Hydro-Aerodynamic Laboratorium, Lyngby (1966), Admiralty Experiment Works (1966), Nagasaki Experimental Tank (1969); Hamburgische Schiffbau-Versuchsanstalt (HSVA) (1976), University of Southampton (1987), Maritime Research institute (MARIN) (1981), Australian Maritime College (AMC) (1995), and National Research Council Institute for Ocean Technology (NRC/IOT) (1996).

In order to compare the measurements made at different facilities, the 11th ITTC (1966) initiated a benchmark

study based on a Mariner type hull form, to compare different captive model test techniques. The results of co-operative tests on the Mariner form showed that the values of derivatives varied quite widely Gertler (1969).

The 23th ITTC Specialist Committee on Esso Osaka have also produced a good recent reference on ship manoeuvring forces, with emphasis on manoeuvring predictions for the Esso Osaka, a tanker that has been the subject of extensive full-scale and model test studies (Crane 1979).

The SIMMAN 2008 workshop was the outgrowth of discussions and planning conducted by the 24th and 25th ITTC Maneuvering Committees. The hull forms chosen for the workshop were those recommended as benchmark ships by the 24th ITTC; two tankers (KVLCC1 and KVLCC2), a containership (KCS) and a surface combatant (DTMB 5415). An extensive model test campaign was performed for each of the three hulls, comprising both PMM and CMT tests in appended and bare hull conditions as well as free model tests. Several of the tests were carried out in more than one facility. Test cases were selected for which the participants should make simulations. Prior to the workshop, the submitted simulation results were compiled and plotted against the benchmark data (Stern & Agdrup 2009).

In order to assess the quality of PMM test results the 21<sup>st</sup> ITTC Manoeuvrability Committee (1996) has formulated a Recommended Standard PMM test procedure, which has been revised several times.

Recently, in parallel with increasing computational power of computers and availability of commercial software, CFD based computational techniques have been widely used to compute the hydrodynamic forces. Besides the time and effort required for mesh generation, CFD based computational methods require several trade-offs to be

\* Corresponding author e-mail: ozden@itu.edu.tr

considered when developing the most appropriate mesh for the prediction of flow around a vessel with a yaw angle. These trade-offs are related to the level of operator skill, time required for creating the mesh, computer power required for solving the problem, and the accuracy of results. Furthermore, CFD based computations strongly depend on the type and number of grid elements and the turbulence model. It is widely accepted that when a CFD based methodology is first applied to a new ship type, it should be validated with the results of model experiments.

In recent years, Turkish Naval Forces in collaboration with ITU and private design offices and shipyards, have been designing and building various types of naval vessels. Standard model tests, such as resistance, powering, and seakeeping are conducted at ITU Ata Nutku Ship Model Basin (ANSMB). However, the lack of manoeuvring test facilities either resulted in sensitive naval design projects being tested abroad, or manoeuvring performance being estimated by less reliable semi-empirical or CFD based methods.

In order to provide the ability to perform PMM tests at ITU-ANSMB towing tank, a collaborative research program was initiated between the Ministry of Defence, ADIK shipyard, and Istanbul Technical University. This program is scheduled to be completed by the end of 2017. Prior to the implementation of the main CPMM, a smaller version was designed, constructed and installed at the circulating water channel (CWC-PMM), in order to test the viability of the main PMM system to be installed at the towing tank. This paper describes the main characteristics both systems and explains the design procedure.

## 2 ITU-CWC-PMM

The ITU CWC has a working section which is 6 m long, 1.5m wide and 1 m deep, and forms a continuous circuit for 2 m<sup>3</sup> of water. 1.5 m diameter axial pump produces circulatory water flow at variable speeds up to a maximum of 1.5 m/s in the working section.

The principal advantage in using a CWC for hydrodynamic testing is the unlimited run-time length, which is not available in a towing tank. Since the water flow passes the model continuously, and assuming no variation in the flow speed over time, the duration of tests can be as long as necessary. This enables to extend PMM testing to low frequencies.

ITU-CWC-PMM has been designed and constructed for testing the viability and software development of the main PMM system.

The main goal for CWC-PMM was to have a lightweight design such that two researchers can handle the set the system for tests so that the usual daily tasks of ANSMB would not be disturbed. This mini PMM has a 1.5m long triangular prism shape main frame made of aluminium sigma profiles. On this frames, an upper and a lower linear 25mm Schneeberger rail have been attached, for guiding the sway motions. Sway motion is imposed by a double side fixed 25mm Gten ball screw which is driven by a 1FK70422AF711RA0 Siemens synchronous servo motor

with a power of 0.82kW and a nominal 3000 RPM. Due to the 1:5 reduction of linear ball screw, use of a reduction gear found unnecessary for sway motion. Yaw table was built out of 6000 grade aluminium where the model was driven by a 1FK70422AF711RA0 Siemens synchronous servo motor attached to a Shimpo VRL120 reduction gear with a ratio of 1:50.

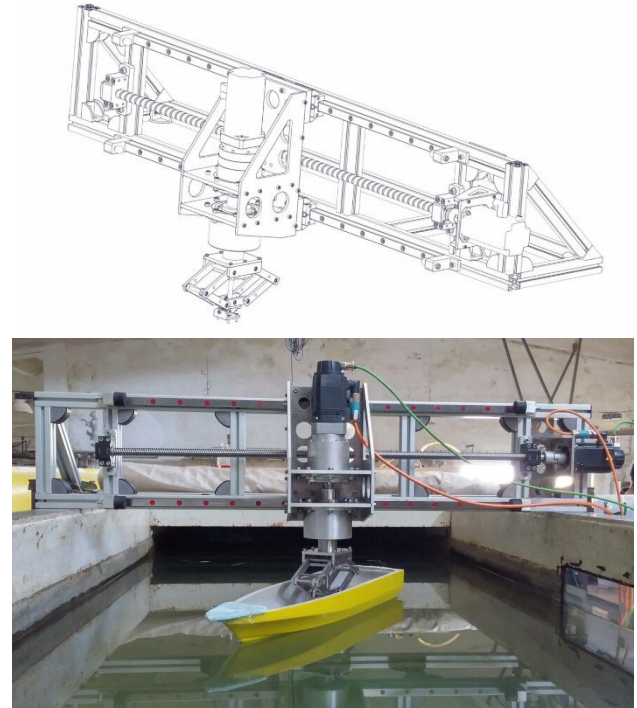


Figure 1, 2: Photo of CWC-PMM system

**Table 1 – ITU-CWC-PMM Specifications**

|                    |   |
|--------------------|---|
| CWC Length         | 6 m   |
| CWC Width          | 1.5 m   |
| CWC Depth          | 1 m   |
| Max Speed          | 1.5 m/s   |
| Planned Tests      | Static drift, pure sway, pure yaw, yaw and drift combined |
| Typical Ship Model | DTMB 5415   |
| Model Length       | 0,763 m   |
| Model Weight       | 1.3 kg  |
| Model Test Speed   | 1.5 m/s   |
| Static Drift Angle | 20 degrees  |
| Yaw Angle          | 20 degrees  |
| Sway Amplitude     | ±0.3125 m   |
| Sway Velocity      | 0.5 m/s   |
| Yaw Rate           | 20 °/s  |

Model is attached to the PMM system with a pantograph which enables to work with models which has different drafts and also frees model for pitch and heave motions while fixing for roll.

The CWC-PMM has a sway amplitude of 0.3125m since the width of the CWC is 1:4 of the main towing tank where the large PMM will be installed. So all the values of CWC-PMM is fixed as one fourth of the main system so called ITU-PMM.

Servomotors of CWC-PMM is selected from the same specifications that would be used in ITU-PMM but with lower torque capacities. By this way it would be possible to use the same software on ITU-PMM which is generated on CWC-PMM. Servo motors controlled by Sinamics S120 motor control modules were PMM motions generated by the use of 6AU1425 Simotion Drive-Based Motion Control Unit.

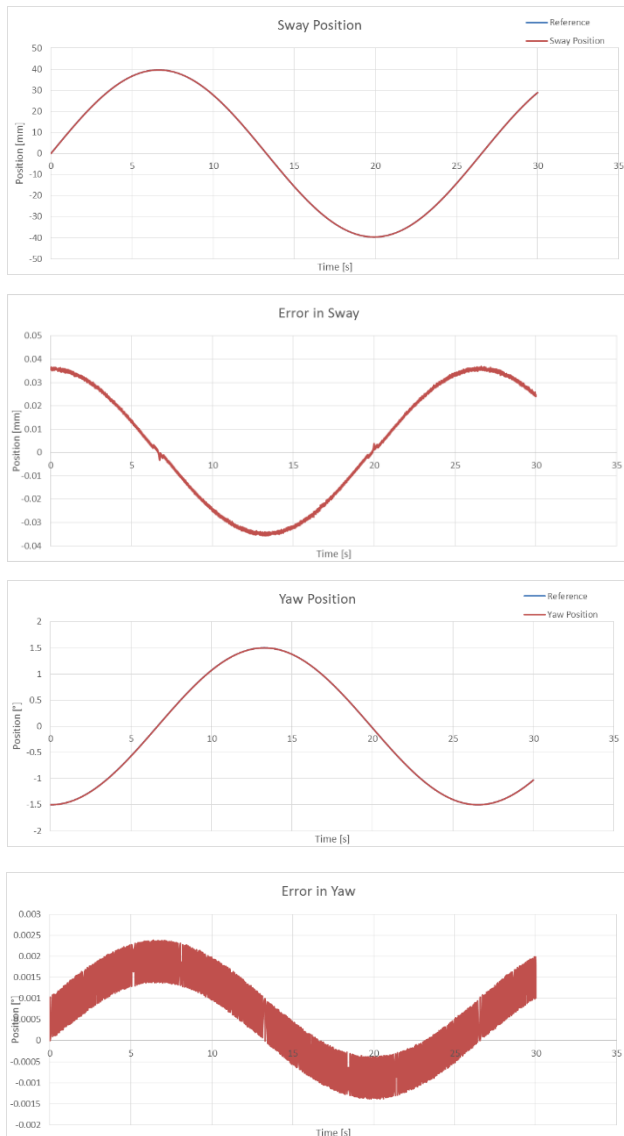


Figure 3, 4, 5, 6: Position comparison of analytically generated and encoder values

One of the unique feature of ITU PMM over the existing PMM systems in different research facilities is the use of

motion controller. In many facilities PMM motions are generated by sliding crank or so called scotch-yoke mechanisms, with these systems it is possible to generate harmonic sinusoidal motions with lower amplitudes. Control systems for scotch-yoke mechanisms are very easy and dealing only for keeping the shaft speed constant on changing loads. Some newer PMM mechanisms use PLC (Programmable Logic Controller) for generation of PMM coordinates and controlling the servo motors to drive the mechanism however ability of PLCs for generating interpolating servo motions found coarse. Thus, in order to get highly precise transient motion, we sacrificed the simplicity of control manner while mechanically simplifying the system.

Investigation of the accuracy of CWC-PMM system, sway and yaw motions has been generated by the Simotion system and imposed to servo motors. Results were compared with the analytically calculated positions. As can be seen in Figure 3 to 6, the error of the system is in magnitude of  $O^3$ .

### 3 ITU-PMM

The ITU towing tank has dimensions of 160 m length, 6 m wide and 4 m depth. The PMM is positioned on a mounting frame on the model carriage. Scale models are attached to the PMM using a strut mount that runs vertically from the rotation post to the top of the model. Two servo-motors are used to provide the PMM motions: one is dedicated to providing translation and the other rotation. The motors are driven under closed loop control to provide the desired sinusoidal motions. However, since the motors are independently controlled, the PMM is also capable of providing non-sinusoidal motions, within the limitations of the mechanism.

The maximum static rotation in the horizontal plane is  $\pm 90^\circ$ . In the dynamic mode, the maximum peak to peak horizontal oscillation is 2.5 m and the maximum peak to peak rotational oscillation is 30°. The oscillatory frequency ranges from 0.01 Hz to 0.20 Hz. The maximum translational rate is therefore 0.19 m/s.

The PMM system has two modes of operation: namely the ‘static’ and ‘dynamic’ modes. The static mode, including steady drift and oblique towing oblique towing with rudder deflection tests, allows the models to be held stationary relative to the moving flow at various angles of incidence. In the dynamic mode, which includes, pure sway, pure yaw, and yaw with drift tests, the PMM system moves in translation and rotation relative to the water velocity.

ITU-PMM is designed to be attached on the aft side of the main carriage of the ANSMB’s large towing tank. A separate system which would be pulled by the carriage was also considered but lifting capacity of the tank crane, storage and installation problems were some of the drawbacks considered and after the conceptual designs showed the possibility of a balcony type lightweight design, it is accepted as a permanent part of the main carriage.

**Table 2: ITU-PMM Specifications**

|                        |  |
|------------------------|--|
| Towing Tank Length     | 160 m  |
| Towing Tank Width      | 6 m  |
| Towing Tank Depth      | 3.4 m  |
| Max Carriage Velocity  | 6.0 m/s  |
| Planned PMM Tests      | Static drift, pure sway, pure yaw, yaw and drift combined                  |
| Typical Ship Model     | DTMB 5415  |
| Model Length           | 3 m  |
| Model Weight           | 250 kg   |
| PMM Max Speed          | 3 m/s  |
| Max Static Drift Angle | 35 derece  |
| Max Yaw Angle          | 20 derece  |
| Sway Amplitude         | $\pm 1.25$ m   |
| Max Sway Speed         | 1.5 m/s  |
| Max Sway Acceleration  | 1 m/s <sup>2</sup>   |
| Max Yaw Rate           | 20 °/s   |
| Max Longitudinal Force | 500 N  |
| Max Transverse Force < | 500 N  |
| Max Yaw Moment         | 500 Nm   |
| Dynamometer            | Izumi 6 Componenet<br>Loadcell<br>Fx, Fy, Fz :500N ,<br>Mx, My, Mz : 500Nm |

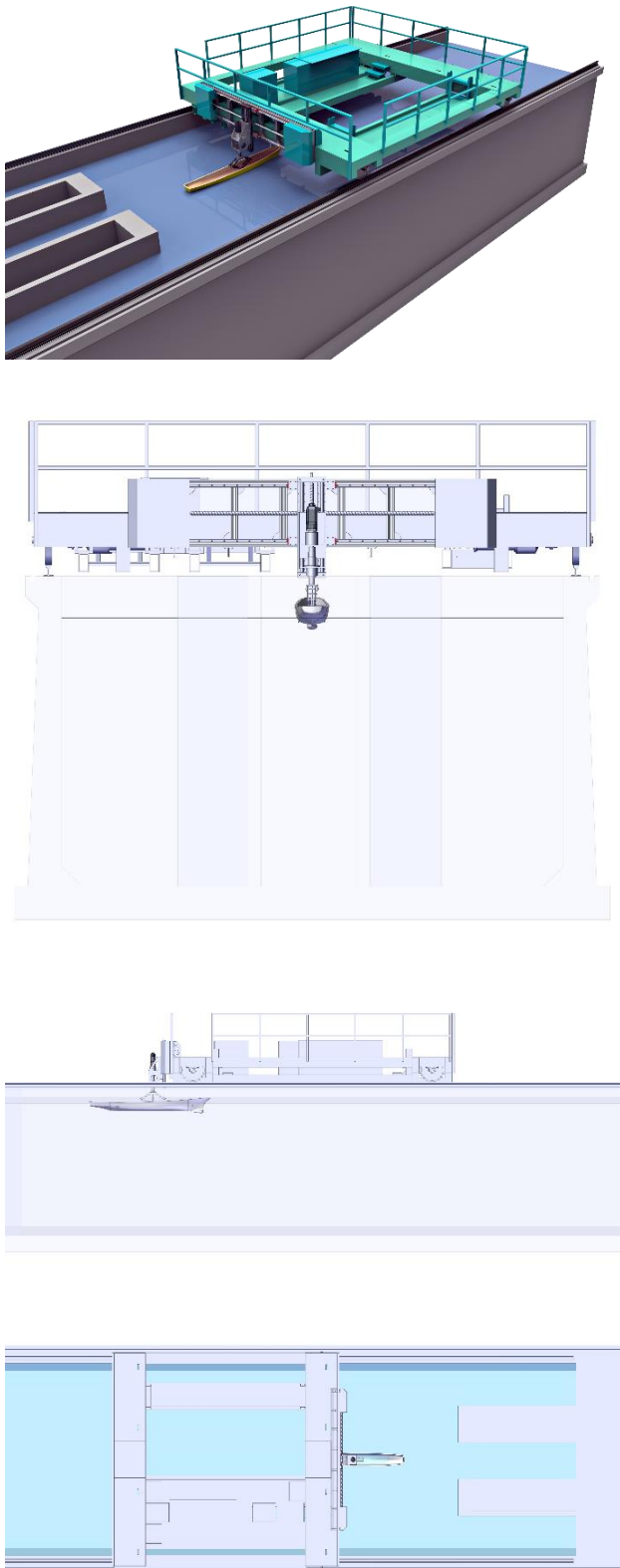


Figure 7: Drawings of the ITU-PMM System.

However, assembling the system on the aft side of the carriage comes with the necessity of some minor modifications on the main frame. Some T profiles need to be attached by bolts or welds at the bottom side to support the PMM system and also some reinforcements at the top side is required. Because topside reinforcements prevents the covers of carriage wheel drive motors, these covers need to be modified. Due to the stiffness and lightweight of sigma profiles experienced on the construction of CWC-PMM system, it is considered to use these kind of profiles also on the ITU-PMM system. Thus, designed PMM system has a width of 4 m in order to allow a sway amplitude of  $\pm 1.25$ m. Same as the CWC-PMM; on aluminium sigma profile frames, an upper and a lower linear 40mm Schneeberger rail have been attached, for guiding the sway motions. Sway motion is imposed by a double side fixed 50mm Gten ball screw which is driven

by a 1FK7064-4CC71-1CA2 Siemens synchronous servo motor with a nominal torque of 12Nm and a nominal 3000 RPM. Due to the 1:5 reduction of linear ball screw, use of a reduction gear found unnecessary for sway motion. Yaw table is planned to be built out of AISI 316L grade stainless steel where the model was driven by a 1FK7064-4CC71-1CA2 Siemens synchronous servo motor attached to a two stage Shimpo VRB180 reduction gear with a ratio of 1:100.

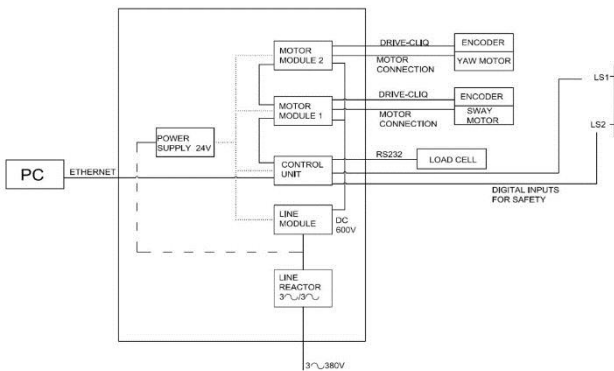


Figure 8: Electrical diagram of the ITU-PMM System.

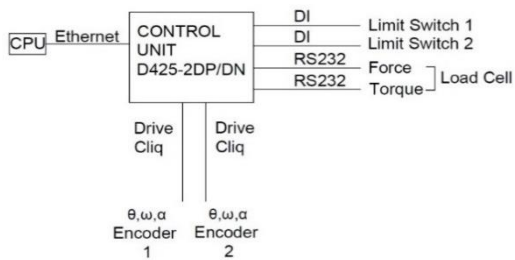


Figure 9: Control system connections

Model is attached to the PMM system with a pantograph which enables to work with models which has different drafts and also frees model for pitch and heave motions while fixing for roll. In order to prevent collision of PMM system with the dock at the end of the towing tank, it was found necessary to have an electrically driven elevator system for the yaw balcony. During the approaching of the car to the dock and for the model attachment, the yaw table and all its assembled parts such as dynamometer, strut, pantograph etc. are elevated. This elevator system also consist of linear rail, car and ball screw mechanisms and an electric motor with brakes.



Figure 10: Izumi multicomponent load cell and apparatus

Although, the primary calculations showed that  $F_x$  and  $F_y$  forces over 500N and  $M_z$  moment over 500Nm is not expected for the planned PMM tests, it is decided to order a multi component loadcell which also measure  $F_z$  force and  $M_x$  and  $M_y$  moments. The capacity of ITU-PMM multi component loadcell (Figure 11) is as follows:  $F_x$ ,  $F_y$ ,  $F_z$ : 500N,  $M_x$ ,  $M_y$ ,  $M_z$ : 500Nm.

Servo motors controlled by Sinamics S120 motor control modules were PMM motions generated by the use of 6AU1425 Simotion Drive-Based Motion Control Unit. Simotion Unit is capable of generating very precise interpolating data for the accurate PMM motions and also other desired transient ship motions. In ITU-PMM, Simotion is generating signals for servo drives and close loop controlling the motion with the feedbacks collected from the motor encoders. Also simultaneously collect loadcell data and correlate with encoder positions thus preparing the PMM test outputs.

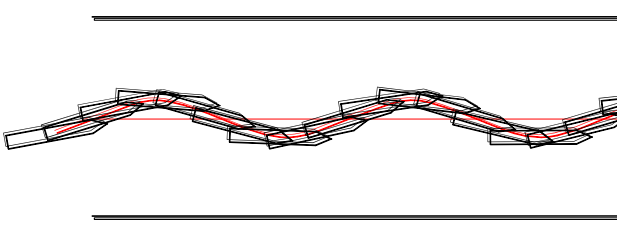


Figure 11: A primary view of the motion tracking software

It will be possible to use the software which is generated by using the CWC-PMM in small scales. A software package of the ITU-PMM is planned to consist; a- a user display where the user can select the parameters and modes of PMM test, b- motion generation software which calculates the motion position signals for servo drives, c-

motion tracking and simulation software which shows the model position during or after the test, d- database for the collected data.

#### 4 CONCLUSIONS

In conclusion, two PMM systems has been designed for ITU Ata Nutku Ship Model Basin; one is for operation on circulation water tunnel and the larger one is for the towing tank. CWT-PMM has been built and the preliminary results obtained by the system is presented. Design preferences of ITU-PMM is described.

#### 5 ACKNOWLEDGEMENTS

This research was sponsored by the Undersecretariat for Defense Industries under Grant 991-LST00-0090-001-000-0. Authors would like to thank Prof. Dr. Ömer Gören and Prof. Dr. Kadir Sariöz for their support, guidance and patience since the very beginning of the project. Authors wish to thank ADİK Shipyard for their support and would also wish to acknowledge Mr Azmi Ak and Mr Sinan Burunsuz of DATUM – Denizaltı Teknolojileri ve Uygulamalı Müh Company, Mr Haluk Çoban from Turkish Lloyd and Önder Er of Er Bobinaj for their valuable help during design and construction of the systems.

#### REFERENCES

- Benedetti, L., Bouscasse, B., Broglia, R., Fabbri, L., La Gala, F., and Lugni, C. (2007), PMM Model Test with DDG51 Including Uncertainty Assessment, (Report) Istituto Nazionale Per Studi Ed Esperienze Di Architettura Navale (INSEAN).
- Cardases, M. H., Hyde, K. M., and Makinson, I. D. (1987). ‘The Design and Construction of a Horizontal Planar Motion Mechanism’, Department of Ship Science, University of Southampton.
- Carrica, P., Ismail, F., Hyman, M., Bhushan, S., and Stern, F. (2013), Turn and Zigzag Maneuvers of a Surface Combatant using a URANS Approach with Dynamic Overset Grids, Journal of Marine Science and Technology, 18, 166–181.
- Gertler, M. (1967). ‘The DTMB Planar-Motion-Mechanism System’, Naval Ship Research and Development Center, Report No 2523.
- Glansdorp, C.C.; A new planar motion mechanism for model oscillation 22nd DRG-Seminar on Advanced Hydrodynamic Testing Facilities The Hague, april 1982
- Goodman, A. (1960), Experimental Techniques and Methods of Analysis used in Submerged Body Research, In Third Symposium on Naval Hydrodynamics, Scheveningen, Netherlands.
- Grim, O., Oltman, P., Sharma, S.D., Wolff K. (1976). ‘CPMC - A Novel Facility for Planar Motion Testing of Ship Models’. Hamburg, Technische Universität Hamburg-Harburg, Bericht Nr 345.
- Keil, H. and Thiemann, H. (1963). ‘Ein Oszillatator zur Ermittlung Hydrodynamischer Massen und Dampfungs-werte’, Institute für Schiffbau, Hamburg, Bericht Nr 120.
- Motori, S. and Fujino, M. (1965). ‘On the Measurement of the Stability derivatives by Means of Forced Yawing Technique’. Journal of Zosen Kiokai **118**.
- Oltmann, P., 2000, “25 years Computerized Planar Motion Carriage at HSVA – A résumé”, International Workshop on Ship Manoeuvrability at the Hamburg Ship Model Basin, Hamburg, 19 pp
- Paulling, J.R. and Sibul, O.J. (1962). ‘New Equipment and Techniques for the Experimental Evaluation of Ship’s Lateral Stability’, University California, Berkeley, IER Report No .
- Simonsen, C. D. (2004), PMM Model Test with DDG51 including Uncertainty Assessment, (Report) FORCE Technology, Lyngby, Denmark.
- Strom-Tejsen, J. and Chislett, H.S. (1966). ‘A Model Testing Technique and Method of Analysis for the Prediction of Steering and Manoeuvring Qualities of Surface Vessels’. Proceedings of 6<sup>th</sup> Symposium on Naval Hydrodynamics, Washington D.C.
- White, F. (1986). Fluid Mechanics. 2nd ed. McGraw- Hill Book Company.
- Zunderdorp, H.J. and Buitenhak, M. (1963). ‘Oscillator Techniques at the Shipbuilding Laboratory’, Technological University, Delft, Report

## Performance Prediction for Tractor type Escort Tugs

Gürbüz Bilici<sup>1</sup>, Çağrı Aydın<sup>1</sup>, Uğur Oral Ünal<sup>1</sup>, Kadir Sarıöz<sup>1\*</sup>

<sup>1</sup>Istanbul Technical University, Faculty of Naval Architecture and Ocean Engineering, 34469 Maslak-Istanbul, Turkey

**Abstract:** This paper presents a numerical methodology to predict the steering and braking forces applied by tractor type escort tugs to large vessels, particularly oil tankers. The towline force applied by the tug to the vessel can be separated into two components: braking force, caused by drag in the direction of motion of the escorted vessel, and steering force, caused by hydrodynamic lift. These forces and the thrust power generated by the propulsion system determine the escort performance of the tug. The essential part of the escort performance prediction methodology is the computation of hydrodynamic forces generated by the tug's hull and the appendages such as skeg. These forces can be converted into the steering and braking force components which define the escort performance of the tug. The hydrodynamic forces are estimated by a semi-empirical method based on model test measurements and a Computational Fluid Dynamics (CFD) based methodology. A comparison of the estimated hydrodynamic forces with those obtained by scaled model experiments is presented. The methodology can easily be used to determine to estimate the greatest steering and braking forces that can be generated by a given escort tug configuration, tanker speed, and type of operation.

**Keywords:** Escort tug, hydrodynamics, CFD.

### 1 INTRODUCTION

It is now widely acknowledged that tug escort is the single most effective mean to reduce risk of ship groundings and collisions during passages through confined waters like the strait of Istanbul (Bosphorus) (OCIMF, 1997). In order to reduce the risks caused by large oil tankers in the Bosphorus, tankers with length over all 250 meter or more are required to be assisted by a suitable escort tug. For the largest tankers with length over all 300 meter or more the Administration is authorized to determine the type, size and number of escort tugs required for a safe passage. This decision is mainly based on the experience of the tug operators and has been a matter of discussion between the ship operators and the regulatory bodies (OCIMF, 2007).

In order to prevent a grounding or collision the escort tug(s) should provide sufficient steering and/or braking forces to substitute the loss of rudder or engine control of the tanker within the speed range from maximum escort speed down to zero speed. This requires precise knowledge of the forces applied by the escort tug as well as the manoeuvring behaviour of the tanker under the effects of water depth, channel bank, hydrodynamic interactions between ships meeting and passing, and the environmental conditions such as wind, wave or current.

The main advantage of escort tugs, contrary to traditional tugs, is the ability to apply indirect towing forces to steer or retard a large vessel. This is achieved by utilizing the hydrodynamic characteristics of the escort hull to generate lift and drag forces by orienting the tug at non-zero angles of attack to the flow. A combination of hull/skeg configuration, propulsion units that can provide thrust in 360°, and specialized towing equipment distinguish an escort tug from conventional tugs. Although there are different types of escort tugs this paper focuses on the

escort performance analysis of tractor type escort tugs (Allan, 2000; Allan and Molyneux, 2004).

Escort tugs could be used in different modes depending on the speed of operation. For speeds of below 6 knots, the tug will operate in “direct” mode and the forces from the tug’s propulsion system will be used to slow or turn the ship. As the speed increases, and particularly at speeds over 8 knots, hydrodynamic forces from the tug’s hull and skeg begin to dominate, and the tug begins to operate in “indirect” mode. In the pure indirect mode the thrusters apply a force perpendicular to the centerline of the tug in order to keep a specific yaw angle. In order to provide the maximum possible steering forces the tug would use all available engine power while keeping the most efficient yaw angle. This is called the powered indirect mode and often results in towline forces exceeding the tug’s rated bollard pull. While pure indirect mode relies primarily on the hydrodynamic effects of the tug hull to create the steering and braking forces, powered indirect mode augments the hydrodynamic force with the thrusters to result in the highest steering forces (Sturmöhfel and Bartels, 1993; Jagannathan et al., 1995).

This paper presents a numerical methodology to estimate the steering and braking forces generated by a given escort tug configuration, tanker speed, and the type of operation. This numerical methodology represents the first stage of an ongoing research program to determine the type, power and number of escort tugs required to minimize the risk of grounding or collision for specific tanker size and environmental conditions.

First a mathematical model for representing the steering and braking forces generated by a tractor type escort tug is presented. It is shown that, in this simplified mathematical model the steering and braking forces generated by an

escort tug can be estimated by using the propeller thrust forces and the hydrodynamic forces (surge and sway) and moment (yaw).

Prediction of hydrodynamic forces and moment due to the tug's hull and skeg is the most crucial part of the methodology. These force components can be calculated by empirical or Computational Fluid Dynamics (CFD) based methods, or measured by scale model tests. It is generally accepted that the most reliable method to estimate the hydrodynamic forces is to conduct scaled model tests (Dabbar and Morgan, 1996; Hensen, 1997). However, because of the cost and time restrictions, model tests are not suitable for early design studies in which a large number of design alternatives need to be analysed. Furthermore, whilst hydrodynamic forces can be predicted with model experiments, this is an impractical method for evaluating the combined tug-tow rope-tanker system (Dabbar and Morgan, 1996). Recently, in parallel with increasing computational power of computers and availability of commercial software, CFD based computational techniques have been widely used to compute the hydrodynamic forces (Quadflieg and Kaul, 2006). However, CFD based methods require precise geometric definition of the hull form and appendages which may not be available at the early stages of the design process. Therefore, a practical semi-empirical method based on model test results may be useful when limited design information is available.

In this study, hydrodynamic forces are estimated by two different methods, a simple empirical one based on a set of manoeuvring derivatives and a CFD based computational methodology. The empirical approach which is based on model test measurements may provide reliable estimates for a specific type of tug but cannot be generalised and also ignores the local design features. On the other hand, CFD based approach takes the local flow characteristics into account and provides a consistent and reliable methodology, despite the obvious disadvantage in terms of the computing time and the effort needed to generate the mesh. The empirical and the CFD based methods are used to estimate the sway and surge force components of the AJAX, a tractor tug for which the experimental data is available (Molyneux and Bose, 2008).

Finally, the hydrodynamic are converted into lift and drag forces which are used to estimate the steering and braking forces applied by an escort tug in pure and powered indirect escort modes.

## 2 QUASI-STATIC ESCORT FORCE ANALYSIS

The quasi-static escort force analysis is based on equilibrium conditions for the indirect towing mode. When considering the tug center of pressure (COP) as a reference point, the primary forces acting on a tractor type escort tug in pure and powered indirect modes are shown in Figure 1 (a) and 1 (b), respectively. The primary forces are referred to as towline tension, net thrust force, hydrodynamic surge and sway forces, and yaw moment. The escort tug applies force to the escorted ship through the towline. The longitudinal component of the towline force with respect

to the escorted ship motion is referred to as the escort braking force and the transverse component is referred to as the escort steering force. The maximum sustainable braking and steering forces generated by the tug determine its escort performance.

The primary forces acting on an escort tug in indirect mode are:

- Towline force,
- Net thrust force,
- Hydrodynamic lift and drag force components and yawing moment.

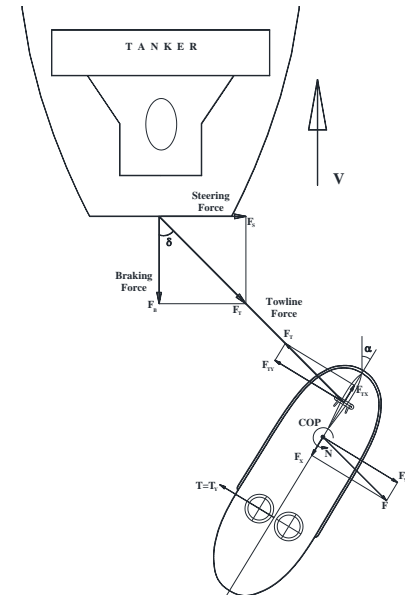


Figure 1.a. Braking and steering force diagram (pure indirect mode)

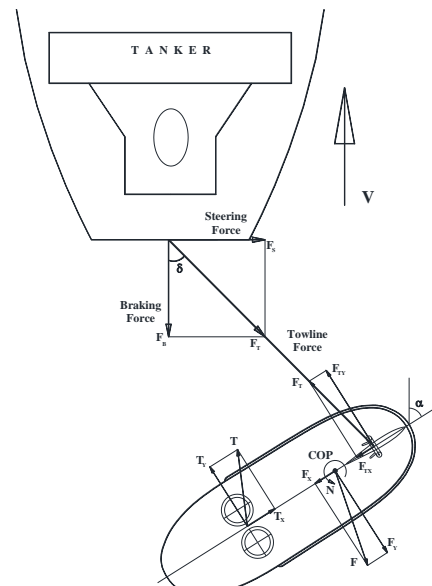


Figure 1.b. Braking and steering force diagram (powered indirect mode)

The escort tug applies force to the escorted ship through the towline. The longitudinal component of the towline force, caused by tug drag, in the direction of the escorted ship motion is referred to as the escort braking force ( $F_B$ ) and the transverse component, caused by hydrodynamic lift, is referred to as the escort steering force ( $F_S$ ). These components depend on the towline force ( $F_T$ ) and the towline angle ( $\delta$ ) as follows:

$$F_S = F_T \sin \delta \quad (1)$$

$$F_B = F_T \cos \delta \quad (2)$$

Depending on the yaw angle of tug relative to tanker centreline ( $\alpha$ ) and the angle of towline to tanker centreline ( $\delta$ ) the ratio of braking force to steering force will vary.

It is possible to achieve high steering and braking forces in indirect mode due to the significant hydrodynamic lift and drag forces generated by a properly designed escort tug hull and skeg. In pure indirect mode, shown in Figure 1 (a), the thrust force is considered to act only in the transverse direction, in the amount required to maintain the set yaw angle. The towline and thrust forces are determined by balancing the forces in the X and Y directions and the yawing moment about the centre of pressure as follows:

$$F_X + F_{TX} + T_X = 0 \quad (3)$$

$$F_Y + F_{TY} + T_Y = 0 \quad (4)$$

$$N + F_{TY}x_{FC} + T_Yx_{PC} = 0 \quad (5)$$

The unknown thrust and towline force components can be obtained as follows:

$$T_X = 0 \quad (6)$$

$$F_{TX} = F_X \quad (7)$$

$$F_{TY} = \frac{N + F_Yx_{PC}}{x_{TC} + x_{PC}} \quad (8)$$

$$T_Y = F_Y - F_{TY} = F_Y - \frac{N + F_Yx_{PC}}{x_{TC} + x_{PC}} = \frac{F_Yx_{TC} - N}{x_{TC} + x_{PC}} \quad (9)$$

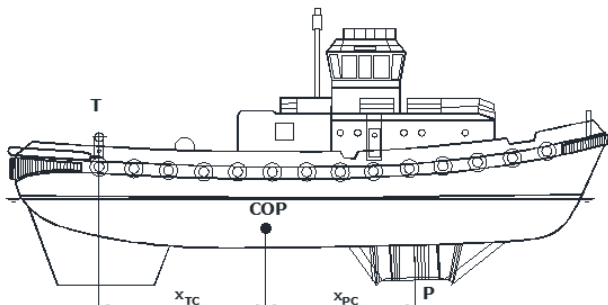


Figure 2. Distances between centre of pressure and towing staple and propellers

The steering and braking force components can be calculated by transforming the towline force from the local escort tug coordinate system to the global coordinate system:

$$F_S = F_{TY} \cos \alpha + F_{TX} \sin \alpha \quad (10)$$

$$F_B = F_{TY} \sin \alpha - F_{TX} \cos \alpha \quad (11)$$

where

$F_{TY}$  : Lateral component of towline force (normal to tug centreline)

$F_{TX}$  : Longitudinal component of towline force (parallel to tug centreline)

$F_Y$  : Lateral component of hydrodynamic force

$F_X$  : Longitudinal component of hydrodynamic force

$N$  : Yawing moment

$T_X$  : Lateral component of thrust

$T_Y$  : Longitudinal component of thrust

$x_{TC}$  : Distance from towing staple to centre of pressure

$x_{PC}$  : Distance from propellers to centre of pressure

In the pure indirect form the thrust power needed to maintain the set yaw angle is only a small fraction of the total thrust power and hence this mode provides a powerful tool to assess the escort performance of various hull and skeg geometries independent of the maximum available tug thrust. To increase the steering force the tug must increase the thrust power to maximum available while keeping the set yaw angle constant, which results in the powered indirect mode, shown in Figure 1 (b). In powered indirect mode, the unknown thrust and towline force components can be obtained as follows:

$$F_{TY} = \frac{N + F_Yx_{PC}}{x_{TC} + x_{PC}} \quad (12)$$

$$T_Y = F_Y - F_{TY} = F_Y - \frac{N + F_Yx_{PC}}{x_{TC} + x_{PC}} = \frac{F_Yx_{TC} - N}{x_{TC} + x_{PC}} \quad (13)$$

$$T_X = \sqrt{BP^2 - T_Y^2} \quad (14)$$

$$F_{TX} = F_X + T_X \quad (15)$$

where, BP represents the static bollard pull of the tug. The steering and braking force components can be calculated in a similar manner as in the pure indirect mode.

### 3 HYDRODYNAMIC FORCES

The towline force applied by the tug to the vessel can be separated into two components: braking force, caused by tug drag in the direction of motion of the escorted vessel, and steering force, caused by hull hydrodynamic lift. The braking and steering force component are also augmented by the forces generated by the propulsion system of the tug.

Calculation of the viscous force components is the most critical part of the modelling. Viscosity affects the flow around the tug in two basic ways. First, in the boundary layer, close to the hull, the fluid velocity is significantly affected by viscosity. At small drift angles the tug's hull can be regarded as a lifting surface with the drift angle taking a role of the conventional angle of attack. At large drift angles, the hull and the appendage damping forces are generated by pressure loss and contribute to the losses in oblique flow with drift and yaw angle velocities by cross-

flow pressure. Both the circulatory and cross-flow forces are present and equally important in typical escort tug manoeuvres.

By assuming that the hull of a tug can be modelled as a low aspect ratio wing, the lift force ( $F_L$ ) and the drag force ( $F_D$ ) can be written as:

$$F_L = \frac{1}{2} \rho U^2 S C_L(\beta, R_n) \quad (16)$$

$$F_D = \frac{1}{2} \rho U^2 S C_D(\beta, R_n) C_L \quad (17)$$

where  $\rho$  is the water density,  $U$  is the speed,  $S$  is a characteristic area,  $C_L$  is the nondimensional lift coefficient,  $C_D$  is the nondimensional drag coefficient,  $\beta$  is the sideslip angle, and  $R_n$  is the Reynolds number.

The lift coefficient is modelled as proportional to the sine of the sideslip angle

$$C_L = C_{L\beta} \sin \beta = C_{L\beta} \frac{v}{U} \quad (18)$$

where  $C_{L\beta}$  is a constant of proportionality and  $v$  is the lateral component of the tug's speed. Applying this to the lift equation gives

$$F_L = \frac{1}{2} \rho U^2 S C_L = \frac{1}{2} \rho U S C_{L\beta} v \quad (19)$$

The drag coefficient is conventionally modelled as a quadratic function of sideslip, with a zero angle drag coefficient as:

$$C_D = C_{D0} + C_{D\beta\beta} \sin^2 \beta \quad (20)$$

where  $C_{D0}$  is a dimensionless drag coefficient at zero angle of sideslip, and  $C_{D\beta\beta}$  describes the induced drag proportional to  $\sin^2 \beta$ . In pure surge motion (i.e. without sideslip), the drag force arising from  $C_{D0}$  can be considered to be the same as the total resistance of the tug according to ITTC formulation;

$$R_T = -\frac{1}{2} \rho S C_{D0} |u| u \quad (21)$$

with

$$C_{D0} = (C_F + \Delta C_F)(1 + k) + C_W \quad (22)$$

Where  $k$  is a correction term, called the form factor, representing the three dimensional form of the hull,  $S$  is the wetted surface area,  $u$  is the longitudinal component of the tug's speed,  $C_F$  is the flat plate friction according to the ITTC 1957 friction line,  $\Delta C_F$  is a hull roughness parameter, and  $C_W$  is the wave making resistance coefficient.

$$C_F = \frac{0.075}{(\log_{10} R_n - 2)^2} \quad (23)$$

where, Reynold's number is given as

$$R_n = \frac{UL}{v} \quad (24)$$

where,  $L$  is the vessel's waterline length, and  $v$  is the kinematic viscosity of water. For hull roughness coefficient,  $\Delta C_F$ , ITTC recommends the following range

$$\Delta C_F = 0.0002 - 0.0015 \quad (25)$$

The drag force is then:

$$\begin{aligned} D &= \frac{1}{2} \rho U^2 S C_D(R_n, \beta) = \frac{1}{2} \rho U^2 S \left[ C_{D0} + C_{D\beta\beta} \left( \frac{v}{U} \right)^2 \right] \\ &= \frac{1}{2} \rho S \left[ U^2 C_{D0} + C_{D\beta\beta} v^2 \right] \end{aligned} \quad (25)$$

Since the lift and drag forces are resolved in the flow axes, they must be converted to the body fixed frame before being added. This is done using the following transformation:

$$\begin{bmatrix} X \\ Y \end{bmatrix} = \begin{bmatrix} -\cos \beta & \sin \beta \\ -\sin \beta & -\cos \beta \end{bmatrix} \begin{bmatrix} D \\ L \end{bmatrix} \quad (26)$$

The longitudinal components of the lift and drag forces are,

$$X_L = L \sin \beta = L \frac{v}{U} = \frac{1}{2} \rho S C_{L\beta} v^2 \quad (27)$$

$$\begin{aligned} X_D &= -D \cos \beta = -D \frac{u}{U} = -\frac{1}{2} \rho S \left[ C_{D0} U u + C_{D\beta\beta} \frac{u v^2}{U} \right] \\ &\approx -\frac{1}{2} \rho S \left[ C_{D0} u^2 + C_{D\beta\beta} v^2 \right] \end{aligned} \quad (28)$$

The total surge force that arise from lift and drag is then:

$$\begin{aligned} X &= X_L + X_D = -\frac{1}{2} \rho S \left[ C_{D0} u^2 + (C_{D\beta\beta} - C_{L\beta}) v^2 \right] \\ &= X_{uu} u^2 + X_{vv} v^2 \end{aligned} \quad (29)$$

Similarly, the transverse components of the lift and drag forces are,

$$Y_L = -L \cos \beta = -L \frac{u}{U} \approx -\frac{1}{2} \rho S C_{L\beta} u v \quad (30)$$

$$\begin{aligned} Y_D &= -D \sin \beta = -D \frac{v}{U} = -\frac{1}{2} \rho S \left[ C_{D0} U v + C_{D\beta\beta} \frac{v^3}{U} \right] \\ &\approx -\frac{1}{2} \rho S \left[ C_{D0} u v + C_{D\beta\beta} \frac{v^3}{U} \right] \end{aligned} \quad (31)$$

Since the side force is dominated by the lower order terms the term corresponding to  $C_{D\beta\beta}$  is omitted.

The shedding of the vortices from the body seems inevitably to imply a separation of the boundary layer. We could assume that the separation process gradually increases with increase of incidence. At some rather significant drift angles (we assume somewhat arbitrarily to

be around 30 degrees) the flow pattern will be dominated by the cross flow and will remain substantially unchanged with further increase of incidence angle. From the work of (Norrbin, 1971), it is known that the cross-flow terms can be approximated using quadratic damping terms in modulus form, as follows

$$Y_{CD} \approx Y_{v|v}|v|v| \quad (32)$$

Then in mathematical terms, the viscous side force acting on the body at moderate drift angles,  $\beta$ , can be presented by a simple summation,

$$\begin{aligned} Y &= Y_L + Y_D + Y_{CD} \\ &= -\frac{1}{2}\rho S(C_{L\beta} + C_{D0})uv + Y_{v|v}|v|v| = Y_v uv + Y_{v|v}|v|v| \end{aligned} \quad (33)$$

where  $Y_v$  is a lift curve slope appropriate to the small angle of incidence, and  $Y_{v|v}|v|$  the cross-drag coefficient determined for specific drift angle range. The yaw moment arising from the side force can be represented in a similar manner

$$N = N_v uv + N_{v|v}|v|v| \quad (34)$$

The roll moment arising from the side force can be calculated as

$$K = Y z_{CP} \quad (35)$$

where  $z_{CP}$  define the vertical location of centre of pressure. The roll moment can also be expressed in the following format:

$$K = K_v uv + K_{v|v}|v|v| \quad (36)$$

The functional dependence of coefficients from the hull geometry and the Reynolds number can be determined from the captive model tests or CFD calculations. Usually the linear coefficient  $Y_v$  is estimated rather reliably. Several empirical formulae have been proposed for conventional ship forms and the following formula based on Ankudinov (1985) formulation:

$$Y'_v / -\pi \left( \frac{T}{L} \right)^2 = 0.25 \left( \frac{C_B B}{T} \right)^2 - 1.5 \left( \frac{C_B B}{T} \right) + 3 \quad (37)$$

At large drift angles, the side force is dominated by cross flow, so that the cross-drag coefficient,  $Y_{v|v}|v|$ , defined on the base of the ship lateral area at large incidence angle (around 90 degrees or so) can be evaluated using the following formula based on (Ankudinov, 1985) formulation

$$Y'_{v|v}|v| = 0.045 + 1.1 \frac{T}{L} + \left( 0.004 \frac{B}{T} - 0.27 \right) \frac{B}{L} \quad (38)$$

Similar formulae for the yaw moment are given as follows:

$$N'_v / -\pi \left( \frac{T}{L} \right)^2 = 0.75 - 0.04 \left( \frac{C_B B}{\pi T} \right) \quad (39)$$

$$N'_{v|v}|v| = -0.75 N'_v \quad (40)$$

A complete set of viscous damping ship hull hydrodynamic coefficients for surge-sway-yaw and roll motions (assuming no heave-pitch) in static drift motion are given below:

$$\text{Surge} \quad X_D = \frac{\rho}{2} L^2 \left( X'_{u|u}|u|u| + X'_{vv}|v|^2 \right) \quad (41)$$

$$\text{Sway} \quad Y_D = \frac{\rho}{2} L^2 \left( Y'_v uv + Y'_{v|v}|v|v| \right) \quad (42)$$

$$\text{Yaw} \quad N_D = \frac{\rho}{2} L^3 \left( N'_v uv + N'_{v|v}|v|v| \right) \quad (43)$$

$$\text{Roll} \quad K_D = \frac{\rho}{2} L^3 \left( K'_v uv + K'_{v|v}|v|v| \right) \quad (44)$$

A significant factor that influence the performance of an escort tug is the skeg geometry. The additional lift and drag forces created by skeg have a significant effect on the maximum achievable steering and braking forces. The lift force provided by the skeg varies depending on the drift angle. From zero degrees to just before stall, the skeg lift coefficient,  $C_{LS}$ , is determined according to Whicker and Fehlner (1958).

$$C_{LS} = \frac{\partial C_{LS}}{\partial \beta} \beta + \frac{C_{Dc}}{AR_e} \left( \frac{\beta}{57.3} \right)^2 \quad (45)$$

where  $\beta$  is the sideslip angle, and

$$\frac{\partial C_{LS}}{\partial \beta} = \frac{1.8 \pi AR_e}{1.8 + \cos \Lambda \sqrt{\frac{AR_e^2}{\cos^4 \Lambda} + 4}} \quad (46)$$

where,  $\Lambda$  is sweep of quarter-chord line and the effective aspect ratio,  $AR_e$ , is defined in terms of the span,  $b$ , and lateral area of the skeg,  $A_{LS}$ , as follows:

$$AR_e = \frac{2b^2}{A_{LS}} \quad (47)$$

The cross flow drag coefficient,  $C_{Dc}$ , is a function of the tip shape and taper ratio,  $\lambda$ , and for a square tip skeg this coefficient is given by;

$$C_{Dc} = 0.1 + 1.6\lambda \quad (48)$$

The skeg is assumed to have NACA 0012 cross sections and the stall angle is taken from (Bertram, 2000), as a function of the aspect ratio. From zero degrees to just before stall, the drag coefficient,  $C_D$ , is determined according to (Whicker and Fehlner 1958)

$$C_{DS} = C_{d0} + \frac{C_{LS}^2}{\pi A R_e e} \quad (49)$$

where,  $C_{d0} = 0.0065$  is the minimum section drag coefficient and  $e = 0.9$  is the Oswald efficiency factor..

#### 4 EXPERIMENTAL DATA

A series of indirect escort tests were conducted at the Institute for Marine Dynamics (IMD) in St. John's, Newfoundland (Molyneux and Bose, 2008). The model used was of the Voith Tractor Escort Tug, *Ajax*, designed by Robert Allan Ltd. (Allan, 2000) for Ostensjo Rederi AS of Haugesund, Norway. The performance requirement for this tug was specified as to develop 150 tonnes of steering force at 10 knots. The particulars of Voith Tractor Escort Tug, *Ajax* are given in Table 1. The hull form tested during the model tests is shown in Figures 3 and 4.

Table 1. Particulars of Voith Tractor Escort Tug, *Ajax* (Molyneux and Bose, 2008)

|                           | Hull only            | Hull and skeg        |
|---------------------------|----------------------|----------------------|
| Length over all (LOA)     | 40.00 m              | 40.00 m              |
| Length of waterline (LWL) | 38.19 m              | 38.19 m              |
| Beam waterline (BWL)      | 14.20 m              | 14.20 m              |
| Draught (T)               | 3.80 m               | 6.86 m               |
| Displacement              | 1276 t               | 1276 t               |
| Lateral area              | 125.4 m <sup>2</sup> | 157.1 m <sup>2</sup> |
| Wetted surface area       |                      | 651 m <sup>2</sup>   |

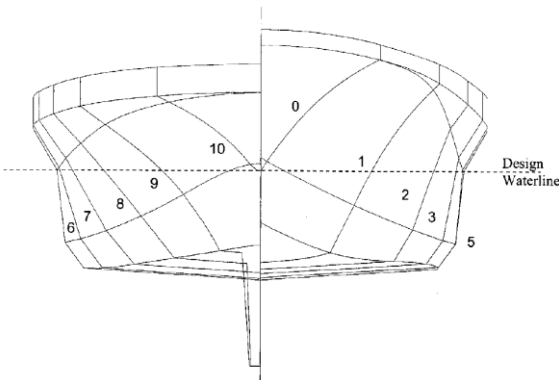


Figure 3. Hull form of the VSP Escort Tug *AJAX* as tested during the model tests (Molyneux and Bose 2008)

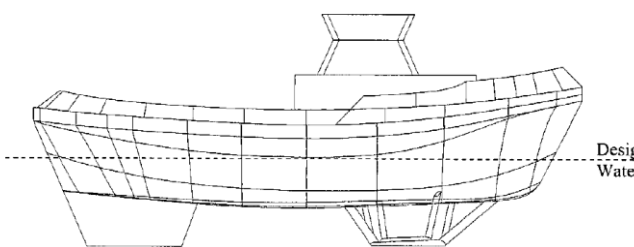


Figure 4. Profile view of the VSP Escort Tug *AJAX*, with skeg and propulsion cage (Molyneux and Bose 2008)

Experiments to measure hull forces were carried out in the Ice Tank of the National Research Council's Institute for Ocean Technology (Molyneux and Bose 2008). The objective of these tests was to measure hydrodynamic forces and moments created by the hull and the appendages on a 1:18 scale model of the tug. The range of ship speeds

was from 4 to 12 knots (with model speeds based on Froude length scaling. Yaw angle was varied between zero and 105 degrees, which covered the full range likely to be encountered during escort operation. The skeg was at upstream end of the hull, for all cases when it was fitted.

The models were fixed at the required yaw angle and measurements were made of surge force, sway force and yaw moment using a Planar Motion Mechanism (PMM). The load measurement system was connected to the tug on an axis along its centreline, at the height of the towing staple on the tug. The model was free to roll about the axis through the towing staple, and free to pitch and heave. Pitch angle, roll angle, heave amplitude and carriage speed were measured, in addition to the surge force  $F_x$  and sway force  $F_y$ .

Forces and moments were measured in the tug-based coordinate system and non-dimensionalized using the coefficients given below

$$C_L = \frac{F_x}{0.5\rho A_L V^2} \quad C_Q = \frac{F_y}{0.5\rho A_L V^2} \quad (50)$$

$C_Q$  is the force coefficient normal to the tug centreline (sway) and  $C_L$  is the force coefficient along the tug's centreline (surge).  $A_L$  is the underwater lateral area of the hull and skeg (if the skeg was fitted),  $\rho$  is the density of the water ( $\text{kg/m}^3$ ) and  $V$  is the speed of the ship (m/s).

#### 5 CFD COMPUTATIONS

##### 5.1 Computational Model and Boundary Conditions

CFD computations were performed with the VSP Escort Tug *AJAX* at 1:18 model scale as in the experimental study of Molyneux and Bose (2008). The three-dimensional (3D) geometry was generated by digitising the hull form and profile view given in Figures 3 and 4. This obligatory approach, indeed, highly affected the geometrical accuracy of the 3D form obtained. Whilst the cases with and without the skeg were both considered, the propulsion cage seen in Figure 4 was simply ignored.

A Cartesian coordinate system was adopted. Due to the high yaw angle introduced in some computational cases, a relatively large solution domain was employed. Accordingly, the computational boundaries at the upstream, downstream, sides and bottom were placed at  $3L$ ,  $10L$ ,  $4L$  and  $2L$ , respectively, from the centroid of the hull, where  $L$  implies the model length. Since the effect of the free surface was not considered in the simulations, the top boundary was simply placed at a height corresponding to that of the design waterline.

Two different grid generation techniques were applied by using state-of-the-art mesh generation software packages in order to have a better understanding about the effect of the grid structure on the solution of high-vorticity cases dealt. One of these techniques is based on the hybrid type unstructured mesh generation which involves the use of quad-dominant surface meshing with hexahedral cell layers in the vicinity of the wall. The flow which is relatively distant from the body, on the other hand, is resolved with tetrahedral cell elements. The other

technique adopted is the well-known cut-cell method which is basically a non-matching block-unstructured volume meshing technique. The surface mesh structure includes both triangle and quadrilateral elements whilst hexahedral cell elements are primarily used throughout the solution domain excluding the near-wall region where tetrahedral cell elements are also involved. Several local mesh refinement blocks can be effectively specified in this meshing technique. The advantage of the former mesh generation technique is the relative accuracy obtained in the near wall flow field due to the quadrilateral/hexagonal cell elements used in this region. Views of the different volume meshes generated are shown in Figure 5 and 6. Care was taken to be able to accurately resolve the boundary layer as well as the viscous sub-layer developing over the body. For his purpose, the  $y^+$  value of the first cell adjacent to the surface was kept around 1 for most part of the hull and skeg.

For practical purposes, in lieu of generating individual volume meshes for each computational case, the meshes were generated for the zero yaw angle condition whilst the inlet boundary conditions were adjusted to introduce the effect of the different yaw angles. The former method would slightly increase the solution accuracy.

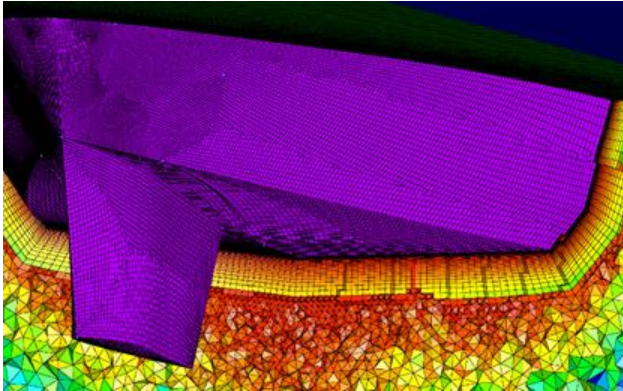


Figure 5. A view of the hybrid volume mesh used (colored by cell volume)

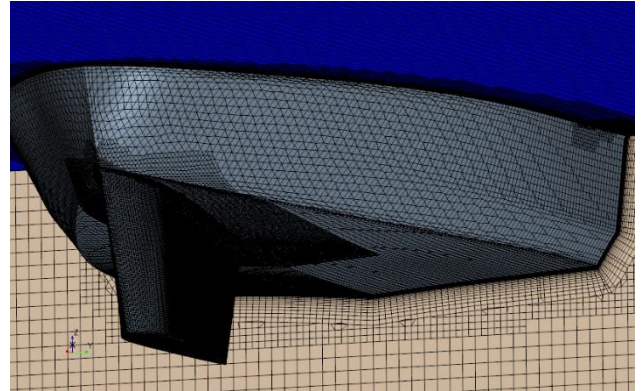


Figure 6. A view of the cut-cell volume mesh used

Two inlet boundaries were specified where the flow velocity components and the turbulence specifications were given. The velocity magnitude of 0.728 m/s was considered which corresponded to a Froude number (Fr) of around 0.16. An insignificant turbulence intensity level of 1% along with the turbulence/molecular viscosity ratio of 1 were set at the inlet boundaries. At the two outlet boundaries, while the atmospheric pressure was specified, the direction of the backflow turbulence was also adjusted according to the yaw angle considered. A symmetry boundary condition, which can be interpreted as a slip wall, was used for the top and bottom boundaries.

A basic grid dependence analysis was conducted for both meshing techniques and for the cases with/without the skeg at a yaw angle of 45°. Three different mesh resolutions were considered for the analyses. The resolution of the meshes was systematically increased at each direction of the coordinate system by a factor of approximately  $\sqrt[3]{2}$ . This approach resulted in nearly doubled cell sizes for the refined mesh structures. Table 2 summarises the main characteristics of the meshes used and the sway force obtained from the simulation with the associated mesh type. As seen from the table, the average  $y^+$  value was kept nearly constant for all meshes in order to fully resolve the viscous sub-layer. The negligible differences obtained between the results of the mesh resolutions B and C pointed out that the B meshes were suitable to perform further simulations with varying yaw angles.

Table 2. Grid Dependence Analysis: Mesh Characteristics and Sway Force

| Case      | Meshing technique | Mesh | Average $y^+$ | Cells on the hull | Average cell aspect ratio | Maximum cell aspect ratio | Total Cells $\times 10^{-6}$ | Sway (N) |
|-----------|-------------------|------|---------------|-------------------|---------------------------|---------------------------|------------------------------|----------|
| Bare hull | Hybrid            | A    | 1.2           | 32,000            | ~7                        | 180                       | 3.50                         | 48.2     |
|           |                   | B    | 1.2           | 64,750            | ~4                        | 120                       | 6.50                         | 47.8     |
|           |                   | C    | 1.2           | 127,320           | ~2                        | 75                        | 10.67                        | 47.6     |
|           | Cut-cell          | A    | 1.1           | 17,111            | 46                        | 75                        | 2.09                         | 47.6     |
|           |                   | B    | 1.1           | 25,882            | 38                        | 66                        | 4.00                         | 47.5     |
|           |                   | C    | 1.1           | 41,277            | 25                        | 42                        | 8.03                         | 47.5     |
| with skeg | Hybrid            | A    | 1.2           | 33,000            | ~6                        | 180                       | 3.68                         | 111.7    |
|           |                   | B    | 1.2           | 68,430            | ~3                        | 130                       | 6.74                         | 110.5    |
|           |                   | C    | 1.2           | 138,800           | ~2                        | 85                        | 12.00                        | 110.7    |
|           | Cut-cell          | A    | 1.0           | 50,029            | 34                        | 75                        | 3.39                         | 112.4    |
|           |                   | B    | 1.0           | 77,419            | 27                        | 63                        | 6.19                         | 110.4    |
|           |                   | C    | 1.0           | 119,985           | 22                        | 51                        | 11.68                        | 109.7    |

## 5.2 Computational Details

Steady, incompressible Reynolds-Averaged-Navier-Stokes (RANS) equations were solved for the CFD simulations. The SST k-w turbulence model (Menter, 1994), which is based on the Boussinesq hypothesis (Tennekes and Lumley, 1972), was used to calculate the turbulence field and hence to model the Reynolds stresses appearing in the RANS equations. The model can be directly integrated through the viscous sub-layer and therefore no special viscous correction for the near-wall was applied. A finite-volume method (Blazek, 2001) was employed with a segregated algorithm to solve the RANS and turbulence transport equations. The standard pressure-correction procedure (SIMPLE) of Patankar (1980) were used for the pressure-velocity coupling. The spatial discretisation of the convective terms was achieved with a second-order-upwind scheme while the viscous terms were discretised with a second-order central difference scheme. The variations of the flow variables such as the drag and velocity in the wake field was systematically checked along with the scaled residuals in order to decide whether the convergence was achieved.

As mentioned previously, CFD simulations can be a very time consuming process. Nowadays, benefiting from the new state-of-the-art grid generation software packages, an experienced CFD engineer can prepare a high-quality computational mesh structure in a few hours. However, the duration of this pre-processing stage still strongly depends on the quality of the solid model being studied and the software/meshing technique used. On the other hand, the processing stage takes a significant amount of time even with the modern computer systems. Nevertheless, provided that the solution is adequately accurate, CFD offers a very detailed information about the flow characteristics and topology throughout the solution domain. As this subject is well beyond the scope of the present paper, only two simple fundamental examples are given in Figures 7 and 8. The strong helical motion downstream of the hull by means of the 3D streamlines is apparent in Figure 7. The detail of the high vorticity zone behind the skeg can also be clearly observed (Figure 8). It should be born in mind that the time and computing power required for a meticulous data analysis and a high-quality, detailed flow visualisation can also be generally quite large.

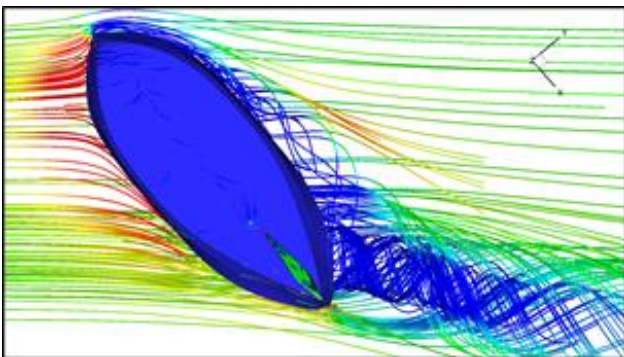


Figure 7. 3D streamlines around the tug  
(45° yaw angle, colored by static pressure)

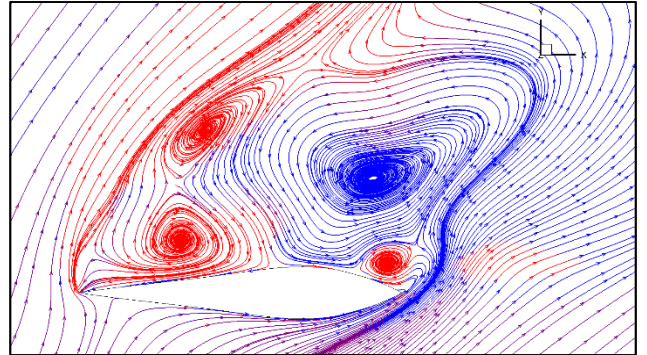


Figure 8. 2D streamlines around the skeg  
(50° yaw angle, colored by vorticity)

## 6 COMPARISON OF THE RESULTS

A comparison of experimentally measured surge and sway force coefficients with those obtained by the semi-empirical approach presented in Section 3 and by CFD computations are shown in Figures 9 and 10. Figure 10 also includes the computational results of Jahra et al. (2015). The computations with the two mesh types presented produced very close results. This indicated that, due to its practical applicability and relatively moderate cell size, the cut-cell meshing method can be preferred for a rapid and effective solution of this kind of hydrodynamic problems. To provide cleaner graphics, only the results involving the cut-cell type mesh were plotted.

As far as the bare hull case is concerned, the results of the CFD computations presented satisfactory agreement with those of the experiments, particularly for the lateral force component coefficient,  $C_Q$ . Although the effect of the free surface and the tug's rolling, pitching and heaving motions were ignored in the simulations, the results were within 10% of those of the experiments. Due to the relatively small values of the surge force, the exact computation of the longitudinal force coefficient,  $C_L$ , was somewhat a problematic task. For the large yaw angles, slightly negative values of  $C_L$  were obtained, which are in fact expected to occur at even larger yaw angles. The effect of the inaccuracies of the model geometry due to the obligatory reasons, remains unclear at this point.

On the other hand, the simulations largely over-predicted the sway force for the cases with the skeg, when the yaw angles were higher than 35° (Figure 10). The stall angle was also over-predicted. The clear reason of this discrepancy lies particularly behind the heeling moment observed in the experiments. As the existence of the skeg substantially increases the sway force compared to that of the bare hull case and shifts the centre of pressure downwards, for the large yaw angles, this introduces a significant heel angle which highly decrease the sway force in the experimental conditions. This heel angle is relatively small for the lower yaw angles and the cases without the skeg so that it does not dramatically affect the associated results. The results clearly point out that an accurate and reliable escort analysis by means of CFD should take the heel angle of the tug into account. The inclusion of the free surface effects would also certainly increase the modelling accuracy as they affect the pressure distribution, particularly, on the

upstream side of the hull, as well as the frictional force component.

## 7 ESCORT PERFORMANCE PREDICTION

The methodology to predict the hydrodynamic forces generated by the hull and the appendages, as presented above, is not only useful to compare different designs but can also be used to determine the geometric characteristics of the hull and appendages. However, in order to determine the escort performance, the forces generated by the propulsion system must be taken into consideration. Depending on the use of propulsive power, an escort tug can operate in ‘pure’ or ‘powered’ indirect modes

In the pure indirect mode, the thrusters apply a force perpendicular to the centreline of the tug in order to keep a

specific yaw angle. The thrust power needed to maintain the set yaw angle is, generally, only a small fraction of the total thrust power. To increase the steering force the tug must increase the thrust power to maximum available while keeping the set yaw angle constant, which results in the powered indirect mode. While pure indirect mode relies primarily on the hydrodynamic effects of the tug hull to create the steering and braking forces, powered indirect mode augments the hydrodynamic force with the thrusters to result in the highest steering forces (Allan and Molyneux, 2004). The thrust and towline force components in pure and powered indirect modes can be estimated by balancing the forces in the X and Y directions and the yawing moment about the centre of pressure as presented in Section 2.

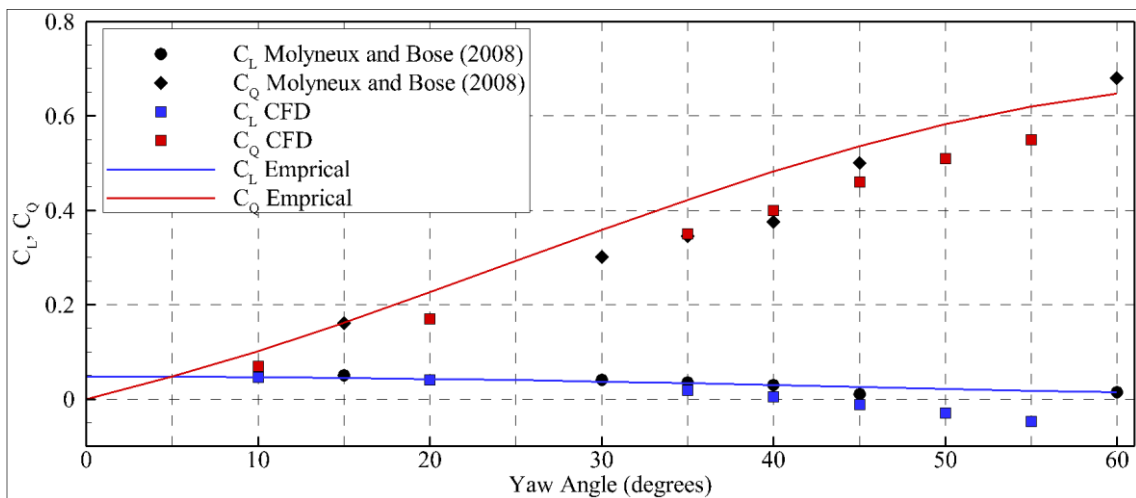


Figure 9. Comparison of measured and predicted hydrodynamic force coefficients  
(Bare Hull,  $\text{Fr} \approx 0.16$ )

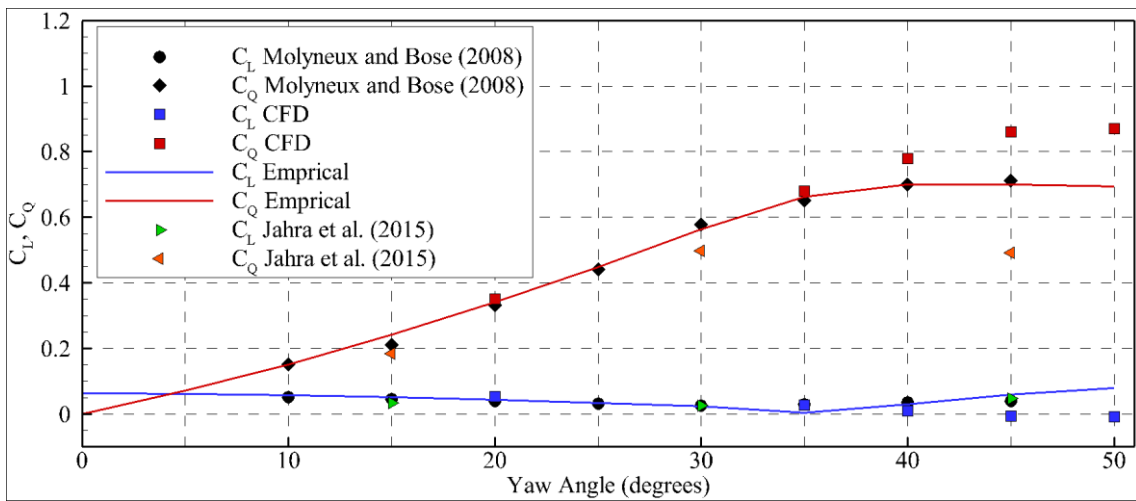


Figure 10. Comparison of measured and predicted hydrodynamic force coefficients  
(with skeg,  $\text{Fr} \approx 0.16$ )

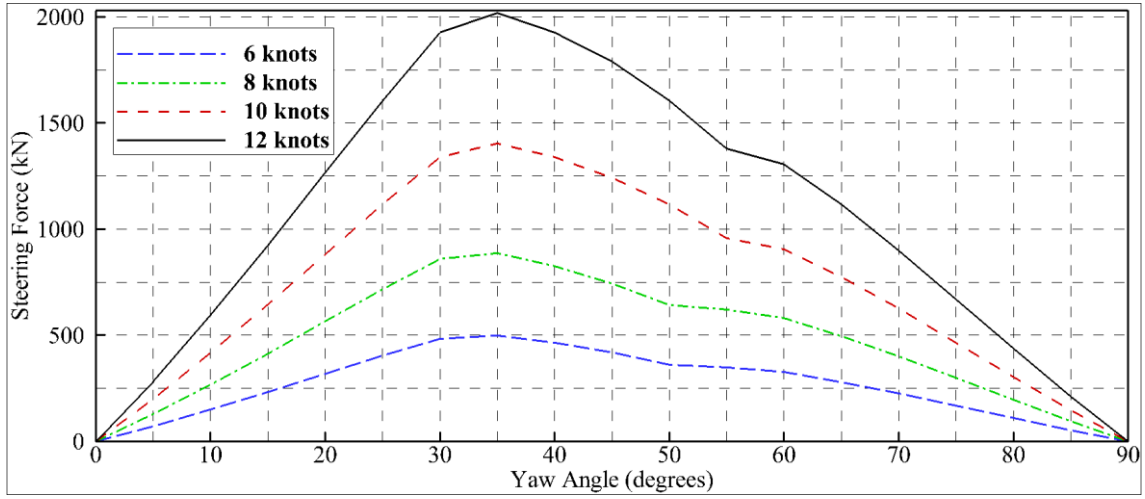


Figure 11. Steering forces for the escort tug AJAX in the pure indirect mode of escort

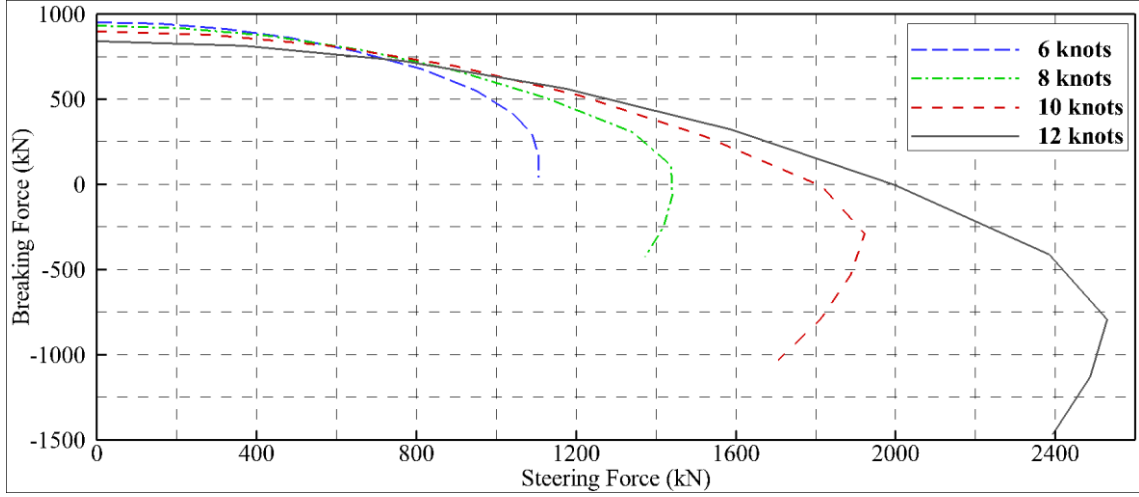


Figure 12. Steering and braking forces for the escort tug AJAX in the powered indirect mode of escort

The steering force of the escort tug AJAX in the pure indirect mode of escort is estimated by the present methodology and presented in Figure 11 for speeds of 6, 8, 10 and 12 knots. In this mode the thrusters apply only enough transverse force to maintain the yaw angle of the tug with no longitudinal thrust component. The thrust power is only a small fraction of the total power.

Although the pure indirect escort performance is a valuable indicator of the hydrodynamic performance, from the operational point of view, the escort performance is represented by the powered indirect mode, in which, maximum thrust power is used to obtain the maximum steering forces. The steering and braking forces for the escort tug AJAX in the powered indirect mode of escort are estimated by the present methodology and presented in Figure 12 for speeds of 6, 8, 10 and 12 knots. It is assumed that a total static thrust power can be provided in any direction.

## 8 CONCLUDING REMARKS

A practical computational methodology to estimate the pure and powered indirect escort performance characteristics of tractor type escort tugs was presented. The methodology is based on two distinct approaches. The

first approach is a semi-empirical method intended to be used at the earliest stages of escort tug design process with little information available. The hydrodynamic lift and drag forces due to the hull and skeg of the tug are estimated by a set of reliable semi-empirical formulae, based on model tests. The second approach is a CFD based computational methodology intended to be used at the later stages of the design process at which a precise geometric definition of the hull and appendages is available.

The semi-empirical method ignores the local flow characteristics and hence expected to give rough estimates about the performance of the vessel. The CFD based computational methodology, on the other hand, is sensitive to the details of the geometry and hence can be used to improve the form of the hull and appendages.

Estimated surge and sway forces were compared with the measurements for a tractor type escort tug, AJAX. Since the semi-empirical approach is specifically formulated for tractor type tugs, it gives excellent correlation with the experimental measurements. The results of CFD simulations, on the other hand, showed satisfactory agreement with those of the experiments, for the bare hull case. As the longitudinal force component is more prone to

the local form variations, the inaccuracies of the model geometry presumably affected the results of the surge force. As the simulations did not take the heeling motion observed in the experiments into account, the sway force was over-predicted for the large yaw angle cases with the skeg. The stall angle was also over-predicted. The results clearly point out that for an accurate and reliable escort analysis by means of CFD, the heeling angle of the tug should be included in the simulations. The inclusion of the free surface effects would also certainly increase the modelling accuracy

Overall, the results indicate that the methodology can be used to estimate escort performance characteristics of tractor type escort tugs either at the earliest stages of the design process at which only the basic design characteristics are available or at a later stage by using the developed CFD based tool for detailed investigations. This methodology could also be used to investigate the effects of main design features, such as the main dimensions, skeg geometry, and the locations of the propellers and the towing point.

## REFERENCES

- Allan R.G. (2000). The Evolution of Escort Tug Technology: Fulfilling a Promise. SNAME Transactions, Vol. 108.
- Allan R.G. and Molyneux D. (2004). Escort Tug Design Alternatives and a Comparison of their Hydrodynamic Performance, SNAME Transactions, Vol. 112.
- Ankudinov V. (1985). Ship Manoeuvring Simulation Model Including Regimes of Slow Speeds and Large Drift Angles. Report for the First International Maritime Simulation Symposium, Munich, Germany.
- Bertram V. (2000). Practical Ship Hydrodynamics. Butterworth-Heinemann.
- Blazek J. (2001). Computational Fluid Dynamics: Principles and Applications. Elsevier, Oxford, UK.
- Dabbar J. M. and Morgan J. M. (1996). Tractor Tug : Conceptual Design to Implementation. Marine Technology, Vol. 33, No 1.
- Hensen H. (1997). Tug use in Port – A Practical Guide, The Nautical Institute.
- Jahra F., Islam M., Thanyamanta W., and Molyneux D. (2015). Investigation of Hydrodynamic Loads and Flow Patterns Near an Escort Tug in Oblique Flows, Proceedings of the ASME 2015 34<sup>th</sup> International Conference on Ocean, Offshore and Arctic Engineering, Newfoundland, Canada, May 31- June 5.
- Jagannathan S., Gray D. L., Mathai T., and de Jong J. (1995). Tanker Escort : Requirements, Assessments, and Validation, SNAME Transactions, Vol. 103.
- Menter F.R. (1994). Two-Equation Eddy-Viscosity Turbulence Models for Engineering Applications. AIAA Journal 32 (8), 1598-1605.
- Molyneux W. D. and Bose N. (2008). Escort Tug at Large Yaw Angle: Comparison of CFD Predictions with Experimental Data. International Journal of Small Craft Technology, Volume 150, Part B1, Transactions of the Royal Institution of Naval Architects.
- Norrbin, N. (1971). Theory and Observations on the Use of a Mathematical Model for Ship Manoeuvring in Deep and Conned Water. Technical Report 63. Swedish State Shipbuilding Experimental Tank. Gothenburg
- OCIMF. (1997). Safety of Navigation through the Bosphorus Strait, Sea of Marmara and Dardanelles, Report submitted by the Oil Companies International Marine Forum (OCIMF), IMO Marine Safety Committee (MSC), MSC 67/7/12.
- OCIMF. (2007). Guidelines for Transiting the Turkish Straits. Briefing Paper for OCIMF Member Companies, Oil Companies International Marine Forum (OCIMF).
- Patankar S.V. (1980). Numerical Heat Transfer and Fluid Flow, McGraw-Hill, New York, USA.
- Quadvlieg F. and Kaul S. (2006). Development of a Calculation Program for Escort Forces of Stern Drive Tug Boats. The 19<sup>th</sup> International Tug&Salvage Convention and Exhibition, Beurs World Trade Center, Rotterdam, Holland, 24-28 April.
- Sturmöhöfel U. and Bartels J-E. (1993). Basic Requirements for Safe Escort Vessels – Theoretical Consideration and Model Measurements. RINA International Conference on Escort Tugs, Design, Construction and Handling – The Way Ahead, London, England.
- Tennekes H., Lumley J.L. (1972). A First Course in Turbulence. MIT Press, Cambridge, UK.
- Whicker L. F. and Fehlner L. F. (1958). Free Stream Characteristics of a Family of Low Aspect Ratio, All Movable Control Surfaces for Application to Ship Design. David Taylor Model Basin, Washington DC, report No 933.

*(Intentionally left blank)*

## A Deforming Grid Approach for Ship Maneuvering Simulations

Omer Faruk Sukas<sup>1\*</sup>, Omer Kemal Kinaci<sup>1</sup>

<sup>1</sup>*Yildiz Technical University, Naval Architecture and Maritime Faculty, 34349 Besiktas-Istanbul, Turkey*

**Abstract:** In this study, a deforming grid strategy is adopted to obtain non-dimensional forces and moments of various KVLCC2 models in different scales. A wide variety of experimental results exist in the literature and the results generated in this study utilizing the deforming grid are compared with the results obtained with the overset grid approach given in a reference article. Similar results were obtained for static drift tests with both meshing strategies. Additionally, the model scale effect is investigated in different drift angles and the numerical uncertainty was calculated. For the pure sway test, it is found out that the deforming grid responds well when the sway amplitude is small. For higher amplitudes, the effectiveness of the deforming grid still remains unknown as more computational results using the overset grid are needed.

**Keywords:** maneuvering, scale effect, overset grid, deforming grid.

### 1 INTRODUCTION

Prediction of the maneuvering forces and moments is one of the complex problems in naval hydrodynamics due to the asymmetric flow around the underwater hull. In ship resistance problems, the ship goes along a straight line, whereas the ship tries to turn or make various kind of motions in maneuvering problems. Unlike the vertical motions in seakeeping simulations, there is no restoration forces in the horizontal plane for maneuvering motions.

Maneuvering abilities of a ship must be determined at the initial design stage and can be evaluated from the model tests, empirical/semi-empirical regression analysis or computer simulations using numerical methods. Experimental model tests are comprised of the free running and captive model tests. The latter experimental option that includes both PMM and rotating arm tests is more confidential to determine the maneuvering coefficients. However, disadvantage of this method is that it is expensive and time consuming. On the other hand, the methods based on empirical database are easy and quick to return results, yet these methods only give suitable prediction of the hydrodynamic derivatives when the main particulars of the ship of interest are proper for the experimental database.

As the high performance computing develops in the last few decades, extensive studies have been made on computational methods to assess the hydrodynamic characteristics of a ship. A wide range of Reynolds Average Navier Stokes (RANS) based CFD methods were used to evaluate maneuvering performance. Furthermore, the results obtained by CFD were generally compared with model test data to show the accuracy for estimating the maneuvering coefficients. Sakamoto et al. validated the results of hydrodynamic derivatives, force and moment coefficients for a surface combatant DTMB 5415 bare hull with static and dynamic PMM simulations

by utilizing their URANS based code CFDShip-Iowa. Also an extended work for the numerical uncertainty has been done to analyze the CFD simulation results. Related investigations about this topic has continued with the studies of He et al. and Kim et al. The targets of these studies were to estimate the linear hydrodynamic derivatives of KCS and KVLCC2 benchmark ships by utilizing unsteady RANS model and comparing numerical results with the model test data. In fact, these hydrodynamic coefficients are obtained to assess the maneuvering performance of the vessel and the next step is to apply the computed coefficients to selected mathematical model to predict the turning circle or zig-zag maneuvers of the model ship. Hajivand and Mousavizadegan performed a similar study and compared the CFD results obtained with the available experimental data. The fourth order Runge-Kutta method were implemented to simulate the turning and zig-zag maneuvers. Similarly with the previous work, the maneuvering characteristic of a fishing vessel were both experimentally and numerically evaluated by Obreja et al. The numerical model was validated with the experimental values of zig-zag and spiral tests in the condition of calm water. Shenoi et al. investigated the maneuvering capability of a container ship by taking into account the roll effect. The main scope of the study was to estimate the maneuvering coefficients with the coupled sway-yaw-roll motions. Moreover, Jin et al. carried out a comprehensive investigation about the effect of ship model size on the linear maneuvering coefficients. KVLCC2 model was selected to predict hydrodynamic forces and moments by using overset grid system for static drift, pure sway and pure yaw tests.

Scale effects on maneuvering forces and moments for the rudder appended container ship model KVLCC2 are investigated in this paper. Numerical simulations of static drift and pure sway test were performed by using

\* Corresponding author e-mail: [ofsukas@yildiz.edu.tr](mailto:ofsukas@yildiz.edu.tr)

deforming grid design for varying drift angles and different model sizes.

## 2 NUMERICAL MODELING

Computations for static drift and pure sway tests were carried out in deep and calm water condition by using RANSE based commercial solver Star-CCM+. In this study, different scale simulations of the KVLCC2 hull have been performed by using unsteady RANSE approach. In order to compare the numerical results with experimental data, 1/45.714, 1/58 and 1/100 bare hull of the KVLCC2 model were considered for static drift tests while only the scale factor of 1/58 rudder appended hull was used for pure sway test. The hull form of the KVLCC2 model and the main dimensions of the hull with respect to scale factors are given in figure 1 and table 1, respectively.



**Figure 1.** Geometrical representation of rudder appended KVLCC2 model.

**Table 1.** Main particulars of the model with different sizes.

| Symbols                       | Main Dimensions |         |        |
|-------------------------------|-----------------|---------|--------|
| $\lambda$                     | 1/45.714        | 1/58    | 1/100  |
| LBP(m)                        | 7.00            | 5.52    | 3.20   |
| B(m)                          | 1.17            | 1.00    | 0.58   |
| T(m)                          | 0.46            | 0.36    | 0.21   |
| $\Delta$ (tonnes)             | 3.27            | 1.61    | 0.32   |
| $I_{xx}$ (kg.m <sup>2</sup> ) | 716.21          | 257.65  | 17.27  |
| $I_{zz}$ (kg.m <sup>2</sup> ) | 10014.43        | 3066.14 | 204.82 |

In maneuvering simulations, the whole domain is created to investigate the asymmetrical flow around the underwater hull. In this study, the boundaries of the control volume were determined based on the ITTC standards [ITCC, 2011, "Practical Guidelines for Ship CFD Application," ITTC Recommended Procedures and Guidelines, 7.5-03-02-03]. It extends 2L<sub>OA</sub> front of the hull, 4L<sub>OA</sub> aft of the hull, 2 L<sub>OA</sub> to the sides, 2 L<sub>OA</sub> below of the model and 1 L<sub>OA</sub> upward of the hull. In order to avoid any blockage effect, the computational domain was created considerably large. Even so, damping boundaries option was enabled to overcome numerical errors caused by any reflected waves. The boundary conditions except flow outlet were prescribed as velocity inlet and pressure outlet condition was dictated to the flow outlet boundary. Also non-slip wall condition was selected for the hull surface. An unstructured trimmed grid design with prism layer was applied to meshing system. Besides, local grid refinements at the free surface and vicinity of the hull were done. The mesh system for the static drift test is illustrated in figure 2.

The speed of the hull was considered as  $Fn = 0.142$ . Hydrodynamic forces and moments were calculated according to the local coordinate system of the ship. For the static drift test, the hull motions were constrained in

only 3DOF (heave, pitch and surge) while the all degree of motions of the hull in the pure sway test were enabled except roll motion in order to compare the results with experimental data. The flow model used is implicit unsteady with segregated solver and the solution algorithm is SIMPLE. Second-order upwind spatial and first-order temporal discretization schemes were used. k- $\epsilon$  model was selected as turbulence model for all simulations. The time step used in the simulations was based on the velocity of the flow and it was determined by using the ITTC procedure below:

$$\Delta t = 0.01 - 0.005L/V \quad (1)$$

where  $L$  is the length of the ship (m) and  $V$  is the ship speed (m/s).

A convergence criterion of residuals by order of  $10^{-3}$  for inner iterations was selected. The solution is accepted as converged when there is a repetitive oscillation of the forces and moments. The domain sizes, boundary conditions, grid and physical settings are same as that used for the pure sway simulations.

## 3 CFD VERIFICATION AND VALIDATION

CFD verification and validation is made using three grid types following the procedure stated by Stern et al. (2001). The procedure is carried out for the static drift test with static drift angle  $\beta = 4^\circ$  for a 1/45.714 scaled model of KVLCC2 to be consistent with the work of Jin et al. (2016). Non-dimensional force  $X'$  (which is presented in the next section) is taken as the integral variable in uncertainty calculations. The total uncertainty  $U_N$  in numerical simulations are given as:

$$U_N = \sqrt{U_I^2 + U_G^2 + U_T^2} \quad (2)$$

Here;  $U_I$  is the iterative uncertainty,  $U_G$  is the grid uncertainty and  $U_T$  is the time step size uncertainty. The simulation results for the three different grids to assess the grid uncertainty  $U_G$  are given in table 2.

**Table 2.** Three different grids and  $X'$  results.

|          | GRID 4  | GRID 3  | GRID 2  | GRID 1  |
|----------|---------|---------|---------|---------|
| ELEMENTS | 640k    | 1600k   | 4000k   | 10000k  |
| $X'$     | -0.0193 | -0.0173 | -0.0172 | -0.0171 |

The numerical uncertainty was calculated for grid 3. The upper and lower limits of  $X'$  are given in table 3. From this table the iterative uncertainty was found to be  $U_I = 2.89\% S_G$ .

**Table 3.** Upper and lower limits for iterative uncertainty.

|        | $S_U$   | $S_L$   | $X'$    |
|--------|---------|---------|---------|
| GRID 3 | -0.0178 | -0.0168 | -0.0173 |

The grid uncertainty with respect to the results given in table 2 is  $U_G = 3.37\% S_G$ . Therefore the total numerical uncertainty is considered to be small and  $U_N = 5.48\% S_G$ . The experimental result of the 1/45.714 scaled model at  $\beta = 4^\circ$  is  $X' = -0.0162$ . The error is bigger than the

total numerical uncertainty  $E > U_N$  and the results are not validated.

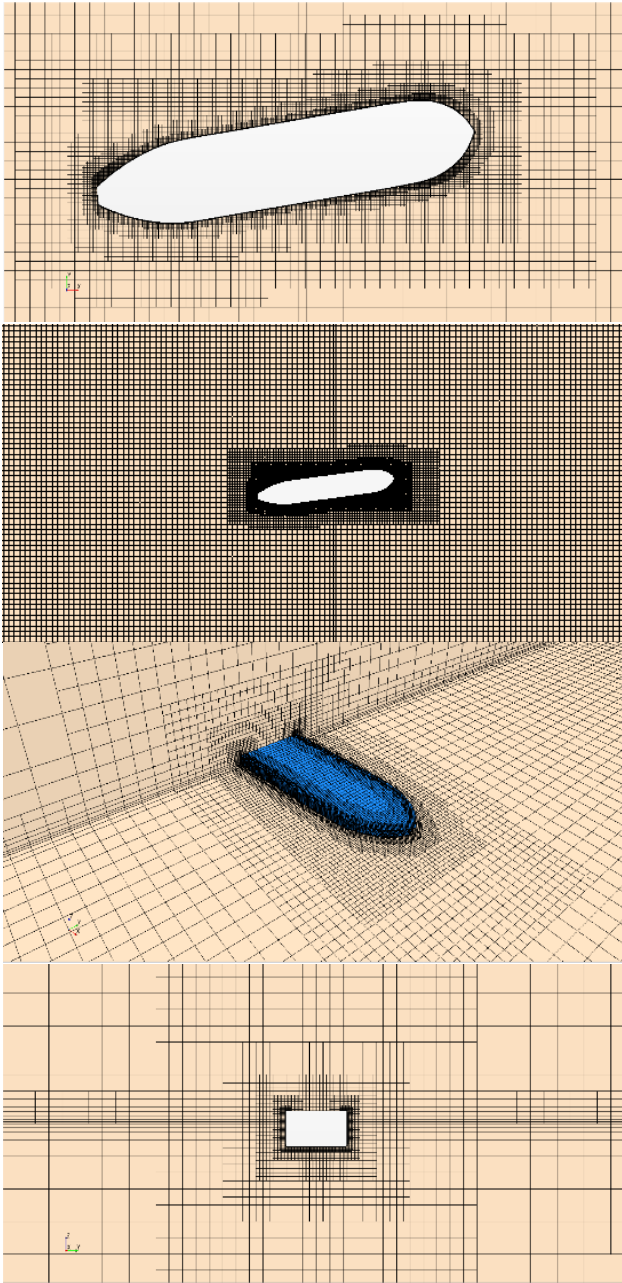


**Figure 2.** Deforming grid system with different perspectives.

## 4 RESULTS

### 4.1 Non-dimensional coefficients

Forces ( $X'$  and  $Y'$ ) and moment ( $N'$ ) acting on the ship are non-dimensionalized using the equations given below:

$$X' = 0.5\rho SV^2 LT \quad (3)$$

$$Y' = 0.5\rho SV^2 LT \quad (4)$$

$$N' = 0.5\rho SV^2 L^2 T \quad (5)$$

### 4.2 Static drift

The static drift numerical simulations were made by fixing the ship in the horizontal ( $xy$ ) plane and letting a velocity inflow. The ship had an angle  $\beta$  with the

incoming flow and it was free to heave and pitch. The ship was towed in a straight course as shown in figure 3.

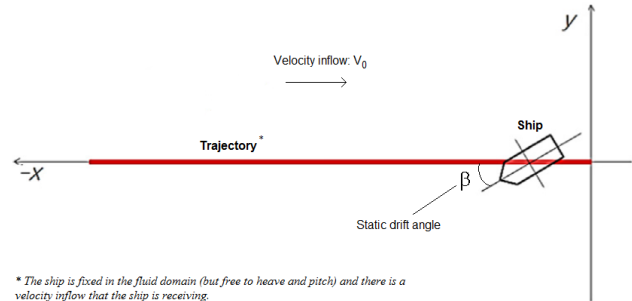


**Figure 3.** A perspective of the numerical static drift test.

The non-dimensional force component along the  $x$ -axis,  $X'$  is given in figure 4 for different scales. It can be said that scaling had a strong impact on  $X'$  as computational results suggested a significant increase in  $|X'|$  as the ship model got smaller. The comparison given in the same figure revealed a satisfactory agreement between the computational results although the slope of the curve obtained in this study was steeper.

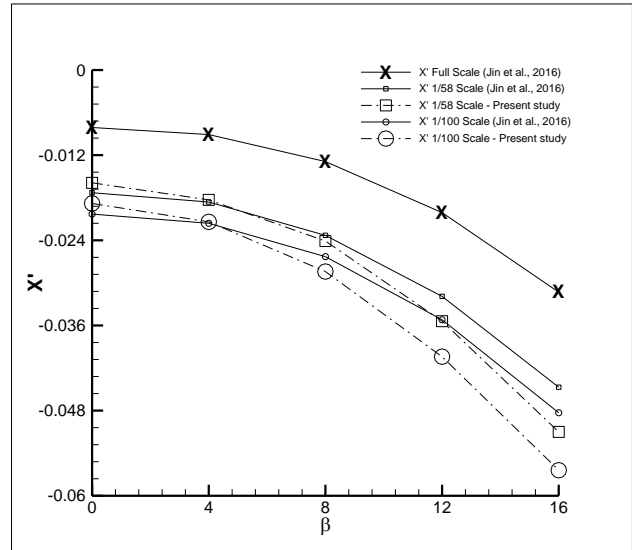


**Figure 4.** Comparison of non-dimensional force  $X'$  with Jin et al. (2016) for different scales.

The non-dimensional force component along the  $y$ -axis,  $Y'$  is given in figure 5. The agreement between the computational results was remarkable. The scale effect was not observed in  $Y'$  as much as it was affecting  $X'$ . Although the difference is more pronounced at higher static drift angles for  $Y'$ , the discrepancy is still much more less.

The underlying reason of the scale affecting  $X'$  much more compared to  $Y'$  is due to the viscous forces affecting a body more significantly in the flow direction. An analogy could be made here with the flow around a wing that has a positive angle of attack. Figure 6 represents a schematic view of an airfoil with a positive angle of attack and a ship with a static drift angle. In aerodynamic applications, the calculation of lift of an airfoil is much less problematic than the calculation of drag due to the

viscous forces affecting the body much more in  $X_0$  direction. The lift is less affected by the viscous forces and it may even be calculated by the potential theory with good accuracy if the angle of attack is not having significant values (it should not reach the stall angle where viscosity initiates vortex shedding from the wing). Therefore it may be said that the lift of a wing is *nearly independent* of the Reynolds number whereas this statement does not hold for the drag. The drag is seriously affected by the Reynolds number which is the ratio of the inertial forces to the viscous forces. The scale effect possessing higher affects on  $X'$  compared to  $Y'$  can be rationalized this way. Therefore, less difference in  $Y'$  in different scales compared to  $X'$  was an expected result.

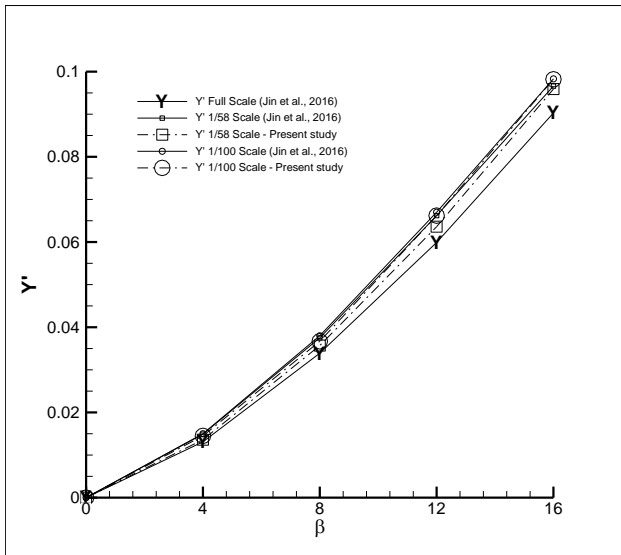


**Figure 5.** Comparison of non-dimensional force  $Y'$  with Jin et al. (2016) for different scales.

The non-dimensional moment  $N'$  is presented in figure 7. From that figure, it may be said that the scale effect does not play a significant role. The only disagreement seems to be the 1/58 scaled model in our study but the underlying issue is not resolved yet. However, it is clear that the calculation of moment on a body in fluid flow is more complex than the calculation of forces because moment is a combination of all forces acting upon a body.

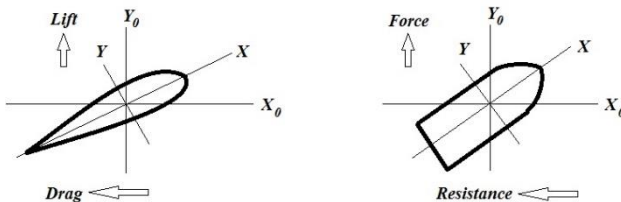


**Figure 6.** A wing with a positive angle of attack and a ship with a static drift angle.

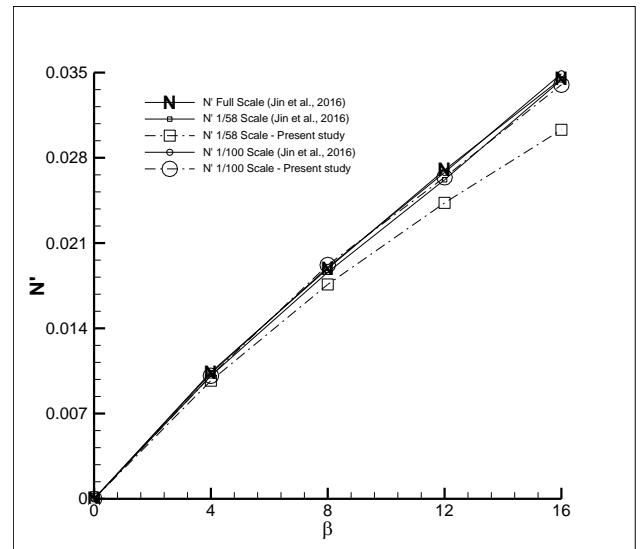


**Figure 7.** Comparison of non-dimensional force  $N'$  with Jin et al. (2016) for different scales.

#### 4.3 Pure sway

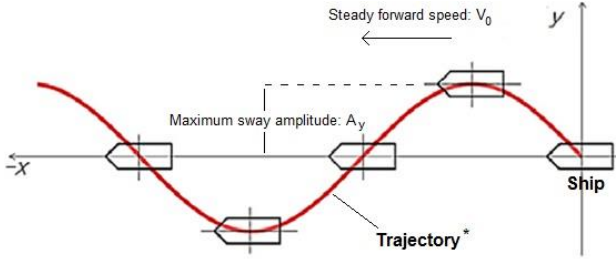
The pure sway test for KVLCC2 was carried out numerically with a Planar Motion Mechanism (PMM) mode implemented in Star CCM+. The governing equations of PMM for the ship position  $R$  whose motions in the vertical direction ( $z$  – axis) are neglected are given as:

$$R_x = V_0 \cdot t \quad (6)$$

$$R_y = A_y \cdot \sin \omega t \quad (7)$$

where  $R_x$  and  $R_y$  denote the positions in the  $x$  and  $y$  axes respectively.  $V_0$  is the steady forward speed,  $A_y$  is the maximum sway amplitude and  $\omega$  is the oscillation frequency.

The numerical analyses were carried out by giving the ship a steady forward speed in the  $x$  direction and letting the fluid domain have this same steady forward speed. In another words, the fluid domain was not fixed and it was moving in the same trajectory with the ship. This helps reducing the possible drastic deformations of the mesh elements in the fluid domain. If the fluid domain was instead a fixed one, then the breadth of the fluid domain should have been bigger so that the ship would not have been affected by the side walls. Moreover, the mesh element deformations might have been reaching an undesired level if the sway amplitude was given higher. The dynamic fluid domain that corresponds with the motions of the ship in the horizontal plane brings such advantages and therefore it was preferred in this work for the pure sway test. A schematic view of the numerical pure sway test is given in figure 8.



\* The trajectory applies to the ship and the fluid domain surrounding it. However, the steady forward speed is only in the x-axis direction.

**Figure 8.** A perspective of the numerical pure sway test.

The non-dimensional forces and moments obtained in this study with the deforming grid were compared with the numerical results of Jin et al. (2016) and experimental results from the SIMMAN 2008 workshop published by Stern et al. (2011). The comparisons are given in figure 9 for one complete cycle of the ship in pure sway. The time  $t$  in that figure was non-dimensionalized by the sway period  $T$ .

The numerical results obtained in this study with the deforming grid seemed to be in very good accordance with the numerical results obtained by Jin et al. (2016) by the overset grid. Speaking in terms of the computational results, there was only some minor discrepancy in the non-dimensional force  $X'$ . The non-dimensional force  $Y'$  and the non-dimensional moment  $N'$  seemed to be nearly on top of each other.

Although the computational results were in very good accordance for  $Y'$ , they seemed to be a little less than what the experimental results suggest. However, this difference was not reflected to the moment imposed on the ship as the difference in  $N'$  between the computational and experimental results were far less than  $Y'$ .

Due to the nature of the implicit unsteady time scheme, the flow around the ship just starts forming at the first sway cycle of the ship. It is considered that at the second cycle, the flow around the ship reaches a more stable state. Therefore for the sake of presenting better results, the second sway cycle of the ship was given in figure 9. Additionally, the pure sway results presented in the same figure was shifted to the left by  $0.1t/T$  to eliminate large nonphysical fluctuations occurring at the beginning of the numerical simulations which was also suggested by Jin et al. (2016).

Although the generated results with the deforming grid seem to be compatible with the overset grid results in this study, it is still unknown how the deforming elements will behave in higher sway amplitudes. There is a risk of generation of highly skewed elements in the fluid domain as the amplitude increases, which might lead to low quality mesh and non-physical results in return.

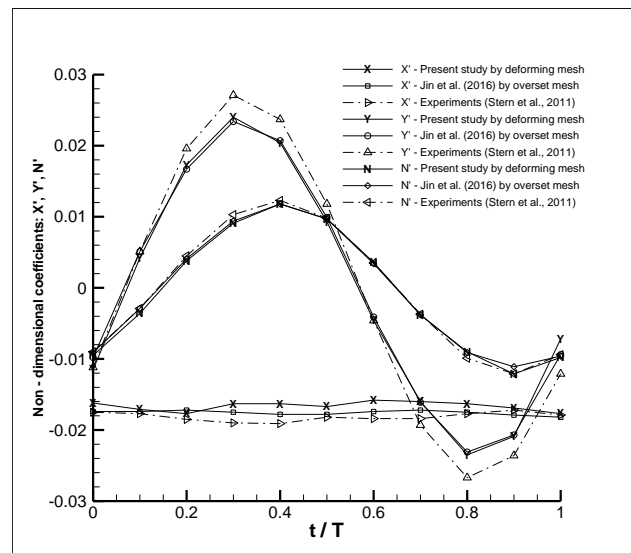


**Figure 9.** Comparison of the results obtained in this study with the numerical results of Jin et al. (2016) and the experiments (Stern et al., 2011).

## 5 CONCLUSIONS

In this study, non-dimensional coefficients of KVLCC2 were obtained using a deforming grid design and they were compared with experiments and another numerical simulation implementing overset grid system. Following statements were made regarding the outcomes of this study:

- Model scale has a strong impact on  $X'$  in static drift test. It does not have that much effect on  $Y'$ .
- Both computational results and experiments are in accordance for the pure sway tests.
- The deforming grid system results are compatible with the overset grid system results in general for small sway amplitudes.

Numerical simulations still continue for the some other scales and pure yaw will also be assessed in further studies. Calculation of maneuvering coefficients will reveal the robustness of the selection of the grid system in numerical simulations.

## REFERENCES

- He, S., Kellett, P., Yuan, S., Incecik, A., Turan, O., Boulogeoris, E. (2016). 'Manoeuvring prediction based on CFD generated derivatives'. *Journal of Hydrodynamics* **28**(2), pp.284-292.
- Hajivand, A., Mousavizadegan, S., H. (2015). 'Virtual simulation of maneuvering captive tests for a surface vessel'. *International Journal of Naval Architecture and Ocean Engineering* **7**(5), pp.848-872.
- ITCC, (2011). 'Practical Guidelines for Ship CFD Application'. *ITTC Recommended Procedures and Guidelines*, 7.5-03-02-03.
- Jin, Y., Duffy, J., Chai, S., Chin, C., Bose, N. (2016). 'URANS study of scale effects on hydrodynamic manoeuvring coefficients of KVLCC2'. *Ocean Engineering* **118**, pp.93-106.

- Kim, H., Akimoto, H., Islam, H. (2015). 'Estimation of the hydrodynamic derivatives by RaNS simulation of planar motion mechanism test'. Ocean Engineering **108**, pp.129-139.
- Obreja, D., Nabergoj, R., Crudu, L., Sandita, P. (2010). 'Identification of hydrodynamic coefficients for manoeuvring simulation model of a fishing vessel '. Ocean Engineering **37**(8-9), pp.678-687.
- Sakamoto, N., Carrica, P. M., Stern, F. (2012). 'URANS simulations of static and dynamic maneuvering for surface combatant: part 1. Verification and validation for forces, moment and hydrodynamic derivatives'. Journal of Marine Science and Technology **17**(4), pp.422-445.
- Shenoi, R., R., Krishnankutty, P., Selvam, R., P. (2016). 'Study of Maneuverability of Container Ship With Nonlinear and Roll-Coupled Effects by Numerical Simulations Using RANSE-Based Solver'. Journal of Offshore Mechanics and Arctic Engineering-Transactions of the ASME **138**(4).
- Stern, F., Wilson, R., V., Coleman, H., W., Paterson, E., G. (2001). 'Comprehensive approach to verification and validation of CFD simulations – Part 1: Methodology and procedures'. Journal of Fluids Engineering – Transactions of the ASME **123**(4), pp.793-802.
- Stern, F. et al. (2011). 'Experience from SIMMAN2008 – The First Workshop on Verification and Validation of Ship Maneuvering Simulation Methods'. Journal of Ship Research **55**(2), pp.135-147.

## **Author Index**

- Angelou, M. 39  
Arslan, S. 31  
Atlar, M. 49, 57  
Ayaz, Z. 75  
Aydın, Ç. 105  
Bal, Ş. 89  
Bilici, G. 105  
Birmingham, R. 67  
Carchen, A. 57  
Chatjigeorgiou, I. K. 21  
Demir, E. 85, 99  
Duman, S. 89  
Faltinsen, O. M. 1  
Gökçay, S.  
Hasegawa, K. 11  
Hu, Z. 67  
Irimagha, E. 67  
İnsel, M.  
Knacı, O. K. 117  
Kurdoğlu, S. 85, 99  
Miles, A. 49  
Miloh, T. 21  
Özden, C. 85, 99  
Quadvlieg, F. 13  
Sarıöz, K. 105  
Sasaki, N. 49, 57  
Saydam, A. Z.  
Shi, W. 57  
Spyrou, K. J. 39  
Sukas, Ö. F. 117  
Takeda, T. 49  
Türkmen, S. 49  
Ünal, U. O. 105  
Woodward, M. 67